

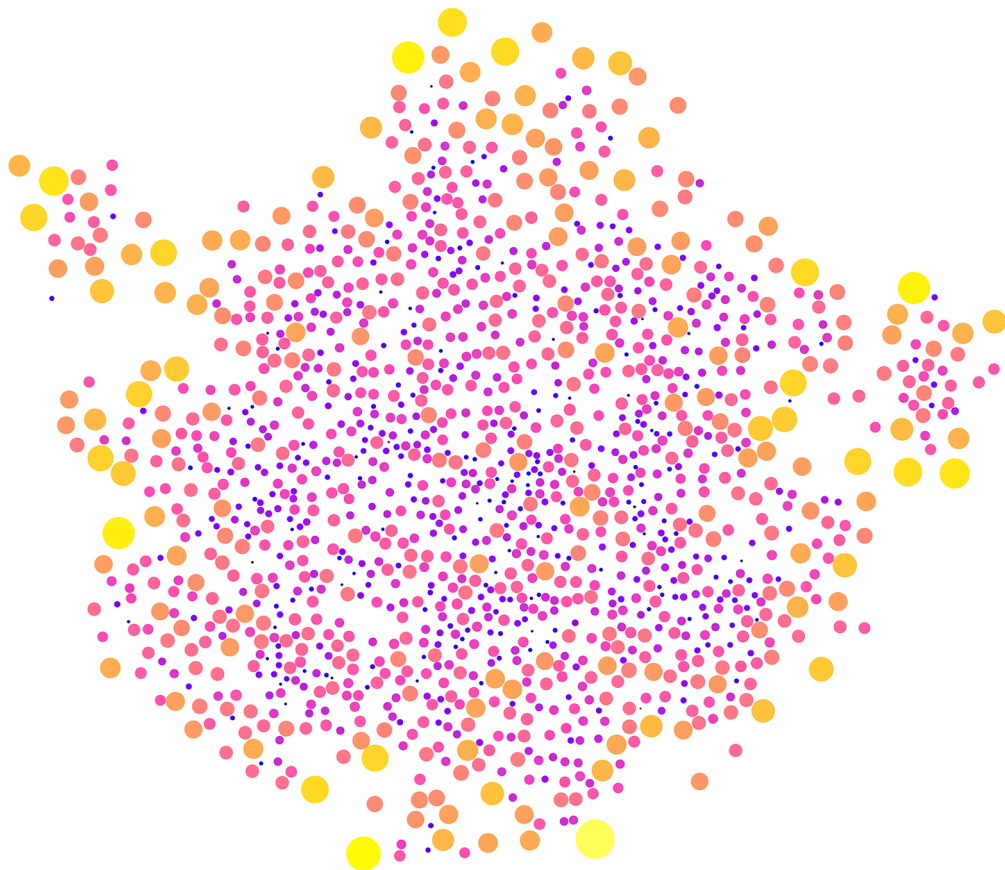
JYU DISSERTATIONS 834

---

Mikko Kuha

# Simulation of Quark-Gluon Plasma Initial States with Monte-Carlo EKRT Model

---



UNIVERSITY OF JYVÄSKYLÄ  
FACULTY OF MATHEMATICS  
AND SCIENCE

JYU DISSERTATIONS 834

---

**Mikko Kuha**

# **Simulation of Quark-Gluon Plasma Initial States with Monte-Carlo EKRT Model**

Esitetään Jyväskylän yliopiston matemaattis-luonnontieteellisen tiedekunnan suostumuksella  
julkisesti tarkastettavaksi Ylistönrinteen auditoriossa FYS1  
lokakuun 25. päivänä 2024 kello 12.

Academic dissertation to be publicly discussed, by permission of  
the Faculty of Mathematics and Science of the University of Jyväskylä,  
in Ylistönrinne, auditorium FYS1, on October 25, 2024, at 12 o'clock.



JYVÄSKYLÄN YLIOPISTO  
UNIVERSITY OF JYVÄSKYLÄ

JYVÄSKYLÄ 2024

Editors

Ilari Maasilta

Department of Physics, University of Jyväskylä

Päivi Vuorio

Open Science Centre, University of Jyväskylä

Copyright © 2024, by the author and University of Jyväskylä

ISBN 978-952-86-0330-6

ISSN 2489-9003

Permanent link to this publication: <http://urn.fi/URN:ISBN:978-952-86-0330-6>

## ABSTRACT

Kuha, Mikko

Simulation of Quark-Gluon Plasma initial states with Monte-Carlo EKRT model

In this thesis, the initial state of the quark gluon plasma (QGP) generated in ultrarelativistic heavy-ion collisions is studied. For this purpose, the author has created from scratch a completely new Monte-Carlo (MC) implementation of the successful Eskola-Kajantie-Ruuskanen-Tuominen (EKRT) initial state model. In this model, the energy density generated in the heavy-ion collision is modelled via minijets, small—down to 1 GeV—transverse momentum  $p_T$  quarks and gluons, produced via perturbative Quantum Chromodynamics (pQCD). A key ingredient is the saturation conjecture, here a local version which fluctuates event-by-event (EbyE), which dynamically controls the generated minijet multiplicity. Among the EbyE fluctuating minijet production, the most important new feature of the model is the rapidity dependence of the output. As the four-momentum of the minijets is fully known, the EbyE fluctuating energy-momentum tensor  $T^{\mu\nu}$  of the QGP initial state can be computed, enabling 3+1D fluid dynamical simulations producing rapidity dependent observables. Another novel feature are the developed parton distribution functions (PDFs) which include spatial dependence in nuclear shadowing in a new way that allows also for the largest density fluctuations in the nuclear matter. Also energy conservation and valence quark number conservation are now considered. Among its other features, the new MC-EKRT event generator includes also a nucleon substructure model and the tracking of the partonic flavour of the generated minijets.

The heart of the MC-EKRT event generator, the calculation of the inclusive pQCD cross section of producing two jets in a nucleon-nucleon collision  $\sigma_{\text{jet}}$  with nuclear shadowing, is employed in the article [PI] to investigate the possibility of the need to account for nuclear shadowing in Monte-Carlo Glauber models by using recent experimental data on heavy vector boson production at the LHC as constraints. The article [PII] introduces the MC-EKRT model in detail. The articles [PII] and [PIII] demonstrate the usage of the MC-EKRT initial states in a centrality-class averaged 3+1D hydrodynamical simulation ([PII]) and in boost independent 2+1D EbyE fluid simulation ([PIII]), yielding excellent agreement with the experimental data in the observed rapidity distributions of the charged particle multiplicity  $dN_{\text{ch}}/d\eta$  in Pb+Pb collisions at  $\sqrt{s_{NN}} = 5.02$  and 2.76 TeV, and in Au+Au collisions at  $\sqrt{s_{NN}} = 200$  GeV, and in their corresponding observed flow coefficients  $v_n$ .

Keywords: Heavy-ion collision, Monte-Carlo simulation, EKRT model, perturbative QCD, Quark-Gluon Plasma, saturation, rapidity distributions, minijets



## TIIVISTELMÄ (ABSTRACT IN FINNISH)

Kuha, Mikko

Kvarkki-gluoniplasman alkutilan simulointi käyttäen Monte-Carlo EKRT -mallia

Tutkin tässä väitöskirjassa ultrarelativistisissa raskasionitörmäyksissä syntyvän kvarkki-gluoniplasman (QGP) hydrodynaamista alkutilaa. Olen ohjelmoinut tätä tarkoitusta varten alusta alkaen uuden Monte Carlo (MC) -toteutuksen jo menestyneestä Eskola-Kajantie-Ruuskanen-Tuominen (EKRT) alkutilamallista. MC-EKRT -mallissa raskasionitörmäyksessä syntyvää energiatiheyttä mallinnetaan minijettien avulla. Minijetit ovat kvanttiväridynamiikan häiriöteorialla (pQCD) tuotettuja kvarkkeja ja gluoneja, joilla on erittäin pieni poikittaisliikemäärä  $p_T$ — jopa 1 GeV. Mallin keskeinen rakennusosa on saturaatio-oletus, joka ottaa huomioon paikalliset ainetiheyden vaihtelut törmäyksestä toiseen (EbyE). Saturaa-tion tehtävä on dynaamisesti rajoittaa tuotettujen minijettien multiplisiteettiä. Sen ohella, että uudessa MC-EKRT:ssä minijettien tuotto vaihtelee EbyE, mallin tärkein uusi ominaisuus on tuotetun QGP-alkutilan rapiditeettiriippuvuus. Koska minijettien neliliikemäärät tunnetaan, voidaan myös QGP-alkutilan energia-liikemääränsensori  $T^{\mu\nu}$  laskea jokaiselle törmäykselle erikseen. Tämä mahdollistaa plasman rapiditeettiriippuvaisten suureiden 3+1 ulotteisen (3+1D) hydrodynaami-sen simulaation. Toinen merkittävä uusi ominaisuus on partonien jakauma-funktiot (PDF:t), jotka ottavat huomioon paikkariippuvuuden ydinvarjostuksessa uudella tavalla, joka sallii myös kaikkein voimakkaimmat tiheysvaihtelut ydin-aineessa. Tekemääni tapahtumageneraattoriin on sisällytetty myös energian ja valenssikvarkkien lukumäärien säilymisvaatimus, sekä nukleonien alirakenne-malli, ja lisäksi sen tuottamien minijettien partonimakua seurataan.

MC-EKRT-tapahtumageneraattorin ytimessä on kahden jetin tuottamisen inklusiivisen pQCD-vaikutusalan  $\sigma_{\text{jet}}$  laskeminen ydinvarjostuksella kahden nukleonin törmäyksessä. Käytimme samaa laskentaa artikkelissa [PI] tutkiessamme tarvetta ottaa huomioon ydinvarjostus Monte Carlo Glauber -malleissa käyttä-mällä rajoitteina viimeaikaisia kokeellisia LHC-tuloksia raskaiden vektoribosoni-en tuotosta. Artikkelissa [PII] käymme MC-EKRT -mallin yksityiskohtaisesti läpi ja annamme esimerkin MC-EKRT-alkutilojen käytöstä keskeisyysluokakeskiarvoistetussa 3+1D hydrodynaamisessa simulaatiossa. Artikkelini [PIII] havainnollis-taa MC-EKRT-alkutilojen käyttöä puskuinvariantissa 2+1D EbyE hydrodynaami-sessa simulaatiossa. Tuottamamme teoreettiset ennusteet yhtenevät erinomaisesti kokeellisten tulosten kanssa varattujen hiukkasten multiplisiteetin rapiditeettiri-ippuvuudesta  $dN_{\text{ch}}/d\eta$  lyijy–lyijy –törmäyksissä energioilla  $\sqrt{s_{NN}} = 5.02$  TeV ja 2.76 TeV, sekä kulta–kulta –törmäyksissä energialla  $\sqrt{s_{NN}} = 200$  GeV. Samoin vastaavien virtauskertoimien  $v_n$  lasketut arvot olivat hyvin yhteneviä kokeellis-esti havaittujen kanssa.

Avainsanat: Raskasionitörmäys, Monte-Carlo simulaatio, EKRT-malli, kvanttiväridynamiikka, häiriöteoria, kvarkki-gluoniplasma, saturaatio

**Author**

Mikko Kuha  
Department of Physics  
University of Jyväskylä  
Finland

**Supervisors**

Professor Kari J. Eskola  
Department of Physics  
University of Jyväskylä  
Finland

University Researcher Harri Niemi  
Department of Physics  
University of Jyväskylä  
Finland

Senior Lecturer Hannu Paukkunen  
Department of Physics  
University of Jyväskylä  
Finland

**Reviewers**

Senior Lecturer Korinna Zapp  
Department of Physics  
Lund University  
Sweden

Emmy Noether Research Group Leader  
Aleksas Mazeliauskas  
Institute for Theoretical Physics  
University of Heidelberg  
Germany

**Opponent**

Professor Kimmo Tuominen  
Department of Physics  
University of Helsinki  
Finland

## PREFACE

This little book represents the culmination of immense work spanning over seven years—almost a quarter of my life—from April 2017 to June 2024. Gone are the days when science was the domain of solitary geniuses in their lonely chambers. I owe my gratitude to a number of people who made this work possible.

First and foremost, I extend my thanks to Drs. Zapp and Mazeliauskas for meticulously reviewing this thesis. Additionally, I appreciate Prof. Tuominen for graciously agreeing to act as my opponent.

Acknowledging the organizations that deserve credit, I begin with the Department of Physics of the University of Jyväskylä, where the thesis work was conducted. My work was also a part of the QCD-theory projects at the Helsinki Institute of Physics and the Center of Excellence in Quark Matter of the Academy of Finland (Projects No. 346325 and 364192). The financial support from the Academy of Finland projects no. 297058 and 330448 significantly contributed to this endeavor. This work is also part of the European Research Council Project No. ERC-2018-ADG-835105 YoctoLHC. Furthermore, during the years 2019–2021, I received grants from the Vilho, Yrjö, and Kalle Väisälä Foundation. Lastly, the computer capacity provided by the Finnish Computing Competence Infrastructure (FCCI) (persistent identifier urn:nbn:fi:research-infras-2016072533), as well as the computation resources from the Finnish IT Center for Science (CSC), project jyy2580, played the crucial role of handling the simulation workload of my research.

I have been incredibly fortunate to work under the guidance of Prof. Kari J. Eskola throughout my academic journey, starting all the way from my Bachelor's thesis. Prof. Eskola's endless patience, tact, and empathy have left an indelible mark on me, serving as a model example of how a superior should treat their employees. This valuable lesson is one I will carry with me for life. My second supervisor Dr. Harri Niemi has been a font of inspiration and support in the project for at least the last five years. With his ironclad expertise, Dr. Niemi is the one who is always correct in the end, and to whom one always should turn when facing difficult decisions. I am also thankful to Dr. Hannu Paukkunen, for co-supervising me during the first legs of my thesis, when we still had little idea of what the simulator would end up looking like. Moreover, I want to thank Dr. Ilkka Helenius for being an irreplaceable collaborator and mentor throughout my thesis work. Special thanks go to my MC-EKRT collaborators: Jussi Auvinen, Henry Hirvonen, and Yuuka Kanakubo. They have had the delight to find all the bugs in my code and re-do all their work after I fixed those issues. Working with them has been an absolute pleasure. The entire CoE group (and its predecessors) has provided me with a wonderful, welcoming, and intellectually stimulating work environment. Our out-of-office gatherings have also been most memorable. To all of you, I am sincerely grateful.

The best luck that I have had during my thesis work must be that I ended up in Holvi, which has evolved far beyond a mere grad student office. The extended

Holvi collaboration has provided delightful distractions from the daily grind. From daily lunches to unforgettable conference cruises with alumni, this community of like-minded individuals has become an extensive network of friends I am honored to know. Special thanks to my older academic siblings and mentors: Pekka, Petja, Jarkko, and Lotta. They have been invaluable sources of silent knowledge and cherished friends. In the same breath, I must mention Topi, Oskari, Miha, and Sami—special companions who shared the voyage in and out of work since our student days, helping me keep the little sanity I have intact. My physics friends from student days deserve recognition for their camaraderie. Their strong social support made completing my studies significantly easier and more enjoyable.

Effective work requires balance. Outside the office, I extend my gratitude especially to Jere, who is the trusted friend everyone wishes to have, and Henri, who tolerates texting with me like we were teenagers. Additionally, I express my thanks to all the people who have played Dungeons and Dragons with me during all these years. That hobby has enriched my life in ways I cannot hope to fully express. I appreciate as well Mikko, Petri, Jere, and Panu for our yearly cottage weekends, which I always start longing for a week after I return home. I also acknowledge the wonderful people from JTY and JDNO for companionship and making Jyväskylä a better place to live.

In recent years, significant changes have shaped my life, and during this transformative phase, I have received immeasurable help and support from remarkable people who share a similar phase of life. My boundless gratitude to you, Ville and Noora, Miha and Tiia, and Petri and Laura, for all the peer support and special moments we have shared with our families.

My parents and the rest of the family have consistently been there for me—both mentally and, at times, financially. They have also always tried their best and stayed patient and listened whenever I have tried to tell them of my scientific pursuits. Everything I am today, and everything I aspire to be in the future, rests upon the foundation laid by them. For building that foundation with love, trust, and care, I am eternally grateful.

Lastly, and most importantly, I want to express my deepest gratitude to Jade—the love of my life—for bearing with me even through the greatest hardships and stress, and for forcing me to also celebrate my successes. Along with Aamos and Elli, you give me reason to rise from bed each morning. For you three, I strive to become a better person each day.

In Jyväskylä, June 2024,

*Mikko Kuha*

## LIST OF INCLUDED ARTICLES

- PI K. J. Eskola, I. Helenius, M. Kuha and H. Paukkunen *Shadowing in inelastic nucleon-nucleon cross section?* Phys. Rev. Lett. 125 **21** 212301(2020).
- PII M. Kuha, J. Auvinen, K. J. Eskola, H. Hirvonen, Y. Kanakubo, H. Niemi *MC-EKRT: Monte Carlo event generator with saturated minijet production for initializing 3+1 D fluid dynamics in high energy nuclear collisions.* Submitted to Phys. Rev. C, arXiv: 2406.17592 [hep-ph] (Jul. 2024).
- PIII H. Hirvonen, M. Kuha, J. Auvinen, K. J. Eskola, Y. Kanakubo, H. Niemi *Effects of saturation and fluctuating hotspots for flow observables in ultrarelativistic heavy-ion collisions.* Phys. Rev. C 110 **3** 034911(2024).

### Author's contribution

The author performed the eikonal minijet model calculations, drew some of the figures and participated in the writing of the manuscript for the article [PI]. The author has programmed from scratch the MC-EKRT event generator, which was introduced and applied in the articles [PII] and [PIII], participated deeply in all the development stages of the novel MC-EKRT framework, as well as computed all the results, drew all the figures and wrote the first draft for the MC-EKRT-part of the article [PII], and participated in the writing of the whole manuscript for the article [PII]. For the article [PIII], the author implemented the nucleon substructure model into the MC-EKRT framework, participated in the development of the ideas and realizations there, and participated in the writing of the article.

# CONTENTS

ABSTRACT

TIIVISTELMÄ (ABSTRACT IN FINNISH)

PREFACE

LIST OF INCLUDED ARTICLES

CONTENTS

1	INTRODUCTION .....	11
2	THE MC-EKRT SIMULATION IN A NUTSHELL.....	15
3	GEOMETRY AND COLLISION OF TWO NUCLEI .....	17
3.1	Nucleon distribution.....	17
3.2	Determining the nuclear collision.....	20
3.2.1	Nucleons with no substructure .....	20
3.2.2	Nucleons with substructure .....	21
3.3	Thickness and overlap functions .....	22
3.3.1	Nucleons .....	22
3.3.2	Nucleon substructure .....	22
3.3.3	Nuclei .....	23
4	PRODUCTION OF MINIJETS .....	24
4.1	Conventional methods of determining a nucleon–nucleon inter- action .....	25
4.1.1	Hard spheres.....	25
4.1.2	Probabilistic collision .....	26
4.2	Sampling the number of dijets in MC-EKRT .....	27
4.3	Minijet cross section.....	27
4.3.1	Differential minijet cross section.....	28
4.3.2	Expectation value of the number of the dijets $\bar{N}_{\text{jets}}^{ab}$ .....	29
4.3.3	Nuclear PDF modifications with spatial dependence.....	31
4.3.3.1	Linear spatial nPDF .....	31
4.3.3.2	Exponential spatial nPDF .....	32
4.3.3.3	Logarithmic-geometric spatial nPDF.....	36
4.3.3.4	Momentum conservation of the PDFs .....	37
4.3.4	Integrated minijet cross section .....	38
4.4	Sampling the properties of the jets.....	41
4.5	About Monte-Carlo Glauber .....	44
5	FILTERING OF THE CANDIDATE MINIJETS .....	46
5.1	Ordering of the dijets .....	46
5.2	EKRT saturation .....	49
5.3	Momentum conservation .....	53
5.4	Valence quark number conservation.....	55

5.5	Ordering of the filters.....	55
6	APPLICATION .....	58
6.1	Centrality selection .....	58
6.2	Qualitative effects of the model parameters.....	60
6.2.1	Saturation parameter $\kappa_{\text{sat}}$ and pQCD $K$ -factor.....	60
6.2.2	Trigger condition and $\sigma_{\text{trig}}^{NN}$ .....	61
6.2.3	Parameters of the minijet production.....	62
6.2.4	Other parameters.....	63
6.3	Input and output .....	63
6.4	Hydrodynamical initial state .....	64
6.4.1	3+1D simulation .....	64
6.4.2	2+1D simulation .....	67
7	CONCLUSIONS AND OUTLOOK .....	69
	REFERENCES.....	72
	APPENDIX 1 INPUT FILES.....	83
1.1	Model parameters .....	83
1.2	Minijet properties in the output .....	86
	INCLUDED ARTICLES	

# 1 INTRODUCTION

The quark gluon plasma (QGP) [1–6] is a state of matter, where quarks and gluons are deconfined, free from their hadronic bound states such as protons and neutrons. The study of the QGP allows to probe the fundamental properties of Quantum Chromodynamics (QCD) [7], the theory describing the strong nuclear interaction and an integral part of the Standard Model of particle physics [8–11].

The formation of this QCD matter, where quarks and gluons are deconfined, is achieved through relativistic heavy ion collisions in the laboratory setting [12–14]. These collisions involve heavy ions, for example gold, xenon or lead nuclei, accelerated to nearly the speed of light in massive accelerator laboratories like Relativistic Heavy Ion Collider (RHIC) and Large Hadron Collider (LHC). The extreme conditions created in these collisions—temperatures over a trillion degrees (over  $2 \times 10^{12}$  K [15]) and energy densities far exceeding those in ordinary nuclear matter—are instrumental in the formation of the QGP. Also in nature, hot QGP is believed to have existed in the first microseconds after the Big Bang, where temperatures were so high that hadrons such as protons and neutrons could not yet form, and quarks and gluons roamed freely [16].

The heavy ion collision is a complex process involving several stages, each with its own unique characteristics and dynamics. As the involved interaction scales and physical phenomena are so varied, no single framework can model the entirety of the process from the first impact all the way to the particles hitting the detectors. The initial state is formed at the moment of the collision, where the ions accelerated to relativistic speed have enough energy to form QGP as they interact via the strong nuclear force. Here, the fastest processes are the ones with high momentum exchange  $Q^2$ , which produce the so called hard particles in the end state [17]. After their production the numerous smaller  $Q^2$  interactions produce most of the matter contributing to the forming QGP [18–20]. After the initial impact, the energy density is extremely high, and the system is far from thermal equilibrium. During this phase, partons (quarks and gluons) interact with each other free from the nucleons (protons and neutrons), and e.g. QCD kinetic theories [21–24] can be used to model the evolution of the system. Until this point, the physical processes stand firmly in the regime of perturbative QCD (pQCD) [25].



As the system continues to expand along the beam direction, it cools and its energy density decreases. As is possible in a non-Abelian gauge theory [26, 27], the asymptotically free running causes the QCD coupling to increase towards lower interaction energies [28, 29] rendering pQCD inapplicable. Here the microscopic physics can be best described by nonperturbative (lattice) QCD [30–32] or effective field theories (EFTs) [33–38] with strongly coupled fields, or by anti-de Sitter/conformal field theory (AdS/CFT) correspondence [39] at the limit of infinite coupling. The system quickly approaches a state of local thermal equilibrium [21, 40], and starts to behave collectively. This phase can be described by hydrodynamic models [41], which take into account the viscosity of the quark-gluon plasma. The plasma behaves like a nearly perfect fluid with a very low viscosity [15]. As the system expands and cools analogously to the early universe, quarks and gluons combine to form hadrons again, in a process known as hadronization or confinement [42]. Afterwards, these hadrons can still interact with each other, leading to chemical reactions that can change the composition of the hadron gas [43]. At a certain point, the system becomes too dilute for inelastic collisions to occur. This is the chemical freeze-out, where the relative abundances of different particle species are fixed [44, 45]. Even after the chemical freeze-out, elastic collisions can still occur, which do not change the particle species but can change their momentum distributions. When the rate of these collisions becomes too low in the cooling, expanding system, kinetic freeze-out is reached [46]. Here the applicability of the hydrodynamic simulation ends. The momentum distribution of particles is fixed, and, after the strong and electromagnetic decays of unstable particles have taken place, the particles stream freely towards the detectors. Physics of the hadrons from a sufficiently late hadron gas phase on can be alternatively described by cascade models incorporating Boltzmann transport [47–50]. These hadrons and their decay products are what is in the end actually observed. All the information from the whole process thus far must be deciphered from their properties, correlations and distribution.

Hydrodynamic models of the QGP most often use relativistic dissipative second-order transient fluid dynamics first introduced by Israel and Stewart [51], which can take into account the non-zero shear and bulk viscosities that may vary as functions of temperature and chemical potential. Relativistic hydrodynamics incorporates the limitations of relativity, like the speed of sound being limited by the speed of light, and a relativistic equation of state (EOS) into the conservation laws that form the basis of classical fluid dynamical models. Israel-Stewart theory further introduces additional relaxation equations for the shear stress tensor and bulk viscous pressure, which enables maintaining causality and stability.

The initial state in hydrodynamical simulations plays a crucial role in determining the evolution and outcomes of the system [52]. The degree of spatial anisotropy and the size of inhomogeneities can significantly affect observables such as particle flow and flow harmonics during the subsequent hydrodynamical expansion [53–58]. Successful frameworks modeling the initial state include Monte Carlo (MC) Glauber models, models that use Color Glass Condensate (CGC) EFT [36–38], and Eskola-Kajantie-Ruuskanen-Tuominen (EKRT) satura-

tion models [55, 59–61]. The MC Glauber approaches [62]—e.g. the widely used  $T_{\text{RENTo}}$  parametrization model [63]—sample the nucleon locations from known nuclear distributions and determine the number of colliding nucleon–nucleon pairs by using the measured inelastic proton–proton cross section. The CGC models like IP-Glasma [64, 65], have gluons as the primary degrees of freedom, in particular at the high-energy limit where the gluons saturate to form a collective strongly interacting field. In EKRT model [55, 59–61], the colliding nuclei are regarded as parton clouds, and a saturation conjecture is used in tandem with pQCD calculation to limit the gluon density produced from the colliding nuclei. There are also various models [66–71] which involve general purpose event generators for high energy nuclear collisions, for instance PYTHIA (Angantyr) [72, 73], HIJING [74, 75], AMPT [76], and EPOS [77–79], in the initial state calculation.

The actual properties of the QGP are extracted from so-called global analyses, in which as many simulated observables as possible are simultaneously fitted to the experimental data from various sources and processes [15, 52, 55, 80–86]. In such analyses, it is of greatest importance to have an initial state that has physical roots in QCD. Whenever a parametrization is used instead of a QCD-dynamical calculation, there exists a possibility that the observed effects in the simulation tell more about the parametrization, and less about the actual physical system that is the QGP droplet.

In this thesis, a deep dive into the entirely novel Monte-Carlo implementation, programmed from scratch by the author, of the EKRT initial state model (MC-EKRT) is presented. In this event generator, the initial energy density produced in the heavy ion collision comes from pQCD production of quarks and gluons of very small— $\mathcal{O}(1 \text{ GeV})$ —transverse momentum  $p_T$  called minijets, whose multiplicity is controlled by the EKRT saturation conjecture. In MC-EKRT, the full energy–momentum tensor  $T^{\mu\nu}$  of the event by event (EbyE) fluctuating initial state, including the rapidity dependence, is extractable. Although not studied in detail in this thesis, the simulator should be able to model also small systems like proton–nucleus (p+A) and perhaps even proton–proton (p+p) in addition to the nucleus–nucleus (A+A) collisions, all consistently within the same framework. The thesis serves as a manual of MC-EKRT, as it documents the physics details of the model and also touches some of the development history to further shed light on the choices made.

The MC-EKRT framework is built from the ground up in this thesis. First, the entirety of the simulation is described shortly in Ch. 2. In rest of the chapters, the model is described in detail in the logical order of the simulation, starting from the nuclear collision geometry and the locations and spatial properties of the nucleons in Ch. 3. Next, in Ch. 4, the minijet producing events are explained in detail, including the eikonal minijet model for nucleon–nucleon scattering which was used in [PI] to study the possibility of the need to account for nuclear shadowing in the Monte-Carlo Glauber models. Ch. 5 discusses the MC-EKRT way of enforcing momentum and valence quark conservation and the local EKRT saturation. Finally, the practical usage and the model parameters of the MC-EKRT simulation are described in Ch. 6 along with the use-case examples in 3+1D and

2+1D fluid dynamical simulation given by articles [PII] and [PIII]. Ch. 7 concludes the thesis and gives an outlook to the future prospects of the model.

## 2 THE MC-EKRT SIMULATION IN A NUTSHELL

The flow chart in Fig. 1 depicts the different stages of the MC-EKRT simulation. The simulation starts with an initialization phase, where all the relevant parameters are either read from the user-provided parameter file, or calculated. After the initialization, the simulator moves into the event generation phase. This phase is run in parallel, using all the CPU resources available. The parallelized algorithm simulates one collision per thread asynchronously. In a given collision, the simulator first generates the colliding nucleons' coordinates in the transverse plane and determines, which are protons and which neutrons. After that, it checks whether the collision trigger condition is satisfied. If it is not, the process starts from the beginning. If a collision is triggered, the simulator goes through all the binary pairs of nucleons, and samples the number of dijets that are produced from each pair and the dijets' kinematic variables and parton flavours. These dijets are then considered as candidates to the outputted initial state. After all the binary pairs of nucleons are processed, the simulator filters the final output from the candidate events. In this filtering, the EKRT saturation is first enforced locally, and then momentum and valence quark number are required to be conserved on a per-nucleon basis. This filtering is done in a transverse momentum  $p_T$  ordered manner, so that the jets which are produced at smaller  $p_T$  (i.e., at later times  $1/p_T$ ) are inhibited by jets produced at larger  $p_T$ . After the filtering, the simulator finally collects the desired quantities from the remaining collection of dijets. When the desired number of nucleus–nucleus collisions is simulated, the simulator moves synchronously to the output phase. Here for example, the centrality classes can be determined or some other analysis on the data can be done before saving, as the raw jet output data of the simulation can grow very large.

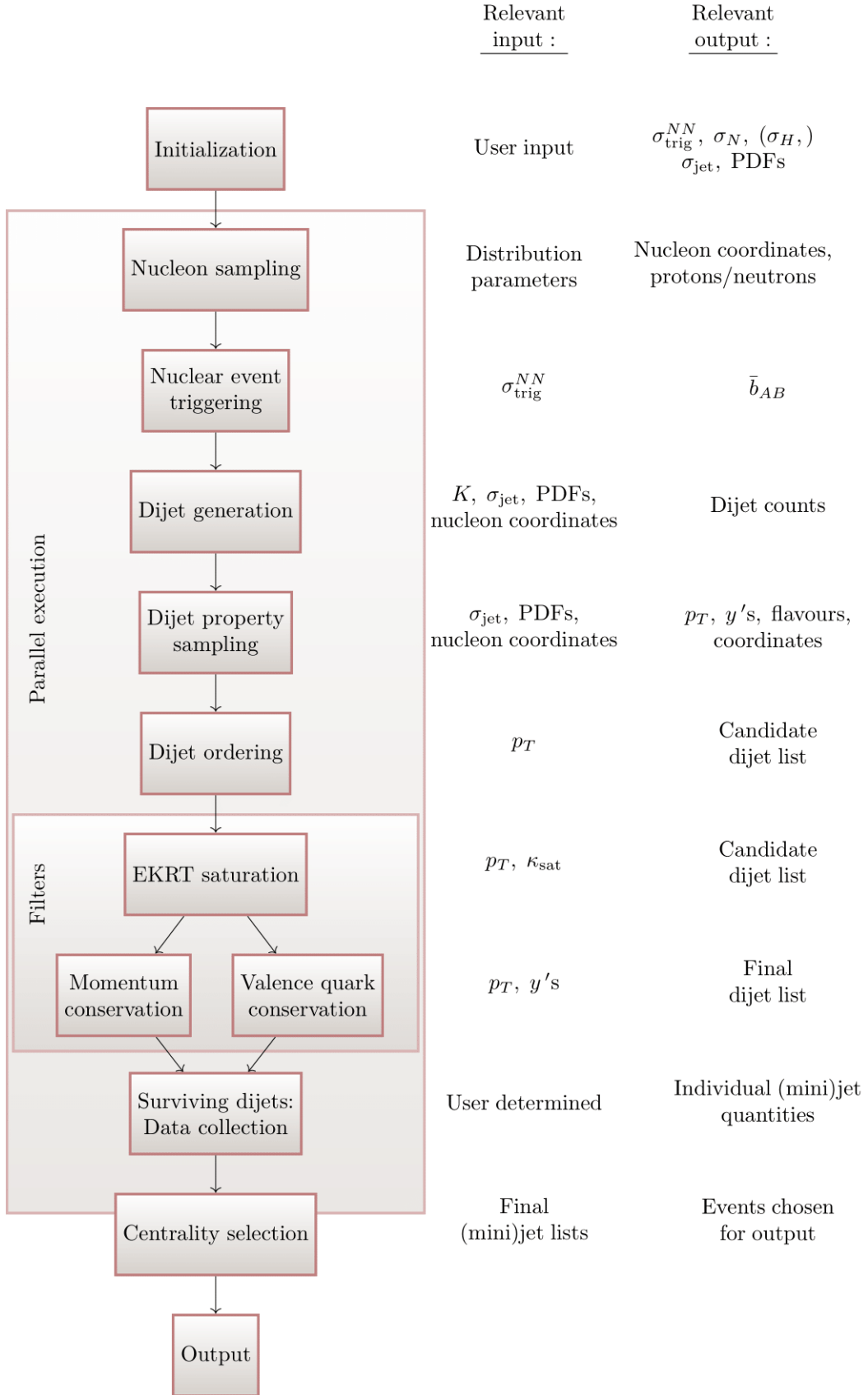


FIGURE 1 A graph depicting the flow of the MC-EKRT simulation.

## 3 GEOMETRY AND COLLISION OF TWO NUCLEI

### 3.1 Nucleon distribution

In the MC-EKRT model, the nuclei are simply collections of nucleons. The distributions of the positions of these nucleons follow the nuclear charge density extracted from low energy electron scattering experiments [87, 88]. These densities are parametrized using a deformed Fermi distribution in spherical coordinates

$$\rho(r, \theta, \phi) = \rho_0 \left\{ 1 + \exp \left( \frac{r - R_A (1 + \beta_2 Y_{20}(\theta) + \beta_3 Y_{30}(\theta) + \beta_4 Y_{40}(\theta))}{d} \right) \right\}^{-1}, \quad (1)$$

where the nuclear radius parameter  $R_A$  is expanded in spherical harmonics  $Y_{20}$ ,  $Y_{30}$  and  $Y_{40}$  using quadrupole, octupole and hexadecapole deformation parameters  $\beta_2$ ,  $\beta_3$  and  $\beta_4$ , and  $d$  is the diffusion parameter. In the case of spherical nuclei such as  $\text{Pb}^{208}$ , the deformation parameters  $\beta$  are all zero and the distribution simplifies into a purely radial two-parameter Fermi (2pF) distribution

$$\rho(r) = \frac{\rho_0}{1 + \exp \left( \frac{r - R_A}{d} \right)}. \quad (2)$$

The normalization constant  $\rho_0$  has no effect on the sampling. The parameters  $d$  (the slope of the distribution),  $R_A$ ,  $\beta_2$ ,  $\beta_3$  and  $\beta_4$  are given as model input by the user, and they are listed e.g. in [87, 88]. For example, for  $\text{Pb}^{208}$   $R_A = 6.624$  fm and  $d = 0.549$  fm. Also  $\text{Au}^{197}$  is approximated as a spherical nucleus, in which case  $R_A = 6.380$  fm and  $d = 0.535$  fm are used. At the current state of the MC-EKRT where only spherically symmetric nuclei have been studied, the nuclei are not rotated in any way after the location sampling. In future, if deformed nuclei were to be simulated, a random rotation should be applied to the orientations of the nuclei for the simulation to account for all the possible shapes of collision systems.

The simulation begins with the sampling of the nucleus–nucleus impact parameter  $\bar{b}_{AB}$  (see Fig. 2). As an arbitrary 2D vector, its probability measure follows

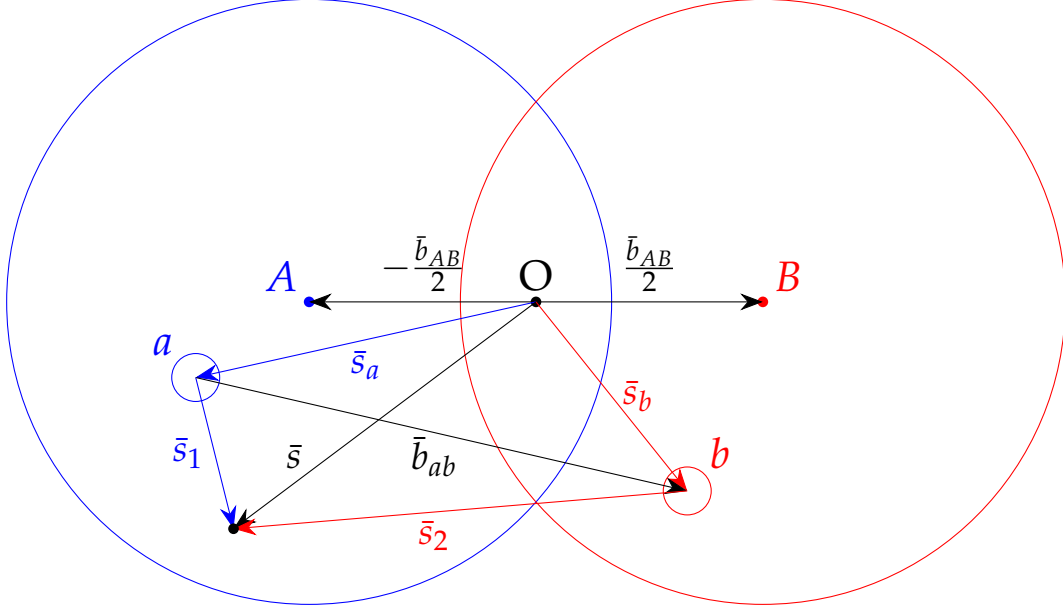


FIGURE 2 The collision system in the transverse plane. The origin  $O$  is defined to be in the middle of the impact parameter vector  $\bar{b}_{AB}$  that connects the centers of masses of the nuclei  $A$  and  $B$ . The nucleon  $a$  with location vector  $\bar{s}_a$  is from  $A$  and similarly the nucleon  $b$  with location vector  $\bar{s}_b$  is from  $B$ . The nucleon–nucleon impact parameter between  $a$  and  $b$  is  $\bar{b}_{ab}$ . An arbitrary point  $\bar{s}$  in the transverse plane is pointed by vectors  $\bar{s}_1$  and  $\bar{s}_2$  originating from  $a$  and  $b$ , respectively.

$b_{AB}db_{AB}d\theta = \frac{1}{2}db_{AB}^2d\theta$ , so  $b_{AB}^2$  can be taken from a uniform distribution. The angle  $\theta$  is not sampled at all, as the collision system does not have any special direction and is thus symmetric with respect to rotations in the transverse plane.

The next step is to sample the positions of the nucleons for the colliding nuclei  $A$  and  $B$  from Eq. (1) by rejection sampling. It is typically assumed that the nucleons cannot be overlapping in the nucleus due to nucleon–nucleon repulsion. Therefore, when the position of one nucleon is sampled, it is compared against the positions of the other nucleons that have already been sampled. If its distance from some nucleon would be smaller than some minimum  $d_{\min}$  ( $= 0.4$  fm by default), the whole nucleus is discarded and the nucleon position sampling starts from the beginning. This introduction of  $d_{\min}$  deforms the radial density profile by a small amount [89] (see Fig. 3). This is an ineffective method of implementing the rejection distance in the sampling, but it suffices here. As long as  $d_{\min} < 0.6$  fm (for  $\text{Pb}^{208}$ ), the nucleon sampling time seems to be negligible.

After determining the nucleon positions, the center of the mass of each nucleus is first calculated, and then shifted to  $(-b_{AB}/2, 0, 0)$  for the projectile nucleus  $A$  and to  $(b_{AB}/2, 0, 0)$  for the target nucleus  $B$  as shown in Fig. 2. This shift also biases the nucleon radial density profile (see Fig. 3). Then, the simulator determines randomly which of the nucleons are neutrons and which are protons. Practically, this is done as follows: Consider the nucleus as a randomly ordered vector of nucleons. The probability that the  $i$ :th nucleon is a proton is then  $\frac{Z-n}{A-i+1}$ ,

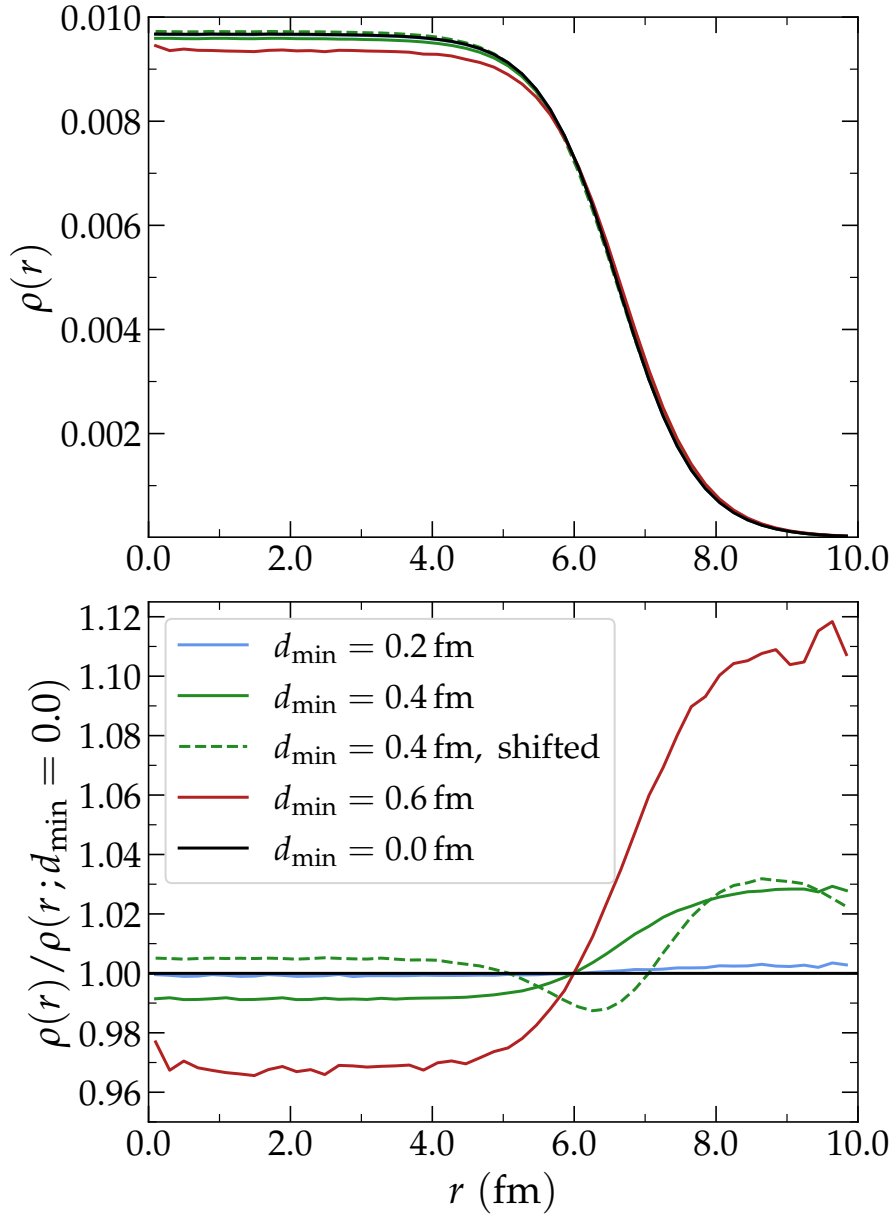


FIGURE 3 (Upper) Radial nucleon distributions of  $Pb^{208}$ , generated with MC-EKRT using different values of the rejection distance  $d_{\min}$ . When generating nuclei for the dashed line with  $d_{\min} = 0.4$  fm, after the nucleons were sampled, they were shifted so that their center of mass coincides with the origin. (Lower) The values of the same distributions in relation to the unbiased ( $d_{\min} = 0.0$  fm) distribution.

where  $Z$  is the charge number of the nucleus,  $n$  is the number of protons that have index  $< i$  and  $A$  is the mass number of the nucleus. Note that here no differences between the spatial distributions of protons and neutrons are assumed, i.e. any effects such as neutron skin are not taken into account. Finally after these steps, the nucleon substructure is generated (see Ch. 3.3.2 for the details).



## 3.2 Determining the nuclear collision

After the nuclei are generated, the simulation next needs to determine whether this particular nucleus–nucleus system produces a collision or not. A great care is needed in choosing this triggering procedure, as e.g. the centrality behaviour of the simulation (see Ch. 6.1 for details) is very sensitive to it. The crux of the procedure is to define a condition, which determines when two nuclei have interacting matter close enough to each other that a collision is defined to happen. If it so happens that the nuclei are generated to have all their matter too far apart from each other, a new system of nuclei is generated from scratch and this one is discarded to avoid any bias in the  $\bar{b}_{AB}$  distribution of the collisions. The triggering conditions used here are similar to the ones used in MC Glauber models [62].

### 3.2.1 Nucleons with no substructure

Consider pairs of nucleons  $(a, b)$ , where  $a$  is from the projectile nucleus and  $b$  is from the target nucleus. Their location vectors in the transverse plane are  $\bar{s}_a$  and  $\bar{s}_b$ , respectively. If there is even one pair, for which the transverse distance

$$\sqrt{(\bar{s}_a - \bar{s}_b)^2} \leq \sqrt{\frac{\sigma_{\text{trig}}^{NN}}{\pi}}, \quad (3)$$

the nucleus pair in question is decided to be colliding. For the triggering cross section  $\sigma_{\text{trig}}^{NN}$  here, in the absence of nucleon substructure, the inelastic nucleon–nucleon cross section is used. This condition corresponds to nucleons being hard spheres colliding.

The used value for  $\sigma_{\text{trig}}^{NN}$  (if it is not given as a user input) is obtained from the fits by COMPETE [90] to the total cross section  $\sigma_{\text{tot}}^{NN}$  and by TOTEM [91] to the elastic cross section  $\sigma_{\text{el}}^{NN}$  in proton–proton scatterings at high energies as

$$\frac{\sigma_{\text{tot}}^{NN}(s_{NN})}{\text{mb}} = 42.6s_{NN}^{-0.46} - 33.4s_{NN}^{-0.545} + 0.307 \log^2(s_{NN}/29.1) + 35.5, \quad (4)$$

$$\frac{\sigma_{\text{el}}^{NN}(s_{NN})}{\text{mb}} = -1.617 \log(s_{NN}) + 0.1359 \log^2(s_{NN}) + 11.84, \quad (5)$$

$$\sigma_{\text{trig}}^{NN}(s_{NN}) = \sigma_{\text{tot}}^{NN}(s_{NN}) - \sigma_{\text{el}}^{NN}(s_{NN}), \quad (6)$$

where  $s_{NN}$  is the center-of-mass-system (CMS) energy squared, in units of  $\text{GeV}^2$ .

For the sake of documenting the model development history of MC-EKRT, originally the plan was to calculate the inelastic nucleon–nucleon cross section  $\sigma_{\text{inel}}^{NN}$  from an eikonal minijet model [19, 92, see also PI] and use that in the triggering:

$$\sigma_{\text{trig}}^{NN} = \sigma_{\text{inel}}^{NN} = \pi \int_0^\infty db^2 \left( 1 - e^{-T_{NN}(\bar{b})\sigma_{\text{jet}}(\sqrt{s}, p_0)} \right), \quad (7)$$

where  $\bar{b}$  is the nucleon–nucleon impact parameter, the overlap function  $T_{NN}(\bar{b})$  is defined in Ch. 3.3.1 and the inclusive two-jet cross section  $\sigma_{\text{jet}}$  (see Ch. 4.3) was to be controlled with momentum cutoff  $p_0$  so that the calculated  $\sigma_{\text{inel}}^{NN}$  would coincide with the measured one. It was also planned to use the nuclear-shadowed inelastic nucleon–nucleon cross sections [PI] in the simulation of minijet production from each nucleon–nucleon pair, which would have resulted in a HIJING-like [74, 75] simulation of (physical) nucleon–nucleon subcollisions. In the end, it proved that such an approach could not reproduce the original EbyE EKRT results [55]. To produce enough minijet multiplicity through the simulation for the local EKRT saturation to provide the desired dynamical regulation of the low  $p_T$ ,  $\sigma_{\text{jet}}$  has to be allowed to be large enough. This in turn means that in an EKRT-saturation approach a nucleus–nucleus collision is to be considered as a collision of two partonic parton clouds rather than a collection of individual, physical nucleon–nucleon subcollisions. If  $\sigma_{\text{inel}}^{NN}$  were then calculated from large enough  $\sigma_{\text{jet}}$  in Eq (7), it would be much larger than the measured one. If used in the triggering, this would lead then to skewed centrality behaviour as the more peripheral collisions would have less minijet multiplicity (this trigger effect is discussed more thoroughly in Ch. 6.2.2), and to larger total nucleus–nucleus collision rate than what is observed. Therefore, to be clear, the presented MC-EKRT simulation uses the measured value of  $\sigma_{\text{inel}}^{NN}$  (from Eq. (6)) only in the triggering of the nucleus–nucleus collision (when no substructure for the nucleons is assumed), but not at all in the simulation of multiple minijet production from the nucleon–nucleon pairs.

### 3.2.2 Nucleons with substructure

In the nucleon substructure model optionally used in MC-EKRT, nucleons consist of  $N$  hotspots (sub-nucleon matter density spikes). To have enough particle multiplicity to match the data even in the most peripheral collisions, the triggering condition needs to be modified when nucleon substructure is introduced. Then, instead of nucleon locations, the triggering condition in Eq. (3) is tested against all hotspot locations  $\bar{s}_a^H$  in the nucleus  $A$  and  $\bar{s}_b^H$  in the nucleus  $B$ :

$$\sqrt{(\bar{s}_a^H - \bar{s}_b^H)^2} \leq \sqrt{\frac{\sigma_{\text{trig}}^{HH}}{\pi}}. \quad (8)$$

In this scenario, the triggering cross section  $\sigma_{\text{trig}}^{HH}$  does not correspond directly to a physical observable. Instead, it needs to be tuned so that it leads to the same inelastic cross section of the nucleus–nucleus collision as what is obtained with the  $\sigma_{\text{inel}}^{NN}$  trigger [PIII] without nucleon substructure. Using this modification, in every collision there is practically always enough overlapping matter to produce minijets. A similar hotspot triggering approach is taken also in [93, 94].

### 3.3 Thickness and overlap functions

#### 3.3.1 Nucleons

The transverse spatial structure of a nucleon is encoded in the nucleon thickness function  $T_N(\bar{s})$ , which is traditionally defined as a  $z$ -coordinate integral of the spatial nucleon density distribution. A way to intuitively interpret the thickness function is as the probability density to find some matter belonging to the nucleon at transverse point  $\bar{s}$ . Consequently, the overlap function  $T_{NN}(\bar{b})$  is related to the probability density that two nucleons, whose centers are separated by an impact parameter vector  $\bar{b}$ , have some overlapping matter. If the simulation is run without nucleon substructure,  $T_N$  is taken to be a 2D Gaussian distribution

$$T_N(\bar{s}) \equiv \frac{1}{2\pi\sigma_N^2} e^{-\frac{\bar{s}^2}{2\sigma_N^2}}, \quad (9)$$

which has the normalization

$$\int d^2\bar{s} T_N(\bar{s}) = 1. \quad (10)$$

The Gaussian width parameter  $\sigma_N$  follows the parametrization [95]

$$\frac{\sigma_N^2}{\text{GeV}^{-2}} = 4.9 + 4\alpha'_p \log\left(\frac{\sqrt{s}}{W_0}\right) \quad (11)$$

with  $\alpha'_p = 0.06$  and  $W_0 = 90$  GeV. As explained in the article [PII], it is derived from the experimental results and the pQCD collinear-factorization formulation [96] of exclusive photoproduction of  $J/\psi$  mesons at HERA [97]. The nucleon–nucleon overlap function  $T_{NN}(\bar{b})$  is then a convolution of two of these thickness functions

$$T_{NN}(\bar{b}) \equiv (T_N * T_N)(\bar{b}) = \int d^2\bar{s} T_N(\bar{s}) T_N(\bar{s} - \bar{b}) = \frac{1}{4\pi\sigma_N^2} e^{-\frac{\bar{b}^2}{4\sigma_N^2}}, \quad (12)$$

and is likewise normalized to

$$\int d^2\bar{b} T_{NN}(\bar{b}) = 1. \quad (13)$$

#### 3.3.2 Nucleon substructure

In the nucleon substructure model used in MC-EKRT, nucleons consist of  $N_H$  normally distributed hotspots. Their thickness functions  $T_H$  are also taken to be Gaussian as in Eq. (9), but with a width parameter  $\sigma_H$ . Model parameters  $N_H$  and  $\sigma_H$  are external user inputs. Using the hotspots, nucleon thickness function is redefined as

$$T_N(\bar{s}) \equiv \frac{1}{N_H} \sum_{i=1}^{N_H} T_H(\bar{s} - \bar{s}_i) = \frac{1}{N_H} \sum_{i=1}^{N_H} \frac{1}{2\pi\sigma_H^2} e^{-\frac{(\bar{s}-\bar{s}_i)^2}{2\sigma_H^2}}, \quad (14)$$

where  $\bar{s}_i$  is the location vector of a hotspot. The hotspots are distributed normally around the nucleon center with a width parameter  $\sqrt{\sigma_N^2 - \sigma_H^2}$  so that when  $N_H \rightarrow \infty$ , the definition in Eq. (14) approaches the definition in Eq. (9). When sampling the hotspot locations, no recentering or hotspot-hotspot repulsion is used.

Also the hotspot-hotspot overlap function  $T_{HH} \equiv T_H * T_H$  needs to be defined like it was done for nucleons in Eq. (12). The nucleon-nucleon overlap function then becomes

$$T_{NN}(\bar{b}_{ab}) = \frac{1}{N_H^2} \sum_{i=1}^{N_H} \sum_{j=1}^{N_H} T_{HH}(b_{ij}) = \frac{1}{N_H^2} \sum_{i=1}^{N_H} \sum_{j=1}^{N_H} \frac{1}{4\pi\sigma_H^2} e^{-\frac{b_{ij}^2}{4\sigma_H^2}}, \quad (15)$$

where the impact parameters  $\bar{b}$  are the vectors connecting the centers of two nucleons  $\bar{b}_{ab} \equiv \bar{s}_b - \bar{s}_a$  and two hotspots  $\bar{b}_{ij} \equiv \bar{s}_j - \bar{s}_i$ .

### 3.3.3 Nuclei

A nucleus is built from  $A$  nucleons, and its thickness function  $T_A$  is therefore a sum of the nucleons' thickness functions:

$$T_A(\bar{s}) \equiv \sum_{a=1}^A T_N(\bar{s} - \bar{s}_a), \quad (16)$$

where  $\bar{s}_a$  is the location vector of a nucleon  $a$  in the transverse plane. By Eq.(10),  $T_A(\bar{s})$  normalizes to

$$\int d^2\bar{s} T_A(\bar{s}) = A. \quad (17)$$

Same as in Eq. (12), the nucleus-nucleus overlap function can be defined as

$$T_{AA}(\bar{b}) \equiv (T_A * T_A)(\bar{b}) = \int d^2\bar{s} T_A(\bar{s}) T_A(\bar{s} - \bar{b}) \quad (18)$$

$$= \int d^2\bar{s} \sum_{a=1}^A T_N(\bar{s} - \bar{s}_a) \sum_{b=1}^A T_N(\bar{s} - \bar{s}_b - \bar{b}) \quad (19)$$

$$= \sum_{a=1}^A \sum_{b=1}^A T_{NN}(\bar{b} - \bar{s}_a + \bar{s}_b) \quad (20)$$

$$= \sum_{a=1}^A \sum_{b=1}^A T_{NN}(\bar{b} + \bar{b}_{ab}), \quad (21)$$

where  $\bar{b}_{ab} \equiv \bar{s}_b - \bar{s}_a$  is the nucleon-nucleon impact parameter. Following Eq.(13),  $T_{AA}(\bar{b})$  has the normalization

$$\int d^2\bar{b} T_{AA}(\bar{b}) = A^2. \quad (22)$$

## 4 PRODUCTION OF MINIJETS

After the nucleus–nucleus collision has been triggered, as described in Ch. 3.2, all the binary nucleon–nucleon pairs are treated as systems that may produce a group of independent (mini)jets ( $p_T \gtrsim \mathcal{O}(1 \text{ GeV})$ ). The model used here is inspired by eikonal minijet models [19, 92], which use a high energy limit of nonrelativistic potential scattering. In those models, the transverse momentum cutoff  $p_0$  (or similar separation of soft and hard physics) is used to normalize the nucleon–nucleon inelastic cross section  $\sigma_{\text{inel}}^{NN}$ , similar to in Eq. (7), to physical values. By contrast, here everything is treated with pQCD, neglecting the effect of nonperturbative (soft) collisions. Instead,  $p_0$  is brought to as low as 1 GeV, still remaining in the perturbative region ( $p_0 \gg \Lambda_{\text{QCD}}$ ). This increases the  $\bar{b}$ -integrated eikonal minijet cross section on the r.h.s. of Eq. (7) to unphysically large values and leads to so abundant production of minijets that the coordinate space is overfilled. That in turn allows the locally fluctuating low- $p_T$  multiplicity to be regulated dynamically by the EKRT saturation. Effectively this increases the robustness of the model by making it rather insensitive to the momentum cutoff  $p_0$ —a sharp distinction to the aforementioned eikonal minijet models.

For each binary nucleon pair, first it is determined how many, if at all, dijets are produced. After that, the output variables (kinematical variables, flavours) for all the jets are sampled. As the generated collision is assumed to be a very high energy interaction of parton clouds extending around Lorentz-contracted nuclei, the events that produce minijets are assumed to all happen simultaneously at  $z = 0$ . As such, there should be no preferred order in which the binary pairs are processed in the simulation. To achieve that, the pairs are processed in a random order. In the current iteration of MC-EKRT this is, in fact, redundant, as all the minijet producing nucleon–nucleon pairs are processed totally independently from each other. Factorization is conserved until the filtering phase of the simulation (see Ch. 5).

Again, to document the MC-EKRT development history, it is mentioned that in the earlier versions of the simulation, the nucleon–nucleon subcollisions were treated as physical, and momentum conservation was enforced on the subcollision level by reducing the available momentum of the nucleons by the amount

reserved by the generated minijet production. In that setup, factorization was broken during processing the subcollisions, and therefore the order in which the processing was done mattered, i.e. randomization of the binary pairs became important. This randomization is still kept in the current MC-EKRT for potential future use, as it has relatively miniscule performance overhead.

## 4.1 Conventional methods of determining a nucleon–nucleon interaction

The very first step in the processing of a binary nucleon pair is to determine whether it produces dijets or not. There are several ways to do this. One option is to consider the nucleons as hard spheres that always collide when they overlap. This is the MC Glauber approach [62], and it can be used in MC-EKRT as an optional feature. Another option is to have a more probabilistic approach of the collision, with collision probability increasing the smaller the transverse distance between the nucleon pair is. This is the approach taken in HIIJING [75], and what was used in the early iterations of MC-EKRT. Both of these methods are discussed here, but in the current MC-EKRT model this collision determination is not done as a separate step at all, as is explained in Ch. 4.2. What the MC Glauber and the probabilistic methods have in common, is that they use the physical inelastic nucleon–nucleon cross section to determine a physical subcollision between the nucleons. In MC-EKRT, the inelastic collision is triggered on the nucleus–nucleus level, and the nucleon–nucleon pairs are not treated as physical collision systems. Instead, the nuclei are thought as interacting clouds of partons provided by the nucleons, once the nuclear collision is triggered. The parton clouds provided by each nucleon–nucleon pair are then possible sources for (mini)jet production.

### 4.1.1 Hard spheres

The hard sphere model was already introduced in Ch. 3.2.1: Consider pairs of nucleons  $(a, b)$ , where  $a$  is from the projectile nucleus and  $b$  is from the target nucleus, with location vectors  $\bar{s}_a$  and  $\bar{s}_b$ , respectively. If the distance in the transverse plane

$$\sqrt{(\bar{s}_a - \bar{s}_b)^2} \leq \sqrt{\frac{\sigma_{\text{inel}}^{NN}}{\pi}}, \quad (23)$$

the pair  $(a, b)$  is deemed to collide. The  $\sigma_{\text{inel}}^{NN}$  here is a nucleon–nucleon inelastic cross section, which does not in general need to be the same as cross section  $\sigma_{\text{trig}}^{NN}$  used for the triggering of the  $A+A$ -collision (see Ch. 3.2), as their role in the properties of the ultimate simulation output is different. The triggering cross section  $\sigma_{\text{trig}}^{NN}$  affects mainly the centrality behaviour as in the larger  $\sigma_{\text{trig}}^{NN}$  allows for more glancing nuclei to be counted as events. By contrast, larger  $\sigma_{\text{inel}}^{NN}$  affects mainly the total number of produced dijets leading to e.g. more transverse energy  $E_T$ .

Therefore—even if their conceptual significance is very close to each other—if they were to be treated as free parameters described by data, their values would not necessarily coincide.

Using the eikonal approximation [19, 92], the value of  $\sigma_{\text{inel}}^{NN}$  can be calculated as

$$\sigma_{\text{inel}}^{NN} = \pi \int db^2 \left( 1 - e^{-T_{NN}(b^2)\sigma_{\text{jet}}} \right), \quad (24)$$

where  $T_{NN}(b^2)$  is the nucleon–nucleon overlap function defined in Ch. 3.3.1 and  $\sigma_{\text{jet}}$  is the inclusive cross section of producing two jets, which can be calculated using pQCD and might include nuclear shadowing (details in Ch. 4.3), as was suggested in the article [PI]. Using the Gaussian  $T_{NN}(b^2)$  from Eq. (12) and a special function exponential integral  $E_1$  [98] the expression in Eq. (24) can be expressed as [99]:

$$\sigma_{\text{inel}}^{NN} = 4\pi\sigma^2 \left( \gamma + \log \left( \frac{\sigma_{\text{jet}}}{4\pi\sigma^2} \right) + E_1 \left( \frac{\sigma_{\text{jet}}}{4\pi\sigma^2} \right) \right), \quad (25)$$

where  $\gamma \approx 0.57722$  is the Euler-Mascheroni constant.

#### 4.1.2 Probabilistic collision

In the probabilistic model, the goal is to have the minijet production be more probable the closer the nucleons are to each other. This is done using a  $b^2$ -differential version of (24):

$$\frac{d\sigma_{\text{inel}}^{NN}}{db^2}(b^2) = \pi \left( 1 - e^{-T_{NN}(b^2)\sigma_{\text{jet}}} \right). \quad (26)$$

To have this function give a collision probability distribution for any  $b^2 > 0$ , it needs to be normalized so that the probability of having a collision is  $0 \leq P_{\text{collision}}(b^2) \leq 1$ . The positive definite  $\frac{d\sigma_{\text{inel}}^{NN}}{db^2}$  has its maximum at  $b^2 = 0$ . The simplest choice is therefore to choose

$$P_{\text{collision}}(b^2) = \frac{\frac{d\sigma_{\text{inel}}^{NN}}{db^2}(b^2)}{\frac{d\sigma_{\text{inel}}^{NN}}{db^2}(b^2 = 0)}, \quad (27)$$

which corresponds to having  $P_{\text{collision}}(b^2 = 0) = 1$ . Note that this choice is at this point arbitrary, as some other  $P_{\text{collision}}(b^2 = 0) < 1$  could equally well be chosen. All else being equal, this would lead to fewer events that produce any minijets per nucleus–nucleus event.

## 4.2 Sampling the number of dijets in MC-EKRT

In the current MC-EKRT model, once the nuclear collision has been triggered, Poissonian statistics is used to determine the number of independent dijet pairs produced from the parton clouds of one binary nucleon pair. For two nucleons  $a$  and  $b$  from the nuclei  $A$  and  $B$ , with the impact parameter  $\bar{b}_{ab}$  (as in Fig. 2), the probability of producing  $n$  independent (mini)jet pairs is

$$P_n(b_{ab}^2, \sqrt{s_{NN}}, p_0, \{\bar{s}_a\}, \{\bar{s}_b\}) \equiv \frac{\left(\bar{N}_{\text{jets}}^{ab}\right)^n}{n!} e^{-\bar{N}_{\text{jets}}^{ab}}, \quad (28)$$

where  $n$  is now a non-negative integer and the expectation value of the number of the dijets from the binary nucleon pair,  $\bar{N}_{\text{jets}}^{ab}$ , is assumed to depend on the impact parameter  $\bar{b}_{ab}$ , available energy  $\sqrt{s_{NN}}$ ,  $p_T$  cutoff  $p_0$ , and the nucleon configurations  $\{\bar{s}_a\}$  and  $\{\bar{s}_b\}$  of the nuclei  $A$  and  $B$ :

$$\bar{N}_{\text{jets}}^{ab} \equiv \bar{N}_{\text{jets}}^{ab}(b_{ab}^2, \sqrt{s_{NN}}, p_0, \{\bar{s}_a\}, \{\bar{s}_b\}) \quad (29)$$

$$= T_{NN}(b_{ab}^2) \sigma_{\text{jet}}(\sqrt{s_{NN}}, p_0, \{\bar{s}_a\}, \{\bar{s}_b\}), \quad (30)$$

where  $T_{NN}$  stands for the nucleon–nucleon overlap defined in Eq. (12), and  $\sigma_{\text{jet}}$  is the integrated inclusive two-jet cross section which will be defined in detail in Ch. 4.3.2. Note that, in Eq. (28),  $n$  can also be zero, so there is no need to decide beforehand whether a minijet producing event occurs. Even then, to reduce the simulation time, the Poissonian distribution is not even sampled if  $\bar{b}$  is so large that  $T_{NN}(b^2) < 10^{-8} \frac{1}{\text{mb}}$  as producing any jets then would be very improbable.

Finally, just as a side remark, note that if the event generator is, as an option, used to mimic the MC Glauber model, and the collision was to be sampled separately as described in Ch. 4.1, a zero-truncated Poissonian distribution needs to be used:

$$P_{n>0}(b^2) \equiv \frac{\left(\bar{N}_{\text{jets}}^{ab}\right)^n}{\left(e^{\bar{N}_{\text{jets}}^{ab}} - 1\right) n!}. \quad (31)$$

The  $n = 0$  case has to be in this case truncated because there should be more than zero dijets if it is already decided that minijets should be produced.

## 4.3 Minijet cross section

The inclusive pQCD cross section of producing two jets in a nucleon–nucleon collision is a key component in several parts of the simulation. Here collinear factorization framework is used [100]. In this picture, in leading order (LO) pQCD, two partons, one from each nucleon, interact and produce two hard partons. This process is depicted in Fig. 4. All the partons are assumed massless, and the number of flavours in the calculation is for simplicity fixed to 5. The information about



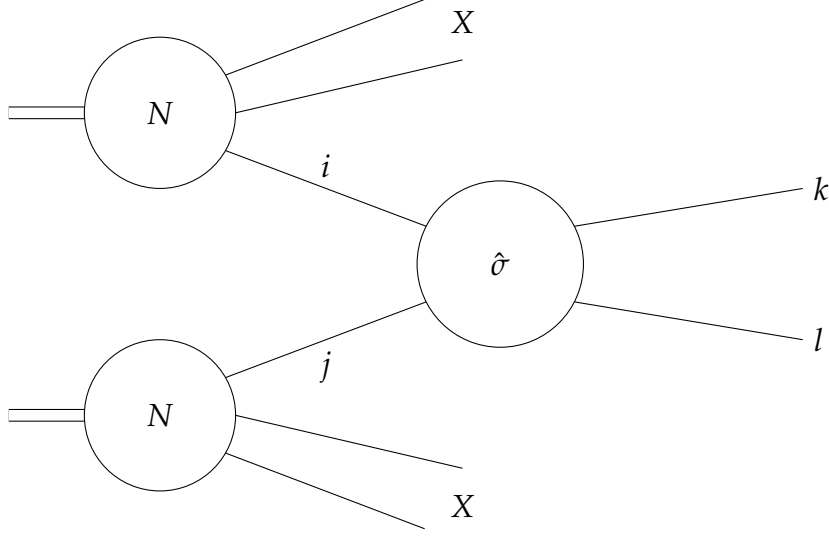


FIGURE 4 Inclusive two jet production in nucleon–nucleon collision using collinear factorization in LO pQCD. In the collision, the partons  $i$  and  $j$  undergo the subprocess  $\hat{\sigma}$  to produce the partons (jets)  $k$  and  $l$ . The nucleons are marked with  $N$ , while  $X$  denotes the remnants of the nucleons.

the nucleons themselves enters the calculation through parton distribution functions (PDFs). A novel feature in MC-EKRT is that the PDFs are unique for all the nucleons individually, and in each event, modified in a spatially dependent way by all the surrounding color charges inside each nucleus. This leads to the cross section also being unique for all the distinct nucleon pairs, of which there are e.g.  $208 \times 208 = 43264$  in a single Pb+Pb collision. Because these calculations are made so numerous times in the simulation, some computational performance considerations are also needed even on the model building level.

#### 4.3.1 Differential minijet cross section

Using collinear factorization, the value of the spatially dependent LO pQCD differential cross section of hard parton production at a transverse point  $\bar{s}$  can be written as [101]

$$\frac{d\sigma_{\text{jet}}(\bar{s}, \{\bar{s}_a\}, \{\bar{s}_b\})}{dp_T^2 dy_1 dy_2} = K \sum_{i,j,k,l} x_1 f_i^{a/A}(\bar{s}, \{\bar{s}_a\}, x_1, Q^2) x_2 f_j^{b/B}(\bar{s}, \{\bar{s}_b\}, x_2, Q^2) \times \frac{d\hat{\sigma}^{ij \rightarrow kl}}{d\hat{t}}(\hat{s}, \hat{t}, \hat{u}), \quad (32)$$

where the factor  $K$  accounts for the missing higher order terms, and the summation is schematic for now (see Ch. 4.3.4). For both of the outgoing hard partons flavoured  $k$  and  $l$ ,  $p_T^2$  is the transverse momentum squared. Their rapidities are  $y_1$  and  $y_2$ , defined as

$$y \equiv \frac{1}{2} \log \frac{E + p_L}{E - p_L}, \quad (33)$$

where  $E$  is the energy and  $p_L$  is the longitudinal component of momentum. The indices  $i$  and  $j$  correspond to the flavours of the partons from the incoming nucleons, and  $f_i^{a/A}$  and  $f_j^{b/B}$  are their spatially dependent parton distribution functions with nuclear modifications (snPDFs), which are defined in Ch. 4.3.3. It is worth emphasizing that through these snPDFs  $\sigma_{\text{jet}}$  is specific for *each* of the nucleon–nucleon pairs, and depends on the spatial configuration of all the other surrounding nucleons in both nuclei, as marked with the notation  $\{\bar{s}_a\}$  and  $\{\bar{s}_b\}$ . The momentum fractions for partons  $i$  and  $j$  are

$$x_1 = \frac{p_T}{\sqrt{s}} (e^{y_1} + e^{y_2}) \quad \text{and} \quad (34)$$

$$x_2 = \frac{p_T}{\sqrt{s}} (e^{-y_1} + e^{-y_2}), \quad (35)$$

respectively.  $Q^2$  is the hard factorization scale related to the process in question. In this work,  $Q^2 = p_T^2$  is used for both the renormalization and the factorization scale. The summation in Eq. (32) is over all the possible LO pQCD  $2 \rightarrow 2$  partonic subprocesses (more on this follows), and  $\hat{\sigma}$  denotes their cross sections. The parton level Mandelstam variables are defined as

$$\hat{s} = 2p_T^2 (1 + \cosh(y_1 - y_2)), \quad (36)$$

$$\hat{t} = -p_T^2 (1 + e^{-(y_1 - y_2)}) \quad \text{and} \quad (37)$$

$$\hat{u} = -p_T^2 (1 + e^{+(y_1 - y_2)}). \quad (38)$$

### 4.3.2 Expectation value of the number of the dijets $\bar{N}_{\text{jets}}^{ab}$

To obtain the spatially dependent, nuclear shadowed expectation value  $\bar{N}_{\text{jets}}^{ab}$  of the Poisson distribution in Eq. (28), Eq. (32) needs to be integrated. The first limitation for the maximal phase space region  $\Omega(\sqrt{s}, p_0)$  of the two jets is  $x_1, x_2 \leq 1$ . For the rapidities in Eq. (32), this translates into

$$|y_1| \leq \text{arcosh} \left( \frac{\sqrt{s}}{2p_T} \right) \quad \text{and} \quad (39)$$

$$-\log \left( \frac{\sqrt{s}}{p_T} - e^{-y_1} \right) \leq y_2 \leq \log \left( \frac{\sqrt{s}}{p_T} - e^{y_1} \right). \quad (40)$$

A second limitation for  $\Omega(\sqrt{s}, p_0)$  is

$$p_0 \leq p_T \leq \frac{\sqrt{s}}{2}, \quad (41)$$

where  $p_0 \gg \Lambda_{\text{QCD}}$  is a hard cutoff scale. The expectation value  $\bar{N}_{\text{jets}}^{ab}$  is then obtained by integrating over the phase space  $\Omega(\sqrt{s}, p_0)$  and the transverse coordinate plane as

$$\begin{aligned} \bar{N}_{\text{jets}}^{ab}(b_{ab}^2, \sqrt{s_{NN}}, p_0, \{\bar{s}_a\}, \{\bar{s}_b\}) = & \\ & K \int d^2\bar{s}_1 d^2\bar{s}_2 \delta^{(2)}(\bar{s}_1 - \bar{s}_2 - \bar{b}) \int_{\Omega(\sqrt{s}, p_0)} dp_T^2 dy_1 dy_2 \sum_{i,j,k,l} \frac{1}{1 + \delta_{kl}} \\ & \times T_N(\bar{s}_1) x_1 f_i^{a/A}(\bar{s}, \{\bar{s}_a\}, x_1, Q^2) T_N(\bar{s}_2) x_2 f_j^{b/B}(\bar{s}, \{\bar{s}_b\}, x_2, Q^2) \\ & \times \frac{d\hat{\sigma}^{ij \rightarrow kl}}{d\hat{t}}(\hat{s}, \hat{t}, \hat{u}), \end{aligned} \quad (42)$$

where the Kronecker symbol  $\delta_{kl}$  prevents the double counting of the phase space in the case of identical particles in the final state, and the transverse vectors  $\bar{s}_1 = \bar{s} - \bar{s}_a$  and  $\bar{s}_2 = \bar{s} - \bar{s}_b$  (see Fig. 2). The term  $T_N(\bar{s}_1) x_1 f_i^{a/A}(\bar{s}, \{\bar{s}_a\}, x_1, Q^2)$  is the number density of the flavour  $i$  partons from the parton cloud around the nucleon  $a$  at the transverse location  $\bar{s}$ , dependent on the locations of not only  $a$  but also all the other nucleons of nucleus  $A$ , as indicated with  $\{\bar{s}_a\}$ . This density, and the similar density from the parton cloud of the nucleon  $b$ , are forced to be probed at the same spatial point by the delta function.

In Eq. (42), the spatially dependent nuclear PDF (snPDF)  $f_i^{a/A}(\bar{s}, \{\bar{s}_a\}, x, Q^2)$  includes the nuclear modifications that, in the general form, depend on the nucleon density of the whole nucleus  $A$  (its nucleon configuration  $\{\bar{s}_a\}$ ) at the location  $\bar{s}$ , i.e., on the nuclear thickness function  $T_A(\bar{s}) = \sum_{a=1}^A T_N(\bar{s} - \bar{s}_a)$  as defined in Eq. (16). Here, this snPDF can be defined with a free nucleon PDF  $f_i^N$  and a spatially dependent nuclear modification factor  $r_i^{a/A}$  as

$$f_i^{a/A}(\bar{s}, \{\bar{s}_a\}, x, Q^2) \equiv r_i^{a/A}(\bar{s}, \{\bar{s}_a\}, x, Q^2) f_i^N(x, Q^2). \quad (43)$$

Using this general form, however, the integrand in Eq. (42) does not factorize into spatial and momentum phase space parts, and the integrals cannot be analytically calculated. Thus, the integration would have to be made *during* the simulation for every nucleon–nucleon pair in each nucleus–nucleus collision. To reduce the computational cost of the simulation, a simplifying restriction is made: Assume that the nuclear modification  $r_i^{a/A}$  depends only on the locations of all the nucleons in  $A$ , namely  $\{\bar{s}_a\}$ , and **not** on the spatial vector  $\bar{s}$ ,

$$f_i^{a/A}(\bar{s}, \{\bar{s}_a\}, x, Q^2) \approx f_i^{a/A}(\{\bar{s}_a\}, x, Q^2) \equiv r_i^{a/A}(\{\bar{s}_a\}, x, Q^2) f_i^N(x, Q^2). \quad (44)$$

With the assumption in Eq. (44), the integral in Eq. (42) now factorizes into spatial and momentum phase time parts, and performing the integrals yields the form

$$\bar{N}_{\text{jets}}^{ab}(b_{ab}^2, \sqrt{s_{NN}}, p_0, \{\bar{s}_a\}, \{\bar{s}_b\}) = T_{NN}(b_{ab}^2) \sigma_{\text{jet}}(\sqrt{s_{NN}}, p_0, \{\bar{s}_a\}, \{\bar{s}_b\}), \quad (45)$$

from Eq. (30), where now

$$\begin{aligned} \sigma_{\text{jet}}(\sqrt{s_{NN}}, p_0, \{\bar{s}_a\}, \{\bar{s}_b\}) &= K \int_{\Omega(\sqrt{s}, p_0)} dp_T^2 dy_1 dy_2 \sum_{i,j,k,l} \frac{1}{1 + \delta_{kl}} \\ &\times x_1 f_i^{a/A}(\{\bar{s}_a\}, x_1, Q^2) x_2 f_j^{b/B}(\{\bar{s}_b\}, x_2, Q^2) \times \frac{d\hat{\sigma}^{ij \rightarrow kl}}{d\hat{t}}(\hat{s}, \hat{t}, \hat{u}). \end{aligned} \quad (46)$$

### 4.3.3 Nuclear PDF modifications with spatial dependence

A parton originating from a bound nucleon that is to experience a hard collision is affected by the partons from multiple nucleons, resulting the effective PDFs of a bound nucleon to distinctly differ from the PDFs of the free nucleons [102–107]. This gives rise to the scale dependent nuclear modifications  $R_i^A$  into the bound nucleon PDFs:

$$f_i^{N/A}(x, Q^2) \equiv R_i^A(x, Q^2) f_i^N(x, Q^2). \quad (47)$$

The function  $f_i^N(x, Q^2)$  is the baseline proton PDF if  $N=p$ . Neutron PDFs can be obtained from the proton PDFs using isospin symmetry. MC-EKRT uses the CT14LO [108] as the baseline free proton PDFs with the LHAPDF [109] interpolation library. The global nuclear modification factor  $R_i^A$  to the PDFs used is from EPS09LO [102].

The nuclear PDF defined in (47) is an average in a sense that it treats all the nucleons in a given nucleus equally. It would be sensible to assume that the nuclear effects are larger in areas where the nuclear density is largest, whereas in the regions where single nucleons are well separated from other nucleons, nucleons would tend to behave more like free nucleons [110–113]. This gives motivation to define such PDFs that the strength of nuclear effects a given nucleon experiences depends on the density of other nucleons in the vicinity. This density is encoded in the nuclear thickness function  $T_A(\bar{s})$  with  $\bar{s}$  being the point in the transverse plane where the parton is probed. The thickness function  $T_A$  is, in the event-by-event fluctuating framework of MC-EKRT, given by the sum of nucleon thickness functions  $T_N$  as defined in Eq. (16).

#### 4.3.3.1 Linear spatial nPDF

Previous studies [110–113] have used an approach where the average nuclear modification factor  $R_i^A$  is given a dependence on the transverse point  $\bar{s}$  by expanding as a power series in  $T_A$ , which is calculated from the average spatial distribution of the nucleons. In a similar spirit, the fluctuating  $T_A$  in MC-EKRT could be used for defining the spatial nuclear correction in Eq.(43) as

$$r_i^A(\bar{s}, \{\bar{s}_a\}, x, Q^2) \equiv 1 + c_i^A(x, Q^2) T_A(\bar{s}) = 1 + c_i^A(x, Q^2) \sum_{a=1}^A T_N(\bar{s} - \bar{s}_a). \quad (48)$$

This approximation of the series with just the first power of  $T_A$  is valid for low values of  $T_A$ , as now  $r_i^A(\bar{s}, x, Q^2) \rightarrow 1$  when  $T_A \rightarrow 0$ , the total nPDF approaches the free nucleon PDF when nuclear thickness is small. The coefficients  $c_i^A$  can be determined by requiring that this definition approaches some globally fitted nPDF  $R_i^A(x, Q^2)$ , like EPS09LO [102], when the PDFs are averaged over the whole nucleus, the spatial dependence is integrated out, and an average over a large collection  $\{A\}$  of sampled nuclei is taken:

$$R_i^A(x, Q^2) \equiv \left\langle \frac{1}{A} \int d^2\bar{s} T_A(\bar{s}) r_i^A(\bar{s}, \{\bar{s}_a\}, x, Q^2) \right\rangle_{\{A\}} \quad (49)$$

$$= \left\langle \frac{1}{A} \int d^2\bar{s} T_A(\bar{s}) \left( 1 + c_i^A(x, Q^2) T_A(\bar{s}) \right) \right\rangle_{\{A\}} \quad (50)$$

$$= 1 + \frac{c_i^A(x, Q^2)}{A} \langle T_{AA}(0) \rangle_{\{A\}} \quad (51)$$

$$\Leftrightarrow c_i^A(x, Q^2) = \frac{A}{\langle T_{AA}(0) \rangle_{\{A\}}} \left( R_i^A(x, Q^2) - 1 \right), \quad (52)$$

where  $T_{AA}$  is the nuclear overlap function defined in Eq. (21), and  $\langle \cdot \rangle_{\{A\}}$  means averaging over all the different sampled nuclei. Note that in (51) it is assumed that the coefficients  $c_i^A$  do not depend on the event-by-event fluctuations (they are the same for all the nuclei  $A$ ), and that all the  $\bar{s}$  dependence is encoded only in the thickness function  $T_A$ .

While enticing due to its simplicity, the definition (48) turned out not to be a good choice for MC-EKRT. Because of the fluctuations in the nucleon positions,  $T_A$  can grow very large, especially in the case of deformed nuclei. For Pb<sup>208</sup>, values over three times the maximum value of the average  $T_A$  were observed. This means that in the shadowing region where  $c_i^A$  is negative,  $r_n$  will actually systematically, for large enough  $T_A$ , be negative, which is unphysical and thus unusable in the LO calculation here.

#### 4.3.3.2 Exponential spatial nPDF

The spatial nPDF can be made positive definite by continuing the expansion in (48) to infinite order, turning it into an exponential function. To simplify all the following calculations, and to speed up the simulations,  $T_A$  is replaced by  $\hat{T}_A^a$ , the average overlap of nucleon  $a$  and the nucleus  $A$ , defined as

$$\hat{T}_A^a(\{\bar{s}_a\}) \equiv \frac{\int d^2\bar{s} T_N(\bar{s} - \bar{s}_a) (T_A(\bar{s}) - T_N(\bar{s} - \bar{s}_a))}{\int d^2\bar{s} T_N(\bar{s} - \bar{s}_a)} \quad (53)$$

$$= \sum_{a' \neq a}^A \int d^2\bar{s} T_N(\bar{s} - \bar{s}_a) T_N(\bar{s} - \bar{s}_{a'}) = \sum_{a' \neq a}^A T_{NN}(\bar{s}_a - \bar{s}_{a'}). \quad (54)$$

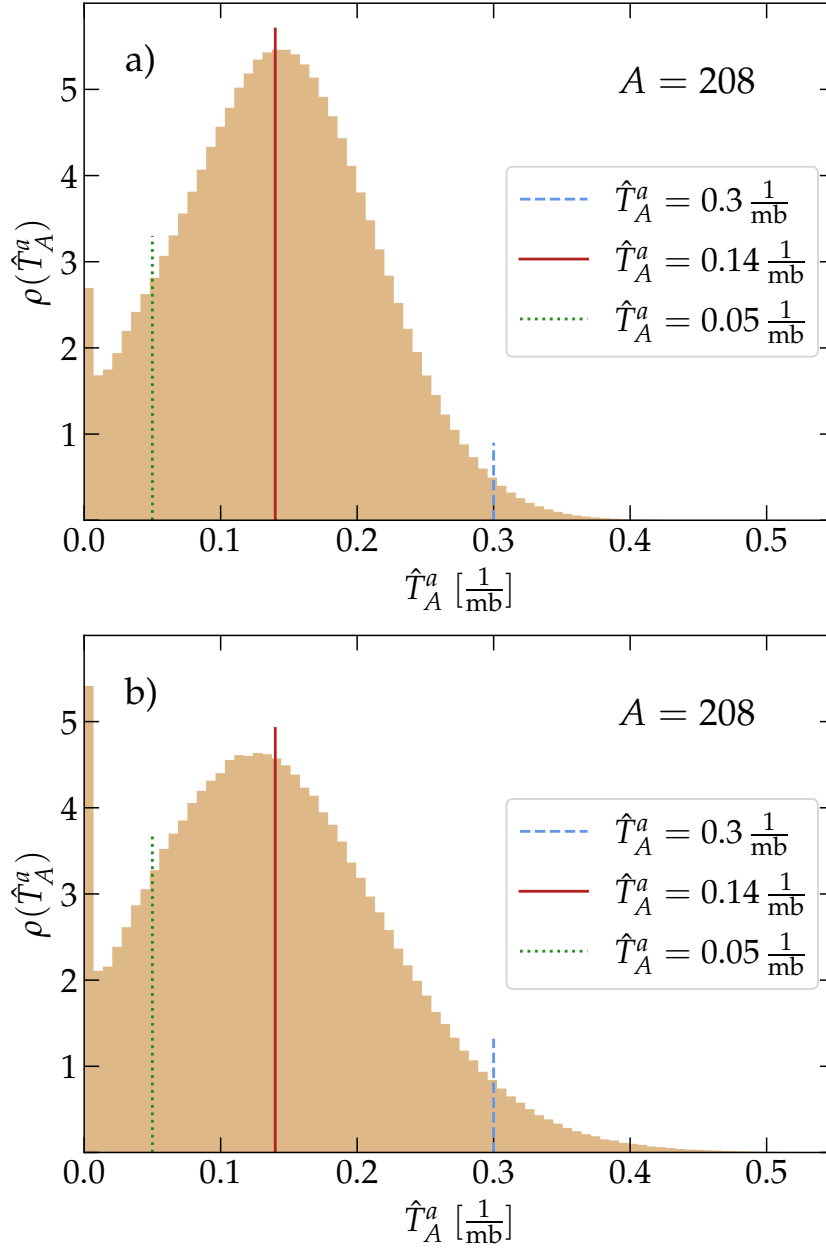


FIGURE 5 The distribution  $\rho(\hat{T}_A^a)$  of the values of  $\hat{T}_A^a$  for nucleons in  $10,000 \text{ Pb}^{208}$  generated with MC-EKRT. The values  $\hat{T}_A^a = 0.3 \frac{1}{\text{mb}}$ ,  $0.14 \frac{1}{\text{mb}}$ , and  $0.05 \frac{1}{\text{mb}}$  represent a nucleon in a dense, average density, and scarce region in the nucleus, respectively. The value  $\hat{T}_A^a = 0.14 \frac{1}{\text{mb}}$  is the median of the distribution in panel a). In panel a), nucleon width is  $\sigma_N = 0.475 \text{ fm}$ , and no nucleon substructure is used. In panel b) otherwise the setup is the same but each nucleon has three hotspots with  $\sigma_H = 0.2 \text{ fm}$ . Panel a) reproduced from [PII].

Here the normalization of  $T_N(\bar{s})$  in Eq. (13) and the definition of the nucleon overlap function  $T_{NN}$  in Eq. (12) are used. An example of the distribution of the values  $\hat{T}_A^a$  can have is shown in Fig. 5. Note that the nucleon  $a$ 's contribution is removed from  $\hat{T}_A$  so that  $\hat{T}_A^a \rightarrow 0$  when  $a$  is very far from the other nucleons. The convenience of  $\hat{T}_A^a$  lies in the fact that it does not depend on the vector  $\bar{s}$ , but only

on the position of nucleon  $a$  in the overall nucleon configuration (the transverse distances  $|\bar{s}_a - \bar{s}_{a'}|$ ). This allows the spatial integral be factored out from the momentum phase space integral in Eq. (42). If not factored, both of the integrals would have to be calculated *during* the simulation for every nucleon–nucleon pair, which would be infeasible. Using  $\hat{T}_A^a$  allows the integrals to be calculated beforehand, while still making each nucleon–nucleon pair specific  $\sigma_{\text{jet}}$  dependent on the structures of both of the surrounding nuclei.

Now the nuclear modification  $r_i^a$  can be defined, this time independent of the spatial vector  $\bar{s}$  as in Eq. (44), as

$$r_i^a(\{\bar{s}_a\}, x, Q^2) \equiv \exp\left(c_i^A(x, Q^2) \hat{T}_A^a(\{\bar{s}_a\})\right). \quad (55)$$

This has the same low  $\hat{T}_A^a$  behaviour as the power series mentioned in Ch. 4.3.3.1. Additionally note that, as by construction  $\hat{T}_A^a \rightarrow 0$  when  $a$  is very far from the other nucleons, also  $r_i^a(\{\bar{s}_a\}, x, Q^2) \rightarrow 1$  and that nucleon's snPDF will approach the PDF of a free proton.

The coefficient  $c_i^A$  will be set like it was done in (51), but this time the equation is not generally analytically invertible:

$$R_i^A(x, Q^2) = \left\langle \frac{1}{A} \int d^2\bar{s} T_A(\bar{s}) \left\langle r_i^A(\{\bar{s}_a\}, x, Q^2) \right\rangle_a \right\rangle_{\{A\}} \quad (56)$$

$$= \left\langle \frac{1}{A} \int d^2\bar{s} T_A(\bar{s}) \left\langle \exp\left(c_i^A(x, Q^2) \hat{T}_A^a(\{\bar{s}_a\})\right) \right\rangle_a \right\rangle_{\{A\}} \quad (57)$$

$$= \left\langle \exp\left(c_i^A(x, Q^2) \hat{T}_A^a(\{\bar{s}_a\})\right) \right\rangle_{a, \{A\}} \quad (58)$$

$$\equiv F\left(c_i^A(x, Q^2)\right), \quad (59)$$

where the normalization (17) of  $T_A$  is again used. Averaging over the different nucleons in a specific nucleus is marked with  $\langle \cdot \rangle_a$ . The function  $F$  is a monotonous function in the values of  $c_i^A$ , so there exists an inverse function that yields the normalization

$$c_i^A(x, Q^2) \equiv F^{-1}\left(R_i^A(x, Q^2)\right). \quad (60)$$

The function  $F$  can be calculated numerically for any given  $c_i^A$  by sampling a large number of nuclei  $A$ . The inverse can then be approximated numerically by creating an interpolation function for a list of values of  $F(c_i^A(x, Q^2))$ , and then inverting that interpolation function.

However, also the exponential ansatz has a problem. The geometric nuclear modification factor  $h \equiv T_A r_i^a$ , which should, after averaging and integrating over the transverse plane, yield the average nuclear modification  $R_i^A$  (see Eqs. (49) and (56)), has problematic behaviour as a function of  $T_A$  in the shadowing region. Using again  $T_A$  in place of  $\hat{T}_A^a$ , the factor reads

$$h(T_A) = T_A(\bar{s}) \exp\left(c_i^A(x, Q^2) T_A(\bar{s})\right). \quad (61)$$

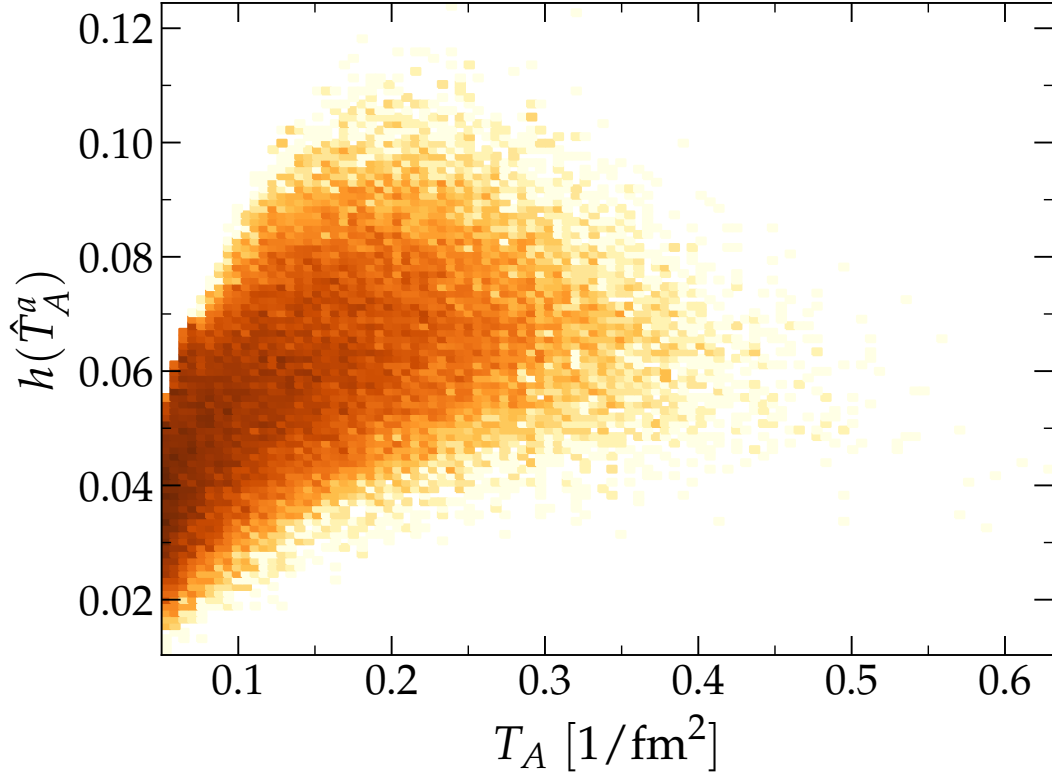


FIGURE 6 The distribution of geometric nuclear modification factor  $h(\hat{T}_A^a)$  values of the exponential snPDFs as defined in Eq. (62), as a function of  $T_A(\bar{s})$ , with  $c=-7$  which corresponds approximately to an average nuclear modification factor  $R \approx 0.4$ . Calculated for 400 randomized nuclei with no nucleon substructure for fixed  $\bar{s}$  values located on a dense grid covering the whole nucleus area in the transverse plane. Note the downward trend of the maximal values of  $h(\hat{T}_A^a)$  in the region  $T_A = 0.2-0.5 \text{ 1/fm}^2$ .

This has a maximum at  $T_A(\bar{s}) = -1/2c_i^A(x, Q^2)$  whenever  $c$  is negative (shading region). This is problematic, as it is not expected to have *less* nuclear flux when there is *more* nuclear matter i.e. larger  $T_A$ , which would here happen at values  $T_A(\bar{s}) > -1/2c_i^A(x, Q^2)$ .

In the MC-EKRT setup, the problem is less clearly defined as the geometric nuclear modification factor equivalent to Eq. (61) would be

$$h(\hat{T}_A^a) = \sum_{a=1}^A T_N(\bar{s} - \bar{s}_a) \exp\left(c_i^A(x, Q^2) \hat{T}_A^a(\{\bar{s}_a\})\right), \quad (62)$$

which does not directly depend on  $T_A(\bar{s}) = \sum_{a=1}^A T_N(\bar{s} - \bar{s}_a)$ , but instead can have multiple values corresponding to the same value of  $T_A$ . This factor is shown in Fig. 6. It can be seen that in the deep shadowing region, the factor (62) cannot reach as large values with higher  $T_A$  as it can with some lower values of  $T_A$ . Therefore, the same problem exists for this setup as there was with the factor (61)

Another matter of concern with the exponential snPDFs comes from the steepness of the exponential function. The nuclear effects might actually get unreasonably large in the antishadowing region due to the large fluctuations in  $\hat{T}_A^a$ .



### 4.3.3.3 Logarithmic-geometric spatial nPDF

The final snPDF version that is ultimately used in MC-EKRT is defined as

$$r_i^a(\{\bar{s}_a\}, x, Q^2) \equiv \begin{cases} 1 + \log(1 + c_i^A(x, Q^2) \hat{T}_A^a(\{\bar{s}_a\})) & \text{if } c \geq 0 \\ \frac{1}{1 - c_i^A(x, Q^2) \hat{T}_A^a(\{\bar{s}_a\})} & \text{if } c < 0 \end{cases} \quad (63)$$

here named logarithmic-geometric snPDF, where “geometric” refers to the geometric series. Three examples of this nuclear modification factor  $r_i^a$  for different nucleons can be seen in Fig. 7. This form is also positive definite, has the same small  $\hat{T}_A^a$  behaviour as the power series mentioned in Ch. 4.3.3.1, and now  $T_A r_i^a$  is always an increasing function in  $T_A$ . The unphysically strong antishadowing is also tamed by the logarithmic behaviour. Here again  $r_i^a(\{\bar{s}_a\}, x, Q^2) \rightarrow 1$  when  $\hat{T}_A^a \rightarrow 0$  for  $a$  that is far from other nucleons.

The coefficient  $c_i^A$  will be set identically as it was done in 4.3.3.2, with

$$R_i^A(x, Q^2) = \left\langle \frac{1}{A} \int d^2\bar{s} T_A(\bar{s}) \left\langle r_i^A(\{\bar{s}_a\}, x, Q^2) \right\rangle_a \right\rangle_{\{A\}} \quad (64)$$

$$= \left\langle r_i^a(\{\bar{s}_a\}, x, Q^2) \right\rangle_{a, \{A\}} \quad (65)$$

$$\equiv F(c_i^A(x, Q^2)). \quad (66)$$

Again the function  $F$  is monotonous in the values of  $c_i^A$ , so it can be inverted to yield the normalization function

$$c_i^A(x, Q^2) \equiv F^{-1}(R_i^A(x, Q^2)), \quad (67)$$

which is again then approximated numerically by creating a linear interpolation function for a list of numerically calculated values of  $F(c_i^A(x, Q^2))$ , and then inverting that interpolation function. Currently, the values of  $F(c_i^A)$  are calculated for a list of 101 values of  $c_i^A$ , spread in 50 logarithmically-even steps from  $-150$  to  $-10^{-3}$  and then another 51 steps from  $10^{-3}$  to  $10^{15}$ , for 10 000 randomly sampled nuclei.

With this choice of form for the snPDFs, the geometric nuclear modification factor  $h(\hat{T}_A^a)$  takes the form

$$h(\hat{T}_A^a) = \sum_{a=1}^A \frac{T_N(\bar{s} - \bar{s}_a)}{1 - c_i^A(x, Q^2) \hat{T}_A^a(\{\bar{s}_a\})} \quad (68)$$

for negative values of  $c_i^A$  instead of the one in Eq. (62). As can be seen from Fig. 8, this time it never has a decreasing trend.

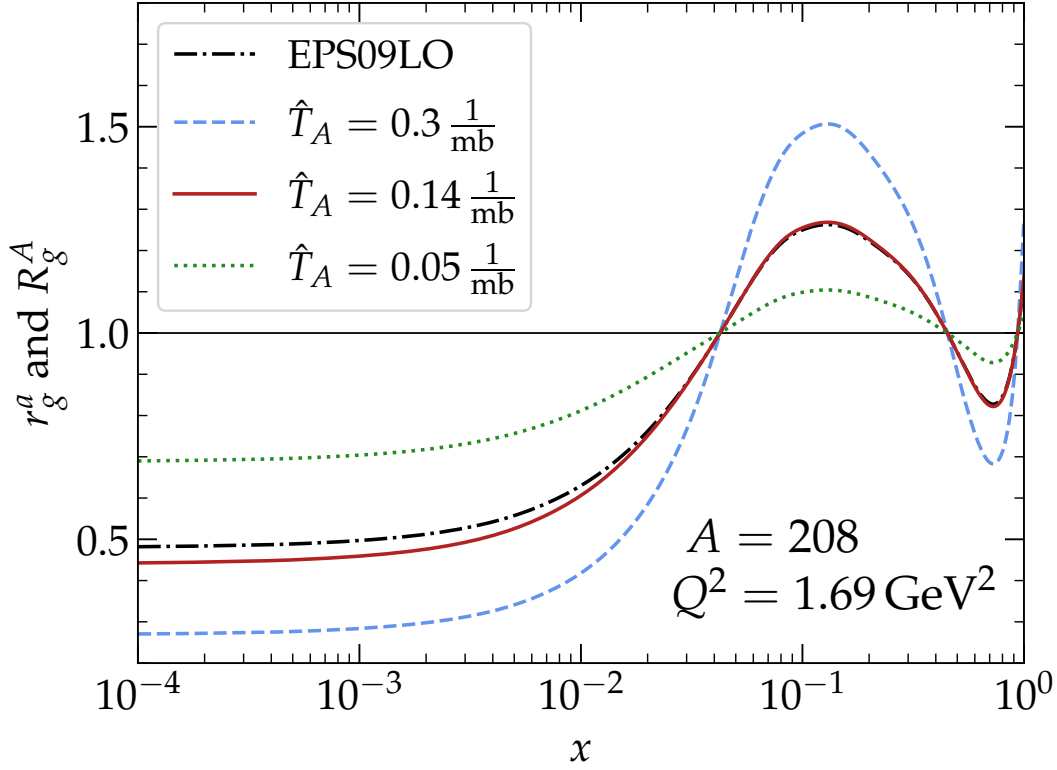


FIGURE 7 The Logarithmic-geometric spatial nuclear modification factor for gluons  $r_g^a$  (Eq. (63)) at a fixed scale of  $Q^2 = 1.69 \text{ GeV}^2$ , with three different values of the average nucleon–nucleus overlap  $\hat{T}_A^a$ , as a function of the momentum fraction  $x$ . The values for  $\hat{T}_A^a$  (see Eq. (54)) correspond to nucleons that are in the dense ( $\hat{T}_A^a = 0.3$ ), scarce ( $\hat{T}_A^a = 0.05$ ) and median ( $\hat{T}_A^a = 0.14$ ) region in the  $\text{Pb}^{208}$  nucleus with no nucleon substructure (see Fig. 5). The global average nPDF EPS09LO [102] is shown for comparison. The smallest  $x$  region, where  $r_g^a < 1$ , is called shadowing region. It is followed by antishadowing ( $r_g^a > 1$ ), EMC-effect ( $r_g^a < 1$  again), and Fermi motion ( $r_g^a > 1$  again) regions. Reproduced from [PII].

To account for the spatial effects especially in the nuclear shadowing region has proved to be a crucial ingredient in describing the centrality behaviour of the experimental data with MC-EKRT initial states. As can be seen in Fig. 9, a significantly higher midrapidity transverse energy  $E_T$  will be produced towards the more peripheral collisions when snPDFs are used than when the traditional, averaged nPDFs are used. This gentler slope persists after hydrodynamical evolution, and is preferred by the experimental data (see [PII]).

#### 4.3.3.4 Momentum conservation of the PDFs

By the definition of the PDFs [101],

$$\int dx \sum_i x r_i^a(\{\bar{s}_a\}, x, Q^2) f_i^p(x, Q^2) = 1 \quad (69)$$

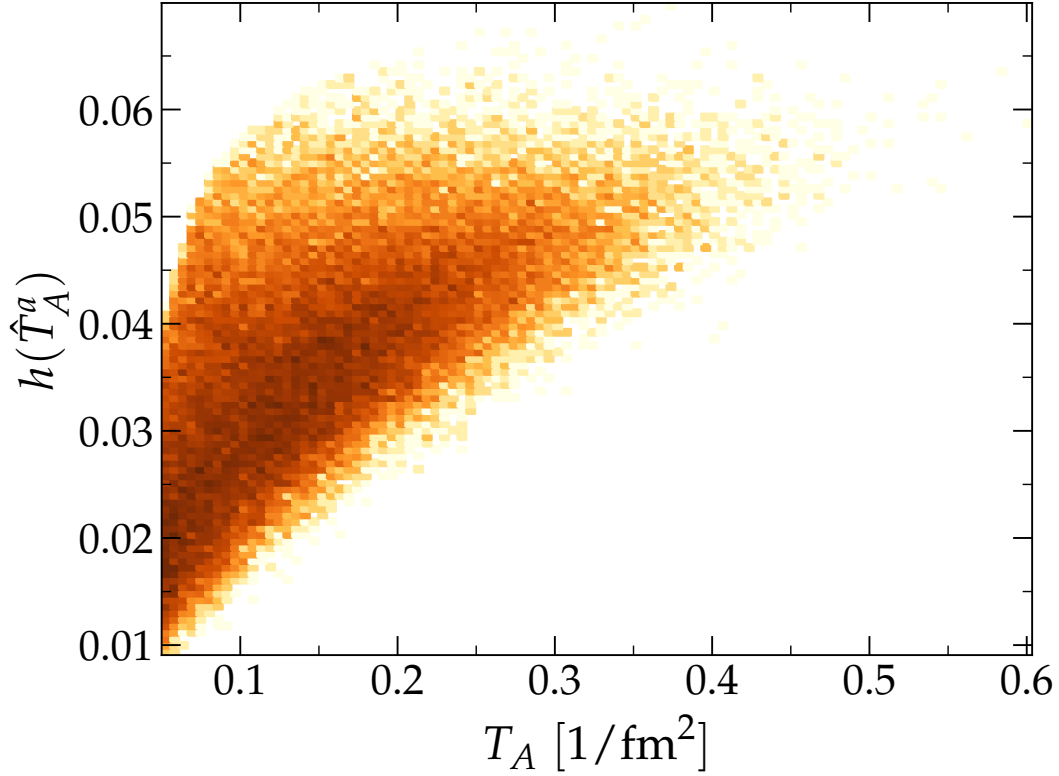


FIGURE 8 The distribution of the nuclear modification factor  $h(\hat{T}_A^a)$  values of the logarithmic-geometric snPDFs as defined in Eq. (68), as a function of  $T_A(\bar{s})$ , with  $c = -25$  which corresponds approximately to an average nuclear modification factor  $R \approx 0.3$ . Calculated for 400 randomized nuclei with no nucleon substructure for fixed  $\bar{s}$  values located on a dense grid covering the whole nucleus area in the transverse plane. Note that the maximal values of  $h(\hat{T}_A^a)$  have a never decreasing trend.

should hold for all protons, and

$$\sum_{a=1}^A \int dx \sum_i x r_i^a(\{\bar{s}_a\}, x, Q^2) f_i^a(x, Q^2) = A \quad (70)$$

should hold for all nuclei. In the snPDFs defined here there are no mechanisms to ensure this. The underlying global nuclear modifications and the baseline proton PDFs, on the other hand, enforce these in their fits. The violation of these conservation laws was investigated for the exponential snPDFs and the logarithmic-geometric ones using a sample size of 20 000 Pb<sup>208</sup> nuclei, see Fig. 10 for the results. The variation from free protons to EPS09LO can be attributed to numerical interpolation and integration errors. Using the logarithmic-geometric snPDFs a percent level accuracy of the conservation laws can be observed.

#### 4.3.4 Integrated minijet cross section

Using a shorthand notation  $x_1 f_g^{a/A}(\{\bar{s}_a\}, x_1, Q^2) \rightarrow g_1$  for gluons from the projectile side and  $x_1 f_q^{a/A}(\{\bar{s}_a\}, x_1, Q^2) \rightarrow q_1$  for all the different quark flavours

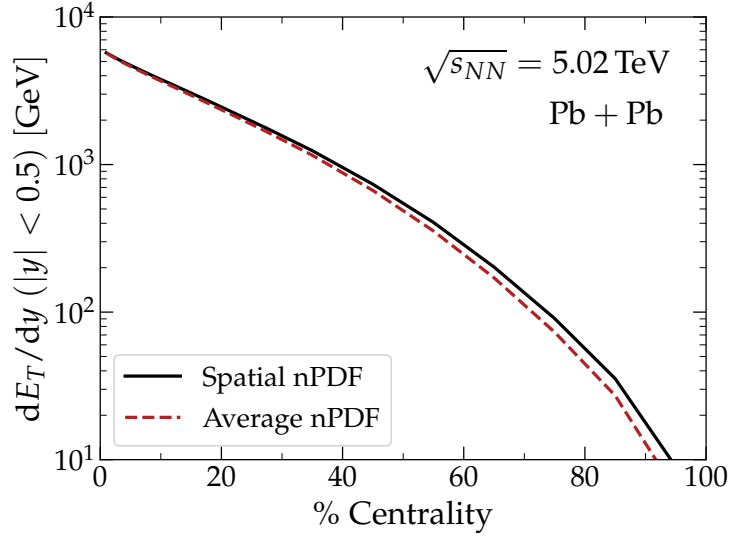


FIGURE 9 The midrapidity minijet transverse energy  $\frac{dE_T}{dy}(|y| < 0.5)$  of the MC-EKRT output, simulated with logarithmic-geometric snPDFs (black solid, see Ch. 4.3.3.3) and with averaged nPDFs (red dashed, EPS09LO [102]), for Pb+Pb collisions at  $\sqrt{s_{NN}} = 5.02$  TeV, as a function of event centrality. Here  $K = 2.2$ ,  $\kappa_{\text{sat}} = 2.5$ ,  $\sigma_N = 0.532$  fm,  $\sigma_H = 0.2$  fm with 3 hotspots, and  $\sigma_{\text{trig}}^{NN} = 11.19$  mb for both curves.

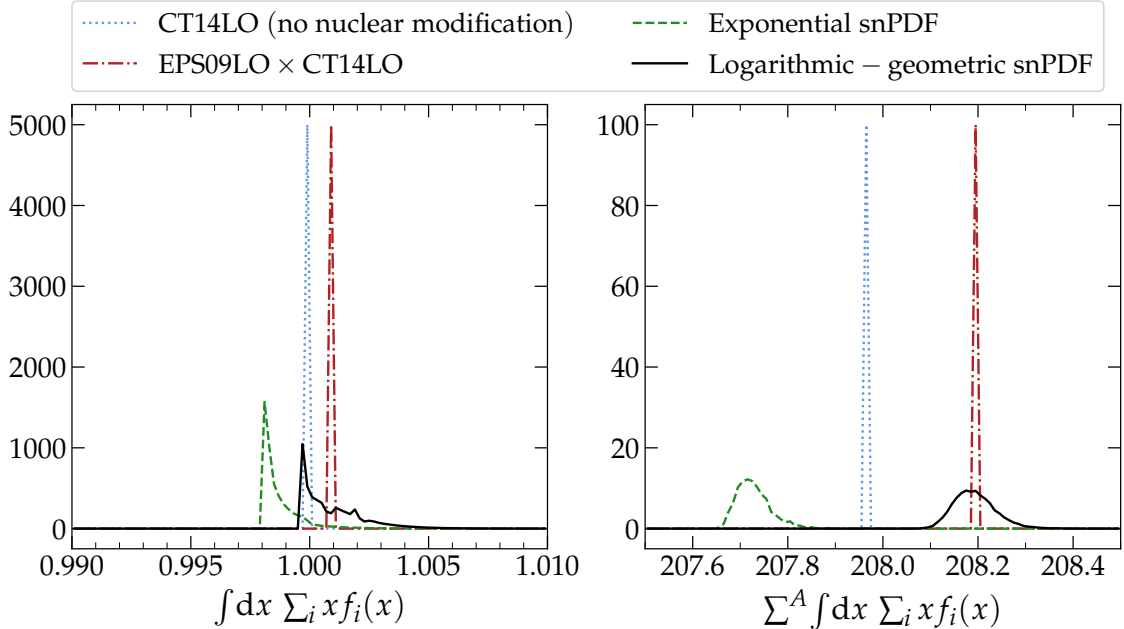


FIGURE 10 The normalized distributions of the momentum conservation integrals of different PDFs for the nucleons in a sample of 20 000  $\text{Pb}^{208}$  nuclei with no nucleon substructure. The left panel has the distributions for the single nucleons (Eq. (69)), while the right panel is summed over whole nuclei (Eq. (70)). The values for the exponential snPDFs varied between 0.998–1.018 (207.64–207.99) and for the logarithmic-geometric ones between 1.000–1.011 (208.07–208.42) in the left (right) panel.

$q \in \{u, d, s, c, b\}$ , and similarly for the antiquarks and  $g_2$  and  $q_2$  for the partons from the target side, the summation in Eq. (45) can be written explicitly as

$$\begin{aligned}
\sigma_{\text{jet}}(\sqrt{s}, p_0) &= K \int_{\Omega} dp_T^2 dy_1 dy_2 \\
&\frac{1}{2} g_1 g_2 \frac{d\hat{\sigma}^{gg \rightarrow gg}}{d\hat{t}} + g_1 g_2 \frac{d\hat{\sigma}^{gg \rightarrow q\bar{q}}}{d\hat{t}} \\
&+ g_1 \sum_q q_2 \frac{d\hat{\sigma}^{gq \rightarrow gq}}{d\hat{t}} + g_1 \sum_{\bar{q}} \bar{q}_2 \frac{d\hat{\sigma}^{g\bar{q} \rightarrow g\bar{q}}}{d\hat{t}} \\
&+ g_2 \sum_q q_1 \frac{d\hat{\sigma}^{qg \rightarrow qg}}{d\hat{t}} + g_2 \sum_{\bar{q}} \bar{q}_1 \frac{d\hat{\sigma}^{\bar{q}g \rightarrow \bar{q}g}}{d\hat{t}} \\
&+ \frac{1}{2} \sum_q q_1 q_2 \frac{d\hat{\sigma}^{qq \rightarrow qq}}{d\hat{t}} + \frac{1}{2} \sum_{\bar{q}} \bar{q}_1 \bar{q}_2 \frac{d\hat{\sigma}^{\bar{q}\bar{q} \rightarrow \bar{q}\bar{q}}}{d\hat{t}} \\
&+ \sum_q \sum_{q' \neq q} q_1 q'_2 \frac{d\hat{\sigma}^{qq' \rightarrow qq'}}{d\hat{t}} + \sum_{\bar{q}} \sum_{\bar{q}' \neq \bar{q}} \bar{q}_1 \bar{q}'_2 \frac{d\hat{\sigma}^{\bar{q}\bar{q}' \rightarrow \bar{q}\bar{q}'}}{d\hat{t}} \\
&+ \left( \sum_q q_1 \right) \left( \sum_{\bar{q}' \neq \bar{q}} \bar{q}'_2 \right) \frac{d\hat{\sigma}^{q\bar{q}' \rightarrow q\bar{q}'}}{d\hat{t}} + \left( \sum_{\bar{q}} \bar{q}_1 \right) \left( \sum_{q' \neq q} q'_2 \right) \frac{d\hat{\sigma}^{\bar{q}q' \rightarrow \bar{q}q'}}{d\hat{t}} \\
&+ \sum_q q_1 \bar{q}_2 \left( \frac{d\hat{\sigma}^{q\bar{q} \rightarrow q\bar{q}}}{d\hat{t}} + \frac{1}{2} \frac{d\hat{\sigma}^{q\bar{q} \rightarrow gg}}{d\hat{t}} + \sum_{q' \neq q} \frac{d\hat{\sigma}^{q\bar{q} \rightarrow q'\bar{q}'}}{d\hat{t}} \right) \\
&+ \sum_{\bar{q}} \bar{q}_1 q_2 \left( \frac{d\hat{\sigma}^{\bar{q}q \rightarrow \bar{q}q}}{d\hat{t}} + \frac{1}{2} \frac{d\hat{\sigma}^{\bar{q}q \rightarrow gg}}{d\hat{t}} + \sum_{q' \neq q} \frac{d\hat{\sigma}^{\bar{q}q \rightarrow \bar{q}'q'}}{d\hat{t}} \right), \tag{71}
\end{aligned}$$

where the extra factors of  $1/2$  are the symmetry factors of the identical final state partons and the functional forms of the subprocess cross sections  $\frac{d\hat{\sigma}^{ij \rightarrow kl}}{d\hat{t}}(\hat{s}, \hat{t}, \hat{u})$  are well known in the literature [101]. As the initial state partons come from the parton clouds of different nucleons, their PDFs are also always different (see Ch. 4.3.3), and therefore e.g. the processes  $g_1 q_2 \rightarrow XY$  are always separately calculated from processes  $q_1 g_2 \rightarrow YX$  even though the subprocess is the same physical process. In MC-EKRT, the final state partons (minijets) are also kept track of. Therefore the  $\hat{u}$ - $\hat{t}$  symmetrization, which is often done in the flavour blind calculation of jet cross sections, cannot be performed. Moreover, all the PDFs for  $u$

and  $d$  quarks are split into valence and sea contributions (whose values of course depend on whether the nucleon is a proton or a neutron),

$$u = u_V + u_S \quad \text{and} \quad (72)$$

$$d = d_V + d_S, \quad (73)$$

so that it is possible to determine if a process was initiated by a valence quark for valence number conservation (more on this in Chs. 4.4 and 5.4).

Using the logarithmic-geometric snPDFs from Ch. 4.3.3.3,  $\sigma_{\text{jet}}$  from Eq. (46) can be integrated numerically. The integral varies from a nucleon–nucleon pair to another, as it depends on the values of  $\hat{T}_A^a$  and  $\hat{T}_B^b$ , which are nucleon specific. Therefore, an interpolation grid for  $\sigma_{\text{jet}}$  is calculated (or read from a file) in the initialization phase of the MC-EKRT simulation. Whenever needed, the values for integrated  $\sigma_{\text{jet}}$  are then read from that grid using linear interpolation. The grid is constructed by computing  $\sigma_{\text{jet}}$  for varying  $\hat{T}_A^a$  and  $\hat{T}_B^b$  from minimal to maximal values in equidistant steps. The number of steps in each dimension is calculated so that the values of  $\sigma_{\text{jet}}$  do not change more than approximately 5% from one grid point to the next. As all the ingredients for the expectation value  $\bar{N}_{\text{jets}}^{ab}$  of the number of the dijets are now defined, some examples of the Poissonian distribution in Eq. (28) can be seen in Fig. 11.

#### 4.4 Sampling the properties of the jets

After the number of the dijet processes in a single nucleon–nucleon pair is determined, as described in Ch. 4.2, the produced jets are given all their properties. First, the integrand on the right hand side of the Eq. (71) is turned into a probability density by normalizing with the full integrated  $\sigma_{\text{jet}}$ . The kinematical variables  $p_T$ ,  $y_1$ , and  $y_2$  of the two jets are then obtained from that distribution using importance sampling [114]. With the kinematical variables set, the same probability density (the integrand on the right hand side of the Eq. (71)) is interpreted as a sum of discrete probability weights for all the different partonic subprocesses. Randomly sampling this sum then yields the subprocess, which in turn determines the flavours of both the incoming and the outgoing partons (jets).

An invertible envelope function

$$E(p_T, y_1, y_2) \geq \frac{d\sigma_{\text{jet}}}{dp_T^2 dy_1 dy_2} \quad \forall p_T, y_1, y_2 \quad (74)$$

has to be defined for the importance sampling. For simplicity, in MC-EKRT a factorized

$$E(p_T, y_1, y_2) = E_{p_T}(p_T)E_{y_1}(y_1)E_{y_2}(y_2) \quad (75)$$

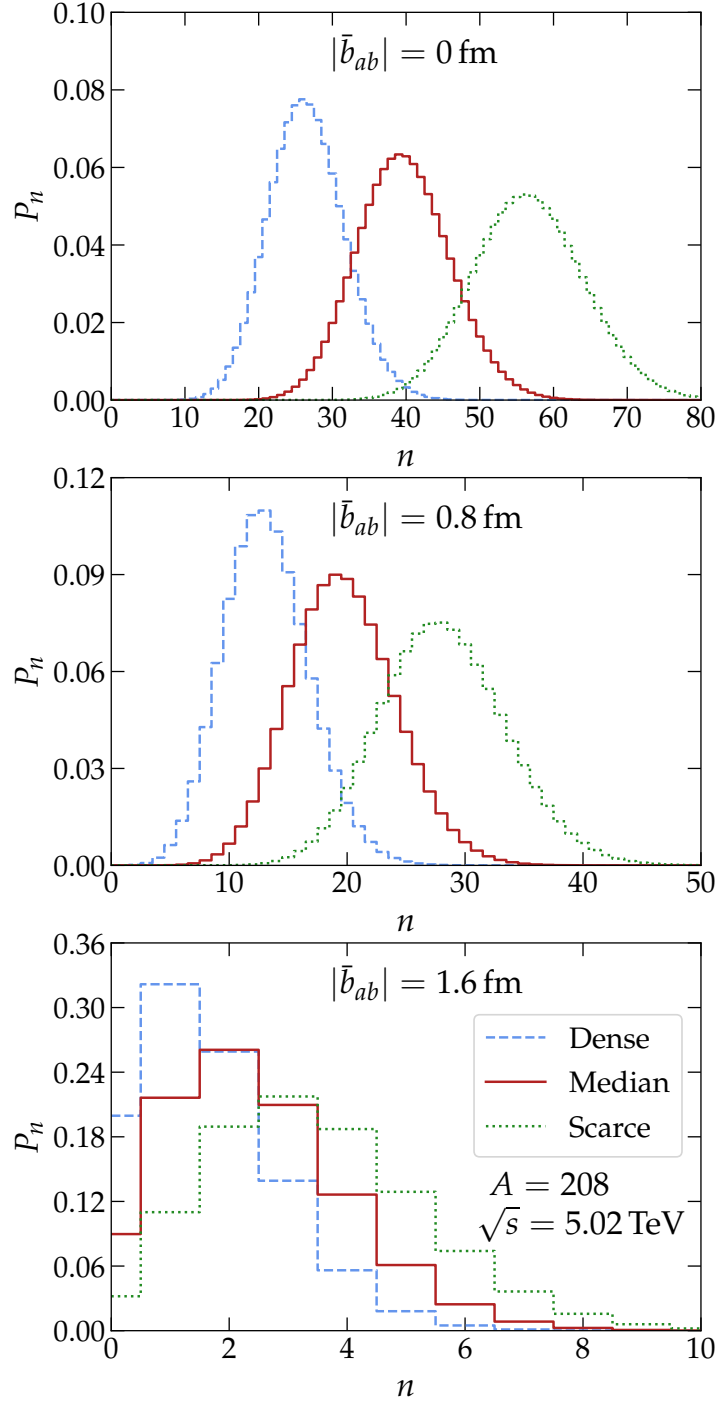


FIGURE 11 Examples of the Poissonian probability distribution  $P_n(b^2)$  for  $n$  independent dijets generated from the parton clouds of one nucleon–nucleon pair for three different values of nucleon–nucleon impact parameter  $\bar{b}$ . The values for the average nucleon–nucleus overlap  $\hat{T}_A^a$  (see Eq. (54)) correspond to nucleons that originate from dense ( $\hat{T}_A^a = 0.3$ ), scarce ( $\hat{T}_A^a = 0.05$ ) and median ( $\hat{T}_A^a = 0.14$ ) region in the  $\text{Pb}^{208}$  nucleus with no nucleon substructure (details of the implementation of the nucleon-configuration dependent nuclear shadowing in Ch. 4.3.3, see also Fig. 5). Reproduced from [PII].

is used. Further still, uniform distributions from  $y_i^{\min}$  to  $y_i^{\max}$  are used for both  $E_{y_i}$ . By examining the behaviour of  $\frac{d\sigma_{\text{jet}}}{dp_T^2}$  when used with varying energies and PDF sets, it was found that a suitable form for  $E_{p_T}$  in MC-EKRT is

$$E_{p_T}(p_T) = \begin{cases} \frac{A}{p_T} & \text{if } p_T \leq B \\ Cp_T^D & \text{if } p_T > B \end{cases} \quad (76)$$

whenever  $p_0 < 2.0 \text{ GeV}$ . If  $p_0 \geq 2.0 \text{ GeV}$ , the  $E_{p_T}(p_T) \propto 1/p_T$  part is not used at all. The constants  $A$ ,  $B$ ,  $C$  and  $D$  are otherwise determined in the initialization phase of the simulation such that  $E_{p_T}$  is continuous everywhere and the condition (74) is met. The need for the  $E_{p_T}(p_T) \propto 1/p_T$  part arises from the used PDFs. Most of the published PDF sets are frozen to a constant value under the scale of  $Q = 1.3 \text{ GeV}$  [108] (pole mass of the charm quark), which causes there to be a drastic change in the slope of  $\frac{d\sigma_{\text{jet}}}{dp_T^2}$  around  $p_T = 1.3 \text{ GeV}$  when the PDF scale is set to  $Q = p_T$ .

After the subprocess is chosen, if there was a  $u$  or  $d$  quark in the initial state, it needs to be decided whether that parton came from a valence or sea contribution to the PDF. In the current version of the MC-EKRT, the following procedure is used. A uniformly distributed random number  $X \in [0, 1]$  is sampled, and then if

$$f_V(\{\bar{s}_a\}, x, Q^2) > X \left( f_V(\{\bar{s}_a\}, x, Q^2) + f_S(\{\bar{s}_a\}, x, Q^2) \right), \quad (77)$$

the dijet is flagged to have a valence quark contribution from the corresponding mother nucleon. The values  $f_V$  and  $f_S$  are the valence and sea contributions to the value that the quark PDF obtains in this particular jet process with its particular parameters and  $x$  and  $Q^2$ , calculated using the sampled variables  $p_T$ ,  $y_1$ , and  $y_2$ . This procedure is equivalent to dividing all the terms in Eq. (71) having  $u$  or  $d$  quarks in the initial state once more, into terms originating from valence quarks and other terms originating from the sea quarks. The valence quark contribution flags come into use when in the end state filtering phase of the simulation valence quark number conservation is enforced (see Ch. 5.4).

Finally, a transverse-plane origination point for the jets needs to be sampled from the distribution that is proportional to the product of the nucleon thickness functions  $T_N$  of the mother nucleons. When there is no nucleon substructure, this product is Gaussian as a product of two Gaussian distributions, so the sampling is straightforward. If nucleon substructure is included in the simulation, the product  $T_N T_N$  is a sum of  $N_H^2$  Gaussian functions, where  $N_H$  is the number of hotspots. This kind of multimodal distribution can be sampled by first choosing a random hotspot pair from a discrete distribution where the probability weights are the peak heights of the Gaussian functions of the hotspot pairs in question. The chosen pair's product  $T_H T_H$  is then again proportional to a normal distribution which can be sampled for the location of the origination point of the dijet.



## 4.5 About Monte-Carlo Glauber

Now, after the nuclear shadowing and the minijet cross section are defined, it can also be explained how it was thought that MC Glauber models could be improved using shadowing, as suggested in article [PI]. In MC Glauber models, the nucleons are sampled from the Woods-Saxon distribution and the  $A+A$  collision is triggered like described in Ch. 3. Then, the total number of binary nucleon–nucleon subcollisions,  $N_{\text{bin}}$ , is determined by the procedure described by Eq. (23) (see e.g. [62, 115]). One of the uses for these simulations is in the experimental side of particle physics. One can use  $N_{\text{bin}}$  from MC Glauber in converting the measured per-event yields of a hard-process observable,  $N_{\text{obs}}/N_{\text{collisions}}$ , in  $A+A$  collisions into cross sections:

$$\sigma_{\text{obs}} = \frac{\sigma_{\text{inel}}^{NN}}{N_{\text{bin}}} \frac{N_{\text{obs}}}{N_{\text{collisions}}}, \quad (78)$$

where  $\sigma_{\text{inel}}^{NN}$  is the same nucleon–nucleon inelastic cross section as in Eq. (23). Combined, Eqs. (23) and (78) establish a complicated relation between  $\sigma_{\text{inel}}^{NN}$  and many of the experimentally determined cross sections in  $A+A$ —via MC Glauber. In LHC Run II heavy electro-weak vector boson production measurements by ATLAS collaboration [116, 117], the nuclear modification factors

$$R_{AA}(y) = \frac{1}{A^2} \frac{\frac{d\sigma_{AA}}{dy}}{\frac{d\sigma_{NN}}{dy}} \quad (79)$$

showed both a normalization-like difference in the rapidity  $y$  dependent minimum bias (no centrality selection) results, and an enhancement towards the peripheral events in the centrality dependent results, compared to the theoretical predictions (see Figs. 1 and 3 in [PI]). In [PI], it was shown that both of these tensions actually went away, if a significantly lower value of  $\sigma_{\text{inel}}^{NN}$  was used. It was further demonstrated that such a lower value of  $\sigma_{\text{inel}}^{NN}$  could be calculated using the eikonal minijet model described in Ch. 3.2.1 (Eq. (7)), with  $\sigma_{\text{jet}}$  calculated using LO pQCD, like in Ch. 4.3 but with averaged nPDFs. This was taken as a possible sign that the new precision data on the standard candles of the initial state like electro-weak bosons actually needs nuclear shadowing effects taken into account in the MC Glauber models. Routinely, the measured free proton  $\sigma_{\text{inel}}^{pp}$  is used in place of  $\sigma_{\text{inel}}^{NN}$ . Afterwards, however, the measurements of Z-bosons by the CMS collaboration [118] and  $W^\pm$ -bosons by the ALICE collaboration [119] did not demonstrate the same effects.

The original idea chased by the study in the article [PI] was to use these MC Glauber results of the well-understood heavy boson processes as a standard candle to constrain the MC-EKRT model. If the used model would have used a physical  $\sigma_{\text{inel}}^{NN}$  calculated from a physical  $\sigma_{\text{jet}}^{NN}$  to determine a collision between physical nucleons, as described in Ch. 4.1, comparisons to MC Glauber results could have been used to fix parameters like cutoff transverse momentum  $p_0$  and

the scale choice  $Q^2$ . In the end, this line of reasoning had to be abandoned in order to obtain a model which is consistent with the previous EbyE EKRT model [55], i.e. to allow for enough minijet production and saturation to match the experimental results, as described in Ch. 3.2.1.

## 5 FILTERING OF THE CANDIDATE MINIJETS

After the dijets are generated from the nucleon–nucleon pairs, as described in Ch. 4, a clearly unphysical overabundance of minijets is observed. This is intentional. All of the produced dijets are next considered as candidates for the initial state of the subsequent evolution of the  $A+A$  collision. To determine the finally allowed physical initial state, the multiplicity of the candidate jets will be reduced by filtering. The local EKRT saturation criterion is expected (and seen in the testing phase when comparing against the data) to be the major driver in the dynamical regulation of the low- $p_T$  jet multiplicity. To allow saturation to be the dominant QCD mechanism that controls the minijet production, that criterion is used first on the list of the dijet candidates. After that, the remaining list is subjected simultaneously to filters that force conservation of momentum and valence quark number per nucleon. The minijet list before and after the full filtering procedure is depicted in Fig. 12. In addition to defining the details of the MC-EKRT model, also the numerous alternative paths that were thought and tested and could have been used in MC-EKRT are described in this chapter, again to document the model development history and to provide a rationale for the choices made.

### 5.1 Ordering of the dijets

The order in which the dijets are passed through the filters affects the output, as the filters are defined in such a manner that the minijets passing the filters earlier will affect which minijets will pass later. Consider the energy budget of a nucleon. The first dijet that is produced from that nucleon will never break the energy budget, so it will never be filtered. If the produced dijets were, for example, handled in some spatial order, the results would be spatially biased to having more survived candidates towards the starting point of the filtering. There are numerous other ways imaginable to bias the results in some manner by negligent ordering. As a matter of fact, any kind of filtering also breaks the

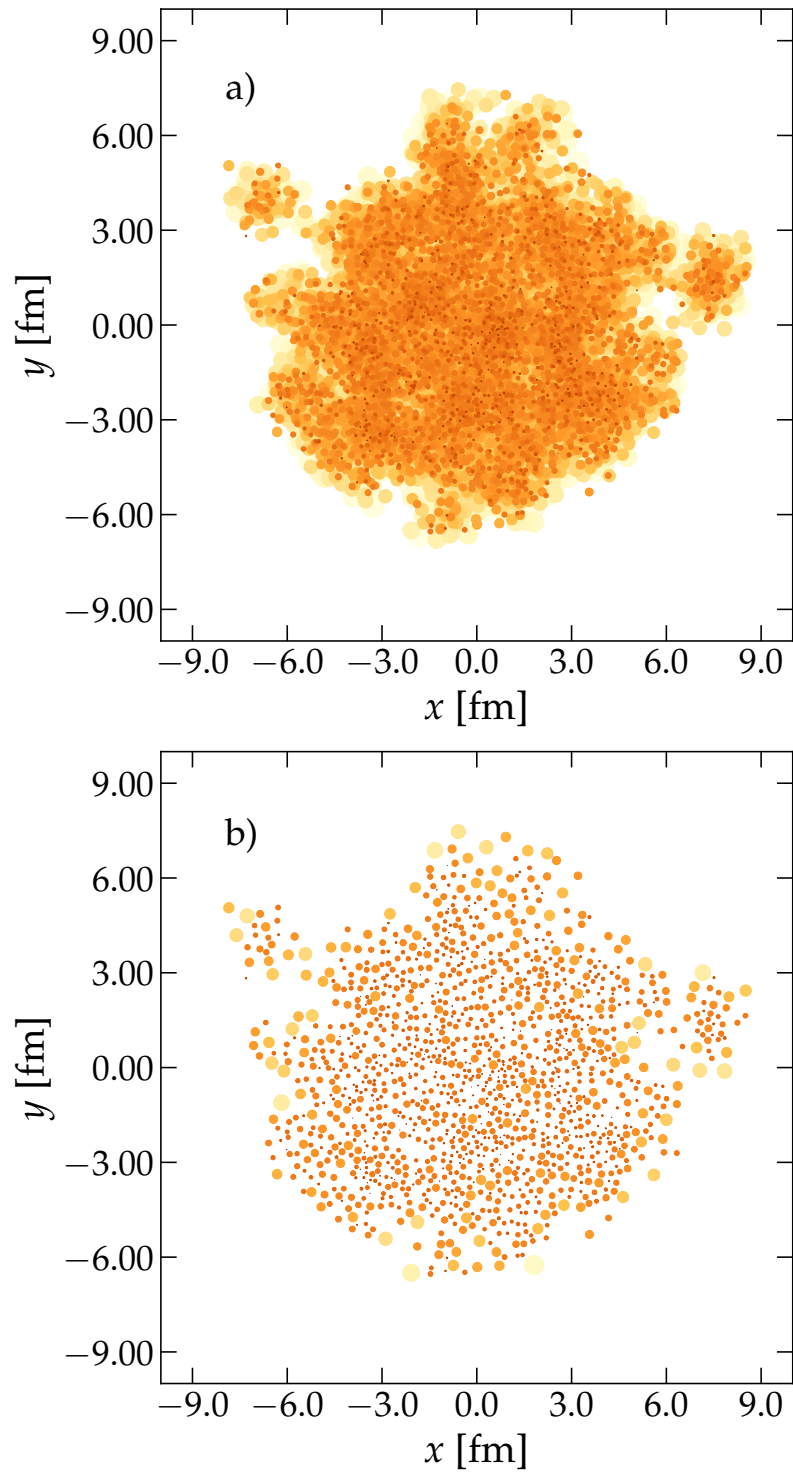


FIGURE 12 The minijets produced in a single central Pb+Pb collision at  $\sqrt{s_{NN}} = 5.02$  TeV in the transverse plane, with parameters  $K = 2.0$  and  $\kappa_{\text{sat}} = 0.5$  with no nucleon substructure. The panel a) depicts all the candidate minijets before the filtering, while panel b) depicts the same minijets after applying all the filters. The radius of a circle representing a minijet is  $1/(\kappa_{\text{sat}} p_T)$ , and the colors are darker for larger  $p_T$ . Image credit Yuuka Kanakubo.

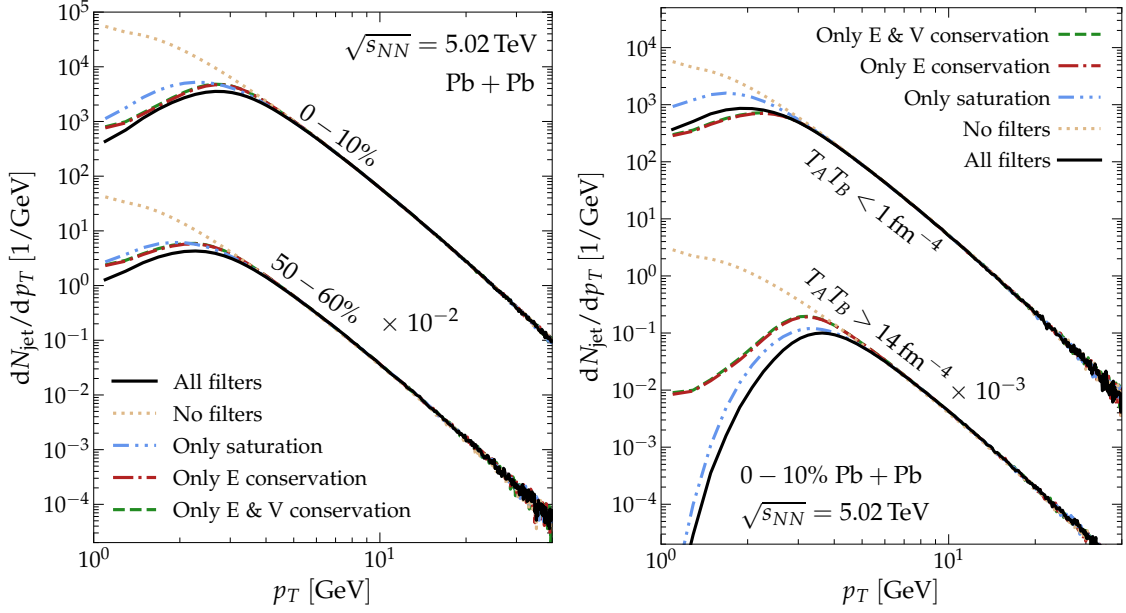


FIGURE 13 The effects of filtering of the candidate events to the produced jet  $p_T$ -spectrum  $\frac{dN_{\text{jet}}}{dp_T}$  in Pb+Pb collisions at  $\sqrt{s_{NN}} = 5.02$  TeV. In the left panel, the spectra are split into minijets from central and peripheral collisions (notice a multiplier on these). In the right panel, the spectra are split by the nuclear density  $T_A T_B$  at the formation location of the dijet into jets produced in a scarce region (higher curves) and in a dense region (lower curves, also a multiplier on these). Here  $K = 2.2$ ,  $\kappa_{\text{sat}} = 2.5$ ,  $\sigma_N = 0.532$  fm,  $\sigma_H = 0.2$  fm with 3 hotspots, and  $\sigma_{\text{trig}}^{NN} = 11.19$  mb.

factorization assumption of the pQCD calculation as the produced minijets are not anymore independent of each other. A great care therefore is needed to choose the ordering in a physically motivated way.

There must not be any spatial dependence in the ordering scheme for it to not introduce any spatial bias. Another limitation comes from the jet  $p_T$ -spectrum, which tells that factorization is a good approximation in  $A+A$  for larger  $p_T$  [102, 106, 120, 121]. The higher-twist effects scale in inverse powers of the virtuality  $Q^2$ , so factorization holds better for the higher scales. Therefore, to maintain factorization, it is reasonable to order the dijets according to their jets'  $p_T$  in order to have the filters cut minijets mainly from the small  $p_T$  region. This conservation of the jet  $p_T$ -spectrum is demonstrated in Fig. 13.

Intuitively, the ordering of the dijets should follow the formation time  $\tau$ . The jets formed first would prevent the processes that might have formed jets at a later time. The choice then boils down to the most valid definition of the formation time. Originating from the uncertainty principle, a typical choice for a jet formed in a hard process with a hard scale  $\sim p_T$  would be

$$\tau = 1/p_T. \quad (80)$$

This is also the case for the latest iteration of MC-EKRT, where the default ordering is with decreasing (minijet)  $p_T$ .

Another possible approach would be to include a rapidity  $y$  dependence into  $\tau$ . Consider a dijet process with virtuality  $Q$ . The jets can be thought to have a formation time  $1/Q$  in their rest frame. The process can be assumed in this calculation to choose from the  $t$ - and  $u$ -channel graphs the one which yields smaller virtuality. This is then boosted into the collider frame with a Lorentz gamma – type factor of  $E/Q$  (where  $E$  is the energy of the jet), to get

$$\tau_i = \frac{E_i}{Q^2} = \frac{\cosh(y_i)}{p_T (1 + e^{-|y_1 - y_2|})}, \quad (81)$$

where  $i = 1$  or  $2$ , and  $E_i = p_T \cosh(y_i)$  and  $Q^2 = \min(|\hat{t}|, |\hat{u}|)$  are used. The formation time of the dijet would then be

$$\tau_{\text{dijet}} = \max(\tau_1, \tau_2). \quad (82)$$

Yet another different formation time could be defined as above in Eq. (81) but calculating the formation time for the whole dijet with rapidity  $y_{\text{dijet}} = \frac{y_1 + y_2}{2}$  directly:

$$\tau_{\text{dijet}} = \frac{1}{Q} \frac{E_{\text{dijet}}}{M_{\text{dijet}}} = \frac{\cosh\left(\frac{y_1 + y_2}{2}\right)}{p_T \sqrt{1 + e^{-|y_1 - y_2|}}}, \quad (83)$$

where  $E_{\text{dijet}}$  is the energy of the dijet,  $M_{\text{dijet}}$  is the invariant mass of the dijet, and  $\frac{E_{\text{dijet}}}{M_{\text{dijet}}}$  is the Lorentz gamma factor.

All three of these different definitions of formation time  $\tau$  were tested for MC-EKRT. In the end, the simplest option (Eq. (80)) was chosen as it was preferred by the experimental data. Both of the rapidity dependent formation times yielded transverse energy distributions  $\frac{dE_T}{dy}$  that were too narrow in rapidity, see Fig. 14. In addition to reproducing the data better, the  $p_T$ -ordering is also supported by purely theoretical view—the factorization holds better for larger virtuality  $Q^2$ , as discussed above, and the virtuality of the minijet production is given here by the factorization scale choice  $Q^2 = p_T^2$ .

## 5.2 EKRT saturation

In the local EKRT saturation criterion used in MC-EKRT, each dijet is considered to have a spatial uncertainty area in the transverse plane around their production location with radius of  $1/p_T$ . An external parameter  $\kappa_{\text{sat}}$ , which acts as a “packing factor” in determining how close to each other the dijets can be produced, is introduced. Consider a dijet candidate with transverse momentum  $p_T^{\text{cand}}$  that is produced in the transverse location  $\vec{s}^{\text{cand}}$ . This candidate is then compared to all of the previously accepted dijets with parameters  $p_T$  and  $\vec{s}$ . If for any of them

$$\sqrt{(s_x - s_x^{\text{cand}})^2 + (s_y - s_y^{\text{cand}})^2} < \frac{1}{\kappa_{\text{sat}}} \left( \frac{1}{p_T} + \frac{1}{p_T^{\text{cand}}} \right), \quad (84)$$

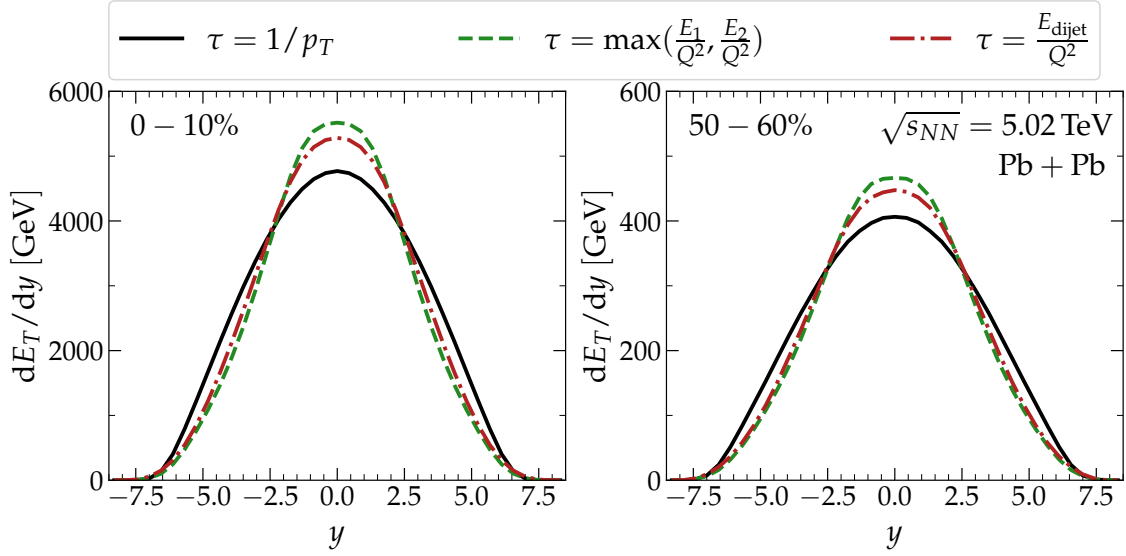


FIGURE 14 A comparison of rapidity distributions of minijet transverse energy  $\frac{dE_T}{dy}$  in central (left panel) and peripheral (right panel) Pb+Pb collisions at  $\sqrt{s_{NN}} = 5.02$  TeV for different definitions of the minijet formation time  $\tau$ . The curves correspond to the definitions of  $\tau$  in Eqs. (80) (black solid), (81) (green dashed), and (83) (red dashdotted). Here  $K = 2.2$ ,  $\kappa_{\text{sat}} = 2.5$ ,  $\sigma_N = 0.532$  fm,  $\sigma_H = 0.2$  fm with 3 hotspots, and  $\sigma_{\text{trig}}^{NN} = 11.19$  mb for all the curves.

the dijet is rejected due to breaking the local saturation criterion. See Fig. 15 for the effect on the transverse energy of the output, and Fig. 13 on the effect on the jet  $p_T$ -spectrum.

The criterion in Eq. (84) stems from the original EKRT framework [55, 59–61] for QCD matter initial conditions. It postulates, that in high energy  $A+A$  collisions, a saturation mechanism arises to dynamically limit the ever rising multiplicity towards the low- $p_T$  (mini)jets. By a direct QCD calculation, this multiplicity massively overshoots the measured one if no limiting mechanism is introduced. Some saturation phenomenon to limit the growth of the gluon PDFs is needed to maintain unitarity [122]. In EbyE EKRT, this saturation is mechanized by introducing a local saturation momentum scale  $p_{\text{sat}}$  that depends on the event-by-event fluctuating local nuclear overlap  $T_{AA}$ . Schematically,  $p_{\text{sat}}$  is found at the scale, where  $2 \rightarrow 2$  processes that would yield jets start to be dominated by higher order processes, namely  $3 \rightarrow 2$ ,  $4 \rightarrow 2$  etc., when the initial gluon densities explode towards low  $x$ . This saturation is hence not a final state saturation of gluons but effectively an upper limit of the gluon flux in the initial state.

At these scales, the initial state is dominated by the gluons. The average local density of  $2 \rightarrow 2$  processes producing minijets can be written as

$$\frac{dN_{AA}^{2 \rightarrow 2}(\bar{b})}{d^2\bar{s}} \approx \frac{1}{2} \int dp_T^2 dy_1 dy_2 T_A(\bar{s}) x_1 f_g(x_1, p_T^2) \times T_B(\bar{s}) x_2 f_g(x_2, p_T^2) \times \frac{d\hat{\sigma}^{2 \rightarrow 2}}{d\hat{t}}, \quad (85)$$

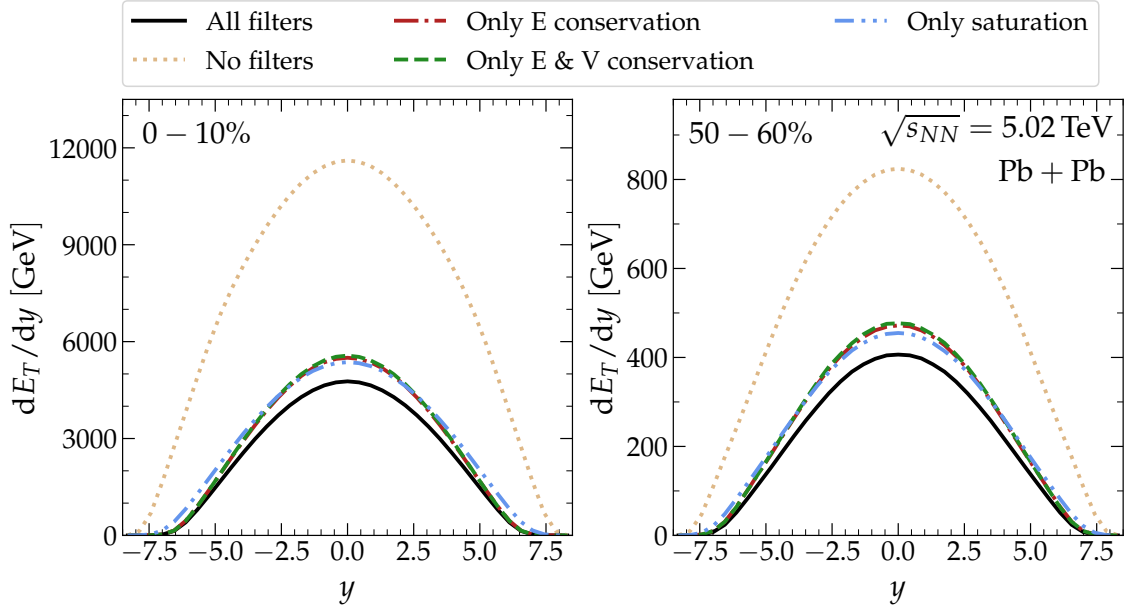


FIGURE 15 The effect of the filtering of the candidate minijets on the rapidity distributions of minijet transverse energy  $\frac{dE_T}{dy}$  in central (left panel) and peripheral (right panel) Pb+Pb collisions at  $\sqrt{s_{NN}} = 5.02$  TeV. Here  $K = 2.2$ ,  $\kappa_{\text{sat}} = 2.5$ ,  $\sigma_N = 0.532$  fm,  $\sigma_H = 0.2$  fm with 3 hotspots, and  $\sigma_{\text{trig}}^{NN} = 11.19$  mb for all the curves.

where  $p_T > p_0$  with momentum cutoff  $p_0$ . Using the fact that the gluon production cross section scales as

$$\frac{d\hat{\sigma}^{2 \rightarrow 2}}{d\hat{t}} \propto \frac{\alpha_s^2}{p_0^4}, \quad (86)$$

and by dimensional analysis, Eq. (85) becomes for central collisions (ignoring rapidity dependence, assuming symmetric collision)

$$\frac{dN_{AA}^{2 \rightarrow 2}(0)}{d^2\bar{s}} \sim (T_A x f_g) \times (T_B x f_g) \times \left( \frac{\alpha_s^2}{p_0^2} \right) \quad (87)$$

with  $x \sim p_0/\sqrt{s_{NN}}$ . Similarly for  $3 \rightarrow 2$  processes it can be written that

$$\frac{dN_{AA}^{3 \rightarrow 2}(0)}{d^2\bar{s}} \sim (T_A x f_g)^2 \times (T_B x f_g) \times \frac{\alpha_s}{p_0^2} \left( \frac{\alpha_s^2}{p_0^2} \right), \quad (88)$$

where the added  $\frac{1}{p_0^2}$  is needed here to cancel the extra dimension introduced by the additional  $T_A$ , and an extra power of  $\alpha_s$  in the  $3 \rightarrow 2$  case is accounted for. It can then be solved that at the saturation scale where  $dN_{AA}^{2 \rightarrow 2} \sim dN_{AA}^{3 \rightarrow 2}$  it also holds that

$$T_A x f_g \sim \frac{p_0^2}{\alpha_s}, \quad (89)$$

which leads to

$$\frac{dN_{AA}^{2 \rightarrow 2}(0)}{d^2\bar{s}} \sim \frac{p_0^2}{\alpha_s} \times \frac{p_0^2}{\alpha_s} \times \frac{\alpha_s^2}{p_0^2} \sim p_0^2 \times \text{constant}, \quad (90)$$



when substituted to Eq. (87). This can now be integrated over the effective nuclear transverse area  $\pi R_A^2$  to obtain

$$N_{AA}^{2 \rightarrow 2}(0) \frac{\pi}{p_0^2} \sim \pi R_A^2, \quad (91)$$

where the factor  $\pi/p_0^2$  can be interpreted as being the transverse area of the mini-jet production process dictated by uncertainty principle. This is the original (geometric) EKRT saturation criterion [59]. The transverse locality was then introduced, in EbyE EKRT [55], by a fairly similar line of reasoning, using the differential transverse energy  $dE_T/d^2\bar{s} \propto dN_{AA}/d^2\bar{s} \times p_0$ .

The evolution from saturation criterion Eq. (91) into criterion Eq. (84) can be seen directly in the basic idea that the jet processes occupy a transverse area  $\propto 1/p_T^2$ , and that the lowest- $p_T$  minijets are cut off when the coordinate space is filled. The packing factor  $\kappa_{\text{sat}}$  is very similar to  $K_{\text{sat}}$  from [55] (parametrically  $\kappa_{\text{sat}}^2 \lesssim K_{\text{sat}}$ ), but their exact numerical values are not comparable due to the differences in the frameworks.

Alternative approaches for saturation were also considered. Mainly the motivation was to introduce a rapidity dependent component to be able to control the width of the rapidity distributions. There were three general approaches. The first was to introduce a rapidity dependent factor directly to the jet radii on the right hand side of Eq. (84). Its form could, for example, be some effective part of gluon–gluon scattering cross section formula inspired by the factorized differential jet production cross section in Eq.(32). The second approach was to add another, rapidity dependent, criterion in addition to the criterion in Eq. (84). This could be, for example, an exclusion region in rapidity around both jet rapidities or dijet rapidity  $y_{\text{dijet}} = \frac{y_1+y_2}{2}$ . The third approach was to mimic the formula (89) more directly, and remove the geometrical picture altogether. In this model, the candidate dijet produced in a transverse location  $\bar{s}$  would be rejected if

$$T_A(\bar{s}) x_1 f_i^{a/A}(\bar{s}, x_1, p_T^2) \frac{\alpha_s(p_T^2)}{p_T^2} > \kappa_{\text{sat}} \quad \text{or} \quad (92)$$

$$T_B(\bar{s}) x_2 f_j^{b/B}(\bar{s}, x_2, p_T^2) \frac{\alpha_s(p_T^2)}{p_T^2} > \kappa_{\text{sat}}, \quad (93)$$

where  $T_A$  and  $T_B$  are the nucleon configuration specific, fluctuating nuclear thickness functions defined in Ch. 3.3.3 and  $f_i^{a/A}$  and  $f_j^{b/B}$  are the similarly fluctuating spatial nPDFs defined in Ch. 4.3.3.

These rapidity dependent saturation criteria and some of their variations were considered and tested. In the end, all the different methods could be tuned to yield mostly very similar results. Thus it was again chosen to use the simplest criterion—the local rapidity-independent one in Eq. (84)—in MC-EKRT.

### 5.3 Momentum conservation

In the beginning of the project that came to be MC-EKRT, it was first planned to conserve the momentum already during the generation of the candidate dijets in a manner not completely unlike what is done in HIJING [74, 75]. This was done by reducing the momentum of the scattering nucleons each time a new dijet was generated, so that the effective  $\sigma_{\text{jet}}$  would then become smaller for the subsequent nucleon–nucleon interactions. This, however, causes the jet  $p_T$ -spectrum to be smaller than in the non-momentum-conserving case, especially towards high- $p_T$  jets. In fact, this effect is the greater the larger jet  $p_T$  gets. This is directly in contradiction with the fact that factorization should hold better the larger the jet  $p_T$  gets. The root of the issue can be understood as follows. The larger the available  $\sqrt{s_{NN}}$  for the nucleon–nucleon collision is, the larger the probability of producing a high- $p_T$  dijet becomes. With decreasing  $\sqrt{s_{NN}}$ , the jet production cross sections decrease and their  $p_T$ -slopes steepen. Hence, with momentum conservation reducing the available  $\sqrt{s_{NN}}$  in the successive nucleon–nucleon collisions, it becomes increasingly less probable to produce high- $p_T$  jets. In the case of HIJING, this bias is documented in [75], and is compensated for by generating the high- $p_T$  jets first whenever such a trigger jet option is chosen.

The method that ultimately ended up in MC-EKRT, and that preserves factorization for high- $p_T$  jets, is to use the following filter after all the candidate minijets are already produced. When processing a dijet process having momentum fractions  $x_1$  and  $x_2$ , and originating from projectile nucleon  $a$ 's and target nucleon  $b$ 's parton clouds, there exists  $n$  already accepted dijet processes from  $a$ 's cloud and  $m$  accepted dijets from  $b$ 's cloud. Linked to these accepted processes, momentum fractions  $(x_1^{(1)}, \dots, x_1^{(n)})$  are used from  $a$  and  $(x_2^{(1)}, \dots, x_2^{(m)})$  are used from  $b$ . Then, if either

$$x_1 + \sum_{a=1}^n x_1^{(a)} > 1 \quad \text{or} \quad (94)$$

$$x_2 + \sum_{a=1}^m x_2^{(a)} > 1, \quad (95)$$

the candidate dijet exceeds the available per-nucleon momentum and is thus rejected. See Fig. 15 for the effect on the transverse energy of the output, and Fig. 13 for the effect on the jet  $p_T$ -spectrum.

This method behaved well and yielded satisfying results as it was tested. Again, to document the model building history, it is noted that, originally, this filter was used simultaneously with the saturation filter for each minijet at a time. Then the flow coefficient  $v_2$ – $v_3$  ratio was inspected (with 2+1 D EbyE hydrodynamics) [PIII] and the model at that time did not achieve the same accuracy as the previous EKRT studies. It was clear that saturation needed to be the most dominant limiting factor on the output, see the discussion in Ch. 5.5. An attempt was then made to relax the momentum conservation criterion somewhat. That

method was ultimately not included in MC-EKRT as applying the saturation filter first before all the other filters was found to be a better solution—especially from the viewpoint of having saturation as the dominant dynamical mechanism for regulating the produced minijet number—but it is still explained here for the sake of completeness.

Again, as in Ch. 4.3.3, the nuclear collision is considered as a collision of two clouds of partons. As the partons contributing to the production of the minijets may come from any of the nucleons in the transverse vicinity, the energy budget can also be extended to consider all the nearby nucleons as follows: Let a given dijet with momentum fractions  $x_1$  and  $x_2$  originate from the scattering of nucleon  $a_0$  from the nucleus  $A$  and nucleon  $b_0$  from the nucleus  $B$ . Let the nucleon  $a_0$  also produce dijets (before considering filters) with nucleons  $(b_1, \dots, b_m)$ . Similarly the collection of nucleons  $(a_0, \dots, a_n)$  is the part of the nucleus  $A$  that the nucleon  $b_0$  produces dijets with. The momentum conservation is then considered on the level of these collections. Let the nucleons  $(b_0, \dots, b_m)$  be associated with momentum fraction limits  $(x_{\max}^{b_0}, \dots, x_{\max}^{b_m})$ , and the nucleons  $(a_0, \dots, a_n)$  with limits  $(x_{\max}^{a_0}, \dots, x_{\max}^{a_n})$ . Now, for the dijet process to be accepted, both conditions

$$x_1 \leq \sum_{i=0}^n x_{\max}^{a_i} \quad \text{and} \quad (96)$$

$$x_2 \leq \sum_{j=0}^m x_{\max}^{b_j} \quad (97)$$

must be true. If the dijet process is accepted from all of the filters, all the limits  $x_{\max}^{a_i}$  and  $x_{\max}^{b_j}$  are reduced by factors

$$\frac{T_{nn}(\bar{s} - \bar{s}_{a_i})}{\sum_{i=0}^n T_{nn}(\bar{s} - \bar{s}_{a_i})} x_1 \quad \text{and} \quad \frac{T_{nn}(\bar{s} - \bar{s}_{b_j})}{\sum_{j=0}^m T_{nn}(\bar{s} - \bar{s}_{b_j})} x_2, \quad (98)$$

respectively, where  $\bar{s}$  is the transverse location of the origination point of the dijet (see Ch. 4.4), and  $\bar{s}_n$  is the transverse location of the nucleon  $n$ . If any of the limits  $x_{\max}$  were to go negative, they are set to zero and the remainder of the momentum fraction is reduced from the other nucleons in their collections, again in the same  $T_{nn}$  weighted manner. This process is continued iteratively until there are no remainders left, and the total reduced from  $x_{\max}^{a_i}$ :s is  $x_1$  and similarly the total reduced from  $x_{\max}^{b_j}$ :s is  $x_2$ . What makes  $T_{nn}$  weighting sensible is that with it in most cases most of the energy in a dijet process is taken from the nucleons that are closest to the process itself.

This method had some merits being a looser requirement than the strict per-nucleon momentum conservation, but it did not solve the problem with  $v_2$ – $v_3$  ratio by itself. Therefore it was decided that the momentum conservation in MC-EKRT would be implemented using the most straightforward and transparent per-nucleon method represented by Eqs. (94) and (95). The problem with the flow coefficient was then solved by changing the ordering of the filters, see the discussion in Ch. 5.5 and [PIII].

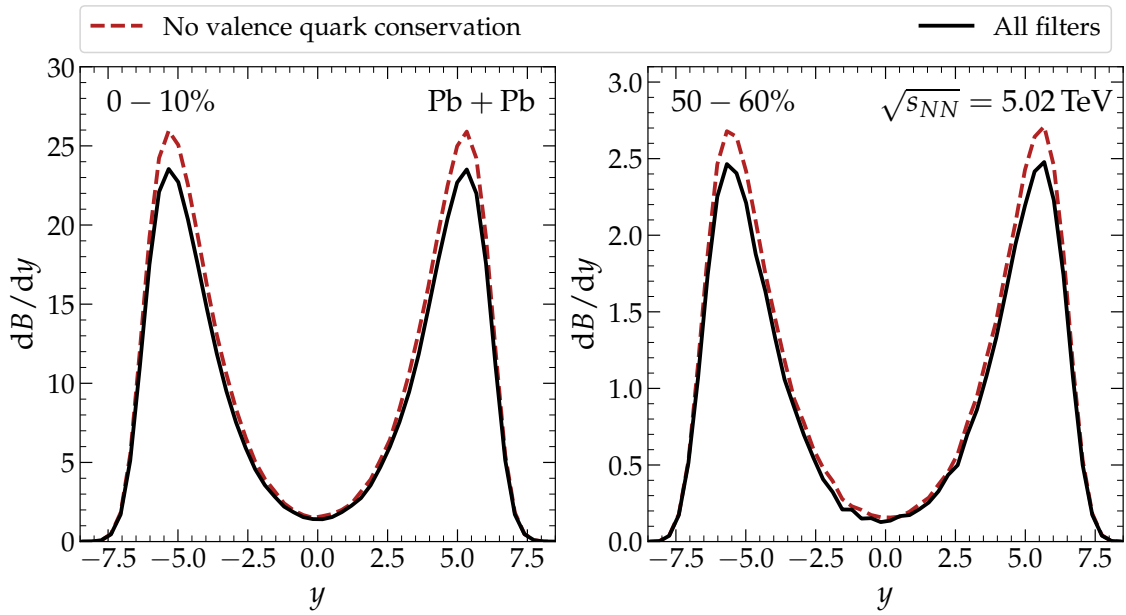


FIGURE 16 The effects of the valence quark number conservation filter on the produced minijet rapidity distribution of the baryon number  $dB/dy$  in central (left panel) and peripheral (right panel) Pb+Pb collisions at  $\sqrt{s_{NN}} = 5.02$  TeV. The curves correspond to the default MC-EKRT model with all the filters enabled (solid black) and with valence quark filter disabled (red dashed). Here  $K = 2.2$ ,  $\kappa_{\text{sat}} = 2.5$ ,  $\sigma_N = 0.532$  fm,  $\sigma_H = 0.2$  fm with 3 hotspots, and  $\sigma_{\text{trig}}^{NN} = 11.19$  mb for both of the curves.

## 5.4 Valence quark number conservation

A valence quark number conservation filter is applied to conserve baryon number and e.g. electromagnetic charge in nucleons. As explained in Ch. 4.4, the dijets that come from valence quark initiated processes are flagged. In the filtering phase, a running count is then kept of the valence quark processes for all the nucleons separately. All the dijets that would increase the valence counts over two  $u$  quarks and one  $d$  quark for proton mother or over one  $u$  quark and two  $d$  quarks for neutron mother will be rejected. This filtering is the most lenient of the three at least in  $A+A$  scatterings when only the number of rejected processes is considered, as gluon-initiated processes clearly dominate the high energy collisions. For smaller systems—e.g.  $p+A$  and especially  $p+p$ —this filter is expected to be more significant, but those studies are beyond the scope of this thesis. See Fig. 16 for the effect on the baryon number in Pb+Pb collisions at the LHC.

## 5.5 Ordering of the filters

The order in which the filters are implemented affects the end results. Consider four candidate dijets A, B, C and D. Say, A blocks B and C blocks D because of mo-

momentum conservation, and B blocks C due to saturation. Now, if the momentum conservation filter were to be sequentially applied first to the list, there would be dijets A and C left for the saturation filter. Both of them would be accepted then. If the filters were applied the other way around, starting with the saturation, dijet C would be blocked first. Then after the momentum conservation filter, the accepted dijets would be A and D, a different set from before.

This effect is amplified by the local nature of the filters. The saturation criterion is geometrical, and the momentum conservation and valence quarks both are affecting single nucleons at a time. Therefore the effects of all of the filters are strongest in the same spatial regions—in the densest regions of the nuclear matter. Considering that they all restrict the same general area, the end state will end up looking fairly similar in many observables no matter what the ordering of the filters is. As expected, global observables like  $E_T$  does not see any remarkable effects from changing the order of the filters in MC-EKRT.

The flip side of this locality of the overlapping of the filters is that the observables that depend on the fine spatial structure, like particle correlators, will undoubtedly be affected by the ordering. Using the logic above based on the global observables, it was first chosen to have all the filters applied simultaneously in MC-EKRT. A candidate dijet would on its turn be checked against all the criteria before it could be accepted to the end state. This setup was working well, until studying the flow coefficient  $v_2$ – $v_3$  ratio in the preparation of the article [PIII]. In predicting that ratio, the accuracy that the previous EKRT models [55, 123] had could not be achieved. The coefficient  $v_3$  would always be much too small compared to  $v_2$  in comparison with the data.

It was suspected, that this disparity to the previous EKRT results might have come from the over-eagerness of the momentum conservation filter. It and the saturation filter work mainly on the same neighbourhoods of jets, and have roughly the same size of an effect at least in terms of  $E_T$ , as can be seen from Figs. 15 and 13. The suspicion was that the simultaneous enforcing of the momentum conservation would wash out the spatial fine structure generated by the saturation filter. To replicate the success of the previous EKRT results in describing the experimental data also with MC-EKRT, the effect of the saturation needed to be maximized. To achieve that, the saturation filter is now applied on the whole set of the candidate dijets *first*. Only after all the candidates have been processed with that, the other filters are then applied to the remaining dijets, simultaneously. Now, the saturation filter does the bulk of the dijet multiplicity regularization and thus the fine structure of the accepted end state dijets is mainly dictated by saturation.

The saturation first –scheme is not only phenomenologically seen to work better, but also physically motivated. If one could do the pQCD calculation to the infinite order, include the higher twist effects, and use ideal many-parton distributions, the momentum would be conserved in the saturation calculation alone without the need of any momentum conservation scheme. But as the theory stands, such a thing cannot be attained, and there are still some momentum conservation left needing to be taken care of after the saturation effect. The capa-

bilities and also limits of the saturation conjecture, as a pQCD regulating mechanism but also as a device to conserve momentum, are among the main motivators of the studies in this thesis.

## 6 APPLICATION

After the final list of the produced jets is filtered from the candidates, as described in Ch. 5, the QCD matter initial conditions are ready to be formed. In this phase of the simulation, all the desired minijet quantities are calculated and the centrality selection is done. The main output from the MC-EKRT simulation is lists of generated jets in user defined centrality classes, but initial state quantities—e.g. minijet transverse energy distributions  $dE_T/dy$ —can also be calculated directly from the simulation. This may be desired for longer runs, as the jet listings grow rapidly to very large filesizes.

Based on the list of MC-EKRT simulated jets, the QCD matter initial conditions can then be computed. In article [PII], 3+1D hydrodynamical simulation was run using centrality bin –averaged initial states constructed from spatially smeared MC-EKRT minijets, to compute rapidity distributions of charged particle multiplicities  $dN_{\text{ch}}/d\eta$  in Pb+Pb collisions at  $\sqrt{s_{NN}} = 5.02$  and 2.76 TeV, and in Au+Au collisions at  $\sqrt{s_{NN}} = 200$  GeV. Also elliptic flow coefficients  $v_2$  were calculated. In article [PIII], EbyE 2+1D boost invariant fluid simulation was used in conjunction with MC-EKRT with nucleon substructure, hotspots, to study the flow coefficients  $v_n$ .

### 6.1 Centrality selection

After all the  $A+A$  events are simulated, they need to be divided into centrality classes to be able to make comparisons with the data. In principle, to make apples-to-apples comparisons with the experimental data, the centrality of an event should be determined from the final state observables—e.g. charged particle multiplicity—after the hydrodynamical simulation. Here, to achieve the desired computational efficiency, a good approximation is to use some minijet quantity  $O$ , that has a monotonous relation with a final state observable, as a proxy to determine the centrality with. Several different such quantities  $O$  can be used. The selected  $O$  is then calculated for each of the  $A+A$  events in a simulation run,

and the events are ordered in terms of decreasing  $O$ . The desired centrality class is then taken from this ordered list. For example, using total  $E_T$  (more on this below) for the centrality selection in a run of 100 000  $A+A$  events, the centrality class 0–2% would correspond to the 2 000 events with the largest total  $E_T$ . In testing it was found that at least the centrality behaviour of midrapidity transverse energy  $dE_T/dy(|y| < 0.5)$  was not very sensitive for the choice of  $O$ , but the following choices are nevertheless implemented in MC-EKRT, and implementing new ones is straightforward.

The minijet quantity  $O$  used in the articles [PII] and [PIII] was the total produced transverse energy  $E_T$ , integrated over rapidity, in the whole  $A+A$  event, which is also the default in MC-EKRT. As the simulation consists of only LO  $2 \rightarrow 2$  massless parton scatterings, the total produced  $E_T$  of the event can then be obtained as

$$E_T^{AA} = \sum_j p_T^j, \quad (99)$$

where  $p_T^j$  is the transverse momentum  $p_T$  carried by jet  $j$ , and  $j$  runs through all the jets in the output of that particular event.

Another possible quantity  $O$  could be the produced minijet transverse energy  $E_T$  in a chosen rapidity window, typically midrapidity  $|y| < 0.5$  or e.g. some forward calorimeter location of an experimental setup. This is calculated otherwise identically to Eq. (99), but the  $p_T$  of a jet is only summed if the jet hits the rapidity window, i.e.

$$E_T^{AA}(|y| < 0.5) = \sum_j \theta(0.5 - |y^j|) p_T^j, \quad (100)$$

where  $\theta$  is the Heaviside step function and  $y^j$  is the rapidity of the jet  $j$ .

In MC Glauber simulations, with hard disk nucleon–nucleon cross sections, quantities  $N_{\text{part}}$  and  $N_{\text{bin}}$  are typically defined.  $N_{\text{part}}$  is the total number of participant nucleons in the  $A+A$  event.  $N_{\text{bin}}$  (sometimes also dubbed  $N_{\text{coll}}$ ) is the total number of nucleon–nucleon subcollisions in the  $A+A$  event. As there is an option to use MC-EKRT in such a setup, and also for the sake of comparison, these are also defined here even though they are not applicable in the default MC-EKRT model. Either one of these or a combination of them could be chosen as the quantity determining centrality. Some noteworthy combinations of  $N_{\text{part}}$  and  $N_{\text{bin}}$  (used in so called two-factor ancestor models, see e.g. [124, 125]) are of the form

$$N_{2F} = x \times (1 - y) \times N_{\text{part}} + y \times N_{\text{bin}}, \quad (101)$$

where the ALICE definition [126] is  $x = 1.0$ ,  $y = 0.199$ , and—in some publications, e.g. [127, 128]—ATLAS has used the definition  $x = 0.5$ ,  $y = 0.09$ . For a given event, each of these  $N_{2F}$  ancestors (rounded down) is associated with  $E_T$  that is generated from a negative binomial distribution whose parameters are tuned iteratively so that the centrality classes of the MC Glauber output match the observed data.



## 6.2 Qualitative effects of the model parameters

The effect of different parameters of the MC-EKRT simulation can be studied qualitatively directly from the distributions of the minijets. For example, the transverse energy  $E_T$  per momentum rapidity  $y$  distributions  $dE_T/dy$  of the minijets are a qualitative proxy for the energy  $E$  per spacetime rapidity  $\eta_s = \frac{1}{2} \ln \left( \frac{t+z}{t-z} \right)$  distributions  $dE/d\eta_s$ . If  $dE_T/dy$  markedly widens, it is to be expected that also  $dE/d\eta_s$  will widen and, furthermore, also the final state rapidity distribution  $dN_{\text{ch}}/dy$  will widen. This is because the energy density will be converted to entropy density and further, after hydrodynamical evolution and decoupling, to number density of charged hadrons. The absolute magnitude of the effect is, however, not directly comparable, as e.g. a steep gradient in  $dE_T/dy$  (and thus in the energy density profile used in the initialization of the hydrodynamics) will cause the pressure gradients in the hydrodynamical evolution to push energy to higher values of  $\eta_s$ , widening  $dE/d\eta_s$  of the output.

### 6.2.1 Saturation parameter $\kappa_{\text{sat}}$ and pQCD $K$ -factor

The most impactful and important tuning parameters of the model are the saturation parameter  $\kappa_{\text{sat}}$  and pQCD  $K$ -factor, which cannot be calculated from anything a priori in the current framework, but must be decided based on the data. Their effects are most intuitive when  $dE_T/dy$  at midrapidity  $|y| < 0.5$  is studied as a function of centrality of the collision, see Fig. 17. Generally, a larger  $K$ -factor causes a larger  $dE_T/dy(|y| < 0.5)$ , regardless of the centrality. Larger  $K$ -factor increases  $\sigma_{\text{jet}}$ , causing more minijets to be produced (see Ch. 4.2). Increasing saturation parameter  $\kappa_{\text{sat}}$  also increases  $dE_T/dy(|y| < 0.5)$ , but more in central collisions than in peripheral ones. Larger  $\kappa_{\text{sat}}$  (weaker saturation) allows more of the minijets to pass the minijet filter. The saturation effects are larger in central collisions, because the strength of the saturation effect depends on the number of produced minijets. Therefore  $\kappa_{\text{sat}}$  can be used to control the centrality slope of  $dE_T/dy(|y| < 0.5)$ , and  $K$ -factor the normalization.

As the  $K$ -factor works by increasing the number of produced candidate minijets, and  $\kappa_{\text{sat}}$  dictates how many of them are filtered away, the limitations on the effects of these parameters are different. As  $\sigma_{\text{jet}}$ , and thus the expectation value of the number of candidate minijets produced from a single nucleon pair, depends linearly on the  $K$ -factor, the mechanism how the minijets get reduced as it is decreased is straightforward. The effect is limited more subtly from above. At some point, no more jets can be added due to the filters. On the other hand, because the filters are applied in the inverse  $p_T$  order, a rising  $K$ -factor will increase the average jet's  $p_T$ . Therefore the produced energy can be continued to be increased quite far by  $K$ -factor even though at some point the amount of jets may not increase as much. This effect of increasing average jet  $p_T$  has not been studied in more detail yet. Previous studies of the next to leading order (NLO) calculation of the minijet production  $K$ -factor have seen values in the single digit

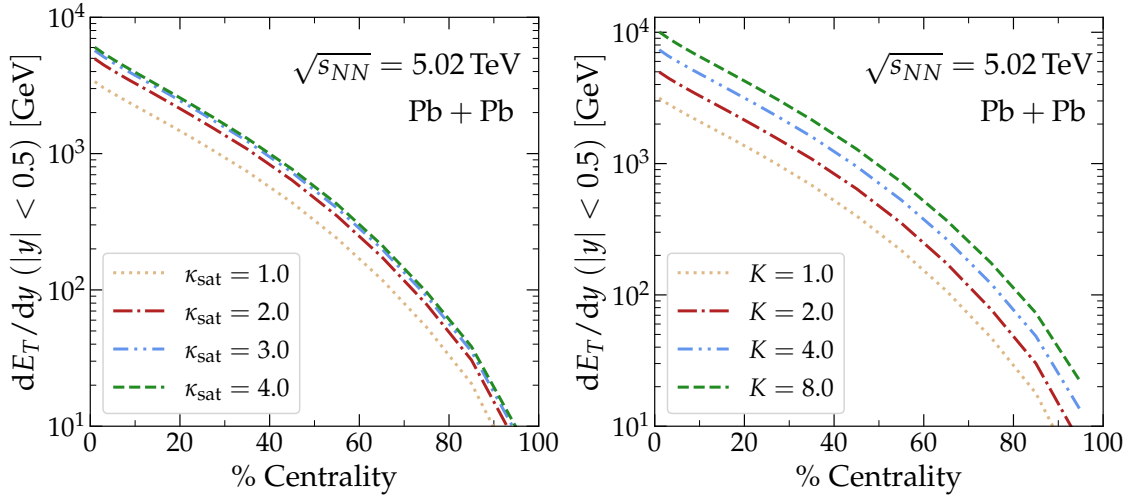


FIGURE 17 The effect of the saturation parameter  $\kappa_{\text{sat}}$  (left panel) and pQCD  $K$ -factor (right panel) on the midrapidity minijet transverse energy  $\frac{dE_T}{dy}(|y| < 0.5)$  of the MC-EKRT output for Pb+Pb collisions at  $\sqrt{s_{NN}} = 5.02$  TeV, as a function of event centrality. Here  $K = 2.0$  for all the curves in the left panel,  $\kappa_{\text{sat}} = 2.0$  for all the curves in the right panel, and  $\sigma_N = 0.532$  fm,  $\sigma_H = 0.2$  fm with 3 hotspots, and  $\sigma_{\text{trig}}^{HH} = 11.19$  mb for all the curves.

range, even up to  $\sim 7$  [129, 130]. The mechanism of the effect of  $\kappa_{\text{sat}}$  is also intuitive. When decreasing, the radii of the dijet processes increase in the transverse plane, and more candidates are filtered out (see Fig. 12). On the other hand, when it is increased, at some point no jets will be filtered out, so there is a dynamical upper limit after which increasing  $\kappa_{\text{sat}}$  does not do anything anymore.

## 6.2.2 Trigger condition and $\sigma_{\text{trig}}^{NN}$

The way that the  $A+A$  events are triggered decides which nuclear configurations will collide. In central collisions there is with high probability always a pair of nucleons close enough to collide. Therefore, changing the triggering cross section  $\sigma_{\text{trig}}^{NN}$  (see Ch. 3.2) affects peripheral collisions the most. The larger  $\sigma_{\text{trig}}^{NN}$  is, the larger the effective radii of the nucleons and thus nuclei can scatter from each other from farther apart. For this reason, the larger  $\sigma_{\text{trig}}^{NN}$  is the less minijets are generated in the most peripheral collisions, as they have smaller expectation value of the number of produced minijets ( $\bar{N}_{\text{jets}}^{ab}$ , see Ch. 4.2). See Fig. 18 for the effect of changing  $\sigma_{\text{trig}}^{NN}$ .

With default setup and no nucleon substructure,  $\sigma_{\text{trig}}^{NN}$  and the proton width  $\sigma_N$  come from the built-in parametrizations (Eqs. (6) and (11)) and the simulation runs smoothly. But if too large a value of  $\sigma_{\text{trig}}^{NN}$  is provided by the user, it can lead to the simulation run hanging, as  $\sigma_{\text{trig}}^{NN}$  is here not in any way coupled to  $\bar{N}_{\text{jets}}^{ab}$ . If a very peripheral collision is barely triggered with one pair of nucleons being just barely within each others reach,  $T_{NN}(b^2)$  will suppress the production of any minijets in that event, exponentially in  $b^2$ . In the current version of MC-EKRT, if

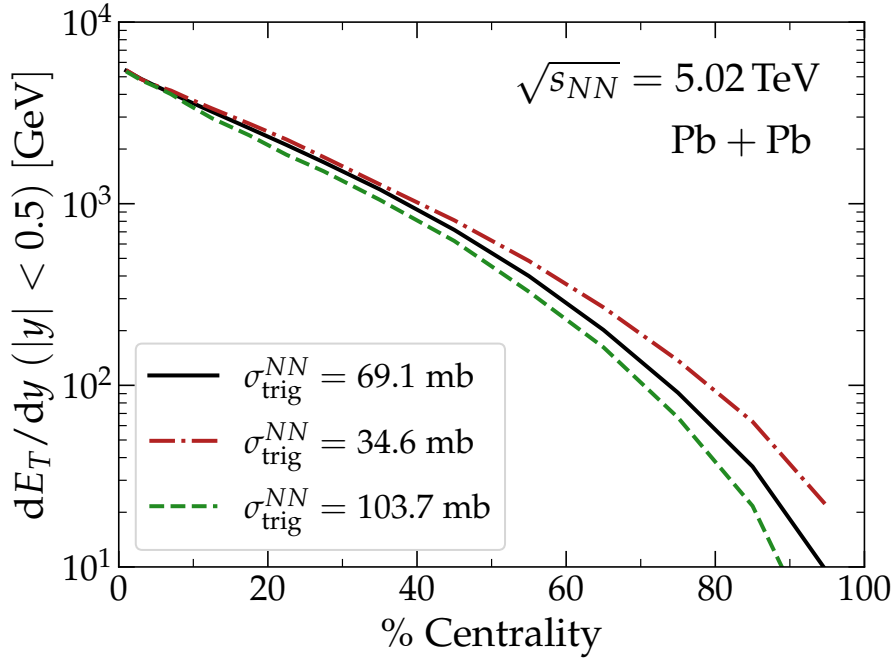


FIGURE 18 The midrapidity minijet transverse energy  $\frac{dE_T}{dy}(|y| < 0.5)$  of the MC-EKRT output, using the trigger  $\sigma_{\text{trig}}^{NN}$  value obtained from the parametrization in Eq. (6) (black solid), half the parametrized value (red dashdotted), and 1.5 times the parametrized value (green dashed), for Pb+Pb collisions at  $\sqrt{s_{NN}} = 5.02$  TeV, as a function of event centrality. Here  $K = 2.0$  and  $\kappa_{\text{sat}} = 2.0$  for all the curves. Nucleon substructure was not used.

there are no minijets in the output of a triggered event, that nuclear configuration will be simulated again ad infinitum. If for that triggering pair  $b^2$  is very large, the simulation will not produce any minijets in any reasonable time, leaving the program hanging. This problem can be even more severe with the nucleon substructure, if the triggering is done according to nucleon–nucleon distance. The hotspots can still be far away from each other even if the centers of the nucleons are relatively close. This can be avoided by triggering according to the hotspot–hotspot distance, as in Ch. 3.2.2.

### 6.2.3 Parameters of the minijet production

The number of minijets produced per a nucleon pair is dictated by  $\bar{N}_{\text{jets}}^{ab}$  (see Ch. 4.2). The width parameter  $\sigma$  (be it the width of a nucleon or a hotspot) in  $T_{NN}$  has a large effect on the number of produced minijets, very similar to the pQCD  $K$ -factor. It is in the current MC-EKRT model obtained from a parametrization of the experimental results (see Ch. 3.3.1), but it is worth noting that the model is very sensitive to it.

The value of the integrated  $\sigma_{\text{jet}}$  is very sensitive to the momentum cutoff  $p_0$ , but the total MC-EKRT model actually *is not* (see Fig. 13). The majority of the extra minijets produced by lowering  $p_0$  will be generated near  $p_T \approx p_0$  region,

which is mostly filtered away by the EKRT saturation. As a QCD calculation,  $\sigma_{\text{jet}}$  is also fairly sensitive to the used PDF set and the factorization and renormalization scales, as can be seen in [PI]. Clearly, the choices for the PDFs and the renormalization/factorization scales are correlated with the value of the  $K$ -factor as well, but these effects are not studied in detail yet.

#### 6.2.4 Other parameters

The collision energy  $\sqrt{s_{NN}}$  dependence is built-in in MC-EKRT as the cross section  $\sigma_{\text{jet}}$  is always calculated separately and the widths of the thickness functions are parametrized, but the energy is assumed to be large enough for collinear factorization to be accurate, and the colliding nuclei are assumed to be contracted to zero thickness. No assumptions are made on the nucleus itself (apart what is said about its nucleon structure in Ch. 3.1), but the majority of the testing is done with  $\text{Pb}^{208}$  and  $\text{Au}^{197}$ . Nothing should prevent the model from working for any other nuclei, as long as the correct PDFs are used and the random rotation for the deformed nuclei is added. The model is also suitable for p+A and even p+p simulation. While very interesting applications, these remain out of the scope of this thesis.

### 6.3 Input and output

The user of the MC-EKRT simulation code is expected to provide a file that specifies the parameters of the simulation run. Its name can be given as a command line argument of the program, and its format and the parameter options can be found in a file called `params_template` and in Appendix 1.1. Another input file can also be given, in which the centrality classes desired to be in the output can be provided. This can be beneficial, if the run is very large and the size of the output files is a concern. The name of the mentioned centrality class file is taken as a parameter in the parameter file. Any number of centrality classes can be specified, and if not otherwise specified, a single class of 0–100% centrality is used. In yet another file, named `output_params`, the jet properties desired to be saved are given. This is again to reduce the output filesize if not every property is needed. The format and available options can be seen in the `output_params` file provided with the code and in Appendix 1.2.

The specified properties of the simulated (mini)jets in the specified centrality classes are output in binary format to separate files for different centrality classes. An example of how said binary files can be read and used can be found in the provided source code `jet_reader.cpp`. Note that it is not necessary to use specifically C++ to read the output files, but as the implementation of integers and floating point numbers is platform dependent in C++, the number representation of the jet properties cannot be universally known but must be determined by the user based on the used platform. Therefore it is often the most straight-

forward to use the provided `jet_reader.cpp` at least as an intermediary. No matter what the number representation, the file always begins by the amount of total  $A+A$  events in this particular file. After this follow the properties of all the events, starting with the most central one. The record of each event starts with the total number of produced minijets. Then all the desired properties of each dijet are listed, one after another. No breaking characters is used at any point.

## 6.4 Hydrodynamical initial state

The MC-EKRT simulation can be used to provide the initial state of the QCD matter for a relativistic hydrodynamical simulation. As the initial state consists of semi-hard and hard partons (jets) whose momenta are fully known, all the components of the energy–momentum tensor  $T^{\mu\nu}$  can, in principle, be computed. In practice, a fair amount of additional work is required, as explained in [PII]. Hydrodynamical simulations need to have a continuous and smooth enough initial state for the evolution algorithm to be stable, while the jets'  $T^{\mu\nu}$  is a collection of discrete spikes.

### 6.4.1 3+1D simulation

In [PII], a 3+1D viscous fluid dynamical simulation is initialized as follows. The MC-EKRT simulated minijets are then propagated as free particles to the proper time surface  $\tau_0 = 1/p_0 (= 0.2 \text{ fm})$  and spacetime rapidity  $\eta_s = y$ , where  $\eta_s = \frac{1}{2} \ln \left( \frac{t+z}{t-z} \right)$  and  $y$  being the momentum rapidity.

A Gaussian smoothing is then used to obtain the event-by-event initial value of the energy component of the energy–momentum tensor  $T^{\tau\tau}(\tau, \mathbf{x}_\perp, \eta_s)$ , which is written in the hyperbolic coordinates with longitudinal proper time  $\tau = \sqrt{t^2 - z^2} = t / \cosh \eta_s$ , transverse coordinate  $\mathbf{x}_\perp$  and  $\eta_s$ . Each minijet  $i$  contributes its momentum into  $T^{\tau\tau}$  as a Gaussian smeared distribution (see details in [PII]). This yields

$$T^{\tau\tau}(\tau, \mathbf{x}_\perp, \eta_s) = \frac{1}{\tau} \sum_i p_{T,i} g_\perp(\mathbf{x}_\perp; \mathbf{x}_{\perp,i}) g_\parallel(\eta_s; \eta_{s,i}) \quad (102)$$

with smearing functions

$$g_\perp(\mathbf{x}_\perp; \mathbf{x}_{\perp,i}) = \frac{C_\perp}{2\pi\sigma_\perp^2} \exp \left[ -\frac{(\mathbf{x}_\perp - \mathbf{x}_{\perp,i})^2}{2\sigma_\perp^2} \right], \quad (103)$$

$$g_\parallel(\eta_s; \eta_{s,i}) = \frac{C_\parallel}{\sqrt{2\pi\sigma_\parallel^2}} \exp \left[ -\frac{(\eta_s - \eta_{s,i})^2}{2\sigma_\parallel^2} \right], \quad (104)$$

where the widths  $\sigma_{\perp}$  and  $\sigma_{\parallel}$  are model parameters determined on the basis of experimental data. The smearing functions are normalized as

$$\int d^2\mathbf{x}_T d\eta_s g_{\perp}(\mathbf{x}_{\perp}; \mathbf{x}_{\perp, i}) g_{\parallel}(\eta_s; \eta_{s, i}) = 1. \quad (105)$$

All the non-diagonal components of  $T^{\mu\nu}$  are then put to zero, while the rest of the diagonal elements are obtained by

$$T^{ij} = P(e) \delta^{ij}, \quad (106)$$

where  $\delta$  is the Kronecker symbol and  $P(e)$  is the isotropic pressure obtained from the equation of state (EoS) of strongly interacting matter at zero net-baryon density. Here, the *s95p-v1* [131] parametrization with a chemical freeze-out at temperature  $T = 150$  MeV is used. The smearing in  $\eta_s$  increases the energy in the system, as the relation  $E = p_T \cosh \eta_s$  is not linear. In [PII], the increase in total energy is observed to be  $\sim 1\%$  for  $\sigma_{\parallel} = 0.15$ , and  $\sim 10\%$  for  $\sigma_{\parallel} = 0.5$ , but the increase is concentrated at the larger values of  $\eta_s$ , which in practice are not relevant for this study.

The event-by-event  $T^{\tau\tau}$  is then converted into entropy density profile using the EoS. These entropy density profiles are then averaged for each centrality class, and then converted back to energy density. This averaging process minimizes the amount of times the computationally very demanding 3+1D fluid simulation needs to be run. The energy density is then fed to the relativistic dissipative second-order transient fluid dynamics simulation (details in [PII, 51, 132, 133]) until the kinetic freeze-out at  $T = 130$  MeV. In obtaining the results shown below, either a constant value or the parametrization *param1* (from [55]) for the shear viscosity over entropy density  $\eta/s$  is used, and bulk viscous effects are ignored. The nucleons had no substructure in MC-EKRT in [PII].

The charged particle multiplicity  $dN_{\text{ch}}/d\eta$  as a function of pseudorapidity  $\eta = \frac{1}{2} \log \frac{|\mathbf{p}| + p_z}{|\mathbf{p}| - p_z}$ , where  $\mathbf{p}$  is the three-momentum of the particle, was obtained [PII] with the setup described above. The results for Pb+Pb collisions at LHC energies and Au+Au collisions at RHIC energy, with comparison to data as reported by ALICE [134, 135] and PHOBOS [136] collaborations, are presented in Fig. 19. The most notable feature of the results is that by fixing  $\kappa_{\text{sat}}$  once, the centrality behaviour of the data is reproduced for all the energies, given that the normalization is also fixed by an energy-dependent  $K$ -factor. The combination of  $\kappa_{\text{sat}}$  and  $K$  is chosen so that a simultaneous good agreement with the measured multiplicities and with the flow coefficient  $v_2$  is achieved, see Fig. 16 in [PII]. The  $\eta$ -dependence is also reproduced remarkably well up to at least  $|\eta| < 2$  for all the energies. At the most off-center rapidities  $|\eta| > 2$ , the simulated distributions were a bit too narrow. This might hint that the per-nucleon momentum conservation criterion might be too strict. This would be in line with the thinking employed in the developing of the snPDFs, that one should imagine the nuclei rather as clouds of partons than as collections of separate nucleons. In any case, the obtained good agreement is a rather non-trivial result, recalling all the required model development steps. The resulting rapidity distributions are also relatively robust against the parameter

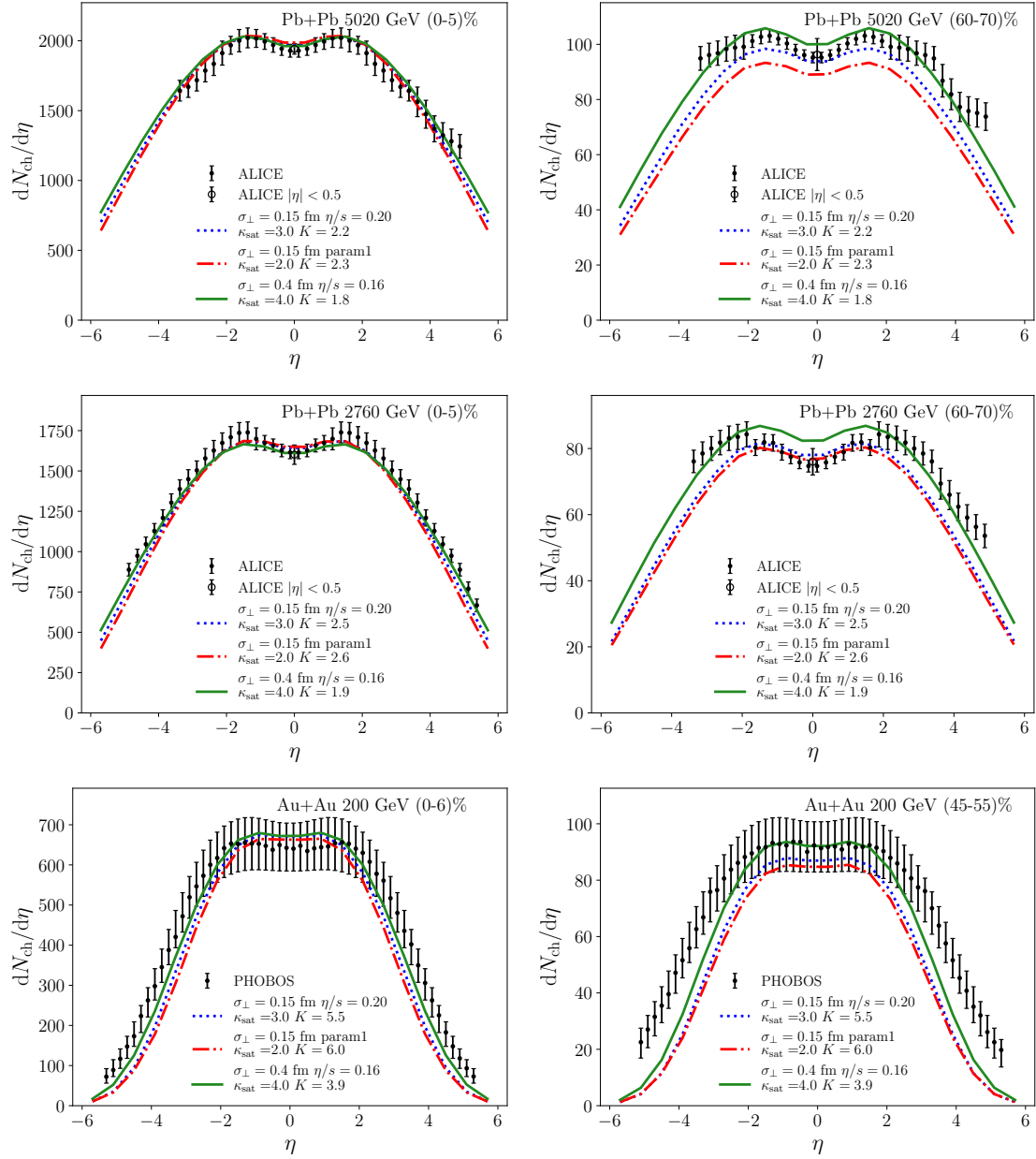


FIGURE 19 Pseudorapidity distribution of the charged particle multiplicity  $\frac{dN_{\text{ch}}}{d\eta}$ , obtained with 3+1D hydrodynamical simulation using centrality class – averaged MC-EKRT initial states [PII] (see 6.4.1), for Pb+Pb collisions at  $\sqrt{s_{NN}} = 5.02$  TeV (top row) and  $\sqrt{s_{NN}} = 2.76$  TeV (middle row), and Au+Au collisions at  $\sqrt{s_{NN}} = 200$  GeV (bottom row). Left hand panels are for central collisions and right hand panels for peripheral collisions. The different curves represent different parameters for MC-EKRT and the fluid simulation, details in [PII]. The values of pQCD  $K$ -factor and saturation parameter  $\kappa_{\text{sat}}$  are, for each curve separately, determined by the experimental data by ALICE and PHOBOS from [134–136]. The  $K$ -factor is treated as a function of energy (constant for each row), while  $\kappa_{\text{sat}}$  is kept constant. Taken from [PII].

changes, which in turn lends support to the conjecture that the driving mechanism in regulating pQCD parton production is indeed saturation.

#### 6.4.2 2+1D simulation

In [PIII], a similar initialization scheme is used, but EbyE and for 2+1D viscous fluid dynamical simulation with nonzero bulk viscosity and dynamical decoupling conditions to better capture the EbyE effects of collective dynamics on observables such as flow coefficients. To reduce the dimensionality from 3+1D to 2+1D, the longitudinal expansion is assumed boost invariant. The dynamical decoupling of the system depends on two criteria [123]: the decoupling happens when the local Knudsen number reaches a constant value  $\sim 1$ , or when the mean free path in the system is of the same order as the system size. Here, as only the midrapidity is concerned by the fluid simulation, the Gaussian smearing of the minijets is needed only in  $\mathbf{x}_\perp$ . Instead of Eq. (102), the initial energy density is given by

$$T^{\tau\tau}(\tau, \mathbf{x}_\perp) = \frac{1}{\tau\Delta y} \sum_i p_{T,i} g_\perp(\mathbf{x}_\perp; \mathbf{x}_{\perp,i}) \theta(\Delta y/2 - |y_i|), \quad (107)$$

where  $\theta$  is the Heaviside theta function that picks only the partons that are produced in the midrapidity  $\Delta y$  and  $g_\perp$  is otherwise as in Eq. (103) but normalized as

$$\int d^2\mathbf{x}_T g_\perp(\mathbf{x}_\perp; \mathbf{x}_{\perp,i}) = 1. \quad (108)$$

Figure 20 shows the results from [PIII] on the flow coefficients  $v_n$  as a function of centrality, compared to the EbyE EKRT results [123] and the ALICE measurements [53], in Pb+Pb collisions at the LHC energies. Of the different EbyE MC-EKRT setups in Fig. 20, one uses the default parametrization (Eq. (11)) for nucleon width  $\sigma_N$  and no nucleon substructure, while the other two use 3 hotspots, one with the default  $\sigma_N$  parametrization and wider hotspots and the other with a stronger energy dependence in  $\sigma_N$  and narrower hotspots. The pQCD  $K$ -factor is first set at  $\sqrt{s_{NN}} = 5.023$  TeV to  $K = 2.5$  for all the curves, and the saturation parameter  $\kappa_{\text{sat}}$  is adjusted so that similar values of charged particle multiplicities  $N_{ch}$  are produced at central collisions. Then, for  $\sqrt{s_{NN}} = 2.76$  TeV, the values of  $\kappa_{\text{sat}}$  are kept constant, and the  $K$ -factors are adjusted similarly to achieve the correct values of  $N_{ch}$  at central collisions. It can be seen that the various fluctuations in the initial states provided by MC-EKRT improve the results of the hydrodynamical simulation—especially concerning the energy dependence—when compared to the previous EKRT results. The addition of the nucleon substructure model is shown to be essential to capture the centrality dependence of the flow coefficients  $v_n$ , and particularly the  $v_3/v_2$  ratio, with narrower hotspots providing the best agreement with the data. This gives further evidence that the saturation should be the principal mechanism regulating the low- $p_T$  minijets, as the strength of the saturation effects first increase when hotspots are added to the model and then even more if the hotspots are made narrower.



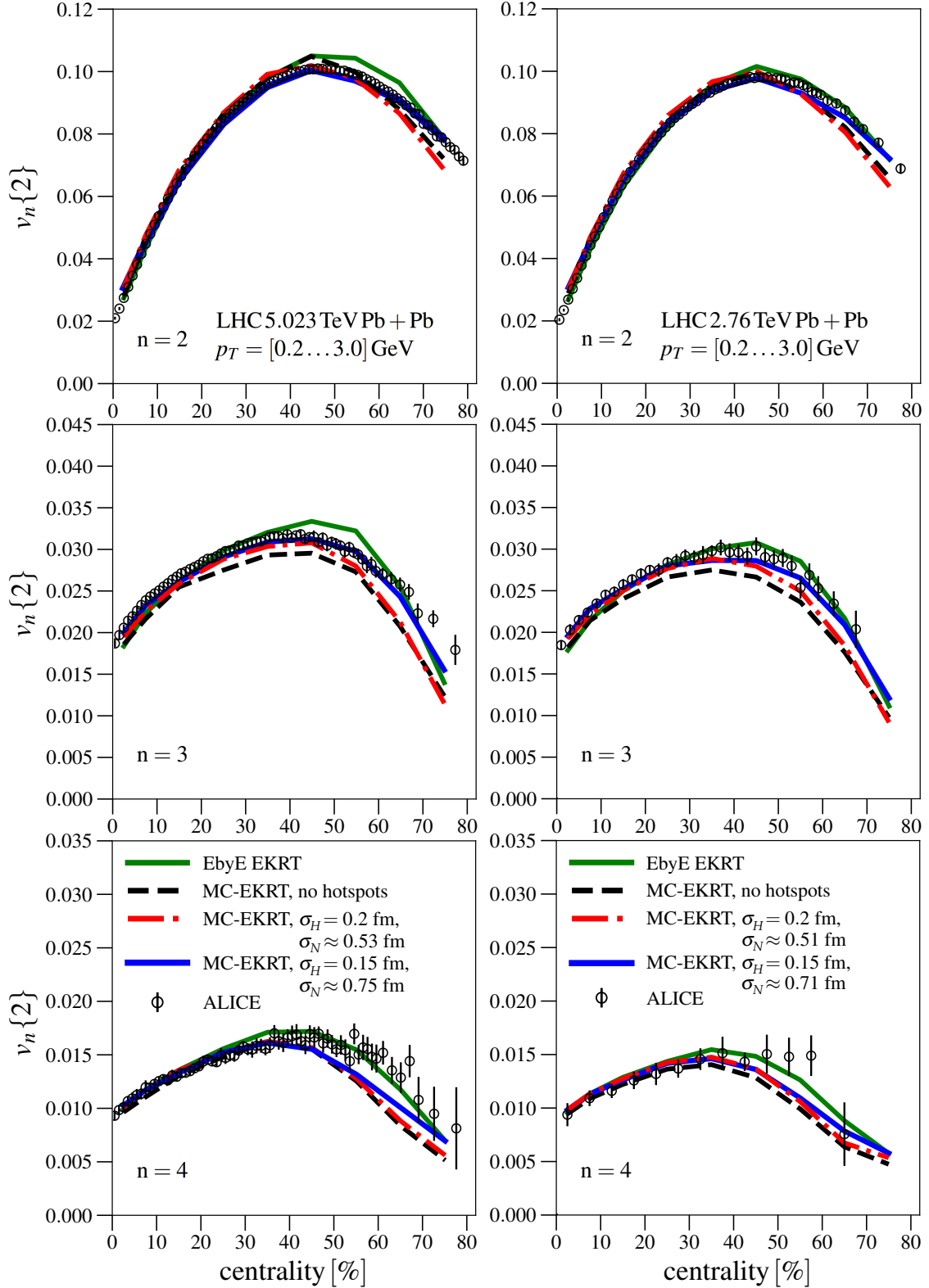


FIGURE 20 The comparison of flow coefficients  $v_n\{2\}$ , for  $n=2$  (top row),  $n=3$  (middle row) and  $n=4$  (bottom row), obtained from 2+1D fluid dynamical simulation using MC-EKRT initial states with different parameters, the EbyE EKRT results from [123], and the measurements by ALICE [53], as a function of centrality. The left (right) hand panels correspond to  $\sqrt{s_{NN}}=5.023$  TeV (2.76 TeV) Pb+Pb collisions at LHC. Taken from [PIII].

## 7 CONCLUSIONS AND OUTLOOK

This thesis explains the ins and outs of the brand new Monte-Carlo implementation of the EKRT initial state model, serving as a technical documentation of the finer details—and the development history—of the model. The event generator based on the presented principles opens a brand new dimension to be explored, event-by-event, with the EKRT saturation framework, which has already had a solid standing in describing the strongly interacting matter initial state for a couple of decades. The new MC-EKRT model with rapidity dependent initial states and minijet multiplicity fluctuations allows for a computation of rapidity-dependent observables, which provide, via a global analysis, further constraints to the QCD matter properties.

In the article [PI], the calculation of electro-weak boson production in Pb+Pb scatterings was studied for the possibility of a data signal of nuclear shadowing in the nucleon–nucleon inelastic scattering cross section used in Monte-Carlo Glauber models. The interpretation of the shadowing signal leaned on the ability to calculate the mentioned inelastic cross section from perturbative QCD using an eikonal minijet model and nuclear shadowed PDFs in calculating the minijet production cross section. While the  $\sigma_{\text{inel}}^{NN}$ -normalized version of the eikonal minijet model is, in the end, not used in MC-EKRT, it was a crucial step in its evolution, and the underlying minijet production calculation is nevertheless still the same.

A robust framework for introducing a spatial dependence to nuclear effects in parton distribution functions of the nucleons bound in nuclei is presented. These logarithmic-geometric snPDFs, which were already used in articles [PII] and [PIII], are applicable—for the very first time—also in the case of the most extreme nucleon density fluctuations found frequently in event-by-event simulations, thanks to a positive definite functional form that has an unbounded domain. The snPDFs are also computationally light enough for event-by-event simulations, as they use a handy density-quantity  $\hat{T}_A^a$  to incorporate the spatial dependence. This quantity  $\hat{T}_A^a$  is the average overlap of nucleon  $a$  and the nucleus  $A$  in a mean field approximation fashion. The resulting snPDFs of a specific nucleon  $a$  depend spatially only on  $a$ 's position relative to the other nucleons,

making the snPDFs unique for each nucleon and each nucleon configuration of the nucleus.

The initial state created by MC-EKRT consists of a collection of dynamically event-by-event fluctuating minijets generated by a fluctuating pQCD model. The full 4-momentum vector, spatial location and partonic flavour is known for each minijet, as well as information about their formation, like nuclear thickness on their location and the PDFs used in the process they were generated in. The multiplicity of the minijet collection is locally in the transverse plane regulated by a new event-by-event version of the EKRT saturation criterion, and the surviving minijet collection conserves momentum and the valence quarks of the initial nuclei on a per-nucleon basis. As seen in the discussion in [PII], this per-nucleon momentum conservation might in the end be too strict a criterion. Further studies are certainly needed on that part.

The full NLO implementation of the  $\sigma_{\text{jet}}$  calculation in the simulation would be a very interesting but quite a non-trivial task, and it would definitely come with a performance cost. The  $K$ -factor used in MC-EKRT could be calculated exactly in NLO accuracy (in [55, 129, 130] this was done for a midrapidity window). Even though the scale dependence remains large for small  $p_T$  at NLO, such a calculation would give a controlled access to the  $p_T$  and  $\sqrt{s_{NN}}$  dependencies of the  $K$ -factor. Still, even if the  $K$ -factor were determined from NLO, another model parameter would have to be introduced to control the optimal scale choice determined by the data, i.e. the number of model parameters would remain the same.

Articles [PII] and [PIII] serve as proofs of concept for the validity of the MC-EKRT model and study its capabilities in catching the intricacies of the nuclear collisions represented by observables such as rapidity distributions of the produced particles and the flow coefficients. They also offer use-case examples of how the minijet output of the MC-EKRT simulation could be used to start a fluid dynamical simulation. As can be seen from the results of the articles [PII] and [PIII], MC-EKRT manages to provide a detailed and well working, novel way to describe the initial state of the QCD matter in a full 3D picture.

There are many avenues to venture in QGP studies. One fascinating direction, which was left untouched by the work in this thesis, is the high multiplicity  $p+A$  events. MC-EKRT is ideal for studying the QCD matter possibly formed there, as the large fluctuations that give rise to those events are inherently part of the model. The effect of these event-by-event fluctuations is intriguing also in  $A+A$ , where the complete initialization of the full energy–momentum tensor  $T^{\mu\nu}$  will probably need parton showering (such as from PYTHIA [72]) to be incorporated in the model. QCD kinetic theory, as in [24], could also be used to bridge the gap from the nonequilibrium of the initial state to the hydrodynamic phase described by the fluid simulations. Another still missing feature is a more detailed treatment of the uncertainty of the minijet production location in the beam direction  $z$ , as currently all the partons are assumed to be produced exactly at  $z = 0$  [137]. Finally, all the studies involving hard probes—especially hard partons which produce hard observable jets and high-energy hadrons—in the strongly interacting matter would naturally benefit from an initial state gener-

ator that can simultaneously generate the probe and the background within one framework, like the one presented in this thesis.

## REFERENCES

- [1] N. Cabibbo and G. Parisi. “Exponential Hadronic Spectrum and Quark Liberation”. In: *Phys. Lett. B* 59 (1975), pp. 67–69. DOI: 10.1016/0370-2693(75)90158-6.
- [2] E. V. Shuryak. “Theory of Hadronic Plasma”. In: *Sov. Phys. JETP* 47 (1978), pp. 212–219.
- [3] A. Bazavov et al. “Equation of State in (2+1)-Flavor QCD”. In: *Phys. Rev. D* 90 (2014), p. 094503. DOI: 10.1103/PhysRevD.90.094503.
- [4] A. Bazavov, P. Petreczky, and J. H. Weber. “Equation of State in 2+1 Flavor QCD at High Temperatures”. In: *Phys. Rev. D* 97.1 (2018), p. 014510. DOI: 10.1103/PhysRevD.97.014510.
- [5] S. Borsanyi et al. “Full Result for the QCD Equation of State with 2+1 Flavors”. In: *Phys. Lett. B* 730 (2014), pp. 99–104. DOI: 10.1016/j.physletb.2014.01.007.
- [6] S. Borsanyi et al. “The QCD Equation of State with Dynamical Quarks”. In: *JHEP* 11 (2010), p. 077. DOI: 10.1007/JHEP11(2010)077.
- [7] H. Fritzsche, M. Gell-Mann, and H. Leutwyler. “Advantages of the Color Octet Gluon Picture”. In: *Phys. Lett. B* 47 (1973), pp. 365–368. DOI: 10.1016/0370-2693(73)90625-4.
- [8] S. L. Glashow. “Partial Symmetries of Weak Interactions”. In: *Nucl. Phys.* 22 (1961), pp. 579–588. DOI: 10.1016/0029-5582(61)90469-2.
- [9] S. Weinberg. “A Model of Leptons”. In: *Phys. Rev. Lett.* 19 (1967), pp. 1264–1266. DOI: 10.1103/PhysRevLett.19.1264.
- [10] P. W. Higgs. “Broken Symmetries and the Masses of Gauge Bosons”. In: *Phys. Rev. Lett.* 13 (1964). Ed. by J. C. Taylor, pp. 508–509. DOI: 10.1103/PhysRevLett.13.508.
- [11] G. 't Hooft. “The Evolution of Quantum Field Theory, From QED to Grand Unification”. In: *Adv. Ser. Direct. High Energy Phys.* 26 (2016), pp. 1–27. DOI: 10.1142/9789814733519\_0001.
- [12] ALICE collaboration. “The ALICE Experiment – A Journey through QCD”. In: *CERN-EP-2022-227* (2022). URL: <https://arxiv.org/abs/2211.04384>.
- [13] CMS collaboration. “Overview of High-Density QCD Studies with the CMS Experiment at the LHC”. In: *CMS-HIN-23-011, CERN-EP-2024-057* (2024). URL: <https://arxiv.org/abs/2405.10785>.
- [14] PHENIX Collaboration. “An Upgrade Proposal from the PHENIX Collaboration”. In: *preprint* (2015). URL: <https://arxiv.org/abs/1501.06197>.
- [15] J. E. Bernhard, J. S. Moreland, and S. A. Bass. “Bayesian Estimation of the Specific Shear and Bulk Viscosity of Quark–Gluon Plasma”. In: *Nature Phys.* 15.11 (2019), pp. 1113–1117. DOI: 10.1038/s41567-019-0611-8.

- [16] D. J. Gross. “The Discovery of Asymptotic Freedom and the Emergence of QCD”. In: *Proc. Nat. Acad. Sci.* 102 (2005), pp. 9099–9108. DOI: 10.1073/pnas.0503831102.
- [17] K. J. Eskola, K. Kajantie, and J. Lindfors. “Quark and Gluon Production in High-Energy Nucleus-Nucleus Collisions”. In: *Nucl. Phys. B* 323 (1989), pp. 37–52. DOI: 10.1016/0550-3213(89)90586-5.
- [18] K. Kajantie, P. V. Landshoff, and J. Lindfors. “Minijet Production in High-Energy Nucleus-Nucleus Collisions”. In: *Phys. Rev. Lett.* 59 (1987), p. 2527. DOI: 10.1103/PhysRevLett.59.2527.
- [19] X.-N. Wang. “Role of Multiple Mini - Jets in High-Energy Hadronic Reactions”. In: *Phys. Rev. D* 43 (1991), pp. 104–112. DOI: 10.1103/PhysRevD.43.104.
- [20] K. J. Eskola and K. Kajantie. “Baryon to Entropy Ratio in Very High-Energy Nuclear Collisions”. In: *Z. Phys. C* 75 (1997), pp. 515–522. DOI: 10.1007/s002880050495.
- [21] R. Baier et al. “‘Bottom up’ Thermalization in Heavy Ion Collisions”. In: *Phys. Lett. B* 502 (2001), pp. 51–58. DOI: 10.1016/S0370-2693(01)00191-5.
- [22] P. B. Arnold, G. D. Moore, and L. G. Yaffe. “Effective Kinetic Theory for High Temperature Gauge Theories”. In: *JHEP* 01 (2003), p. 030. DOI: 10.1088/1126-6708/2003/01/030.
- [23] A. Kurkela et al. “Effective Kinetic Description of Event-by-Event Pre-Equilibrium Dynamics in High-Energy Heavy-Ion Collisions”. In: *Phys. Rev. C* 99.3 (2019), p. 034910. DOI: 10.1103/PhysRevC.99.034910.
- [24] A. Kurkela et al. “Matching the Nonequilibrium Initial Stage of Heavy Ion Collisions to Hydrodynamics with QCD Kinetic Theory”. In: *Phys. Rev. Lett.* 122.12 (2019), p. 122302. DOI: 10.1103/PhysRevLett.122.122302.
- [25] L. D. Faddeev and V. N. Popov. “Feynman Diagrams for the Yang-Mills Field”. In: *Phys. Lett. B* 25 (1967). Ed. by J.-P. Hsu and D. Fine, pp. 29–30. DOI: 10.1016/0370-2693(67)90067-6.
- [26] C. G. Callan Jr. “Broken Scale Invariance in Scalar Field Theory”. In: *Phys. Rev. D* 2 (1970), pp. 1541–1547. DOI: 10.1103/PhysRevD.2.1541.
- [27] K. Symanzik. “Small Distance Behavior in Field Theory and Power Counting”. In: *Commun. Math. Phys.* 18 (1970), pp. 227–246. DOI: 10.1007/BF01649434.
- [28] D. J. Gross and F. Wilczek. “Ultraviolet Behavior of Nonabelian Gauge Theories”. In: *Phys. Rev. Lett.* 30 (1973). Ed. by J. C. Taylor, pp. 1343–1346. DOI: 10.1103/PhysRevLett.30.1343.
- [29] H. D. Politzer. “Reliable Perturbative Results for Strong Interactions?” In: *Phys. Rev. Lett.* 30 (1973). Ed. by J. C. Taylor, pp. 1346–1349. DOI: 10.1103/PhysRevLett.30.1346.

- [30] R. Gupta. “Introduction to Lattice QCD: Course”. In: *Les Houches Summer School in Theoretical Physics, Session 68: Probing the Standard Model of Particle Interactions*. July 1997, pp. 83–219.
- [31] S. Muroya et al. “Lattice QCD at Finite Density: An Introductory Review”. In: *Prog. Theor. Phys.* 110 (2003), pp. 615–668. DOI: 10.1143/PTP.110.615.
- [32] C. Ratti. “Lattice QCD and Heavy Ion Collisions: A Review of Recent Progress”. In: *Rept. Prog. Phys.* 81.8 (2018), p. 084301. DOI: 10.1088/1361-6633/aabb97.
- [33] C. P. Burgess. “Introduction to Effective Field Theory”. In: *Ann. Rev. Nucl. Part. Sci.* 57 (2007), pp. 329–362. DOI: 10.1146/annurev.nucl.56.080805.140508.
- [34] G. T. Bodwin, E. Braaten, and G. P. Lepage. “Rigorous QCD Analysis of Inclusive Annihilation and Production of Heavy Quarkonium”. In: *Phys. Rev. D* 51 (1995). [Erratum: *Phys.Rev.D* 55, 5853 (1997)], pp. 1125–1171. DOI: 10.1103/PhysRevD.55.5853.
- [35] N. Brambilla et al. “Potential NRQCD: An Effective Theory for Heavy Quarkonium”. In: *Nucl. Phys. B* 566 (2000), p. 275. DOI: 10.1016/S0550-3213(99)00693-8.
- [36] E. Iancu and R. Venugopalan. “The Color Glass Condensate and High-Energy Scattering in QCD”. In: *Quark-Gluon Plasma 4*. Ed. by R. C. Hwa and X.-N. Wang. 2003, pp. 249–3363. DOI: 10.1142/9789812795533\_0005.
- [37] H. Weigert. “Evolution at Small  $x(B_j)$ : The Color Glass Condensate”. In: *Prog. Part. Nucl. Phys.* 55 (2005), pp. 461–565. DOI: 10.1016/j.pnpnp.2005.01.029.
- [38] F. Gelis et al. “The Color Glass Condensate”. In: *Ann. Rev. Nucl. Part. Sci.* 60 (2010), pp. 463–489. DOI: 10.1146/annurev.nucl.010909.083629.
- [39] P. Kovtun, D. T. Son, and A. O. Starinets. “Viscosity in Strongly Interacting Quantum Field Theories from Black Hole Physics”. In: *Phys. Rev. Lett.* 94 (2005), p. 111601. DOI: 10.1103/PhysRevLett.94.111601.
- [40] A. Kurkela and E. Lu. “Approach to Equilibrium in Weakly Coupled Non-Abelian Plasmas”. In: *Phys. Rev. Lett.* 113.18 (2014), p. 182301. DOI: 10.1103/PhysRevLett.113.182301.
- [41] U. Heinz and R. Snellings. “Collective Flow and Viscosity in Relativistic Heavy-Ion Collisions”. In: *Ann. Rev. Nucl. Part. Sci.* 63 (2013), pp. 123–151. DOI: 10.1146/annurev-nucl-102212-170540.
- [42] J. Greensite. *An Introduction to the Confinement Problem*. Vol. 821. 2011. DOI: 10.1007/978-3-642-14382-3.
- [43] A. Bazavov et al. “Equation of State and QCD Transition at Finite Temperature”. In: *Phys. Rev. D* 80 (2009), p. 014504. DOI: 10.1103/PhysRevD.80.014504.

- [44] P. Braun-Munzinger, K. Redlich, and J. Stachel. “Particle Production in Heavy Ion Collisions”. In: (2003). Ed. by R. C. Hwa and X.-N. Wang, pp. 491–599. DOI: 10.1142/9789812795533\_0008.
- [45] F. Becattini and R. Fries. “The QCD Confinement Transition: Hadron Formation”. In: *Landolt-Bornstein* 23 (2010). Ed. by R. Stock, p. 208. DOI: 10.1007/978-3-642-01539-7\_8.
- [46] E. Schnedermann, J. Sollfrank, and U. W. Heinz. “Thermal Phenomenology of Hadrons from 200-A/GeV S+S Collisions”. In: *Phys. Rev. C* 48 (1993), pp. 2462–2475. DOI: 10.1103/PhysRevC.48.2462.
- [47] J. Chen et al. “Nonequilibrium Kinetic Freeze-out Properties in Relativistic Heavy Ion Collisions from Energies Employed at the RHIC Beam Energy Scan to Those Available at the LHC”. In: *Phys. Rev. C* 104.3 (2021), p. 034901. DOI: 10.1103/PhysRevC.104.034901.
- [48] N. Götz, L. Constantin, and H. Elfner. “Role of Initial Transverse Momentum in a Hybrid Approach”. In: *preprint* (2023). URL: <https://arxiv.org/abs/2312.05001>.
- [49] S. A. Bass et al. “Microscopic Models for Ultrarelativistic Heavy Ion Collisions”. In: *Prog. Part. Nucl. Phys.* 41 (1998), pp. 255–369. DOI: 10.1016/S0146-6410(98)00058-1.
- [50] H. Song, S. A. Bass, and U. Heinz. “Viscous QCD Matter in a Hybrid hydrodynamic+Boltzmann Approach”. In: *Phys. Rev. C* 83 (2011), p. 024912. DOI: 10.1103/PhysRevC.83.024912.
- [51] W. Israel and J. M. Stewart. “Transient Relativistic Thermodynamics and Kinetic Theory”. In: *Annals Phys.* 118 (1979), pp. 341–372. DOI: 10.1016/0003-4916(79)90130-1.
- [52] H. Song et al. “200 A GeV Au+Au Collisions Serve a Nearly Perfect Quark-Gluon Liquid”. In: *Phys. Rev. Lett.* 106 (2011). [Erratum: *Phys.Rev.Lett.* 109, 139904 (2012)], p. 192301. DOI: 10.1103/PhysRevLett.106.192301.
- [53] S. Acharya et al. “Energy Dependence and Fluctuations of Anisotropic Flow in Pb-Pb Collisions at  $\sqrt{s_{NN}} = 5.02$  and 2.76 TeV”. In: *JHEP* 07 (2018), p. 103. DOI: 10.1007/JHEP07(2018)103.
- [54] S. Acharya et al. “Anisotropic Flow in Xe-Xe Collisions at  $\sqrt{s_{NN}} = 5.44$  TeV”. In: *Phys. Lett. B* 784 (2018), pp. 82–95. DOI: 10.1016/j.physletb.2018.06.059.
- [55] H. Niemi, K. J. Eskola, and R. Paatelainen. “Event-by-Event Fluctuations in a Perturbative QCD + Saturation + Hydrodynamics Model: Determining QCD Matter Shear Viscosity in Ultrarelativistic Heavy-Ion Collisions”. In: *Phys. Rev. C* 93.2 (2016), p. 024907. DOI: 10.1103/PhysRevC.93.024907.
- [56] X. Zhu et al. “Correlations of Flow Harmonics in 2.76A TeV Pb-Pb Collisions”. In: *Phys. Rev. C* 95.4 (2017), p. 044902. DOI: 10.1103/PhysRevC.95.044902.



- [57] W. Zhao, H.-j. Xu, and H. Song. “Collective Flow in 2.76 A TeV and 5.02 A TeV Pb+Pb Collisions”. In: *Eur. Phys. J. C* 77.9 (2017), p. 645. DOI: 10.1140/epjc/s10052-017-5186-x.
- [58] S. McDonald et al. “Hydrodynamic Predictions for Pb+Pb Collisions at 5.02 TeV”. In: *Phys. Rev. C* 95.6 (2017), p. 064913. DOI: 10.1103/PhysRevC.95.064913.
- [59] K. J. Eskola et al. “Scaling of Transverse Energies and Multiplicities with Atomic Number and Energy in Ultrarelativistic Nuclear Collisions”. In: *Nuclear Physics B* 570.1 (2000), pp. 379–389. DOI: 10.1016/S0550-3213(99)00720-8.
- [60] K. J. Eskola, K. Kajantie, and K. Tuominen. “Centrality Dependence of Multiplicities in Ultrarelativistic Nuclear Collisions”. In: *Phys. Lett. B* 497 (2001), pp. 39–43. DOI: 10.1016/S0370-2693(00)01341-1.
- [61] R. Paatelainen et al. “Fluid Dynamics with Saturated Minijet Initial Conditions in Ultrarelativistic Heavy-Ion Collisions”. In: *Physics Letters B* 731 (2014), pp. 126–130. DOI: 10.1016/j.physletb.2014.02.018.
- [62] M. L. Miller et al. “Glauber Modeling in High Energy Nuclear Collisions”. In: *Ann. Rev. Nucl. Part. Sci.* 57 (2007), pp. 205–243. DOI: 10.1146/annurev.nucl.57.090506.123020.
- [63] J. S. Moreland, J. E. Bernhard, and S. A. Bass. “Alternative Ansatz to Wounded Nucleon and Binary Collision Scaling in High-Energy Nuclear Collisions”. In: *Phys. Rev. C* 92.1 (2015), p. 011901. DOI: 10.1103/PhysRevC.92.011901.
- [64] B. Schenke, P. Tribedy, and R. Venugopalan. “Fluctuating Glasma Initial Conditions and Flow in Heavy Ion Collisions”. In: *Phys. Rev. Lett.* 108 (2012), p. 252301. DOI: 10.1103/PhysRevLett.108.252301.
- [65] O. Garcia-Montero, H. Elfner, and S. Schlichting. “McDIPPER: A Novel Saturation-Based 3+1D Initial-State Model for Heavy Ion Collisions”. In: *Phys. Rev. C* 109.4 (2024), p. 044916. DOI: 10.1103/PhysRevC.109.044916.
- [66] L. Pang, Q. Wang, and X.-N. Wang. “Effects of Initial Flow Velocity Fluctuation in Event-by-Event (3+1)D Hydrodynamics”. In: *Phys. Rev. C* 86 (2012), p. 024911. DOI: 10.1103/PhysRevC.86.024911.
- [67] D. Pablos et al. “Minijet Quenching in a Concurrent Jet+hydro Evolution and the Nonequilibrium Quark-Gluon Plasma”. In: *Phys. Rev. C* 106.3 (2022), p. 034901. DOI: 10.1103/PhysRevC.106.034901.
- [68] K. Werner. “Core-Corona Procedure and Microcanonical Hadronization to Understand Strangeness Enhancement in Proton-Proton and Heavy Ion Collisions in the EPOS4 Framework”. In: *Phys. Rev. C* 109.1 (2024), p. 014910. DOI: 10.1103/PhysRevC.109.014910.
- [69] Y. Kanakubo, Y. Tachibana, and T. Hirano. “Interplay between Core and Corona Components in High-Energy Nuclear Collisions”. In: *Phys. Rev. C* 105.2 (2022), p. 024905. DOI: 10.1103/PhysRevC.105.024905.

- [70] S. Cao et al. “Multistage Monte-Carlo Simulation of Jet Modification in a Static Medium”. In: *Phys. Rev. C* 96.2 (2017), p. 024909. DOI: 10.1103/PhysRevC.96.024909.
- [71] M. Okai et al. “New Approach to Initializing Hydrodynamic Fields and Mini-Jet Propagation in Quark-Gluon Fluids”. In: *Phys. Rev. C* 95.5 (2017), p. 054914. DOI: 10.1103/PhysRevC.95.054914.
- [72] C. Bierlich et al. “A Comprehensive Guide to the Physics and Usage of PYTHIA 8.3”. In: *SciPost Phys. Codeb.* 2022 (2022), p. 8. DOI: 10.21468/SciPostPhysCodeb.8.
- [73] C. Bierlich et al. “The Angantyr Model for Heavy-Ion Collisions in PYTHIA8”. In: *JHEP* 10 (2018), p. 134. DOI: 10.1007/JHEP10(2018)134.
- [74] M. Gyulassy and X.-N. Wang. “HIJING 1.0: A Monte Carlo Program for Parton and Particle Production in High-Energy Hadronic and Nuclear Collisions”. In: *Comput. Phys. Commun.* 83 (1994), p. 307. DOI: 10.1016/0010-4655(94)90057-4.
- [75] X.-N. Wang and M. Gyulassy. “HIJING: A Monte Carlo Model for Multiple Jet Production in Pp, pA and AA Collisions”. In: *Phys. Rev. D* 44 (1991), pp. 3501–3516. DOI: 10.1103/PhysRevD.44.3501.
- [76] Z.-W. Lin et al. “A Multi-phase Transport Model for Relativistic Heavy Ion Collisions”. In: *Phys. Rev. C* 72 (2005), p. 064901. DOI: 10.1103/PhysRevC.72.064901.
- [77] T. Pierog et al. “EPOS LHC: Test of Collective Hadronization with Data Measured at the CERN Large Hadron Collider”. In: *Phys. Rev. C* 92.3 (2015), p. 034906. DOI: 10.1103/PhysRevC.92.034906.
- [78] K. Werner and B. Guiot. “Perturbative QCD Concerning Light and Heavy Flavor in the EPOS4 Framework”. In: *Phys. Rev. C* 108.3 (2023), p. 034904. DOI: 10.1103/PhysRevC.108.034904.
- [79] K. Werner. “Revealing a Deep Connection between Factorization and Saturation: New Insight into Modeling High-Energy Proton-Proton and Nucleus-Nucleus Scattering in the EPOS4 Framework”. In: *Phys. Rev. C* 108.6 (2023), p. 064903. DOI: 10.1103/PhysRevC.108.064903.
- [80] J. E. Bernhard et al. “Applying Bayesian Parameter Estimation to Relativistic Heavy-Ion Collisions: Simultaneous Characterization of the Initial State and Quark-Gluon Plasma Medium”. In: *Phys. Rev. C* 94.2 (2016), p. 024907. DOI: 10.1103/PhysRevC.94.024907.
- [81] S. A. Bass, J. E. Bernhard, and J. S. Moreland. “Determination of Quark-Gluon-Plasma Parameters from a Global Bayesian Analysis”. In: *Nucl. Phys. A* 967 (2017). Ed. by U. Heinz, O. Evdokimov, and P. Jacobs, pp. 67–73. DOI: 10.1016/j.nuclphysa.2017.05.052.
- [82] D. Everett et al. “Multisystem Bayesian Constraints on the Transport Coefficients of QCD Matter”. In: *Phys. Rev. C* 103.5 (2021), p. 054904. DOI: 10.1103/PhysRevC.103.054904.

- [83] G. Nijs et al. “Bayesian Analysis of Heavy Ion Collisions with the Heavy Ion Computational Framework Trajectum”. In: *Phys. Rev. C* 103.5 (2021), p. 054909. DOI: 10.1103/PhysRevC.103.054909.
- [84] J. E. Parkkila, A. Onnerstad, and D. J. Kim. “Bayesian Estimation of the Specific Shear and Bulk Viscosity of the Quark-Gluon Plasma with Additional Flow Harmonic Observables”. In: *Phys. Rev. C* 104.5 (2021), p. 054904. DOI: 10.1103/PhysRevC.104.054904.
- [85] J. E. Parkkila et al. “New Constraints for QCD Matter from Improved Bayesian Parameter Estimation in Heavy-Ion Collisions at LHC”. In: *Phys. Lett. B* 835 (2022), p. 137485. DOI: 10.1016/j.physletb.2022.137485.
- [86] G. Nijs and W. van der Schee. “A Generalized Hydrodynamizing Initial Stage for Heavy Ion Collisions”. In: (2023).
- [87] C. W. De Jager, H. De Vries, and C. De Vries. “Nuclear Charge and Magnetization Density Distribution Parameters from Elastic Electron Scattering”. In: *Atom. Data Nucl. Data Tabl.* 14 (1974), pp. 479–508. DOI: 10.1016/S0092-640X(74)80002-1.
- [88] H. De Vries, C. W. De Jager, and C. De Vries. “Nuclear Charge and Magnetization Density Distribution Parameters from Elastic Electron Scattering”. In: *Atom. Data Nucl. Data Tabl.* 36 (1987), pp. 495–536. DOI: 10.1016/0092-640X(87)90013-1.
- [89] C. Loizides, J. Nagle, and P. Steinberg. “Improved Version of the PHOBOS Glauber Monte Carlo”. In: *SoftwareX* 1–2 (2015), pp. 13–18. DOI: 10.1016/j.softx.2015.05.001.
- [90] J. R. Cudell et al. “Benchmarks for the Forward Observables at RHIC, the Tevatron-Run II, and the LHC”. In: *Phys. Rev. Lett.* 89.20 (2002), p. 201801. DOI: 10.1103/PhysRevLett.89.201801.
- [91] G. Antchev et al. “First Measurement of Elastic, Inelastic and Total Cross-Section at  $\sqrt{s_{NN}}=13$  TeV by TOTEM and Overview of Cross-Section Data at LHC Energies”. In: *Eur. Phys. J. C* 79.2 (2019), p. 103. DOI: 10.1140/epjc/s10052-019-6567-0.
- [92] L. Durand and P. Hong. “QCD and Rising Total Cross-Sections”. In: *Phys. Rev. Lett.* 58 (1987), pp. 303–306. DOI: 10.1103/PhysRevLett.58.303.
- [93] C. Loizides. “Glauber Modeling of High-Energy Nuclear Collisions at the Subnucleon Level”. In: *Phys. Rev. C* 94.2 (2016), p. 024914. DOI: 10.1103/PhysRevC.94.024914.
- [94] P. Boek et al. “GLISSANDO 3: GLauber Initial-State Simulation AND mOre..., Ver. 3”. In: *Comput. Phys. Commun.* 245 (2019), p. 106850. DOI: 10.1016/j.cpc.2019.07.014.
- [95] C. Flett. *Exclusive Observables to NLO and Low  $x$  PDF Phenomenology at the LHC*. PhD thesis, U. Liverpool (main). 2021. DOI: 10.17638/03123138.

- [96] K. J. Eskola et al. “Exclusive  $J/\Psi$  Photoproduction in Ultraperipheral Pb + Pb Collisions at the CERN Large Hadron Collider Calculated at next-to-Leading Order Perturbative QCD”. In: *Phys. Rev. C* 106.3 (2022), p. 035202. DOI: 10.1103/PhysRevC.106.035202.
- [97] S. Chekanov et al. “Exclusive Photoproduction of  $J/\Psi$  Mesons at HERA”. In: *Eur. Phys. J. C* 24 (2002), pp. 345–360. DOI: 10.1007/s10052-002-0953-7.
- [98] M. Abramowitz and I. A. Stegun. *Handbook of Mathematical Functions: With Formulas, Graphs, and Mathematical Tables*. Dover Publications, June 1965.
- [99] Kuha, M. *Eikonal Minijet Model for Proton-Proton Collisions*. MSc Thesis. University of Jyväskylä, 2017. URL: <http://urn.fi/URN:NBN:fi:jyu-201703311843>.
- [100] J. C. Collins, D. E. Soper, and G. F. Sterman. “Factorization of Hard Processes in QCD”. In: *Adv. Ser. Direct. High Energy Phys.* 5 (1989), pp. 1–91. DOI: 10.1142/9789814503266\_0001.
- [101] E. Eichten et al. “Super Collider Physics”. In: *Rev. Mod. Phys.* 56 (1984). [Addendum: *Rev.Mod.Phys.* 58, 1065–1073 (1986)], pp. 579–707. DOI: 10.1103/RevModPhys.56.579.
- [102] K. J. Eskola, H. Paukkunen, and C. A. Salgado. “EPS09 — A New Generation of NLO and LO Nuclear Parton Distribution Functions”. In: *J. High Energy Phys.* 2009.04 (2009), p. 065. DOI: 10.1088/1126-6708/2009/04/065.
- [103] K. J. Eskola et al. “EPPS16: Nuclear Parton Distributions with LHC Data”. In: *Eur. Phys. J. C* 77.3 (2017), p. 163. DOI: 10.1140/epjc/s10052-017-4725-9.
- [104] K. J. Eskola et al. “EPPS21: A Global QCD Analysis of Nuclear PDFs”. In: *Eur. Phys. J. C* 82.5 (2022), p. 413. DOI: 10.1140/epjc/s10052-022-10359-0.
- [105] I. Helenius, M. Walt, and W. Vogelsang. “NNLO Nuclear Parton Distribution Functions with Electroweak-Boson Production Data from the LHC”. In: *Phys. Rev. D* 105.9 (2022), p. 094031. DOI: 10.1103/PhysRevD.105.094031.
- [106] R. Abdul Khalek et al. “nNNPDF3.0: Evidence for a Modified Partonic Structure in Heavy Nuclei”. In: *Eur. Phys. J. C* 82.6 (2022), p. 507. DOI: 10.1140/epjc/s10052-022-10417-7.
- [107] P. Duwentäster et al. “Impact of Heavy Quark and Quarkonium Data on Nuclear Gluon PDFs”. In: *Phys. Rev. D* 105.11 (2022), p. 114043. DOI: 10.1103/PhysRevD.105.114043.
- [108] S. Dulat et al. “New Parton Distribution Functions from a Global Analysis of Quantum Chromodynamics”. In: *Phys. Rev. D* 93.3 (2016), p. 033006. DOI: 10.1103/PhysRevD.93.033006.
- [109] A. Buckley et al. “LHAPDF6: Parton Density Access in the LHC Precision Era”. In: *Eur. Phys. J. C* 75 (2015), p. 132. DOI: 10.1140/epjc/s10052-015-3318-8.

- [110] I. Helenius et al. “Impact-Parameter Dependent Nuclear Parton Distribution Functions: EPS09s and EKS98s and Their Applications in Nuclear Hard Processes”. In: *JHEP* 07 (2012), p. 073. DOI: 10.1007/JHEP07(2012)073.
- [111] K. J. Eskola. “Shadowing Effects on Quark and Gluon Production in Ultrarelativistic Heavy Ion Collisions”. In: *Z. Phys. C - Particles and Fields* 51.4 (1991), pp. 633–642. DOI: 10.1007/BF01565590.
- [112] S. R. Klein and R. Vogt. “Inhomogeneous Shadowing Effects on J / Psi Production in dA Collisions”. In: *Phys. Rev. Lett.* 91 (2003), p. 142301. DOI: 10.1103/PhysRevLett.91.142301.
- [113] R. Vogt. “Shadowing Effects on the Nuclear Suppression Factor,  $R(dAu)$ , in d+Au Interactions”. In: *Phys. Rev. C* 70 (2004), p. 064902. DOI: 10.1103/PhysRevC.70.064902.
- [114] Herman Kahn and Theodore E. Harris. “Estimation of Particle Transmission by Random Sampling”. In: *National Bureau of Standards applied mathematics series* 12 (1951), pp. 27–30.
- [115] C. Loizides, J. Kamin, and D. d’Enterria. “Improved Monte Carlo Glauber Predictions at Present and Future Nuclear Colliders”. In: *Phys. Rev. C* 97.5 (2018). [Erratum: *Phys.Rev.C* 99, 019901 (2019)], p. 054910. DOI: 10.1103/PhysRevC.97.054910.
- [116] ATLAS collaboration. “Measurement of  $W_{\pm}$  Boson Production in Pb+Pb Collisions at  $\sqrt{s_{NN}} = 5.02$  TeV with the ATLAS Detector”. In: *Eur. Phys. J. C* 79.11 (2019), p. 935. DOI: 10.1140/epjc/s10052-019-7439-3.
- [117] ATLAS collaboration. “Z Boson Production in Pb+Pb Collisions at  $\sqrt{s_{NN}} = 5.02$  TeV Measured by the ATLAS Experiment”. In: *Phys. Lett. B* 802 (2020), p. 135262. DOI: 10.1016/j.physletb.2020.135262.
- [118] A. M. Sirunyan et al. “Constraints on the Initial State of Pb-Pb Collisions via Measurements of Z-Boson Yields and Azimuthal Anisotropy at  $\sqrt{s_{NN}} = 5.02$  TeV”. In: *Phys. Rev. Lett.* 127.10 (2021), p. 102002. DOI: 10.1103/PhysRevLett.127.102002.
- [119] S. Acharya et al. “ $W_{\pm}$ -Boson Production in p-Pb Collisions at  $\sqrt{s_{NN}} = 8.16$  TeV and PbPb Collisions at  $\sqrt{s_{NN}} = 5.02$  TeV”. In: *JHEP* 05 (2023), p. 036. DOI: 10.1007/JHEP05(2023)036.
- [120] P. Duwentäster et al. “Impact of Heavy Quark and Quarkonium Data on Nuclear Gluon PDFs”. In: *Phys. Rev. D* 105.11 (2022), p. 114043. DOI: 10.1103/PhysRevD.105.114043.
- [121] R. Paatelainen et al. “Multiplicities and pT Spectra in Ultrarelativistic Heavy Ion Collisions from a Next-to-Leading Order Improved Perturbative QCD + Saturation + Hydrodynamics Model”. In: *Phys. Rev. C* 87.4 (2013), p. 044904. DOI: 10.1103/PhysRevC.87.044904.
- [122] L. V. Gribov, E. M. Levin, and M. G. Ryskin. “Semihard Processes in QCD”. In: *Phys. Rept.* 100 (1983), pp. 1–150. DOI: 10.1016/0370-1573(83)90022-4.

- [123] H. Hirvonen, K. J. Eskola, and H. Niemi. “Flow Correlations from a Hydrodynamics Model with Dynamical Freeze-out and Initial Conditions Based on Perturbative QCD and Saturation”. In: *Phys. Rev. C* 106.4 (2022), p. 044913. DOI: 10.1103/PhysRevC.106.044913.
- [124] D. Kharzeev, E. Levin, and M. Nardi. “Color Glass Condensate at the LHC: Hadron Multiplicities in Pp, pA and AA Collisions”. In: *Nucl. Phys. A* 747 (2005), pp. 609–629. DOI: 10.1016/j.nuclphysa.2004.10.018.
- [125] W.-T. Deng, X.-N. Wang, and R. Xu. “Hadron Production in P+p, p+Pb, and Pb+Pb Collisions with the HIJING 2.0 Model at Energies Available at the CERN Large Hadron Collider”. In: *Phys. Rev. C* 83 (2011), p. 014915. DOI: 10.1103/PhysRevC.83.014915.
- [126] ALICE collaboration. “Centrality Determination in Heavy Ion Collisions”. In: ALICE-PUBLIC-2018-011, ALICE-PUBLIC-2018-011 (2018).
- [127] ATLAS collaboration. “Study of Photon-Jet Momentum Correlations in Pb+Pb and Pp Collisions at  $\sqrt{s_{NN}} = 5.02$  TeV with ATLAS”. In: (2016). URL: <https://cds.cern.ch/record/2220772>.
- [128] ATLAS collaboration. “Measurement of Muon Pairs Produced via  $\Gamma\gamma$  Scattering in Nonultraperipheral Pb+Pb Collisions at  $\sqrt{s_{NN}}=5.02$  TeV with the ATLAS Detector”. In: *Phys. Rev. C* 107.5 (2023), p. 054907. DOI: 10.1103/PhysRevC.107.054907.
- [129] K. J. Eskola and K. Tuominen. “Transverse Energy from Minijets in Ultrarelativistic Nuclear Collisions: A Next-to-leading Order Analysis”. In: *Phys. Rev. D* 63 (2001), p. 114006. DOI: 10.1103/PhysRevD.63.114006.
- [130] K. J. Eskola and K. Tuominen. “Production of Transverse Energy from Minijets in Next-to-Leading Order Perturbative QCD”. In: *Phys. Lett. B* 489 (2000), pp. 329–336. DOI: 10.1016/S0370-2693(00)00946-1.
- [131] P. Huovinen and P. Petreczky. “QCD Equation of State and Hadron Resonance Gas”. In: *Nucl. Phys. A* 837 (2010), pp. 26–53. DOI: 10.1016/j.nuclphysa.2010.02.015.
- [132] E. Molnar, H. Niemi, and D. H. Rischke. “Numerical Tests of Causal Relativistic Dissipative Fluid Dynamics”. In: *Eur. Phys. J. C* 65 (2010), pp. 615–635. DOI: 10.1140/epjc/s10052-009-1194-9.
- [133] E. Molnar et al. “Influence of Temperature-Dependent Shear Viscosity on Elliptic Flow at Backward and Forward Rapidities in Ultrarelativistic Heavy-Ion Collisions”. In: *Phys. Rev. C* 90.4 (2014), p. 044904. DOI: 10.1103/PhysRevC.90.044904.
- [134] J. Adam et al. “Centrality Dependence of the Pseudorapidity Density Distribution for Charged Particles in Pb-Pb Collisions at  $\sqrt{s_{NN}} = 5.02$  TeV”. In: *Phys. Lett. B* 772 (2017), pp. 567–577. DOI: 10.1016/j.physletb.2017.07.017.

- [135] E. Abbas et al. "Centrality Dependence of the Pseudorapidity Density Distribution for Charged Particles in Pb-Pb Collisions at  $\sqrt{s_{NN}} = 2.76$  TeV". In: *Phys. Lett. B* 726 (2013), pp. 610–622. DOI: 10.1016/j.physletb.2013.09.022.
- [136] B. B. Back et al. "The Significance of the Fragmentation Region in Ultrarelativistic Heavy Ion Collisions". In: *Phys. Rev. Lett.* 91 (2003), p. 052303. DOI: 10.1103/PhysRevLett.91.052303.
- [137] K. J. Eskola and X.-N. Wang. "Space-Time Structure of Initial Parton Production in Ultrarelativistic Heavy Ion Collisions". In: *Phys. Rev. D* 49 (1994), pp. 1284–1292. DOI: 10.1103/PhysRevD.49.1284.

## APPENDIX 1 INPUT FILES

### APPENDIX 1.1 Model parameters

All the parameters of an MC-EKRT run are given in a parameter file. The name of the parameter file is given as a command line argument, or if none are given, the parameters are read from the file called `params_template`. The available parameters are (default values in parentheses):

- `name`: Name of the run, affects the output filenames. ("example\_name")
- `sigmajet_filename`: Name of the file where the call table for the values of  $\sigma_{\text{jet}}$  (see Ch. 4.3.2) is stored. ("example\_sigma\_jet.dat")
- `read_sigmajets_from_file`: If `true`, the call table for the values of  $\sigma_{\text{jet}}$  is not calculated at the start of the simulation, but read from the file named by the parameter `sigmajet_filename`. The values need to be calculated again, if anything affecting the snPDFs (nucleon distributions,  $\sigma_N$ , hotspots),  $p_0$  or  $\sqrt{s_{NN}}$  changes. Changing other parameters, such as pQCD  $K$ -factor, does not affect the  $\sigma_{\text{jet}}$  file. (`false`)
- `centrality_filename`: Name of the file where the output centrality bins (see Ch. 6.3) are stored. ("centrality\_bins.csv")
- `n_events`: Number of the total nucleus–nucleus events that is to be simulated. (2000)
- `b_max`: Maximum absolute value of the nucleus–nucleus impact parameter  $\bar{b}_{AB}$  in units of fm. (20)
- `b_min`: Minimum absolute value of the nucleus–nucleus impact parameter  $\bar{b}_{AB}$  in units of fm. (0)
- `sqrt_s`: The center of momentum system energy  $\sqrt{s_{NN}}$  of the simulation in units of GeV. (5020.0)
- `K_factor`: The pQCD  $K$ -factor. (2.0)
- `Kappa_factor`: The saturation parameter  $\kappa_{\text{sat}}$ . (2.0)
- `p0`: Transverse momentum lower cutoff  $p_0$  in units of GeV. (1.0)
- `proton_width_static`: If `true`, the proton width parameter  $\sigma_N$  is a user defined number. If `false`, it is calculated from the parametrization in Eq. (11). (`false`)
- `proton_width`: The value of the proton width parameter  $\sigma_N$  in units of fm. Only used if `proton_width_static=true`. (0.573)



- `sigma_inel_trigger`: The value of the  $\sigma_{\text{trig}}^{NN}$  used for nucleus–nucleus event triggering (see Ch. 3.2) in units of mb. If left 0, calculated from the parametrization in Eq. (6). (0)
- `envelope_marginal`: As the maximum value of  $\frac{d\sigma_{\text{jet}}}{dp_T^2 dy_1 dy_2}$  needed to form the envelope function described in Ch. 4.4 is approximate, the envelope needs to be padded by a marginal so that Eq. (74) always holds. This parameter determines the size of that padding. Lower values lead to faster simulation, but are more bound to error. If Eq. (74) is violated because of too tight a margin, the program will tell so in the output. (1.05)
- `A`: The mass number of the projectile nucleus. (208)
- `B`: The mass number of the target nucleus. (208)
- `ZA`: The atomic number of the projectile nucleus. (82)
- `ZB`: The atomic number of the target nucleus. (82)
- `nuclear_RA`: The radius  $R_A$  (see Ch. 3.1) of the projectile nucleus in units of fm. (6.62435)
- `nuclear_RB`: The radius  $R_A$  (see Ch. 3.1) of the target nucleus in units of fm. (6.62435)
- `nuclear_dA`: The diffusion parameter  $d$  (see Ch. 3.1) of the projectile nucleus in units of fm. (0.5498)
- `nuclear_dB`: The diffusion parameter  $d$  (see Ch. 3.1) of the target nucleus in units of fm. (0.5498)
- `nuclear_beta2A`: The quadrupole deformation parameter  $\beta_2$  (see Ch. 3.1) of the projectile nucleus. (0.0)
- `nuclear_beta2B`: The quadrupole deformation parameter  $\beta_2$  (see Ch. 3.1) of the target nucleus. (0.0)
- `nuclear_beta3A`: The octupole deformation parameter  $\beta_3$  (see Ch. 3.1) of the projectile nucleus. (0.0)
- `nuclear_beta3B`: The octupole deformation parameter  $\beta_3$  (see Ch. 3.1) of the target nucleus. (0.0)
- `nuclear_beta4A`: The hexadecapole deformation parameter  $\beta_4$  of the projectile nucleus (see Ch. 3.1). (0.0)
- `nuclear_beta4B`: The hexadecapole deformation parameter  $\beta_4$  of the target nucleus (see Ch. 3.1). (0.0)
- `rad_max`: Nucleons' maximum distance from the nucleus center in units of fm. (30)

- `correct_overlap_bias`: If `true`, the nucleons are forced to have a minimum distance  $d_{\min}$  from each other (see Ch. 3.1). (`true`)
- `nn_min_dist`: The value of the nucleon–nucleon minimum distance  $d_{\min}$  (see Ch. 3.1) in units of fm. Only used if `correct_overlap_bias=true`. (`0.4`)
- `shift_cms`: If `true`, after the nucleon locations are sampled, they are all shifted so that their center of the mass is at the nucleus center (see Ch. 3.1). (`true`)
- `hotspots`: If `true`, the nucleon substructure model is used (see Ch. 3.3.2). (`false`)
- `n_hotspots`: The number of hotspots in the nucleon substructure (see Ch. 3.3.2). Only used if `hotspots=true`. (`3`)
- `hotspot_width`: The gaussian width  $\sigma_H$  of the hotspots (see Ch. 3.3.2) in units of fm. Only used if `hotspots=true`. If left 0, 20% of the  $\sigma_N$  value is used. (`0.0`)
- `is_mc_glauber`: If `true`, the hard sphere model of nucleon–nucleon scatterings is used (see Ch. 4.1.1) and the simulation emulates MC Glauber model. (`false`)
- `sigma_inel_NN`: The value of the  $\sigma_{\text{inel}}^{NN}$  used for nucleon–nucleon collision triggering in the hard sphere model, when MC Glauber model is emulated, in units of mb. Only used if `is_mc_glauber=true`. (`70`)
- `only_protons`: If `true`, all the nucleons' PDFs are proton PDFs. (`false`)
- `use_npdfs`: If `true`, nuclear shadowing (by EPS09LO [102]) is used (see Ch. 4.3.3). (`true`)
- `use_snpdfs`: If `true`, the logarithmic-geometric spatial nPDFs are used (see Ch. 4.3.3.3). If `false`, the average EPS09LO nPDFs are used. Only used if `use_npdfs=true`. (`true`)
- `save_endstate_jets`: If `false`, the simulation is run but the final state minijets are not saved into files (see Ch. 6.3). (`true`)
- `end_state_filtering`: If `false`, no filters are applied to the candidate events, they are all accepted (see Ch. 5). (`true`)
- `is_saturation`: If `true`, the candidate events are subjected to the EKRT saturation filter (see Ch. 5.2). (`true`)
- `is_mom_cons`: If `true`, the candidate events are subjected to the per nucleon momentum conservation filter (see Ch. 5.3). (`true`)
- `is_val_cons`: If `true`, the candidate events are subjected to the valence quark number conservation filter (see Ch. 5.4). (`true`)

## APPENDIX 1.2 Minijet properties in the output

The file `output_params` specifies, which minijet properties should be saved in the output files. The minijets are saved as pairs of minijets (dijets). The following properties are available (the nucleons participating in the production of the dijet are the nucleon  $a$  from the projectile nucleus  $A$  and the nucleon  $b$  from the target nucleus  $B$ ):

- `t01`: The formation time  $1/p_T$  of the minijet associated with the rapidity  $y_1$  in units of  $1/\text{GeV}$ .
- `t02`: The formation time  $1/p_T$  of the minijet associated with the rapidity  $y_2$  in units of  $1/\text{GeV}$ .
- `x`: The  $x$ -coordinate of the dijet formation location in units of fm.
- `y`: The  $y$ -coordinate of the dijet formation location in units of fm.
- `pt`: The transverse momentum  $p_T$  of the minijets in units of GeV.
- `y1`: The momentum rapidity  $y_1$  of one of the minijets.
- `y2`: The momentum rapidity  $y_2$  of one of the minijets.
- `tata`: The value of  $T_A(\bar{s})T_B(\bar{s})$  (see Ch. 3.3.3), where  $\bar{s} = (x, y)$  is the dijet formation location, in units of  $1/\text{mb}^2$ .
- `init1`: The parton flavour of the parton taken from  $a$ .
- `init2`: The parton flavour of the parton taken from  $b$ .
- `final1`: The parton flavour of the minijet associated with the rapidity  $y_1$ .
- `final2`: The parton flavour of the minijet associated with the rapidity  $y_2$ .
- `ia`: The index of  $a$ . Unique for all the nucleons from  $A$ .
- `ib`: The index of  $b$ . Unique for all the nucleons from  $B$ .
- `xa`: The  $x$ -coordinate of  $a$  in units of fm.
- `ya`: The  $y$ -coordinate of  $a$  in units of fm.
- `za`: The  $z$ -coordinate of  $a$  in units of fm.
- `xb`: The  $x$ -coordinate of  $b$  in units of fm.
- `yb`: The  $y$ -coordinate of  $b$  in units of fm.
- `zb`: The  $z$ -coordinate of  $b$  in units of fm.
- `a_is_neutron`: A Boolean flag of the neutron status of the nucleon  $a$ .
- `b_is_neutron`: A Boolean flag of the neutron status of the nucleon  $b$ .



## ORIGINAL PAPERS

### I

#### SHADOWING IN INELASTIC NUCLEON-NUCLEON CROSS SECTION?

by

K. J. Eskola, I. Helenius, M. Kuha and H. Paukkunen

Phys. Rev. Lett. 125 **21**, 212301 (2020).

<https://doi.org/10.1103/PhysRevLett.125.212301>

Reproduced with kind permission of American Physical Society.

## Shadowing in Inelastic Nucleon-Nucleon Cross Section?

Kari J. Eskola<sup>1,†</sup>, Ilkka Helenius<sup>2,\*</sup>, Mikko Kuha<sup>1,‡</sup>, and Hannu Paukkunen<sup>1,§</sup>

<sup>1</sup>University of Jyväskylä, Department of Physics, P.O. Box 35, FI-40014 University of Jyväskylä, Finland  
and Helsinki Institute of Physics, P.O. Box 64, FI-00014 University of Helsinki, Finland

 (Received 2 April 2020; revised 9 July 2020; accepted 16 October 2020; published 18 November 2020)

Experimental results of inclusive hard-process cross sections in heavy-ion collisions conventionally lean on a normalization computed from Glauber models where the inelastic nucleon-nucleon cross section  $\sigma_{\text{nn}}^{\text{inel}}$ —a crucial input parameter—is simply taken from proton-proton measurements. In this Letter, using the computed electroweak boson production cross sections in lead-lead collisions as a benchmark, we determine  $\sigma_{\text{nn}}^{\text{inel}}$  from the recent ATLAS data. We find a significantly suppressed  $\sigma_{\text{nn}}^{\text{inel}}$  relative to what is usually assumed, show the consequences for the centrality dependence of the cross sections, and address the phenomenon in an eikonal minijet model with nuclear shadowing.

DOI: [10.1103/PhysRevLett.125.212301](https://doi.org/10.1103/PhysRevLett.125.212301)

**Introduction.**—In high-energy nucleus-nucleus collisions, the main goals are to study the properties of strongly interacting matter and QCD dynamics in the nuclear environment (for a recent review see, e.g., [1]). In these collisions, the produced particle multiplicity correlates strongly with the collision geometry: the more central the collision, typically the higher the multiplicity. Experimentally, the centrality classification is obtained by ordering the events according to their multiplicity or transverse energy into bins of equal fraction, say 10%, of all events. Conventionally, 0%–10% (90%–100%) centrality refers to the events of highest (lowest) multiplicities and 0%–100% to all events, minimum bias.

Inclusive hard processes ( $h$  for hard) in turn are rarer processes of a large momentum scale whose cross sections in nucleus-nucleus collisions are traditionally obtained by converting the measured per-event yields  $N_h^c/N_{\text{evt}}^c$  in a centrality class  $c$  into hard nucleon-nucleon cross sections  $\sigma_h^c$  through

$$\sigma_h^c = \frac{\sigma_{\text{nn}}^{\text{inel}} N_h^c}{\langle N_{\text{bin}} \rangle_c N_{\text{evt}}^c}, \quad (1)$$

where  $\langle N_{\text{bin}} \rangle_c$  is the mean number of independent inelastically interacting nucleon-nucleon pairs, binary collisions, in the centrality class  $c$ , and  $\sigma_{\text{nn}}^{\text{inel}}$  is the inelastic nucleon-nucleon cross section. The model-dependent quantity  $\langle N_{\text{bin}} \rangle_c$  here is obtained from the Monte Carlo (MC) Glauber model [2]. The nuclear modification ratio  $R_{AA}^{h,c}$

is then obtained by dividing  $\sigma_h^c$  by the corresponding minimum-bias cross section in proton-proton collisions where  $A$  refers to the colliding nuclei.

This method of constructing hard cross sections is a routine procedure in the heavy-ion measurements at RHIC and at the LHC, and it has been used, e.g., to construct nuclear modification ratios for jets [3–6] and hadrons [7–13], which, in turn, are widely used in theoretical studies of jet quenching [14–16] and partonic energy loss [17–20]. In the same way, Eq. (1) forms the basis for measuring centrality-dependent cross sections of direct photon [21–23] and electroweak (EW) boson [24–27] production, which can be used to study, e.g., nuclear effects in parton distribution functions (PDFs) [28,29].

The basic inputs of the Glauber model are the nuclear geometry and  $\sigma_{\text{nn}}^{\text{inel}}$  [2]. In the MC Glauber model, the positions of the nucleons are sampled event by event according to the nuclear density profile, usually the Woods–Saxon distribution [30]. The probability for an interaction between two nucleons depends on their mutual distance and  $\sigma_{\text{nn}}^{\text{inel}}$ . As a result, cross-section measurements through Eq. (1) depend on  $\sigma_{\text{nn}}^{\text{inel}}$  in a nontrivial way. An established procedure dating back to early fixed-target experiments, such as E178 at Fermilab [31], is to take the value of  $\sigma_{\text{nn}}^{\text{inel}}$  and its energy dependence from proton-proton measurements. However, at high enough energies, like those at the LHC, the particle production becomes sensitive to QCD dynamics at small momentum fractions  $x$  where some suppression is expected due to gluon shadowing [32–34] or saturation phenomena [35–37]. Such effects become more pronounced in heavy nuclei and toward lower scales, so one could argue that, in collisions involving heavy ions, the value of  $\sigma_{\text{nn}}^{\text{inel}}$  should also be reduced relative to what is measured in proton-proton collisions. Through Eq. (1), this would then change the obtained hard cross sections and nuclear modification ratios and thereby affect

Published by the American Physical Society under the terms of the [Creative Commons Attribution 4.0 International](https://creativecommons.org/licenses/by/4.0/) license. Further distribution of this work must maintain attribution to the author(s) and the published article's title, journal citation, and DOI. Funded by SCOAP<sup>3</sup>.

all the subsequent analyses that take these measured cross sections as an input. In this way, the value of  $\sigma_{\text{nn}}^{\text{inel}}$  is critical and could have far-reaching consequences, e.g., for the precision studies of jet quenching and other related phenomena. Thus, an alternative benchmark for  $\sigma_{\text{nn}}^{\text{inel}}$  is called for.

As proposed in Ref. [28], the Glauber model and its inputs could be tested by studying the production of well known “standard candles,” such as EW bosons, in Pb + Pb collisions at the LHC, but so far this has been limited by the precision of the LHC Run-I measurements [24–26,38]. Thanks to the increased luminosity and collision energy of Run II, the recent  $W^\pm$ - and Z-boson measurements by ATLAS [39,40] have pushed the precision to a few-percent level, enabling now a more precise Glauber model calibration. In the present Letter, we use these ATLAS data to study the possible nuclear suppression of  $\sigma_{\text{nn}}^{\text{inel}}$  in Pb + Pb collisions. Since the ALICE measurement [41] is less precise and has no reference p + p data, we leave it out of the analysis. The idea is to first establish the EW-boson cross sections by using next-to-next-to-leading order (NNLO) perturbative QCD (pQCD) with state-of-the-art PDFs for protons and nuclei. Using the theory prediction on the left-hand side of Eq. (1), we can then determine  $\sigma_{\text{nn}}^{\text{inel}}$  within the same MC Glauber implementation as in the experimental analyses. We find that the data favor a significant suppression in  $\sigma_{\text{nn}}^{\text{inel}}$ . We also demonstrate that the unexpected enhancement seen by ATLAS in the ratios  $R_{\text{PbPb}}^{W^\pm, Z}$  toward peripheral collisions disappears with the found smaller value of  $\sigma_{\text{nn}}^{\text{inel}}$ . In addition, we show that the suppression of  $\sigma_{\text{nn}}^{\text{inel}}$  is compatible with predictions from an eikonal minijet model with nuclear shadowing.

*Nuclear suppression in  $\sigma_{\text{nn}}^{\text{inel}}$ .*—The observables we exploit in this work to extract  $\sigma_{\text{nn}}^{\text{inel}}$  are the rapidity-dependent nuclear modification ratios for  $W^\pm$  and Z-boson production in different centrality classes. Experimentally these are defined as

$$R_{\text{PbPb}}^{\text{exp}}(y) = \frac{1}{\langle T_{\text{PbPb}} \rangle} \frac{\frac{1}{N_{\text{evt}}} dN_{\text{PbPb}}^{W^\pm, Z}/dy}{d\sigma_{\text{pp}}^{W^\pm, Z}/dy}, \quad (2)$$

where the per-event yield is normalized into nucleon-nucleon cross section by dividing with the mean nuclear overlap  $\langle T_{\text{PbPb}} \rangle = \langle N_{\text{bin}} \rangle_c / \sigma_{\text{nn}}^{\text{inel}}$  obtained from a MC Glauber model calculation. For minimum-bias collisions, the same quantity can be calculated directly as a ratio between the cross sections in Pb + Pb and p + p collisions,

$$R_{\text{PbPb}}^{\text{theor}}(y) = \frac{1}{(208)^2} \frac{d\sigma_{\text{PbPb}}^{W^\pm, Z}/dy}{d\sigma_{\text{pp}}^{W^\pm, Z}/dy}, \quad (3)$$

which is completely independent of the Glauber modeling. We have calculated the cross sections in Eq. (3) at NNLO with the MCFM code (version 8.3) [42]. For the protons, we

use the recent NNPDF3.1 PDFs [43], which provide an excellent agreement to ATLAS data for  $W^\pm$  and Z-boson production in p + p collisions at  $\sqrt{s} = 5.02$  TeV [44]. The nuclear modifications for the PDFs are obtained from the centrality-independent EPPS16 NLO analysis [45], which includes Run-I data for  $W^\pm$  and Z production in p + Pb collisions at the LHC [46–48] and provides an excellent description of the more recent Run-II data [49]. The available NNLO nuclear PDFs [50,51] do not include any constraints beyond deeply inelastic scattering, so the applied PDFs provide currently the most accurately constrained setup for the considered observables. The factorization and renormalization scales are fixed to the respective EW-boson masses.

The ratios  $R_{\text{PbPb}}^{\text{theor}}$  and  $R_{\text{PbPb}}^{\text{exp}}$  are compared in the upper panel of Fig. 1. For  $W^\pm$ ,  $R_{\text{PbPb}}^{\text{exp}}$  is formed by dividing the normalized yield in Pb + Pb from Ref. [39] with the corresponding cross section in p + p from Ref. [44], adding the uncertainties in quadrature. The plotted experimental uncertainties do not include the uncertainty in  $\langle T_{\text{PbPb}} \rangle$ . The theoretical uncertainties derive from the EPPS16 error sets

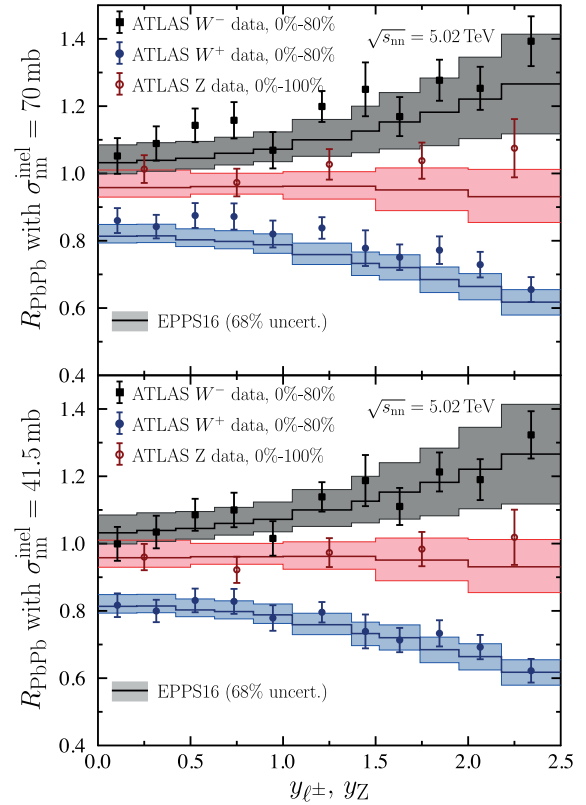


FIG. 1. Nuclear modification ratios of  $W^\pm$  and Z, computed from pQCD (solid lines with error bands) and from ATLAS data [39,40] with  $\sigma_{\text{nn}}^{\text{inel}} = 70$  mb (upper panel) and 41.5 mb (lower panel).

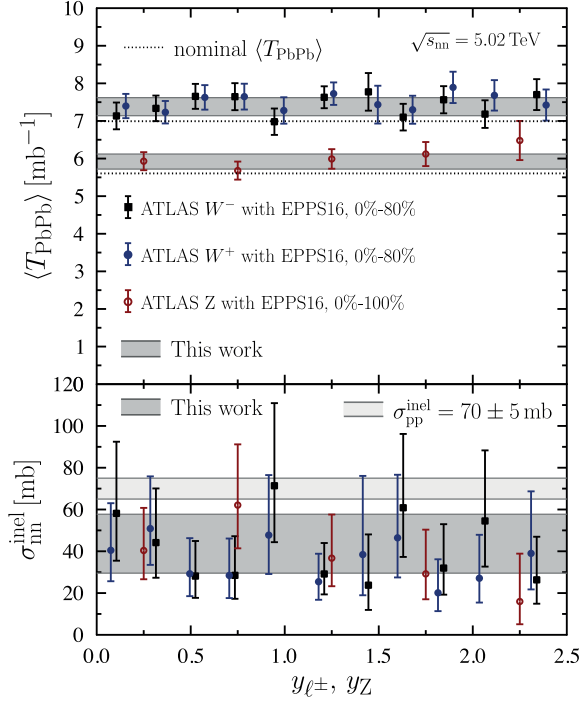


FIG. 2. Extracted values of the mean nuclear overlap functions (upper panel) and  $\sigma_{\text{nn}}^{\text{inel}}$  (lower panel). The dark gray bands show the values obtained by fitting  $\sigma_{\text{nn}}^{\text{inel}}$  and the dashed lines and the light gray band corresponds to the nominal  $\sigma_{\text{pp}}^{\text{inel}}$ .

and correspond to the 68% confidence level. Note that the  $W^\pm$  measurement is for 0%–80% centrality instead of full 0%–100%. However, for rare processes like the EW bosons, the contribution from the 80%–100% region is negligible, so the comparison with the minimum-bias calculations is justified. It is evident that with  $\sigma_{\text{nn}}^{\text{inel}} = 70 \text{ mb}$  both the  $W^\pm$  and the  $Z$  data tend to lie above the calculated result, which we will interpret as an evidence of nuclear suppression in  $\sigma_{\text{nn}}^{\text{inel}}$  as explained below.

By equating Eqs. (2) and (3), we can convert each data point to  $\langle T_{\text{PbPb}} \rangle$ . The outcome is shown in the upper panel of Fig. 2. The obtained values tend to be higher than the nominal  $\langle T_{\text{PbPb}} \rangle = 5.605 \text{ mb}^{-1}$  (0%–100%) and  $\langle T_{\text{PbPb}} \rangle = 6.993 \text{ mb}^{-1}$  (0%–80%), which assume  $\sigma_{\text{nn}}^{\text{inel}} = 70 \text{ mb}$  (see Table I). The fact that the preferred values of  $\langle T_{\text{PbPb}} \rangle$  are independent of the rapidity strongly suggests that the original mismatch in  $R_{\text{PbPb}}$  is a normalization issue—the nuclear PDFs predict the rapidity dependence correctly.

Since each  $\langle T_{\text{PbPb}} \rangle$  maps to  $\sigma_{\text{nn}}^{\text{inel}}$  through MC Glauber, we can also directly convert  $R_{\text{PbPb}}^{\text{exp}}$  to  $\sigma_{\text{nn}}^{\text{inel}}$ . Here, we have used TGlauberMC (version 2.4) [52], which is the same MC Glauber implementation as in the considered ATLAS analyses. The centrality classification is done with a two-component model, including negative binomial fluctuations [53] similar to the ALICE prescription [54] with

parameters from Ref. [55]. The obtained values of  $\langle T_{\text{PbPb}} \rangle$  are in an excellent agreement with the ATLAS values in Refs. [39,40] in all centrality classes when using the nominal, unsuppressed value  $\sigma_{\text{nn}}^{\text{inel}} = 70 \text{ mb}$ . The values of  $\sigma_{\text{nn}}^{\text{inel}}$  extracted from each data point are shown in Fig. 2. It is obvious that the data prefer a value of  $\sigma_{\text{nn}}^{\text{inel}}$ , which is less than the  $\sigma_{\text{pp}}^{\text{inel}} = 70 \text{ mb}$  obtained from p + p data.

To quantify the optimal  $\sigma_{\text{nn}}^{\text{inel}}$ , we fit its value by requiring a match between  $R_{\text{PbPb}}^{\text{exp}}$  and  $R_{\text{PbPb}}^{\text{theor}}$  treating the EPPS16 uncertainties as Gaussian correlated errors. In practice, we define a  $\chi^2$  function by

$$\chi^2 = \sum_i \left[ \frac{\mathcal{N}_i R_{\text{PbPb},i}^{\text{exp}} - R_{\text{PbPb},i}^{\text{theor}} + \sum_k f_k \beta_i^k}{\mathcal{N}_i \delta_i^{\text{exp}}} \right]^2 + T \sum_k f_k^2$$

$$\mathcal{N}_i = \langle T_{\text{PbPb}}^i(\sigma_{\text{pp}}^{\text{inel}}) \rangle / \langle T_{\text{PbPb}}^i(\sigma_{\text{nn}}^{\text{inel}}) \rangle, \quad (4)$$

where  $i$  runs over the data points and  $k = 1, \dots, 20$  over the number error-set pairs in EPPS16. The factors  $\mathcal{N}_i$  with  $\sigma_{\text{pp}}^{\text{inel}} = 70 \text{ mb}$  account for the shifted normalizations when  $\sigma_{\text{nn}}^{\text{inel}}$  changes. Also the data uncertainties  $\delta_i^{\text{exp}}$  are scaled by this factor to avoid D’Agostini bias [56]. The tolerance  $T = 1.645^2$  in the penalty term takes into account scaling the 90% confidence limit uncertainties of EPPS16 into 68% and  $\beta_i^k \equiv [R_{\text{PbPb},i}^{\text{theor}}(S_k^+) - R_{\text{PbPb},i}^{\text{theor}}(S_k^-)]/2$ , where  $S_k^+$  and  $S_k^-$  are the positive and negative variations, respectively, of EPPS16 error sets. The  $\chi^2$  is minimized with respect to  $\sigma_{\text{nn}}^{\text{inel}}$  and  $f_k$  (1 + 20 parameters). We find

$$\sigma_{\text{nn}}^{\text{inel}} = 41.5_{-12.0}^{+16.2} \text{ mb},$$

where the uncertainties follow from the  $\Delta\chi^2 = 1$  criterion. The resulting values for  $\langle T_{\text{PbPb}} \rangle$  and  $\sigma_{\text{nn}}^{\text{inel}}$  are compared to the data-extracted values in Fig. 2, and the renormalized data for  $R_{\text{PbPb}}$  are compared to theoretical predictions in the lower panel of Fig. 1. It is worth stressing that different final states prefer a very similar suppressed value of  $\sigma_{\text{nn}}^{\text{inel}}$  and that a very good agreement in  $R_{\text{PbPb}}$  is found when normalizing with  $\langle T_{\text{PbPb}} \rangle$  calculated using the suppressed cross section in the MC Glauber calculation.

*Centrality dependence.*—Even the quite significant suppression in  $\sigma_{\text{nn}}^{\text{inel}}$  leads to rather modest modifications in  $\langle T_{\text{PbPb}} \rangle$  for central and (close-to) minimum-bias collisions. The impact, however, grows toward more peripheral centrality classes (see Table I). To illustrate this, Fig. 3 compares the centrality-dependent  $R_{\text{PbPb}}^{\text{exp}}$  before and after rescaling the data by  $\langle T_{\text{PbPb}}(\sigma_{\text{pp}}^{\text{inel}}) \rangle / \langle T_{\text{PbPb}}(\sigma_{\text{nn}}^{\text{inel}}) \rangle$  using the fitted  $\sigma_{\text{nn}}^{\text{inel}}$ . The left-hand panels show the original ATLAS data, including the quoted  $\langle T_{\text{PbPb}} \rangle$  uncertainties. In the right-hand panels, the data have been rescaled, and the uncertainties follow from the  $\sigma_{\text{nn}}^{\text{inel}}$  fit. The striking effect is that the mysterious rise toward more peripheral collisions in the original data becomes compatible with a negligible centrality dependence, the central values indicating perhaps a mildly decreasing trend toward peripheral bins. As

TABLE I. Mean nuclear overlap functions  $\langle T_{\text{PbPb}} \rangle [1/\text{mb}]$  for ATLAS centrality classes with nominal and fitted  $\sigma_{\text{nn}}^{\text{inel}}$ .

$\sigma_{\text{nn}}^{\text{inel}}$	70.0 mb	57.7 mb	41.5 mb	29.5 mb
0%–2%	28.26	28.39	28.55	28.69
2%–4%	25.51	25.67	25.91	26.10
4%–6%	23.09	23.28	23.55	23.80
6%–8%	20.94	21.14	21.45	21.73
8%–10%	19.00	19.23	19.56	19.86
10%–15%	16.08	16.31	16.67	17.02
15%–20%	12.58	12.83	13.22	13.59
20%–25%	9.762	10.01	10.40	10.78
25%–30%	7.487	7.722	8.102	8.469
30%–40%	4.933	5.138	5.474	5.808
40%–50%	2.628	2.780	3.036	3.300
50%–60%	1.281	1.378	1.550	1.733
60%–80%	0.395	0.435	0.510	0.595
80%–100%	0.052	0.060	0.076	0.096
0%–80%	6.993	7.143	7.385	7.624
0%–100%	5.605	5.726	5.923	6.118

discussed, e.g., in the ATLAS publications [39,40], such a suppression could be expected from selection and geometrical biases associated with the MC Glauber modeling [57]. Also other effects such as the possible centrality dependence of  $\sigma_{\text{nn}}^{\text{inel}}$  and the neutron-skin effect [58,59] may become relevant to explain the data behavior in the far periphery. However, for minimum-bias collisions, the suppression effect arises mainly from midcentral collisions (0%–60%), so the resulting value for  $\sigma_{\text{nn}}^{\text{inel}}$  is robust against the phenomena occurring in the periphery.

*Minijets with shadowing.*—To study the plausibility of the obtained suppression in  $\sigma_{\text{nn}}^{\text{inel}}$ , we calculate its value in an eikonal model for minijet production with nuclear shadowing. The model is based on a similar setup as in Ref. [60], but in the eikonal function we include only the contribution from the hard minijet cross section  $\sigma_{\text{jet}}(\sqrt{s_{\text{nn}}}, p_0, [Q])$ , calculated at leading order in pQCD. The transverse-momentum cutoff  $p_0$  (which depends on  $\sqrt{s_{\text{nn}}}$ , scale choice  $Q$ , and the proton thickness) and the width of the assumed Gaussian proton thickness function we fix so that the model reproduces  $\sigma_{\text{pp}}^{\text{inel}} = 70$  mb matching the COMPETE

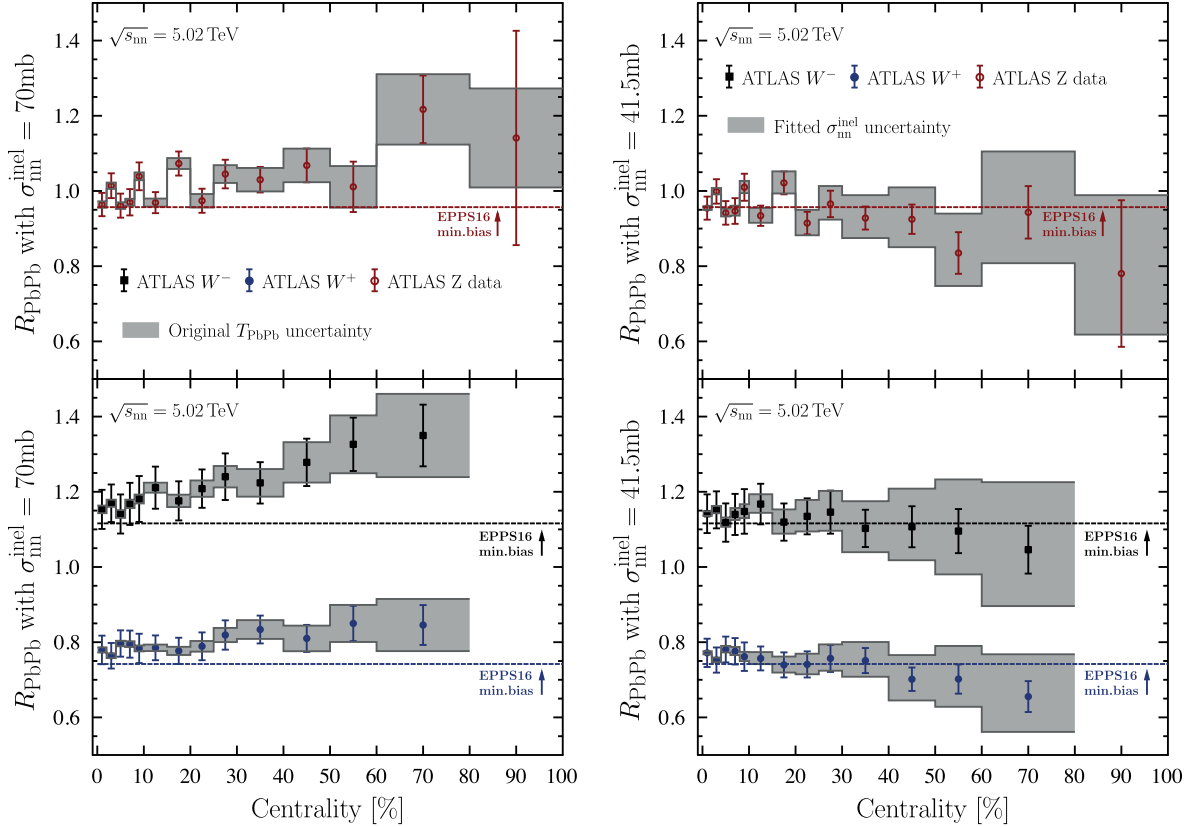


FIG. 3. The centrality-dependent nuclear modification ratios for  $W^\pm$  and Z-boson production in Pb + Pb collisions from ATLAS [39,40] compared to NNLO pQCD calculation with EPPS16 nuclear modification with the nominal value of  $\sigma_{\text{nn}}^{\text{inel}} = 70.0$  mb (left) and with the nuclear-suppressed value  $\sigma_{\text{nn}}^{\text{inel}} = 41.5$  mb (right).



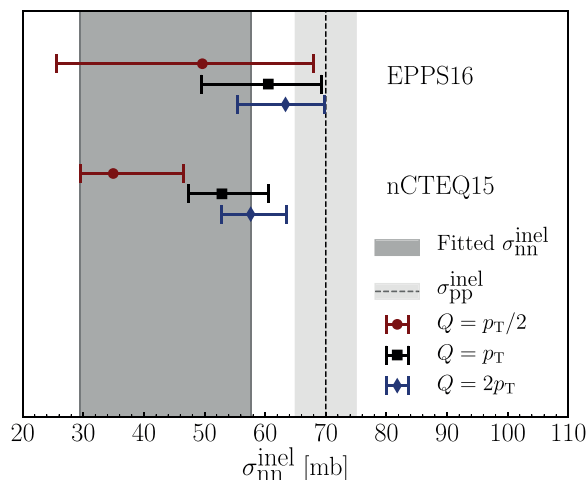


FIG. 4. Predictions for  $\sigma_{nn}^{\text{inel}}$  from an eikonal minijet model with the EPPS16 and nCTEQ15 nuclear PDFs for three scale choices. The fitted  $\sigma_{nn}^{\text{inel}}$  is indicated with the dark gray band and the nominal  $\sigma_{pp}^{\text{inel}}$  with the light gray band.

analysis [61] at  $\sqrt{s} = 5.02$  GeV. The free proton PDFs are here CT14lo [62], and we take the nuclear PDF modifications from the EPPS16 [45] and nCTEQ15 [63] analyses. The results for  $\sigma_{nn}^{\text{inel}}$ , obtained with  $p_0$  and proton thickness function width fixed to the p + p case, are shown in Fig. 4. The error bars are again from the nuclear PDFs scaled to the 68% confidence level. As expected at the few-GeV scales, the predicted  $\sigma_{nn}^{\text{inel}}$  depends strongly on the factorization and renormalization scale  $Q$ , but within the uncertainties the nuclear suppression obtained from the fits to the ATLAS  $W^\pm$  and  $Z$  data seems compatible with the eikonal model predictions with both nuclear PDFs.

**Summary.**—In the canonical approach, the normalization for the measured per-event yields in nuclear collisions is obtained from the Glauber model taking the value of  $\sigma_{nn}^{\text{inel}}$  from proton-proton measurements. Contrary to this, our strategy was to compare the state-of-the-art pQCD calculations with the measured  $W^\pm$  and  $Z$ -boson  $R_{\text{PbPb}}$  and thereby unfold the value for  $\sigma_{nn}^{\text{inel}}$  at  $\sqrt{s_{\text{nn}}} = 5.02$  TeV. We find that the recent high-precision ATLAS data from Run II prefer the value  $\sigma_{nn}^{\text{inel}} = 41.5^{+16.2}_{-12.0}$  mb, which is significantly lower than  $\sigma_{pp}^{\text{inel}} = 70 \pm 5$  mb. This new benchmark value for  $\sigma_{nn}^{\text{inel}}$  in  $\sqrt{s_{\text{nn}}} = 5.02$  TeV Pb + Pb collisions is the main result of the present work. Such a suppression is in line with the expectations from an eikonal minijet model, including nuclear shadowing, but is not necessarily tied only to the shadowing phenomenon. Remarkably, when using the fitted value for  $\sigma_{nn}^{\text{inel}}$ , the unexpected enhancements of  $R_{\text{PbPb}}$  in peripheral collisions disappear and the results become compatible with no centrality dependence. A possible hint of a slight decreasing trend toward peripheral collisions is observed that would be qualitatively in line with possible selection and geometrical biases. Our results

thus suggest that the standard paradigm of using  $\sigma_{pp}^{\text{inel}}$  as an input to Glauber modeling potentially leads to a misinterpretation of the experimental data. The possible suppression could be further scrutinized by repeating the experimental analysis using a measured luminosity to convert the yields into cross sections or by measuring the total hadronic Pb + Pb cross section at  $\sqrt{s_{\text{nn}}} = 5.02$  GeV with high enough precision.

We thank Mirta Dumancic for discussion concerning the ATLAS measurements. We acknowledge the Academy of Finland, projects 297058, 330448 (K. J. E.), 308301 (H. P. and I. H.), and 331545 (I. H.), and the Väisälä Foundation (M. K.) for financial support. The Finnish IT Center for Science (CSC) is acknowledged for the computing time through the Project No. jyy2580.

\*Corresponding author.

ilkka.m.helenius@jyu.fi

†kari.eskola@jyu.fi

‡mikko.a.kuha@student.jyu.fi

§hannu.t.paukkunen@jyu.fi

- [1] W. Busza, K. Rajagopal, and W. van der Schee, *Annu. Rev. Nucl. Part. Sci.* **68**, 339 (2018).
- [2] M. L. Miller, K. Reygers, S. J. Sanders, and P. Steinberg, *Annu. Rev. Nucl. Part. Sci.* **57**, 205 (2007).
- [3] B. Abelev *et al.* (ALICE Collaboration), *J. High Energy Phys.* **03** (2014) 013.
- [4] V. Khachatryan *et al.* (CMS Collaboration), *Phys. Rev. C* **96**, 015202 (2017).
- [5] G. Aad *et al.* (ATLAS Collaboration), *Phys. Lett. B* **719**, 220 (2013).
- [6] M. Aaboud *et al.* (ATLAS Collaboration), *Phys. Lett. B* **790**, 108 (2019).
- [7] A. M. Sirunyan *et al.* (CMS Collaboration), *J. High Energy Phys.* **10** (2018) 138.
- [8] V. Khachatryan *et al.* (CMS Collaboration), *J. High Energy Phys.* **04** (2017) 039.
- [9] G. Aad *et al.* (ATLAS Collaboration), *J. High Energy Phys.* **09** (2015) 050.
- [10] S. Acharya *et al.* (ALICE Collaboration), *Phys. Lett. B* **788**, 166 (2019).
- [11] S. Acharya *et al.* (ALICE Collaboration), *J. High Energy Phys.* **11** (2018) 013.
- [12] A. Adare *et al.* (PHENIX Collaboration), *Phys. Rev. C* **93**, 024901 (2016).
- [13] S. S. Adler *et al.* (PHENIX Collaboration), *Phys. Rev. C* **69**, 034910 (2004).
- [14] J. D. Bjorken, Report No. FERMILAB-PUB-82-059-THY (1982).
- [15] G.-Y. Qin and X.-N. Wang, *Int. J. Mod. Phys. E* **24**, 1530014 (2015); *Quark-Gluon Plasma 5*, edited by X.-N. Wang, (World Scientific, 2016), pp. 309–372, [https://doi.org/10.1142/9789814663717\\_0007](https://doi.org/10.1142/9789814663717_0007).
- [16] D. d’Enterria, *Relativistic Heavy Ion Physics*, edited by R. Stock (Landolt-Börnstein, 2010), Vol. 23, Chap. 6.4, [https://doi.org/10.1007/978-3-642-01539-7\\_16](https://doi.org/10.1007/978-3-642-01539-7_16).

- [17] F. Arleo, *Phys. Rev. Lett.* **119**, 062302 (2017).
- [18] C. Andrés, N. Armesto, M. Luzum, C. A. Salgado, and P. Zurita, *Eur. Phys. J. C* **76**, 475 (2016).
- [19] Y.-T. Chien, A. Emerman, Z.-B. Kang, G. Ovanessian, and I. Vitev, *Phys. Rev. D* **93**, 074030 (2016).
- [20] K. C. Zapp, F. Krauss, and U. A. Wiedemann, *J. High Energy Phys.* **03** (2013) 080.
- [21] G. Aad *et al.* (ATLAS Collaboration), *Phys. Rev. C* **93**, 034914 (2016).
- [22] S. Chatrchyan *et al.* (CMS Collaboration), *Phys. Lett. B* **710**, 256 (2012).
- [23] S. Afanasiev *et al.* (PHENIX Collaboration), *Phys. Rev. Lett.* **109**, 152302 (2012).
- [24] G. Aad *et al.* (ATLAS Collaboration), *Eur. Phys. J. C* **75**, 23 (2015).
- [25] G. Aad *et al.* (ATLAS Collaboration), *Phys. Rev. Lett.* **110**, 022301 (2013).
- [26] S. Chatrchyan *et al.* (CMS Collaboration), *Phys. Lett. B* **715**, 66 (2012).
- [27] S. Chatrchyan *et al.* (CMS Collaboration), *Phys. Rev. Lett.* **106**, 212301 (2011).
- [28] H. Paukkunen and C. A. Salgado, *J. High Energy Phys.* **03** (2011) 071.
- [29] I. Helenius, K. J. Eskola, and H. Paukkunen, *J. High Energy Phys.* **05** (2013) 030.
- [30] R. D. Woods and D. S. Saxon, *Phys. Rev.* **95**, 577 (1954).
- [31] J. E. Elias, W. Busza, C. Halliwell, D. Luckey, P. Swartz, L. Votta, and C. Young, *Phys. Rev. D* **22**, 13 (1980).
- [32] J.-w. Qiu, *Nucl. Phys.* **B291**, 746 (1987).
- [33] N. Armesto, *J. Phys. G* **32**, R367 (2006).
- [34] L. Frankfurt, V. Guzey, and M. Strikman, *Phys. Rep.* **512**, 255 (2012).
- [35] L. V. Gribov, E. M. Levin, and M. G. Ryskin, *Phys. Rep.* **100**, 1 (1983).
- [36] L. D. McLerran and R. Venugopalan, *Phys. Rev. D* **49**, 2233 (1994).
- [37] F. Gelis, E. Iancu, J. Jalilian-Marian, and R. Venugopalan, *Annu. Rev. Nucl. Part. Sci.* **60**, 463 (2010).
- [38] S. Chatrchyan *et al.* (CMS Collaboration), *J. High Energy Phys.* **03** (2015) 022.
- [39] G. Aad *et al.* (ATLAS Collaboration), *Eur. Phys. J. C* **79**, 935 (2019).
- [40] G. Aad *et al.* (ATLAS Collaboration), *Phys. Lett. B* **802**, 135262 (2020).
- [41] S. Acharya *et al.* (ALICE Collaboration), *Phys. Lett. B* **780**, 372 (2018).
- [42] R. Boughezal, J. M. Campbell, R. K. Ellis, C. Focke, W. Giele, X. Liu, F. Petriello, and C. Williams, *Eur. Phys. J. C* **77**, 7 (2017).
- [43] R. D. Ball *et al.* (NNPDF Collaboration), *Eur. Phys. J. C* **77**, 663 (2017).
- [44] M. Aaboud *et al.* (ATLAS Collaboration), *Eur. Phys. J. C* **79**, 128 (2019); **79**, 374(E) (2019).
- [45] K. J. Eskola, P. Paakkinen, H. Paukkunen, and C. A. Salgado, *Eur. Phys. J. C* **77**, 163 (2017).
- [46] V. Khachatryan *et al.* (CMS Collaboration), *Phys. Lett. B* **750**, 565 (2015).
- [47] V. Khachatryan *et al.* (CMS Collaboration), *Phys. Lett. B* **759**, 36 (2016).
- [48] G. Aad *et al.* (ATLAS Collaboration), *Phys. Rev. C* **92**, 044915 (2015).
- [49] A. M. Sirunyan *et al.* (CMS Collaboration), *Phys. Lett. B* **800**, 135048 (2020).
- [50] M. Walt, I. Helenius, and W. Vogelsang, *Phys. Rev. D* **100**, 096015 (2019).
- [51] R. A. Khalek, J. J. Ethier, and J. Rojo (NNPDF Collaboration), *Eur. Phys. J. C* **79**, 471 (2019).
- [52] C. Loizides, J. Nagle, and P. Steinberg, *SoftwareX* **1–2**, 13 (2015).
- [53] While modifying  $\sigma_{nn}^{inel}$ , the parameters of the two-component model should be adjusted to maintain a good description of the measured multiplicity or transverse energy distribution. However, as the change in  $\sigma_{nn}^{inel}$  can be accurately compensated purely by increasing the mean of the negative binomial distribution not affecting the resulting  $\langle T_{PbPb} \rangle$ , the presented results would remain unmodified. Similarly, the observed increase of  $T_{PbPb}$  is not sensitive to the applied centrality selection criterion.
- [54] B. Abelev *et al.* (ALICE Collaboration), *Phys. Rev. C* **88**, 044909 (2013).
- [55] ALICE Collaboration, Report No. ALICE-PUBLIC-2018-011 (2018).
- [56] G. D’Agostini, *Nucl. Instrum. Methods Phys. Res., Sect. A* **346**, 306 (1994).
- [57] C. Loizides and A. Morsch, *Phys. Lett. B* **773**, 408 (2017).
- [58] H. Paukkunen, *Phys. Lett. B* **745**, 73 (2015).
- [59] I. Helenius, H. Paukkunen, and K. J. Eskola, *Eur. Phys. J. C* **77**, 148 (2017).
- [60] X.-N. Wang, *Phys. Rev. D* **43**, 104 (1991).
- [61] J. R. Cudell, V. V. Ezhela, P. Gauron, K. Kang, Yu. V. Kuyanov, S. B. Lugovsky, E. Martynov, B. Nicolescu, E. A. Razuvaev, and N. P. Tkachenko (COMPETE Collaboration), *Phys. Rev. Lett.* **89**, 201801 (2002).
- [62] S. Dulat, T.-J. Hou, J. Gao, M. Guzzi, J. Huston, P. Nadolsky, J. Pumplin, C. Schmidt, D. Stump, and C. P. Yuan, *Phys. Rev. D* **93**, 033006 (2016).
- [63] K. Kovarik *et al.*, *Phys. Rev. D* **93**, 085037 (2016).



## II

# MC-EKRT: MONTE CARLO EVENT GENERATOR WITH SATURATED MINIJET PRODUCTION FOR INITIALIZING 3+1 D FLUID DYNAMICS IN HIGH ENERGY NUCLEAR COLLISIONS

by

M. Kuha, J. Auvinen, K. J. Eskola, H. Hirvonen, Y. Kanakubo, H. Niemi

Submitted to Phys. Rev. C, arXiv: 2406.17592 [hep-ph] (Jul. 2024).

# MC-EKRT: Monte Carlo event generator with saturated minijet production for initializing 3+1 D fluid dynamics in high energy nuclear collisions

Mikko Kuha, Jussi Auvinen, Kari J. Eskola, Henry Hirvonen, Yuuka Kanakubo, Harri Niemi  
*University of Jyväskylä, Department of Physics, P.O. Box 35, FI-40014 University of Jyväskylä, Finland, and  
 Helsinki Institute of Physics, P.O.Box 64, FI-00014 University of Helsinki, Finland*

We present a novel Monte-Carlo implementation of the EKRT model, MC-EKRT, for computing partonic initial states in high-energy nuclear collisions. Our new MC-EKRT event generator is based on collinearly factorized, dynamically fluctuating pQCD minijet production, supplemented with a saturation conjecture that controls the low- $p_T$  particle production. Previously, the EKRT model has been very successful in describing low- $p_T$  observables at mid-rapidity in heavy-ion collisions at the LHC and RHIC energies. As novel features, our new MC implementation gives a full 3-dimensional initial state event-by-event, includes dynamical minijet-multiplicity fluctuations in the saturation and particle production, introduces a new type of spatially dependent nuclear parton distribution functions, and accounts for the conservation of energy/momentum and valence-quark number. In this proof-of-principle study, we average a large set of event-by-event MC-EKRT initial conditions and compute the rapidity and centrality dependence of the charged hadron multiplicities and elliptic flow for the LHC Pb+Pb and RHIC Au+Au collisions using 3+1 D viscous fluid-dynamical evolution. Also event-by-event fluctuations and decorrelations of initial eccentricities are studied. The good agreement with the rapidity-dependent data suggests that the same saturation mechanism that has been very successful in explaining the mid-rapidity observables, works well also at larger rapidities.

## I. INTRODUCTION

The theory of the strong interaction, Quantum Chromodynamics (QCD), predicts that at very high energy densities, at temperatures  $T \gtrsim 150 - 160$  MeV and at a vanishing baryochemical potential, strongly interacting matter is in the form of a quark-gluon plasma (QGP) [1–4]. Such extreme conditions can be momentarily created and the properties of the QGP experimentally studied in laboratory by colliding heavy ions at ultrarelativistic energies at the CERN Large Hadron Collider (LHC) and the Brookhaven National Laboratory (BNL) Relativistic Heavy Ion Collider (RHIC). In these collisions, the "heating" of the matter necessary for the QGP formation is obtained from the kinetic energy of the colliding nuclei, through copious primary production of QCD quanta, quarks and gluons [5].

The QCD system formed in ultrarelativistic heavy-ion collisions is expected to experience various spacetime evolution stages: initial formation of a nearly-thermalized QGP, expansion and cooling of the QGP, transition of the QGP into a hadron resonance gas (HRG), expansion and cooling of the HRG, and finally decoupling of the HRG into non-interacting hadrons, out of which the resonances still decay before they can be detected. The dynamical expansion stages of QCD matter can be described with relativistic dissipative fluid dynamics [6–21] which nowadays is a cornerstone in the event-by-event analysis of heavy-ion observables.

The heavy-ion programs at the LHC and RHIC aim especially at the determination of the QCD matter properties, such as the temperature dependencies of the specific shear and bulk viscosities and other transport coefficients, from the experimental data. In practice, this can be achieved only by performing a fluid-dynamics based "global analysis", a simultaneous study of various dif-

ferent (low-transverse-momentum) observables from as many types of collision systems as possible. These analyses have evolved from pioneering works [12, 14, 17] (see also [22]) to those with a proper Bayesian statistical analysis and well defined uncertainty estimates [21, 23–31]. So far, the analyses have mainly focused on studies at mid-rapidity, where one assumes a longitudinally boost symmetric (but 3-dimensionally expanding) system described by the 2+1 D fluid dynamical equations of motion. The studies of rapidity-dependent observables requires a full 3+1 D implementation of viscous fluid dynamics [9–11, 32–38]. Recently, global analyses have been also extended into this direction [39–41]. Moreover, neural networks have been developed for studying rare observables [42, 43].

In such global analyses, the results obtained for the QCD matter properties are strongly correlated with the the assumed fluid-dynamical initial conditions. Then, if the initial states are obtained from an ad hoc parametrization that is blind to QCD dynamics – as is typically the case, see e.g. [21, 24–27, 29–31] – it is not at all clear whether the initial densities such as the ones extracted from the global analysis could actually be realized in the studied nuclear collisions. It is therefore of paramount importance to try to study and model the QCD collision dynamics responsible for the QCD matter initial conditions. Works into this direction include the developments of the IP-Sat+MUSIC (Impact parameter dependent saturation + MUSIC for Ion Collisions) model [10, 14, 44], the EKRT (Eskola-Kajantie-Ruuskanen-Tuominen) model [17, 45–47], the EPOS (Energy conservation + Parallel scattering + factorization + Saturation) model [48–53], the AMPT (A Multi-Phase Transport) model [38, 54], and the Dynamical Core-Corona Initialization model [55, 56] with initial state generated by Pythia Angantyr [57], as well as initial

state models such as in Refs. [58, 59].

In this work, we adopt, and significantly further develop, the pQCD and saturation -based EKRT model for computing event-by-event initial conditions of the QCD matter produced in nucleus-nucleus collisions at the LHC and at the highest RHIC energies. The leading idea in the EKRT model [17, 45–47] is that at sufficiently high collision energies the nucleus-nucleus collisions can be described as collisions of parton clouds rather than a collection of Glauber-model like nucleon-nucleon collisions. Then, gluons and quarks that are produced with transverse momenta ( $p_T$ ) of the order of a few GeV, minijets, become so copiously produced [60, 61] that their production processes start to overlap in the transverse coordinate space [62], which dynamically generates a saturation scale ( $p_{\text{sat}}$ ) that suppresses softer particle production [47].

The original versions of the EKRT model [45, 46], combined with longitudinally boost invariant 1+1 D ideal fluid dynamics, predicted successfully the LHC and RHIC hadron multiplicities and  $p_T$  distributions at mid-rapidity in central collisions [45, 63], and, with 2+1 D fluid dynamics, also the centrality dependence of these and of the elliptic flow coefficients ( $v_2$ ) of the azimuthal angle asymmetries [64, 65]. Based on a well-defined (collinear- and infrared-safe) pQCD calculation of minijet transverse energy production [47, 66, 67], the model was extended to next-to-leading order (NLO) in Ref. [47]. Combined then with shear-viscous fluid dynamics, the NLO-improved EKRT model described well the centrality dependent hadron multiplicities,  $p_T$  distributions and  $v_2$  at mid-rapidity both at RHIC and LHC, systematically indicating a relatively low value for the QCD matter shear-viscosity-to-entropy ( $\eta/s$ ) ratio [47].

An event-by-event version of the EKRT model (EbyE-EKRT) was developed in Ref. [17]. The pioneering global analysis of a multitude of LHC and RHIC bulk (low- $p_T$ ) observables presented in Ref. [17] demonstrated a very good overall agreement with the measurements, and resulted in improved constraints for the temperature dependence of  $\eta/s$ . Very interestingly (but not unexpectedly), also the Bayesian global analysis of LHC bulk observables of Ref. [26], which used QCD-blind parametrized initial states, confirmed that the initial density profiles predicted by the EbyE-EKRT [17] and the IP-Sat models [44] gave the best match with those obtained from the Bayesian inference.

The first attempt to perform a Bayesian global analysis of LHC and RHIC bulk observables using directly the EKRT initial states as input for the fluid-dynamics, for studying the effects of the EoS and for obtaining statistically controlled uncertainty estimates on the temperature dependence of  $\eta/s$ , can be found in Ref. [28]. The latest developments in the EKRT-initiated 2+1 D fluid-dynamics framework are a dynamically determined decoupling, which improves the description of peripheral collisions, and the inclusion of bulk viscosity. These developments are presented in Ref. [22] together with a

demonstration of a very good simultaneous global fit to bulk observables from various collision systems at the LHC and RHIC, and the corresponding extracted specific shear and bulk viscosities of QCD matter. Finally, the first study of how deep convolutional neural networks can be trained to predict hydrodynamical bulk observables from the EbyE-EKRT-generated energy density profiles, and how they can significantly speed up the statistics-expensive EbyE analysis of rare flow correlators especially, can be found in Ref. [42].

The predictive power of the EbyE-EKRT model originates from the underlying collinearly factorized NLO pQCD calculation. The model has been remarkably successful, especially in genuinely predicting bulk observables at mid-rapidity also for higher LHC energies, 5.02 TeV Pb+Pb collisions [68], as well as for collisions of deformed nuclei, 5.44 TeV Xe+Xe collisions at [69] – see the data comparisons e.g. Refs. [22, 70]. However, there still is a number of shortcomings with the EKRT-model that need to be addressed.

First, for addressing also rapidity-dependent observables, the EbyE-EKRT initial state model should be extended to off-central rapidities and then coupled to 3+1 D viscous fluid dynamics.

Second, the average number of (or the average  $E_T$  from) the parton-parton collisions is thus far in the EKRT saturation model computed as a product of a nuclear overlap function and ( $p_T$  weighted) collinearly factorized integrated minijet cross section. This assumes essentially independent partonic collisions, and as discussed in Ref. [62], especially towards larger rapidities at the LHC one easily violates the conservation of energy and baryon number. This problem clearly needs to be addressed together with the rapidity dependence.

Third, thus far in the EbyE-EKRT [17], the local fluctuations of the saturation scale, and thus of the computed energy densities, in the transverse coordinate plane are only of a geometrical origin, i.e. they follow only from the sampled fluctuating positions of the nucleons inside the colliding nuclei. Dynamical, local EbyE fluctuations in the minijet multiplicity, inducing then further local EbyE fluctuations to the saturation scale and hence to the energy densities, should clearly be accounted for. Only by including these fluctuations can the EKRT model be relevantly applied to the studies of smaller collision systems, i.e. proton-nucleus and perhaps even proton-proton collisions.

Fourth, in an EbyE analysis the factorized minijet cross sections must be computed using nuclear parton distribution functions (nPDFs) that depend on the transverse position ( $\bar{s}$ ) in each of the colliding nuclei. The spatial dependence can be modeled in terms of a power series of the nuclear thickness function,  $T_A(\bar{s})$ , as was done e.g. in EPS09s nPDFs [71] that are used in EbyE-EKRT. The EbyE fluctuating  $T_A$ 's, however, often reach so large values (up to more than 3 times the largest average  $T_A(0)$ ) that the  $T_A$ -applicability range of EPS09s is significantly exceeded. In EbyE-EKRT this problem was solved by an



ad-hoc extrapolation of the saturation scale towards the larger values of  $T_A$ . Clearly, this problem is not EKRT-specific but should be addressed for the benefit of any factorized EbyE study of centrality dependence of hard processes, where spatial dependence of nPDFs is needed.

In this paper, we address these shortcomings and the arising uncertainties in solving them, for the first time in the EKRT-model framework. In particular, we introduce a completely new Monte Carlo EKRT event-generator, which we name *MC-EKRT* [72], for computing EbyE fluctuating initial states for fluid dynamics in nuclear collisions. We couple the MC-EKRT minijets to 3+1 D shear-viscous fluid dynamics [73], and discuss the various uncertainties in doing this. In this proof-of-principle paper we do not, however, aim at a full EbyE global analysis, yet, but instead study the model systematics by computing averaged initial conditions for each centrality class by summing over a large set of event-by-event MC-EKRT initial states. Running then 3+1 D shear-viscous fluid dynamics with these, we can meaningfully compare the MC-EKRT results against the measured pseudorapidity distributions of charged hadrons in different centrality classes, and also elliptic flow coefficients in semi-central collisions in Pb+Pb collisions at the LHC and Au+Au collisions at RHIC. We also study the decorrelation of eccentricities in spacetime rapidity, which was to our knowledge discussed first in [36, 54].

The paper is organized as follows: In Sec. II we define the MC-EKRT model framework and discuss how the previous shortcomings are solved. Section III discusses our fluid-dynamics setup, and how the 3+1 D fluid dynamics is initialized with the computed MC-EKRT minijet states. Comparisons against LHC and RHIC data, and the results for the decorrelation of eccentricities, are shown in Sec. IV. Finally, conclusions and outlook are given in Sec. V.

## II. MONTE CARLO EKRT MODEL SETUP

Let us first see how the geometric saturation criterion that we will employ in the MC-EKRT set-up below, arises using collinearly factorized lowest-order pQCD  $2 \rightarrow 2$  gluonic processes as the basis and imagining the colliding nuclei as parton (gluon) clouds [45, 74]. In an inelastic nucleus-nucleus collision at an impact parameter  $\bar{b}_{AA}$ , the average transverse density of the number of gluon-gluon collisions that are producing minijets with  $p_T$  above a cut-off  $p_0$  and at rapidities  $y_{1,2}$ , is

$$\frac{dN_{AA}^{2 \rightarrow 2}(\bar{b}_{AA})}{d^2\bar{s}} = T_A(\bar{s}_1)T_A(\bar{s}_2)\frac{1}{2}\int_{p_0} dp_T^2 dy_1 dy_2 \times x_1 g(x_1, Q^2) x_2 g(x_2, Q^2) \times \frac{d\hat{\sigma}^{2 \rightarrow 2}}{d\hat{t}} \quad (1)$$

where  $T_A(\bar{s})$  is the standard nuclear thickness function obtained as an integral of the nuclear density over the longitudinal coordinate,  $\bar{s}_{1,2} = \bar{s} \pm \bar{b}_{AA}/2$  are the transverse

coordinates,  $g(x, Q^2)$  are the gluon PDFs,  $x_{1,2} \sim p_T/\sqrt{s}$  are the longitudinal momentum fractions of the colliding gluons and  $Q \sim p_T$  is the factorization/renormalization scale,  $\hat{t}$  is a Mandelstam variable for the partonic scattering and  $d\hat{\sigma}^{2 \rightarrow 2}/d\hat{t} \sim \alpha_s^2/p_T^4$  is the  $2 \rightarrow 2$  LO pQCD gluonic cross section.

On dimensional grounds, and ignoring the rapidity dependence, we may write for a symmetric system in central collisions [17]

$$\frac{dN_{AA}^{2 \rightarrow 2}(0)}{d^2\bar{s}} \sim (T_A x g) \times (T_A x g) \times \left(\frac{\alpha_s}{p_0}\right)^2, \quad (2)$$

where  $x \sim p_0/\sqrt{s}$ . Correspondingly, for  $3 \rightarrow 2$  processes, which can be expected to become important at small  $x$ , where the initial gluon densities become large, we would on dimensional grounds write, assuming here the double-PDFs from the nucleus 1 (and similarly for the other nucleus),

$$\frac{dN_{AA}^{3 \rightarrow 2}(0)}{d^2\bar{s}} \sim (T_A x g)^2 \times T_A x g \times \frac{\alpha_s}{p_0^2} \left(\frac{\alpha_s}{p_0}\right)^2, \quad (3)$$

where we have accounted for the extra power of  $\alpha_s$  in the numerator, and for the  $p_0^2$  in the denominator canceling the dimension of the extra  $T_A$  there in the double-PDF. Saturation effects are expected to become dominant, and softer parton production suppressed, when  $dN_{AA}^{3 \rightarrow 2} \sim dN_{AA}^{2 \rightarrow 2}$ , i.e. when

$$T_A x g \sim \frac{p_0^2}{\alpha_s}. \quad (4)$$

Substituting this back to Eq. (2), and integrating over an effective nuclear transverse area  $\pi R_A^2$  ( $R_A$  being the nuclear radius), gives the geometrical EKRT scaling law, introduced in Ref. [45]

$$N_{AA}^{2 \rightarrow 2}(0) \frac{\pi}{p_0^2} \sim \pi R_A^2, \quad (5)$$

where  $\pi/p_0^2$  can be interpreted as a transverse formation-area for a produced dijet [45, 62]. Thus, the minijet production saturates when the minijet production processes fill the available transverse area in the nuclear collision.

In the MC-EKRT set-up introduced below, we will take the above geometric interpretation of saturation as our starting point, when deciding on an event-by-event and on a parton-by-parton basis, whether the produced minijet system becomes locally saturated. With the above discussion, we would also like to emphasize that saturation in the EKRT model is *not* fusion of produced final-state gluons, but saturation of the minijet production processes themselves.

Our MC-EKRT simulation of a nucleus-nucleus ( $A+B$ ) collision proceeds through the following steps, each of which will be discussed in more detail in this and the following sections.

**1.** Sample the positions of the nucleons in  $a \in A$  and  $b \in B$  from the Woods-Saxon distribution, keeping track of the proton/neutron identity of each nucleon (Sec. II A).

**2.** Sample the impact parameter for the  $A+B$  collision similarly as in the MC Glauber model (Sec. IIB), and check whether the chosen trigger condition for the  $A+B$  collision is fulfilled. If it is not, start again from item 1 (Sec. IIC).

**3.** If the  $A+B$  collision is triggered, find all the binary  $ab$  pairs of nucleons,  $a \in A$  and  $b \in B$ . Then go through the generated list of the  $ab$  pairs and regard each  $ab$  pair as a possible independent source of multiple minijet production. Sample the number of produced minijet pairs, dijets, for each  $ab$  pair from a Poissonian probability distribution (Sec. IID1).

**4.** For each produced dijet, sample the parton flavors and momenta from collinearly factorized LO pQCD cross sections (Sec. IID2), using nuclear PDFs that depend on the transverse positions of  $a \in A$  and  $b \in B$  (Sec. IID3). For quark-initiated processes, decide (sampling the LO pQCD cross sections) whether the colliding quarks are valence quarks or sea quarks (Sec. IID2). Sample also the transverse production point for each dijet from a Gaussian overlap function for each nucleon pair  $ab$  (Sec. IID1).

**5.** Consider all the generated dijets as candidates for the final minijet-state of this  $A+B$  event. For filtering away the excess (unphysical) dijets, order the dijet candidates according to the transverse momentum  $p_T$  of the minijets forming the dijet (Sec. IIE).

**6.** Filter the excess dijets in the order of decreasing  $p_T$ , by imposing a local geometric EKRT saturation criterion (cf. Eq. (5)). If a dijet gets filtered, both final-state partons are removed (Sec. IIE).

**7.** Filter the surviving dijets further by imposing conservation of energy and valence quark number for each nucleon, doing the filtering again in the order of decreasing  $p_T$ . Optionally, this filtering step can be ignored, or chosen to be done simultaneously with the dijet filtering in step 6 (Sec. IIE).

**8.** Collect the MC-EKRT minijet output data for the surviving dijets: the  $\mathbf{p}_T$  vector, the rapidity, and the flavour of each minijet, along with the transverse location of each dijet's formation point, to be used in Sec. IIIB. Order the  $A+B$  events according to the total minijet  $E_T$  (a scalar sum of minijet  $p_T$ 's) for the centrality selection (Sec. IIF).

A separate interface is then developed to initialize fluid dynamics, with the following steps:

**9.** Propagate the surviving minijets as free particles to the proper time surface  $\tau_0 = 1/p_0$ , assuming that minijets with momentum rapidity  $y$  move along the corresponding spacetime rapidity  $\eta_s = y$ . The parameter  $p_0$  here is the smallest partonic  $p_T$  allowed in the pQCD cross sections for the dijet candidates (Sec. IIIB1).

**10.** Feed the minijets into 3+1 D fluid dynamics as initial conditions at  $\tau_0$ : At each  $\eta_s$  and transverse-coordinate grid cell, using a Gaussian smearing, convert the minijet transverse energy  $E_T$  into a local energy density (Sec. IIIB2).

**11.** Run 3+1 D viscous fluid dynamics with these mini-

jet initial conditions, in principle event by event. Note, however, that in the present exploratory study we are testing the model setup using averaged initial states for each centrality class (Sec. IIIB3). We do not couple the fluid dynamics with a hadron cascade afterburner but run fluid dynamics until the freeze-out of the system. Resonance decays are accounted for, as usual (Sec. IIIA).

**12.** Form the observables for which statistics is collected (Sec. IV).

Next, we look at the above steps in more detail, and also specify the few parameters that the MC-EKRT minijet event generator has.

### A. Nucleon configurations of $A$ and $B$

First, we construct the nucleon structure of the colliding nuclei. Here, we essentially follow the procedure nowadays standard in the Monte Carlo Glauber approach [75]. The distributions of the positions of the nucleons are taken to follow the nuclear charge densities extracted from low energy electron scattering experiments [76, 77]. The lead nucleus,  $\text{Pb}^{208}$  (used at the LHC) is assumed perfectly spherical, and as the gold nucleus  $\text{Au}^{197}$  (used at RHIC) is also nearly spherical, the current version of the MC-EKRT assumes spherically symmetric nuclei  $A$  and  $B$ . Thus, the azimuthal angle  $\phi \in [0, 2\pi]$  and the cosine of the polar angle  $\cos\theta \in [-1, 1]$  are sampled from a uniform distribution, while the radial coordinate  $r$  is sampled from the two-parameter Fermi (2pF) distribution, the Woods-Saxon distribution [78],

$$\rho_{\text{WS}}(r) = \frac{\rho_0}{1 + \exp\left(\frac{r-R_A}{d}\right)}, \quad (6)$$

where  $R_A$  is the nuclear radius and  $d$  is the diffusion parameter. For the lead and gold nuclei we study here,  $(R_A, d) = (6.624, 0.550)$  fm and  $(6.380, 0.535)$  fm, correspondingly [76]. The normalization constant  $\rho_0$  is fixed by requiring the volume integral of  $\rho_{\text{WS}}(r)$  to give  $A$ , but in the simulation here  $\rho_0$  has no effect. The nuclei which have nucleons with positions closer to each other than  $d_{\text{min}} = 0.4$  fm, are discarded and sampled again. The introduction of an exclusion radius  $d_{\text{min}}$  is known to slightly deform the radial density profile [75, 79], but we neglect this small effect here.

### B. Impact parameter sampling

Next, the squared impact parameter,  $\bar{b}_{AB}^2$ , for the  $A+B$  collision is sampled from a uniform distribution. As long as the colliding nuclei are spherically symmetric on the average, we do not need to randomly rotate the nuclei. We can fix the impact parameter vector, as a vector in the transverse  $(x, y)$  plane, to be on the  $x$ -axis, pointing from the nucleus  $A$  to the nucleus  $B$  – see Fig. 1.

Once the positions of the nucleons in each nucleus –  $\{\bar{s}_a\}$  in  $A$  and  $\{\bar{s}_b\}$  in  $B$  – have been determined,

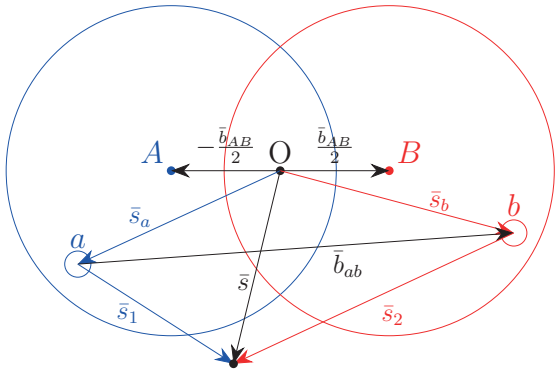


FIG. 1: Projection of the  $A+B$  collision system into the transverse plane. The impact parameter vector  $\bar{b}_{AB}$ , extending from the center-of-mass of the nucleus  $A$  to the center-of-mass of the nucleus  $B$ , is along the  $x$ -axis (axes are not shown), with the origin  $O$  in the middle. The location vectors of the nucleons  $a \in A$  and  $b \in B$  are  $\bar{s}_a$  and  $\bar{s}_b$ , respectively. The impact parameter between the nucleons  $a$  and  $b$  is  $\bar{b}_{ab}$ .

the center of the mass of the projectile nucleus  $A$  is shifted to  $(-b_{AB}/2, 0)$  and that of the target nucleus  $B$  to  $(b_{AB}/2, 0)$ , thus fixing the origin  $O$  of the collision frame. Finally,  $Z_A$  ( $Z_B$ ) of the nucleons in  $A$  ( $B$ ) are randomly labeled as protons and the rest as neutrons, i.e. we neglect possible effects arising from the differences of proton and neutron density distributions (such as a neutron skin), in this study.

### C. Trigger condition for the $A+B$ collision

Next, our simulation checks whether an inelastic collision between the generated nucleon configurations  $A$  and  $B$  takes place. We devise the trigger condition for the  $A+B$  collision as follows: Assuming a hard-sphere scattering of two nucleons,  $a \in A$  and  $b \in B$ , with a cross section  $\sigma_{\text{trig}}^{ab}(s_{NN})$  at a nucleon-nucleon center-of-momentum system (CMS) energy  $\sqrt{s_{NN}}$ , an  $A+B$  collision takes place if for at least one of the  $ab$  pairs the squared transverse distance between  $a$  and  $b$  does not exceed  $\sigma_{\text{trig}}^{ab}(s_{NN})/\pi$ . In terms of the transverse-coordinate vectors introduced in Fig. 1, with nucleons  $a \in A$  and  $b \in B$ , their transverse positions at  $\bar{s}_a$  and  $\bar{s}_b$ , and impact parameters  $\bar{b}_{ab}$ , the triggering condition for the  $A+B$  collision is fulfilled if at least for one  $ab$  pair

$$|\bar{b}_{ab}| = |\bar{s}_b - \bar{s}_a| \leq \sqrt{\sigma_{\text{trig}}^{ab}(s_{NN})/\pi}. \quad (7)$$

If the above condition is not met, new nucleon configurations  $A$  and  $B$ , and a new impact parameter  $b_{AB}^2$  are generated. For the triggering cross section  $\sigma_{\text{trig}}^{ab}(s_{NN})$  we use the inelastic nucleon-nucleon cross section  $\sigma_{\text{inel}}^{NN}(s_{NN})$ , calculated as

$$\sigma_{\text{inel}}^{NN}(s_{NN}) = \sigma_{\text{tot}}^{NN}(s_{NN}) - \sigma_{\text{el}}^{NN}(s_{NN}), \quad (8)$$

where the total cross section  $\sigma_{\text{tot}}^{NN}$  is obtained from a fit by COMPETE [80],

$$\sigma_{\text{tot}}^{NN}(s_{NN})/\text{mb} = 42.6s^{-0.46} - 33.4s^{-0.545} + 0.307 \log^2(s/29.1) + 35.5, \quad (9)$$

and the elastic cross section from a fit by TOTEM [81],

$$\sigma_{\text{el}}^{NN}(s_{NN})/\text{mb} = -1.617 \log(s) + 0.1359 \log(s)^2 + 11.84, \quad (10)$$

with  $s = s_{NN}/\text{GeV}^2$ . For the CMS energies  $\sqrt{s_{NN}} = 5020, 2700, 200$  GeV, which we study here, this gives  $\sigma_{\text{inel}}^{NN}(s_{NN}) = 69.14, 62.96, 41.78$  mb, correspondingly.

We emphasize that  $\sigma_{\text{inel}}^{NN}$  is here used only for the triggering of the nuclear collision, i.e. for determining the inelastic  $A+B$  cross-section. It does not play any other role in what follows.

### D. Multiple dijet production

#### 1. Probability distribution and nucleon thickness function

If the trigger condition is fulfilled, the collision between  $A$  and  $B$  takes place. The  $A+B$  collision here is assumed to be a very high-energy one, and furthermore a collision of two large parton clouds, which are originating from the sampled nucleons and extending around the Lorentz contracted nuclei. In this case, the multiple minijets originating from each  $ab$  pair are produced practically instantaneously around  $z \sim 0$ , and simultaneously everywhere in the transverse plane.

At this stage of our setup, all the  $ab$  pairs can be considered to be fully independent from each other, they just divide the interaction of the two large nuclear parton-clouds into  $ab$  contributions. Saturation and energy conservation, which will here be imposed in the order of decreasing minijet  $p_T$ , do not depend on the ordering of the  $ab$  pairs, either. Thus, in our setup the ordering of the  $ab$  pairs becomes irrelevant <sup>1</sup>.

Next, all the  $ab$  nucleon pairs will be considered as potential sources for multiple minijet (dijet) production. In each  $ab$  contribution, the candidate dijets are supposed to be produced independently from each other, hence Poissonian statistics is used in sampling the number of produced dijets. Then, the probability of producing  $n \geq 0$  independent dijets from the pair  $ab$ , where the locations of  $a$  and  $b$ , in the fixed nucleon configurations of this event, are  $\bar{s}_a$  and  $\bar{s}_b$ , correspondingly, and whose impact parameter thus is  $\bar{b}_{ab} = \bar{s}_b - \bar{s}_a$ , is

$$P_n(\{\bar{s}_a\}, \{\bar{s}_b\}, p_0, \sqrt{s_{NN}}) = \frac{(\bar{N}_{\text{jets}}^{ab})^n}{n!} e^{-\bar{N}_{\text{jets}}^{ab}}, \quad (11)$$

<sup>1</sup> Note, however, that if one models nuclear collisions as subsequent energy-conserving NN subcollisions (like e.g. in HIJING [82]), then the ordering (randomization) of the  $ab$  pairs would be important.



where the average number of dijets produced from the pair  $ab$  is

$$\bar{N}_{\text{jets}}^{ab} \equiv \bar{N}_{\text{jets}}^{ab}(p_0, \sqrt{s_{NN}}, \{\bar{s}_a\}, \{\bar{s}_b\}) \quad (12)$$

$$= T_{NN}(\bar{b}_{ab}) \sigma_{\text{jet}}^{ab}(p_0, \sqrt{s_{NN}}, \{\bar{s}_a\}, \{\bar{s}_b\}) \quad (13)$$

where  $\sigma_{\text{jet}}^{ab}$  is an integrated inclusive pQCD cross section for producing a pair of minijets with transverse momenta  $p_T \geq p_0$  and any rapidities (details of obtaining  $\sigma_{\text{jet}}^{ab}$  will be explained in Sec. IID 2), and with the notation  $\{\bar{s}_a\}$  ( $\{\bar{s}_b\}$ ) we underline that the computed pQCD cross section here depends both on the location  $\bar{s}_a$  ( $\bar{s}_b$ ) of the nucleon  $a \in A$  ( $b \in B$ ) and on the positions of all other nucleons in the nucleon configuration forming the nucleus  $A$  ( $B$ ) in each event. Above,  $T_{NN}$  is the nucleon-nucleon overlap function,

$$T_{NN}(\bar{b}_{ab}) = \int d^2s T_N(\bar{s} - \bar{s}_a) T_N(\bar{s} - \bar{s}_b) \quad (14)$$

$$= \int d^2s_1 T_N(\bar{s}_1) T_N(\bar{s}_1 - \bar{b}_{ab}) \quad (15)$$

where the transverse vectors  $\bar{s} - \bar{s}_a \equiv \bar{s}_1$  and  $\bar{s} - \bar{s}_b \equiv \bar{s}_1 - \bar{b}_{ab} \equiv \bar{s}_2$  measure the transverse distance from the centers of the nucleons  $a \in A$  and  $b \in B$ , correspondingly, see Fig. 1. Here,  $T_N$  is the nucleon thickness function, which is obtained from the spatial density distribution  $\rho_N$  as

$$T_N(\bar{s}) = \int_{-\infty}^{\infty} dz \rho_N(\mathbf{x}), \quad (16)$$

where  $\mathbf{x} = (\bar{s}, z)$ . Both  $T_N$  and  $T_{NN}$  are normalized to one through the transverse integrals,

$$\int d^2s T_N(\bar{s}) = \int d^3x \rho_N(\mathbf{x}) = 1, \quad (17)$$

$$\int d^2s T_{NN}(\bar{s}) = 1. \quad (18)$$

It should also be emphasized that in writing Eq. (12) into the form of Eq. (13), we are assuming that the PDFs carry spatial dependence in that they do (quite strongly) depend on the locations  $\bar{s}_a$  of  $a \in A$  and  $\bar{s}_b$  of  $b \in B$ , as well as on the positions of all the other nucleons in  $A$  and  $B$  (which all are fixed for one  $A+B$  collision event), but that for each nucleon  $a \in A$  and  $b \in B$  we have fixed PDFs that do not depend on the variable  $\bar{s}$  appearing in Eq. (14). This allows us to factorize the nucleon-nucleon overlap function  $T_{NN}$  from the minijet cross section  $\sigma_{\text{jet}}^{ab}$  in Eq. (13).

Following Ref. [17], we extract  $\rho_N$ , and thereby  $T_N$ , from exclusive  $J/\psi$  photo-production cross sections that have been measured in  $\gamma + p \rightarrow J/\psi + p$  collisions at HERA [83]. As discussed e.g. in Ref. [84], the amplitude of this process is proportional to generalized parton distribution functions (GPDs) and a two-parton form factor  $F_N(t)$  that depends on the Mandelstam variable  $t$  and is

linked to  $\rho_N$  via a 3D Fourier transform,

$$F_N(t) = \int d^3x e^{i\mathbf{q}\cdot\mathbf{x}} \rho_N(\mathbf{x}), \quad (19)$$

where  $|\mathbf{q}|^2 = |t|$ , and  $F_N(0) = 1$ . As the GPDs become ordinary PDFs at the forward limit, and as the  $J/\psi$  mass scale is of the same order of magnitude as the dominant minijet  $p_T$  scale, the above  $\rho_N$  should to a good approximation describe also the corresponding partonic spatial density related to the PDFs we use here. The measured HERA cross sections show a behavior  $d\sigma/dt \propto e^{-b|t|}$ , with a slope parameter  $b$  that depends on the photon-proton system c.m.s. energy  $W$  as

$$b/\text{GeV}^{-2} = b_0 + 4\alpha'_P \log\left(\frac{W}{W_0}\right), \quad (20)$$

where  $b_0$ ,  $\alpha'_P$  and  $W_0$  are constants. Here, identifying  $W = \sqrt{s_{NN}}$ , our default choice is the parametrization from Ref. [85] (also used in [84]), with  $b_0 = 4.9$ ,  $\alpha'_P = 0.06$  and  $W_0 = 90$  GeV. Then, an inverse Fourier transform of  $F_N(t) = \exp(-b|t|/2) = \exp(-b|\mathbf{q}|^2/2)$  results in a 3D Gaussian density,

$$\rho_N(\mathbf{x}) = \int \frac{d^3q}{(2\pi)^3} e^{-i\mathbf{q}\cdot\mathbf{x}} F_N(t) \quad (21)$$

$$= \left(\frac{1}{2\pi\sigma_N^2}\right)^{3/2} \exp\left(-\frac{|\mathbf{x}|^2}{2\sigma_N^2}\right), \quad (22)$$

and a 2D Gaussian thickness function,

$$T_N(\bar{s}) = \frac{1}{2\pi\sigma_N^2} \exp\left(-\frac{|\bar{s}|^2}{2\sigma_N^2}\right), \quad (23)$$

with a width parameter  $\sigma_N^2 \equiv b$ . With the parametrization (20), we have  $\sigma_N = 0.478$  (0.472) fm, at  $\sqrt{s_{NN}} = 5.02$  (2.76) TeV at the LHC, and  $\sigma_N = 0.445$  fm for  $\sqrt{s_{NN}} = 200$  GeV at RHIC.

Then, with the Gaussian forms for  $T_N$ , also the nucleon-nucleon overlap function in Eq. (15) can be expressed in a closed form, which also becomes a Gaussian,

$$T_{NN}(\bar{b}_{ab}) = \frac{1}{4\pi\sigma_N^2} \exp\left(-\frac{|\bar{b}_{ab}|^2}{4\sigma_N^2}\right). \quad (24)$$

Once the number of the independent dijet candidates has been sampled, each dijet candidate is assigned a spatial production point  $\bar{s}$  that is sampled from the product distribution  $T_N(\bar{s} - \bar{s}_a) T_N(\bar{s} - \bar{s}_b)$ .

The modeling here is inspired by the eikonal minijet models [86, 87] which are high-energy limits of potential scattering, but we emphasize the different roles of the parameter  $p_0$  in these models. In MC-EKRT, the impact parameter integral of the eikonal  $1 - P_0 = 1 - \exp(-T_{NN}(b)\sigma_{\text{jet}}(p_0))$  is *not* normalized to an inelastic NN cross section  $\sigma_{\text{inel}}^{NN}(s_{NN})$  but is allowed to obtain larger values. Instead, the parameter  $p_0$  needs to be chosen so small, of the order 1 GeV, that minijets are

produced so abundantly that they overfill the coordinate space, so that saturation can become effective in regulating the smallest- $p_T$  minijet production. For this reason, our results are also fairly *insensitive* to the value of  $p_0$ , unlike typically in the eikonal minijet models. Notice also that as we extend the value of  $p_0$  to unphysically low values (but still keeping it in the pQCD region,  $p_0 \gg \Lambda_{\text{QCD}}$ ), and since we are considering the earliest moments in the collision,  $\tau \lesssim 1/p_0$ , we do not include any soft particle production component, but consider only the (semi)hard

(mini)jet production in what follows.

## 2. Dijet kinematics and parton chemistry

A key element in our MC-EKRT framework is the differential LO pQCD cross section of hard parton production [88, 89]

$$\frac{d\sigma_{\text{jet}}^{ab}(\{\bar{s}_a\}, \{\bar{s}_b\})}{dp_T^2 dy_1 dy_2} = K \sum_{ij\langle kl \rangle} x_1 f_i^{a/A}(\{\bar{s}_a\}, x_1, Q^2) x_2 f_j^{b/B}(\{\bar{s}_b\}, x_2, Q^2) \frac{d\hat{\sigma}^{ij \rightarrow kl}}{d\hat{t}}(\hat{s}, \hat{t}, \hat{u}), \quad (25)$$

where  $y_1$  and  $y_2$  are the rapidities of the two final-state partons,  $p_T$  is the transverse momentum of each of them,  $f_i^{a/A}(\{\bar{s}_a\}, x_1, Q^2)$  ( $f_j^{b/B}(\{\bar{s}_b\}, x_2, Q^2)$ ) is the nucleon-configuration-specific PDF of a parton flavor  $i$  ( $j$ ) of the bound nucleon  $a \in A$  ( $b \in B$ ) which is centered at  $\bar{s}_a$  ( $\bar{s}_b$ ) in the nucleon configuration of each event, and  $x_1$  ( $x_2$ ) is the parton's longitudinal momentum fraction,  $Q^2$  is the factorization/renormalization scale which we set equal to  $p_T$ , and  $\frac{d\hat{\sigma}^{ij \rightarrow kl}}{d\hat{t}}$  are the differential LO pQCD cross sections, which depend on the parton-level Mandelstam variables  $\hat{s}$ ,  $\hat{t}$ , and  $\hat{u}$ . The notation  $\langle kl \rangle$  indicates a sum over pairs of final-state partons, so that, say,  $u_1 g_2 \rightarrow ug$  and  $u_1 g_2 \rightarrow gu$  are the same process and hence are not to be counted as two separate ones, whereas  $u_1 g_2 \rightarrow ug$  and  $g_1 u_2 \rightarrow ug$  naturally are two different processes as the initial-state partons originate from different nucleons. Notice also that since we aim to follow the partons' identities as well, we do not introduce any  $t, u$ -symmetrized cross sections which are often used when observable jet cross sections are studied. In the present exploratory study, in the interest of the simulation speed and as there anyways are various other uncertainties and scale dependence present, we do not (yet) attempt to perform an NLO calculation similar to that in [66, 67] but account

for the missing higher order terms simply by a  $K$ -factor that is a constant for a fixed  $\sqrt{s_{NN}}$  and that will be fitted to the  $A+A$  data separately at the LHC and at RHIC. Then, in LO, the momentum fractions can be expressed in terms of the transverse momentum  $p_T$  and rapidities of each minijet as

$$x_{1,2} = \frac{p_T}{\sqrt{s_{NN}}} (e^{\pm y_1} + e^{\pm y_2}), \quad (26)$$

and the Mandelstam variables become

$$\hat{s} = 2p_T^2 (1 + \cosh(y_1 - y_2)), \quad (27)$$

$$\hat{t} = -p_T^2 (1 + e^{-(y_1 - y_2)}), \quad (28)$$

$$\hat{u} = -p_T^2 (1 + e^{+(y_1 - y_2)}). \quad (29)$$

Once the spatially dependent nuclear PDFs (PDFs of nucleons  $a$  and  $b$ ) have been devised (see discussion below), Eq. (25) can be integrated over the momentum phase space, to give the minijet cross section  $\sigma_{\text{jet}}^{ab}(p_0, \sqrt{s_{NN}}, \{\bar{s}_a\}, \{\bar{s}_b\})$  which is employed in Eq. (11). Explicitly, accounting for the symmetry factors for the identical final-state partons, we have

$$\sigma_{\text{jet}}^{ab}(p_0, \sqrt{s_{NN}}, \{\bar{s}_a\}, \{\bar{s}_b\}) = K \int dp_T^2 dy_1 dy_2 \sum_{ij\langle kl \rangle} \frac{1}{1 + \delta_{kl}} x_1 f_i^{a/A}(\{\bar{s}_a\}, x_1, Q^2) x_2 f_j^{b/B}(\{\bar{s}_b\}, x_2, Q^2) \frac{d\hat{\sigma}^{ij \rightarrow kl}}{d\hat{t}}(\hat{s}, \hat{t}, \hat{u}), \quad (30)$$

where, assuming a fixed lower limit  $p_0 = 1$  GeV for  $p_T$ , the integration limits become

$$p_0 \leq p_T \leq \sqrt{s_{NN}}/2, \quad |y_1| \leq \text{arcosh}(1/x_T), \quad (31)$$

$$-\log(2/x_T - e^{-y_1}) \leq y_2 \leq \log(2/x_T - e^{y_1}), \quad (32)$$

with  $x_T = 2p_T/\sqrt{s_{NN}}$ .

With these elements, the dijet kinematics and parton chemistry can be straightforwardly generated. Once the number of independent dijets from an interaction of nucleons  $a \in A$  and  $b \in B$  has been determined using the

Poissonian probabilities of Eq. (11), the transverse momentum  $p_T$  and rapidities  $y_1, y_2$  of each (mini)jet in the dijet are obtained with rejection sampling from the differential minijet cross section (integrand) of Eq. (30). With the fixed kinematic variables, we then sample Eq. (30) again for the parton process type that fixes the flavors of the participating partons. If the parton process involves a quark from either  $a$  or  $b$ , we also identify each participating quark as a sea quark or as a valence quark again on the basis of Eq. (30) (i.e. the PDFs, in this case,  $(f_q^{a/A} - f_q^{a/A})/f_q^{a/A}$  being the probability for obtaining a valence quark). Finally, one minijet in each dijet is assigned an azimuth angle  $\phi$  from a flat distribution and its partner is then an angle  $\pi$  apart in the  $2 \rightarrow 2$  kinematics assumed here.

### 3. EbyE fluctuating spatial nuclear PDFs

Systematic global analyses of collinearly factorized nuclear PDFs (nPDFs) indicate that bound-nucleon PDFs clearly differ from the free-proton PDFs, see e.g. Refs. [90–95]. The resulting nuclear modifications in the bound-proton PDFs  $f_i^{p/A}$  can be quantified with

$$f_i^{p/A}(x, Q^2) = R_i^{p/A}(x, Q^2) f_i^p(x, Q^2), \quad (33)$$

where  $i$  denotes the parton flavor,  $f_i^p$  is the free-proton PDF and  $R_i^{p/A}$  is the nuclear modification. The corresponding neutron PDFs are obtained using isospin symmetry. The above PDFs and their modifications are, however, *spatial averages* of the nPDFs, they do not account for the dependence of the nuclear density and especially not its fluctuations, i.e. for the fact that in the lowest-density regions the nuclear effects should vanish whereas in the high-density regions they should be larger than in the average  $R_i^{p/A}$ . These spatial effects can become significant especially in the small- $x$  region relevant for lowest- $p_T$  minijet production of interest here, hence they are an important contributing factor in computing hydrodynamic initial density profiles that directly influence the centrality dependence of observables like multiplicities and flow coefficients. Therefore, in an EbyE simulation such as MC-EKRT here, we cannot use the spatially averaged nPDFs but need to introduce *EbyE-fluctuating* spatially dependent nPDFs (snPDFs), where the nuclear modifications are sensitive to the nucleon-density fluctuations from event to event. As we will discuss below, this turns out to be a non-trivial problem in an EbyE simulation where there are large density fluctuations present.

Originally, our idea was to directly utilize the available non-fluctuating snPDFs, such as EPS09s [71], where the nuclear modifications are encoded in as a power series of the average (optical Glauber) nuclear thickness function,  $T_A^{\text{WS}}(\bar{s}) = \int dz \rho_{\text{WS}}(\mathbf{x})$ , as follows:

$$f_i^{p/A}(\bar{s}, x, Q^2) = f_i^p(x, Q^2) r_i^{p/A}(\bar{s}, x, Q^2), \quad (34)$$

where  $f_i^p$  again are the free-proton PDFs, and the nuclear modification part,

$$r_i^{p/A}(\bar{s}, x, Q^2) = 1 + \sum_{n=1}^4 c_n^i(x, Q^2) [T_A^{\text{WS}}(\bar{s})]^n, \quad (35)$$

where the coefficients  $c_n^i$  are  $A$ -independent, is normalized to the known (EPS09 [90]) average nuclear modifications,

$$R_i^{p/A}(x, Q^2) = \frac{1}{A} \int d^2s T_A^{\text{WS}}(\bar{s}) r_i^{p/A}(\bar{s}, x, Q^2). \quad (36)$$

Alternatively, as done e.g. in Refs. [96–98], one could in the interest of the simulation speed truncate the above power series at the second term, allow some residual  $A$  dependence in the remaining single coefficient, and obtain

$$f_i^{p/A}(\bar{s}, x, Q^2) = f_i^p(x, Q^2) [1 + c_A^i(x, Q^2) T_A^{\text{WS}}(\bar{s})], \quad (37)$$

where again the normalization to the average modifications  $R_i^{p/A}(x, Q^2)$  would give

$$c_A^i(x, Q^2) = \frac{A}{T_{AA}(0)} \left( R_i^{p/A}(x, Q^2) - 1 \right), \quad (38)$$

with  $T_{AA}(0) = \int d^2s [T_A^{\text{WS}}(\bar{s})]^2$ . Then, with the nuclear density fluctuations present in an EbyE simulation, one could essentially just replace the average  $T_A^{\text{WS}}$  by the fluctuating  $T_A(\bar{s}) = \sum_a T_N(\bar{s} - \bar{s}_a)$ , where  $T_N$  is the Gaussian density from Eq. (23). This procedure does *not*, however, work, because in practice the maximal density at which the above approaches are applicable is the maximum of the average density [61],  $T_A^{\text{WS}}(0) = 2\rho_0 d \log(1 + e^{R_A/d})$ , and now with fluctuations we encounter densities that easily exceed this (see Fig. 2 ahead), and can be even more than  $3T_A^{\text{WS}}(0)$ .

In particular with the latter approach above, in the small- $x$  nuclear shadowing region, where  $R_i^{p/A}(x, Q^2) < 1$  and thus  $c_A^i(x, Q^2) < 0$ , when a negative  $c_A^i$  is accompanied by a large enough  $T_A(\bar{s})$ , the spatial PDFs become negative, which cannot be allowed in LO. A possible cure for this could be to introduce an exponentiated ansatz for the above power series (motivated by Ref. [99]),

$$1 + c_A^i(x, Q^2) T_A(\bar{s}) \rightarrow \exp(c_A^i(x, Q^2) T_A(\bar{s})). \quad (39)$$

However, with density fluctuations, in the region where  $T_A(\bar{s}) \gg T_A^{\text{WS}}(0)$ , also this form leads to too fast attenuating small- $x$  parton densities in that the density function  $T_A(\bar{s}) \exp(c_A^i(x, Q^2) T_A(\bar{s}))$  (whose  $\bar{s}$ -integral is normalized to  $R_i^{p/A}(x, Q^2)$ ), is not a monotonically rising function of  $T_A(\bar{s})$  contrary to what it should be. This problem can be solved by using an another ansatz function, such as

$$1 + c_A^i(x, Q^2) T_A(\bar{s}) \rightarrow 1/(1 - c_A^i(x, Q^2) T_A(\bar{s})) \quad (40)$$

instead, which, when multiplied by  $T_A(\bar{s})$ , conveniently gives a positive-definite function that is monotonously rising with  $T_A(\bar{s})$ . In the antishadowing region where  $c_A^i(x, Q^2) > 0$ , and where the  $A$ -dependence of the nuclear modification is modest in any case, such a function would at large  $T_A$ 's lead to violation of the per-nucleon momentum sum rule that is assumed in the global PDF analyses. We have tested that this problem can be solved approximately (conserving momentum on a percent level) by choosing a more modestly increasing logarithmic function

$$1 + c_A^i(x, Q^2)T_A(\bar{s}) \rightarrow 1 + \log(1 + c_A^i(x, Q^2)T_A(\bar{s})). \quad (41)$$

Equations (40) and (41) above are therefore the functional choices we make in what follows.

Now, exploiting these preliminary observations, we can construct the needed snPDFs,  $f_i^{a/A}(\{\bar{s}_a\}, x_1, Q^2)$ , which are sensitive to the location  $\bar{s}_a$  of the nucleon  $a$  in the nucleus  $A$ , and thereby also to the surrounding nucleon density in each event (indicated by  $\{\bar{s}_a\}$ ), but which do *not* depend on the intra-nucleon density  $T_N(\bar{s})$  of the nucleon  $a$  or its fluctuations. This is the approximation which we have used in writing Eq. (13) in its form, where the minijet cross section depends spatially only on the locations of the nucleons  $a$  and  $b$  but does not contain any transverse-coordinate integrals.

First, for each fixed nucleon configuration in the nucleus  $A$  (correspondingly for  $B$ ), we define a nuclear thickness function  $T_A^a$  from where the contribution from

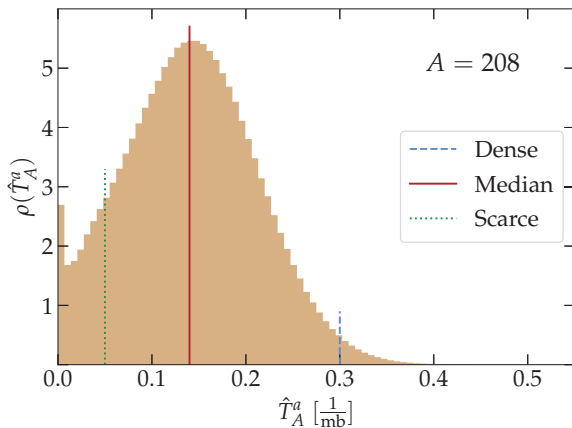


FIG. 2: Normalized distribution of the average nuclear thickness function  $\hat{T}_A^a$  experienced by a nucleon  $a \in A$ , defined in Eq. (45), for the nucleus  $\text{Pb}^{208}$ , sampled from 10 000 nuclei. For comparison, optical Glauber  $T_A^{\text{WS}}(0) \approx 0.212/\text{mb}$ . The vertical lines indicate the example-density regions to which we refer as “dense” (dashed blue line), “median” (solid red line) and “scarce” (dotted green line). The peak at the smallest values of  $\hat{T}_A^a$  arises at the edge of the nucleus where the inter-nucleon distance becomes larger than the nucleonic width  $\sigma_N$ .

the nucleon  $a$ , whose center is at  $\bar{s}_a$ , has been excluded,

$$T_A^a(\bar{s}) \equiv \sum_{a' \neq a}^A T_N^{a'}(\bar{s} - \bar{s}_{a'}). \quad (42)$$

Then the average nuclear thickness function experienced by the nucleon  $a \in A$  can be defined as

$$\hat{T}_A^a(\{\bar{s}_a\}) \equiv \frac{\int d^2\bar{s} T_N(\bar{s} - \bar{s}_a) T_A^a(\bar{s})}{\int d^2\bar{s} T_N(\bar{s} - \bar{s}_a)} \quad (43)$$

$$= \sum_{a' \neq a}^A \int d^2\bar{s} T_N(\bar{s} - \bar{s}_a) T_N^{a'}(\bar{s} - \bar{s}_{a'}) \quad (44)$$

$$= \sum_{a' \neq a}^A T_{NN}^{aa'}(\bar{b}_{aa'}), \quad (45)$$

where we have used the normalization of  $T_N^a$  and Eqs. (42) and (15) with  $\bar{b}_{aa'} = \bar{s}_a - \bar{s}_{a'}$ , and where the overlap functions  $T_{NN}^{aa'}(\bar{b}_{aa'})$  are of the same Gaussian form as that in Eq. (24). Two things are to be noted here: First, for a specific nucleon  $a$  in a nucleus  $A$  with a fixed (random) nucleon configuration,  $\hat{T}_A^a(\{\bar{s}_a\})$  is a fixed number, whose value depends on the positions of the other nucleons ( $a'$ ) relative to the nucleon  $a$ . Second, the effect of the above self-exclusion is that in the region of very low nucleon density, which is the case in an event where a single nucleon  $a$  is far from other nucleons  $a'$ , the density  $T_N(\bar{s} - \bar{s}_{a'})$  vanishes, bringing thus also  $\hat{T}_A^a$  appropriately to zero. The distribution of  $\hat{T}_A^a$  for a lead nucleus is shown in Fig. 2.

Now, essentially using  $\hat{T}_A^a$  in place of  $T_A^{\text{WS}}$ , we define the EbyE fluctuating snPDFs for a nucleon  $a$  analogously to the above discussion, as follows:

$$f_i^{a/A}(\{\bar{s}_a\}, x, Q^2) = f_i^a(x, Q^2) r_i^{a/A}(\{\bar{s}_a\}, x, Q^2), \quad (46)$$

where  $\bar{s}_a$  is the location of the nucleon  $a \in A$ , which is fixed for each nucleon configuration (i.e., in each event), and the nuclear modification is

$$r_i^{a/A}(\{\bar{s}_a\}, x, Q^2) = \theta(c_A^i(x, Q^2)) \left[ 1 + \log(1 + c_A^i(x, Q^2) \hat{T}_A^a(\{\bar{s}_a\})) \right] + \frac{\theta(-c_A^i(x, Q^2))}{1 - c_A^i(x, Q^2) \hat{T}_A^a(\{\bar{s}_a\})}, \quad (47)$$

where  $\theta$  is the Heaviside step function. Because of the reasons discussed above, we have chosen the above functional forms for ensuring an appropriate behaviour of the modifications in  $\hat{T}_A^a$ , accurate enough momentum conservation, and a correct small- $\hat{T}_A^a$  limit. As explained above, at the limit of vanishing nucleon density, i.e. if  $a$  is an isolated single nucleon far away from other nucleons,  $\hat{T}_A^a \rightarrow 0$  and thus also  $r_i^{a/A}(\{\bar{s}_a\}, x, Q^2) \rightarrow 1$ .

The coefficient function  $c_A^i(x, Q^2)$  in Eq. (47) is determined for fixed  $x$  and  $Q^2$  by requiring that the average modification, which is obtained by averaging first over all the nucleons  $a$  in each nucleus and then averaging over a large sample of nuclei  $A$ , becomes  $R_i^{p/A}(x, Q^2)$  of Eq. (33),

$$R_i^{p/A}(x, Q^2) = \left\langle \frac{1}{A} \sum_a r_i^{a/A}(\{\bar{s}_a\}, x, Q^2) \right\rangle_{\{A\}} \quad (48)$$

$$\equiv F(c_A^i(x, Q^2)), \quad (49)$$

where  $\langle \dots \rangle_{\{A\}}$  denotes the latter average. Note that here for each parton flavor  $i$  we are summing the modifications  $r_i^{a/A}$  that are related to the bound proton's  $R_i^{p/A}$  (e.g. related to  $R_{uv}^{p/A}$  we sum  $r_{uv}^{p/A}$  from  $Z$  protons and  $r_{d\nu}^{n/A} = r_{u\nu}^{p/A}$  from  $A - Z$  neutrons). Since we assume isospin symmetry and as the locations of the protons and neutrons are sampled from the same Woods-Saxon distribution, we do not need to keep track of the nucleon identity here but can take all nucleons to be just protons. The function  $F(c_A^i)$  is a monotonous function of  $c_A^i$ , so it can be inverted to yield the normalization function

$$c_A^i(x, Q^2) = F^{-1} \left( R_i^{p/A}(x, Q^2) \right). \quad (50)$$

The function  $F$  can be calculated numerically for any given  $c_A^i$  by sampling a large number of nuclei  $A$ . The inverse can then be approximated by creating an interpolation function for a list of numerically calculated values of  $F(c_A^i(x, Q^2))$ , and then inverting that interpolation function. In what follows, in computing the nucleon-configuration-specific PDFs  $f_i^{a/A}(\{\bar{s}_a\}, x, Q^2)$  in Eq. (46), we obtain the coefficients  $c_A^i(x, Q^2)$  in Eq. (50) using the EPS09LO average modifications [90], and the free-proton PDFs correspondingly from the CT14LO set [100] using the LHAPDF library [101].

In Fig. 3 we compare the spatially dependent, nucleon-configuration-specific gluon modifications  $r_g^{a/A}(\{\bar{s}_a\}, x, Q^2)$ , computed from Eq. (47), with the average nuclear gluon modifications  $R_g^A(x, Q^2)$ , obtained from the EPS09LO nPDFs, for a lead nucleus at a

scale  $Q^2 = 1.69 \text{ GeV}^2$ . To illustrate how in the densest (scarcest) regions the nuclear effects become larger (smaller) than in the average modification  $R_g^A(x, Q^2)$ , we show the snPDF gluon modifications for three different fixed values of the average thickness function  $\hat{T}_A^a(\bar{s}_a)$ .

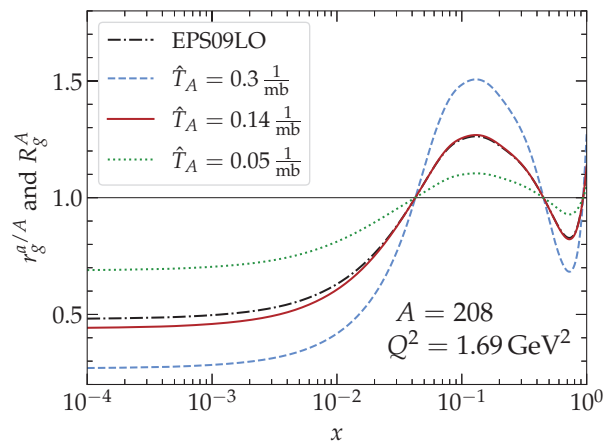


FIG. 3: Comparison of the snPDF gluon modification  $r_g^{a/A}(\{\bar{s}_a\}, x, Q^2 = 1.69 \text{ GeV}^2)$  of Eq. (47) (dashed blue, solid red and dotted green curves) with the average EPS09LO [90] gluon modification  $R_g^A(x, Q^2 = 1.69 \text{ GeV}^2)$  (dashed-dotted black curve) for the nucleus  $\text{Pb}^{208}$ . The fixed values  $\hat{T}_A^a(\{\bar{s}_a\}) = 0.3, 0.14,$  and  $0.05 \text{ 1/mb}$ , chosen here as input for  $r_g(\{\bar{s}_a\}, x, Q^2 = 1.69 \text{ GeV}^2)$ , are representatives for a nucleon in the dense, median, and scarce density regions, correspondingly, see Fig. 2.

We have now discussed the elements necessary for obtaining the nucleon-nucleon overlap function  $T_{NN}(\bar{b}_{ab})$  and the integrated minijet cross section  $\sigma_{\text{jet}}^{ab}(\{\bar{s}_a\}, \{\bar{s}_b\}, p_0, \sqrt{s_{NN}})$  that go into the calculation of the probability distributions of multiple minijet production in nucleon-nucleon collisions in Eq. (11). Figure 4 shows examples of these distributions in Pb+Pb collisions at  $\sqrt{s_{NN}} = 5.02 \text{ TeV}$  and  $p_0 = 1 \text{ GeV}$  at three different nucleon-nucleon impact parameters  $\bar{b}_{ab}$ , and choosing both nucleons,  $a \in A$  and  $b \in B$ , from the same densest, scarcest and median density regions of  $A$  and  $B$  as in Fig. 3,  $\hat{T}_A^a(\bar{s}_a) = \hat{T}_B^b(\bar{s}_b) = 0.3, 0.05,$  and  $0.14 \text{ 1/mb}$ . The figure nicely illustrates the large fluctuations of the minijet multiplicity due to various sources. The minijet multiplicity is heavily sensitive not only to the nucleon-nucleon impact parameter  $\bar{b}_{ab}$  (the larger  $\bar{b}_{ab}$  the smaller  $\bar{N}_{\text{jets}}^{ab}$ ) but also to the spatial dependence of the



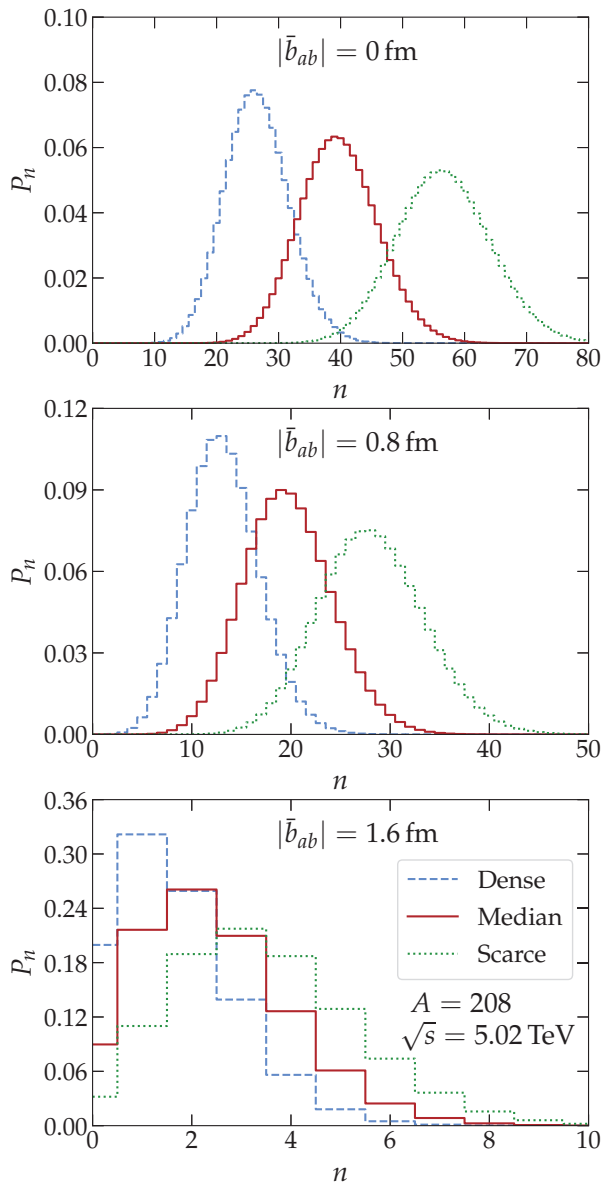


FIG. 4: Examples of the Poissonian probability distributions  $P_n$  of Eq. (11) for multiple candidate-dijet production with partonic  $p_T \geq 1$  GeV from a nucleon pair  $ab$ ,  $a \in A$  and  $b \in B$ , at some fixed nucleon-nucleon impact parameters  $\bar{b}_{ab}$  in Pb+Pb collisions at  $\sqrt{s_{NN}} = 5.02$  TeV. The values used for  $\sigma_{\text{jet}}^{ab}$  (with  $K = 2$ ) here are chosen so that they represent the cases where both of the nucleons originate from the same dense (dashed blue curves), median (solid red curves) and scarcest (dotted green curves) density regions as in Fig. 3.

nPDFs (large fluctuations at fixed  $\bar{b}_{ab}$ ). We also see the role of shadowing and its spatial dependence, in that the colliding nucleons that come from the densest (scarcest)

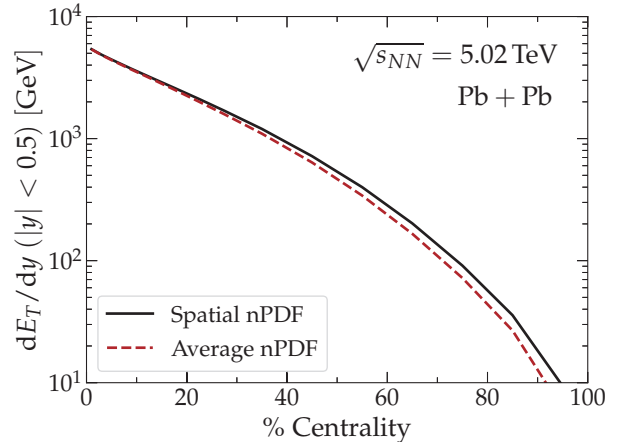


FIG. 5: Minijet transverse energy in the mid-rapidity unit as a function of the collision centrality in  $\sqrt{s_{NN}} = 5.02$  TeV Pb+Pb collisions, as predicted from the MC-EKRT model using snPDFs (solid lines) and spatially averaged nPDFs (dashed lines). Here  $K = 2$  and  $\kappa_{\text{sat}} = 2$ , see Sec. II E for the details of minijet filtering and Sec. II F for the details of the centrality selection.

nuclear density regions produce clearly less (more) dijet multiplicity than those who originate from the median-density regions.

In Fig. 5, we show the centrality dependence of the produced minijet transverse energy at mid-rapidity that is obtained from our MC-EKRT model with snPDFs and with average nPDFs. The figure very clearly demonstrates why it is important to account for the spatial dependence of the nPDFs (the details of the centrality selection and the imposed minijet filtering will be discussed below). As can be seen in the figure, in central collisions, where the minijet production on the average originates from the average nuclear-overlap regions (volume effect), the spatial nuclear effects due to the snPDFs average essentially to those obtained with spatially averaged nPDFs. Towards peripheral collisions, however, where scarcer regions of the nuclei are colliding and where the nuclear effects in the snPDFs become smaller, the difference to the average-nPDF results becomes increasingly larger. As the figure shows, we can expect easily over 20% changes relative to the average-nPDF results, which is a significant effect when we compare the MC-EKRT results (after hydrodynamic evolution) with experimental data (Sec. IV ahead).

#### E. Minijet filtering by saturation and conservation of energy & valence quark number

After the dijet candidates have been generated from all the nucleon-nucleon pairs as described in Sec. II D, the next step in the MC-EKRT simulation is to filter away

the excessive dijets on the basis of saturation, and conservation of energy/momentum and valence-quark numbers. Ideally of course the energy/momentum conservation should not be needed at all, as ideal multiparton distributions should conserve momentum, but as these are not available, and especially not to all orders as would be required here in the context of saturation, we have to impose energy/momentum conservation separately from the saturation. As we assume saturation to be the decisive dynamical mechanism that regulates minijet production at low transverse momenta, saturation-based filtering is done first, and conservation of momentum only after that. With such phenomenological details, experimental data is our guide as well: we have tested, averaging over the minijets falling into the mid-rapidity unit and feeding them into 2+1 D hydrodynamics event-by-event, that we reproduce systematically more correctly the measured ratio of the flow coefficients  $v_2$  and  $v_3$  [102] when the energy/momentum-conservation filtering is performed after the saturation-filtering and also when the latter filtering has as little effect as possible.

As is obvious, any kind of filtering breaks the factorization assumption of our pQCD calculation as the produced minijets are then not anymore independent of each other. The higher-twist effects (causing saturation here) die out in inverse powers of the virtuality  $Q^2$ , so that at the highest values of  $p_T$ , factorization is expected to hold. Also the global analysis of nPDFs [92, 94, 95] and jet production in minimum-bias proton-nucleus collisions [103] indicate this to be the case. Thus, to maintain factorization at the highest values of  $p_T$ , the list of all candidate dijets in an  $A+B$  collision is next ordered in decreasing  $p_T$ . Both filterings are then done, separately, in this order, starting from the jets with highest values of  $p_T$ , and rejecting all those dijets that fulfill the filtering conditions.

Guided by the geometric EKRT saturation criterion, Eq. (5), each dijet is assumed to have a spatial uncertainty area of a radius  $\propto 1/p_T$  in the transverse plane around the dijet production point. Consider a dijet candidate whose transverse momentum is  $p_T^{\text{cand}}$ , and transverse production point is  $\bar{s}^{\text{cand}}$ . All of the previously accepted dijets with corresponding parameters  $p_T \geq p_T^{\text{cand}}$  and  $\bar{s}$  are then inspected, and if for any of them

$$|\bar{s} - \bar{s}^{\text{cand}}| < \frac{1}{\kappa_{\text{sat}}} \left( \frac{1}{p_T} + \frac{1}{p_T^{\text{cand}}} \right), \quad (51)$$

the dijet candidate is rejected. The parameter  $\kappa_{\text{sat}}$  introduced here is an external fit parameter, which acts as a ‘‘packing factor’’ in determining how close to each other the dijets can be produced. Notice that parametrically  $\kappa_{\text{sat}}^2 \propto K_{\text{sat}}$  of Ref. [17], and that the smaller  $\kappa_{\text{sat}}$  the stronger the saturation, i.e. the more dijet candidates get rejected.

After the saturation filtering above, the remaining, still  $p_T$ -ordered, list of accepted dijets is then subjected to the filtering according to energy/momentum conservation. Again here it is not obvious, or even clear, whether

the momentum should be conserved for each nucleon separately, or only for the whole nucleus as a parton cloud, or something in between. Here, to be consistent with what is typically done in the global analyses of the nPDFs, we require energy conservation at the nucleon level as a default. We do, however, test also the case where no separate energy/momentum conservation is required in addition to saturation.

To force the energy/momentum conservation (energy conservation, for short) per nucleon for a given dijet candidate with momentum fractions  $x_1^{\text{cand}}$  in a projectile nucleon  $a \in A$  and  $x_2^{\text{cand}}$  in a target nucleon  $b \in B$ , we proceed as follows: Assume that we have a list of  $n$  already accepted dijets that involve the same projectile nucleon  $a$ , and  $m$  previously accepted dijets that involve the same target nucleon  $b$ . These dijets have momentum fractions  $(x_1^{(1)}, \dots, x_1^{(n)})_a$  and  $(x_2^{(1)}, \dots, x_2^{(m)})_b$  associated with  $a$  and  $b$ , respectively. Now, if either

$$x_1^{\text{cand}} + \sum_{i=1}^n x_1^{(i)} > 1 \quad \text{or} \quad x_2^{\text{cand}} + \sum_{j=1}^m x_2^{(j)} > 1, \quad (52)$$

the dijet candidate is rejected due to the breaking of the per-nucleon energy budget.

The third filtering, performed simultaneously with the above energy conservation, is the forcing of the valence quark number conservation. As explained earlier in Sec. IID 2, we can keep track of whether each candidate dijet involves valence quarks from the nucleons  $a \in A$  and/or  $b \in B$ . If a candidate dijet involves a valence quark of a specific flavor either from  $a$  or from  $b$ , and if either  $a$  or  $b$  has already consumed all its valence quarks of that flavor in the prior parton scatterings at  $p_T > p_T^{\text{cand}}$ , then the candidate dijet is rejected. For the multiplicities and elliptic flow that we will study later in this paper, this filtering causes a negligible effect but we nevertheless build it in for interesting further studies in the future.

As an illustration, in Fig. 6 we show the transverse-plane distribution of dijet production points before and after the filterings in a single central event. The radius of each disk surrounding the production points is  $1/(\kappa_{\text{sat}} p_T)$ . As seen in the left panel, the candidate dijets overoccupy the transverse plane. As a result of applying the saturation condition of Eq. (51), none of the disks overlap in the right panel.

## F. Centrality selection

To determine which centrality percentile each  $A+B$  collision belongs to, one needs to classify the events according to, e.g., the produced minijet transverse energy  $E_T$  in a chosen rapidity window. Alternatively, when running hydrodynamics with the minijet initial conditions, converting  $E_T$  into initial state densities, one can use either initial state entropy or final state multiplicity as the criterion. In this work, in the interest of simulation speed, we do the centrality selection according to the

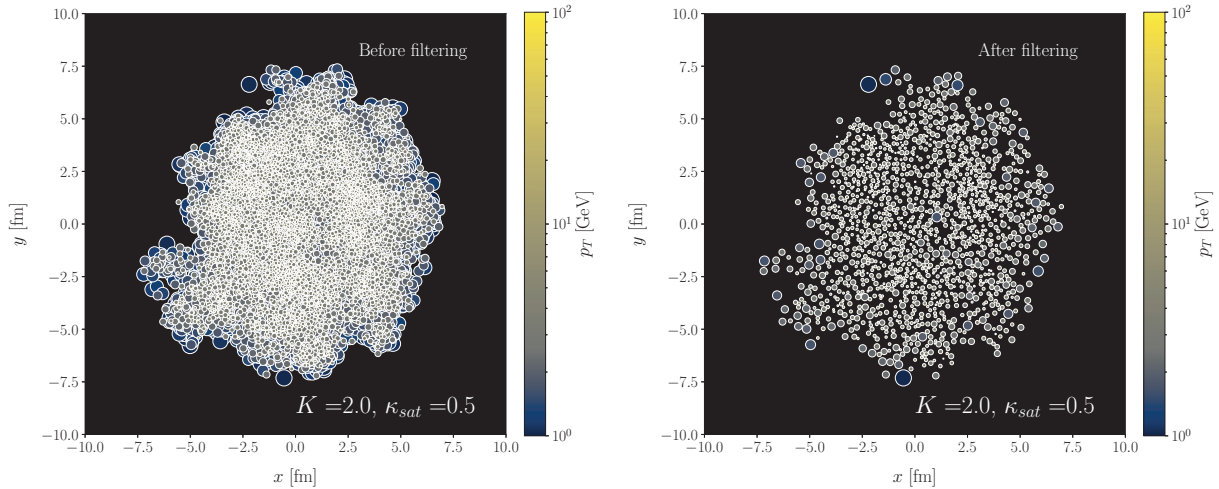


FIG. 6: Illustration of the effects of saturation and energy-conservation in the transverse distribution of produced dijets in one central event. Left panel shows the production points of all the candidate dijets, and the right panel the case after the filterings. The radius of the disk surrounding each dijet production point is  $1/(\kappa_{\text{sat}} p_T)$ . Here for the illustration, we use  $K = 2$ , and  $\kappa_{\text{sat}} = 0.5$ .

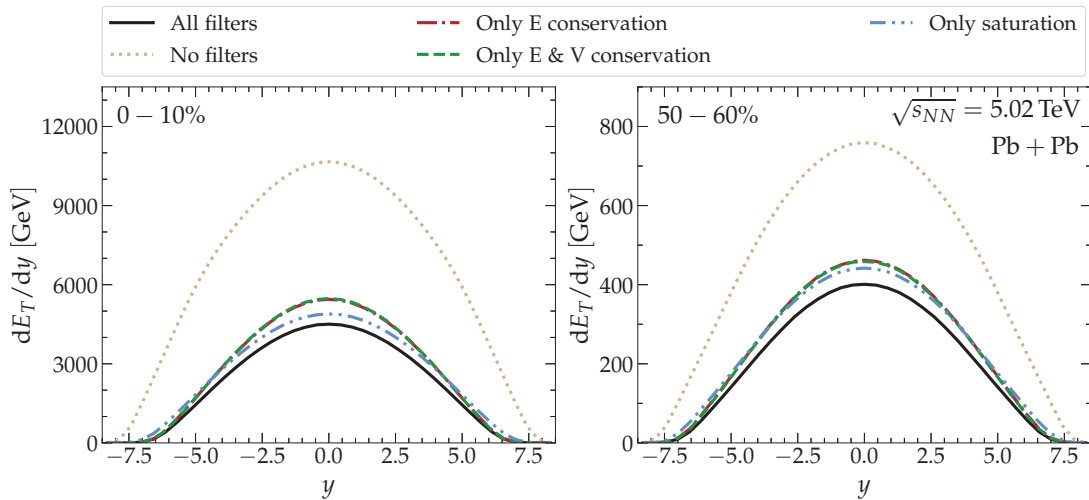


FIG. 7: The effects of the EKRT saturation, energy-conservation and valence-quark number conservation filters to the production of minijet transverse energy  $dE_T/dy$ , as a function of rapidity  $y$ , in central (left panel) and peripheral Pb+Pb collisions (right panel) at  $\sqrt{s_{NN}} = 5.02$  TeV. Here  $K = 2$  and  $\kappa_{\text{sat}} = 2$ .

total minijet  $E_T$  produced (after the filterings) anywhere in rapidity. We have checked that the results would be very similar if e.g. a central rapidity unit would be used. Concretely then, for a simulation of, say, 10 000  $A+B$  collisions, the 0-5 % centrality class refers to the collection of 500 collisions with the highest total transverse energy.

### G. Systematics of minijet filtering

Figures 7 and 8 illustrate the effect of the three filters. Figure 7 shows the rapidity distribution of the transverse energy originating from the dijets, obtained as a scalar sum of minijet  $p_T$ 's, plotted for 0-10 % central (left panel) and 50-60 % central (right panel) Pb+Pb collisions at  $\sqrt{s_{NN}} = 5.02$  TeV, computed with  $K = 2$ , and  $\kappa_{\text{sat}} = 2$ . The figure demonstrates first a considerable reduction of  $E_T$  when going from all the candidate



dijets (dotted brown curves) down to those who pass the saturation filter (dashed-double-dotted blue curves), and then a clearly smaller reduction down to those who pass also the energy-conservation and valence quark filters in addition (solid black curves). As expected, for this quantity the effect of the valence quark filtering is very small (see the overlapping dashed-dotted red and dashed green curves). Interestingly, however, we notice that imposing only the energy-conservation filter without saturation (dashed-dotted red curves) would lead to a similar result in  $E_T$  as the saturation filter alone, which essentially is a result of ordering the dijet candidates according to the minijet  $p_T$ . Here again, we note that although not visible in these plots, we have checked that the  $v_2/v_3$  ratio prefers a strongest possible saturation [102], and also that imposing only the energy-conservation filter (when realized as in here) typically leads to too narrow rapidity distributions.

Figure 8 then, correspondingly, shows the  $p_T$  distribution of (mini)jets at all rapidities, originating from the dijets which have not been filtered at all (dotted brown curves), from those dijets that survived first the saturation filter (dashed-double-dotted blue curves) and then also the energy-conservation and valence-quark filters (black solid curves). In the left panel, we see – as is expected by construction – how factorization in central collisions (upper set of curves) remains unbroken at  $p_T \gtrsim 5$  GeV, while both filters start to have an effect at  $p_T \lesssim 5$  GeV. In peripheral collisions (lower set of curves), where the minijet multiplicities are smaller and therefore saturation becomes effective at smaller  $p_T$ , factorization remains unbroken until slightly smaller values of  $p_T$  than in central collisions. We again also see how saturation filter, the one imposed first, dominates here over that of energy conservation, and also that the saturation filter tends to remove dijets at slightly larger values of  $p_T$  than the energy-conservation filter (see dashed-double-dotted blue and the dotted-dashed red curves). Also here the valence quark conservation causes a negligible effect. The right panel of Fig. 8 is to demonstrate the difference of (mini)jet production in different spatial regions of central collisions: In the dilute overlap regions (upper set of curves) the factorization-breaking saturation and energy-conservation effects set in at clearly smaller values of  $p_T$  than in the regions of densest overlap (lower set of curves).

Figures 9 and 10 show the minijet transverse energy production in the central rapidity unit as a function of centrality in Pb+Pb collisions at  $\sqrt{s_{NN}} = 5.02$  TeV, computed with various values of the fit parameters  $K$  and  $\kappa_{\text{sat}}$ , with all filters imposed in Fig. 9, and with only the saturation filter imposed Fig. 10. As can be seen from the right panels, where  $\kappa_{\text{sat}} = 2$  is fixed, changing  $K$  changes mainly the overall normalization but essentially not the centrality slope of the produced  $E_T$  (and hence the final multiplicities as well). The energy-conservation filter weakens the  $K$  dependence, because with a larger  $K$ -factor the energy-conservation filter removes more can-

didate dijets. The left panels in turn show how, for a fixed value of  $K = 2$ , changing  $\kappa_{\text{sat}}$  changes both the normalization and especially the centrality slope. Here the energy-conservation filter in turn weakens the  $\kappa_{\text{sat}}$  dependence, as with a larger  $\kappa_{\text{sat}}$  there is less saturation and more minijet production and the energy conservation filter becomes more efficient in removing candidate dijets. In any case, as long as  $\kappa_{\text{sat}}$  does not become too large, and especially if only the saturation-filter is imposed,  $\kappa_{\text{sat}}$  serves as a centrality-slope parameter for the mid-rapidity multiplicities, whereas the  $K$ -factor controls mainly their normalization. This observation is exploited in what follows (Sec. IV), in finding the possible values for  $\kappa_{\text{sat}}$  and  $K$  with which we can reproduce the measured charged-hadron multiplicities.

### III. FLUID DYNAMICAL EVOLUTION AND PARTICLE SPECTRA

The MC-EKRT computation gives the initially produced parton state. In order to compare with the measured data, we need to first propagate the partons to a proper time  $\tau_0$  for initializing the 3+1 D fluid dynamics, then compute the subsequent spacetime evolution of the matter, and eventually determine the experimentally measurable momentum spectra of hadrons.

#### A. Fluid dynamical framework

The spacetime evolution is computed using 3+1 D fluid dynamics, applying the code package developed in Ref. [73]. The fluid dynamical framework employed is the relativistic dissipative second-order transient fluid dynamics [104], originally formulated by Israel and Stewart [105].

The basic equations of motion governing the evolution of a fluid are the local conservation laws for energy, momentum and conserved charges, like the net-baryon number. In the following we, however, will neglect the conserved charges. In this case the state of the fluid is given by its energy-momentum tensor that can be decomposed with the help of the Landau-picture fluid 4-velocity  $u^\mu$  as

$$T^{\mu\nu} = eu^\mu u^\nu - P\Delta^{\mu\nu} + \pi^{\mu\nu}, \quad (53)$$

where  $\Delta^{\mu\nu} = g^{\mu\nu} - u^\mu u^\nu$  is a projection operator,  $e = T^{\mu\nu}u_\mu u_\nu$  is the energy density in the local rest frame,  $P = -\frac{1}{3}\Delta_{\mu\nu}T^{\mu\nu}$  is the isotropic pressure, and  $\pi^{\mu\nu} = T^{(\mu\nu)}$  is the shear-stress tensor. The angular brackets project the symmetric and traceless part of the energy-momentum tensor that is orthogonal to the fluid 4-velocity. We will also neglect the bulk viscous pressure, and the isotropic pressure is given by the equation of state (EoS) of the strongly interacting matter at zero net-baryon density,  $P = P(e)$ . In the Landau picture the

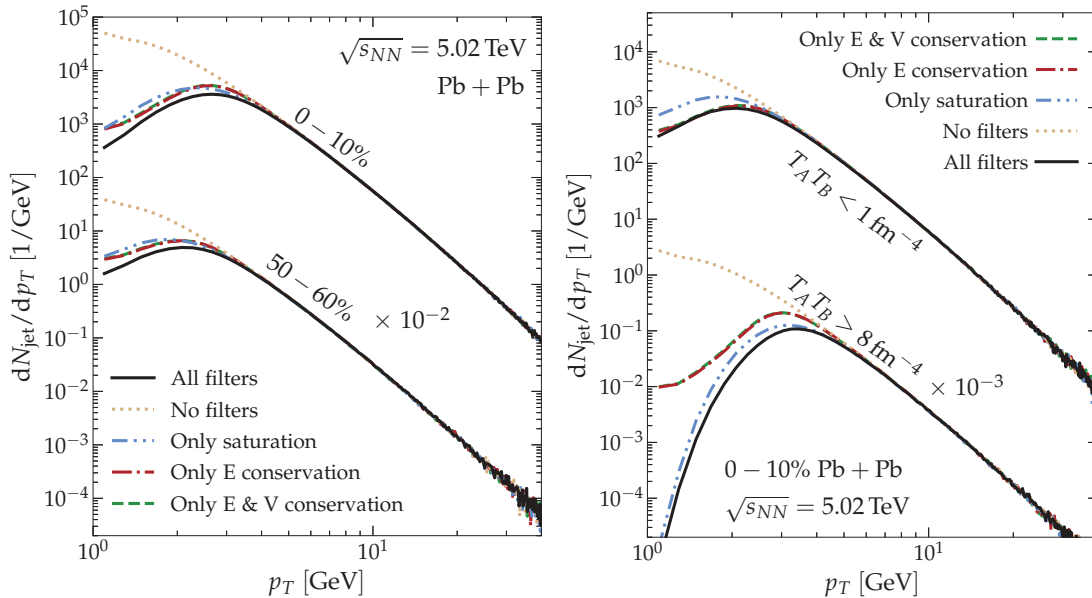


FIG. 8: The effects of the EKRT saturation and the energy- and valence-quark conservation filters to the transverse momentum distribution of produced (mini)jets in Pb+Pb collisions at  $\sqrt{s_{NN}} = 5.02$  TeV, in 0-10% and 50-60% centrality classes (left panel) and in the different overlap-density regions in the 0-10% central collisions (right panel). Here  $K = 2$  and  $\kappa_{\text{sat}} = 2$ . For the lower set of curves in both panels, notice the downward scalings by the factors indicated in the panels.

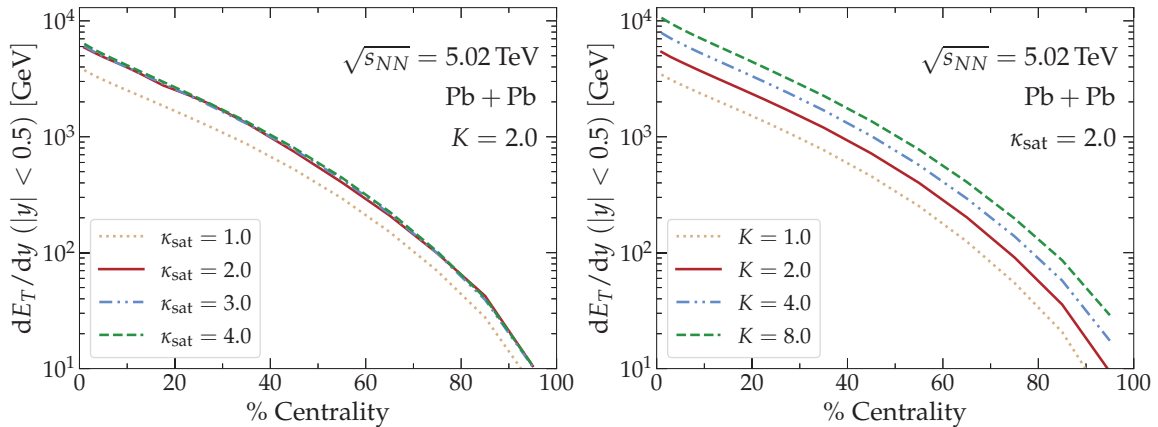


FIG. 9: Centrality dependence of minijet transverse energy in the mid-rapidity unit in Pb+Pb collisions at  $\sqrt{s_{NN}} = 5.02$  TeV, corresponding to one fixed value of  $K = 2$  and various values of  $\kappa_{\text{sat}}$  (left panel), and to one fixed value of  $\kappa_{\text{sat}} = 2$  and various values of  $K$  (right panel), with all filters imposed. The red solid curve is the same in both panels.

fluid 4-velocity is a time-like, normalized eigenvector of the energy-momentum tensor, defined by  $T^\mu_\nu u^\nu = e u^\mu$ . The energy diffusion current  $W^\mu = \Delta^{\mu\alpha} T_{\alpha\beta} u^\beta$  is then zero and does not contribute to the energy-momentum tensor.

In the formalism by Israel and Stewart [105], the equations of motion for the remaining dissipative quantity,

shear-stress tensor, are given by [104, 106]

$$\begin{aligned} \tau_\pi \frac{d}{d\tau} \pi^{\langle\mu\nu\rangle} + \pi^{\mu\nu} &= 2\eta\sigma^{\mu\nu} + 2\tau_\pi \pi_\alpha^{\langle\mu} \omega^{\nu\rangle\alpha} \\ -\delta_\pi \pi \pi^{\mu\nu} \theta - \tau_\pi \pi_\alpha^{\langle\mu} \sigma^{\nu\rangle\alpha} &+ \varphi_7 \pi_\alpha^{\langle\mu} \pi^{\nu\rangle\alpha}, \end{aligned} \quad (54)$$

where  $\sigma^{\mu\nu} = \nabla^{\langle\mu} u^{\nu\rangle}$  and  $\omega^{\mu\nu} = \frac{1}{2} (\nabla^\mu u^\nu - \nabla^\nu u^\mu)$  are the strain-rate and vorticity tensors, respectively,  $\theta = \nabla^\mu u_\mu$  is the volume expansion rate, and the gradient is

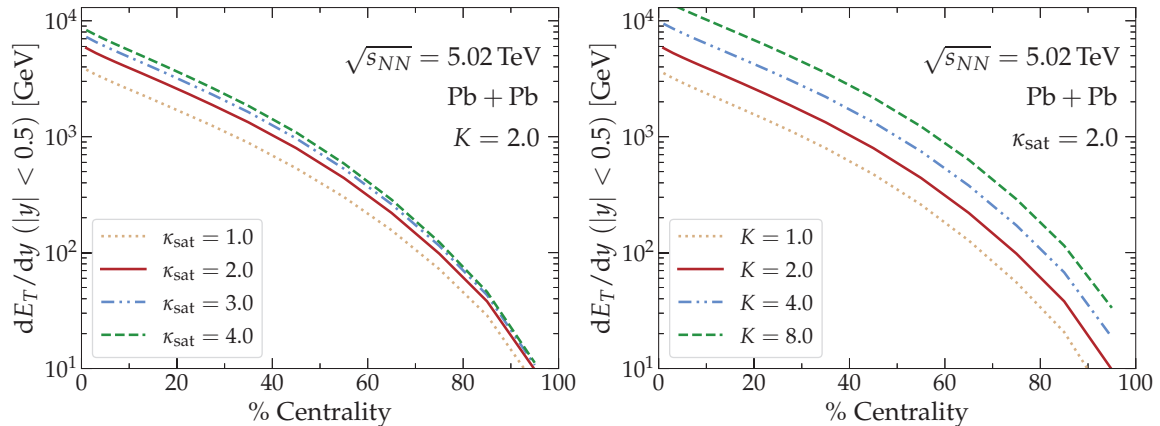


FIG. 10: The same as in Fig. 9 but with only the saturation filter imposed.

defined as  $\nabla^\mu = \Delta_\alpha^\mu \partial^\alpha$ . The coefficient  $\eta$  is the shear viscosity,  $\tau_\pi = 5\eta/(e + P)$  is the shear relaxation time, and the remaining coefficients of the second-order terms are taken from the 14-moment approximation to massless gas [104, 106, 107], i.e.  $\delta_{\pi\pi} = (4/3)\tau_\pi$ ,  $\tau_{\pi\pi} = (10/7)\tau_\pi$ , and  $\varphi_7 = 9/(70P)$ . The shear viscosity over entropy density  $\eta/s$  is chosen such that it roughly reproduces the elliptic flow in semi-central collisions. For the EoS of strongly interacting matter we use the *s95p-v1* [108] parametrization, which interpolates between the lattice QCD at high temperatures and the hadron resonance gas model at low temperatures. The partial chemical freeze-out at  $T = 150$  MeV is encoded into the hadronic part of the EoS as temperature-dependent chemical potentials for each hadron,  $\mu_h = \mu_h(T)$  [109].

The Israel-Stewart equations together with the conservation laws are solved numerically in 3+1 dimensions [73] using the SHASTA algorithm [110] in  $(\tau, x, y, \eta_s)$ -coordinates, where

$$\tau = \sqrt{t^2 - z^2} \quad (55)$$

is the longitudinal proper time, and

$$\eta_s = \frac{1}{2} \ln \left( \frac{t+z}{t-z} \right) \quad (56)$$

is the spacetime rapidity. The grid resolution is  $\Delta\eta_s = 0.15$ ,  $\Delta x = \Delta y = 0.15$  fm, and  $\Delta\tau = 0.05$  fm. For further details of the algorithm, see Refs. [73, 111].

The final spectra of free hadrons are obtained by computing the Cooper-Frye integrals [112] on a constant-temperature decoupling surface, with  $T_{\text{dec}} = 130$  MeV. The momentum distributions of hadrons on the decoupling surface are given by the 14-moment approximation, so that the single-particle momentum distribution function of a hadron  $h$  is

$$f_h(p^\mu, x) = f_{0h} \left( 1 + (1 \pm f_{0h}) \frac{p_\mu p_\nu \pi^{\mu\nu}}{2T^2(e + P)} \right), \quad (57)$$

where  $+$ ( $-$ ) is for bosons (fermions),  $p^\mu$  is the 4-momentum of a hadron  $h$ , and  $f_{0h} = f_{0h}(T, \mu_h)$  is the corresponding Bose-Einstein or Fermi-Dirac equilibrium distribution function. The Cooper-Frye integral is computed for all the hadrons included into the hadron resonance gas part of the EoS. As explained in Ref. [73], after computing the full spectra of hadrons,  $dN_h/dy dp_T^2 d\phi$ , the spectra are interpreted as probability densities and they are randomly sampled to obtain a set of hadrons with 4-momenta  $p_h^\mu$ . For the unstable hadrons the corresponding 2- and 3-particle strong and electromagnetic decays are then computed. The sampling procedure is then repeated several times in order to get smooth momentum distributions for the hadrons that are stable under strong decays.

## B. Initialization

The equations of fluid dynamics take the energy-momentum tensor as an initial condition at a fixed initial proper time  $\tau_0$ . However, an MC-EKRT event consists of a set of partons, and we need to convert this set to the corresponding  $T^{\mu\nu}(\tau_0, x, y, \eta_s)$  using the momenta of the produced particles. There are two essential ingredients in this. First, we need to propagate the particles to a fixed proper time  $\tau_0 = 1/p_0$ , and for the determination of densities from a finite set of particles, we need to define an averaging volume where the components of the energy-momentum tensor are computed.

Naively, the grid size, e.g.  $\Delta x$  or  $\Delta\eta_s$  in the numerical algorithm to solve the Israel-Stewart theory would provide such an averaging volume. However, the grid defines rather a discretization of the continuous fields in the hydrodynamic equations of motion, and in principle we should be able to take the limit to the continuum, i.e.  $\Delta x, \Delta\eta_s \rightarrow 0$ , and at this limit densities are no

longer well defined smooth functions. Thus, we should distinguish between the averaging volume and the numerical resolution. The procedure with which we define the averaging volume through Gaussian smearing and obtain the corresponding densities is described below. We note that here we will eventually only construct the local energy density from the MC-EKRT computation, and neglect the initial velocity and shear-stress components. Moreover, we do not take into account the event-by-event fluctuations in the hydrodynamical phase, but compute the initial conditions as averages over a large sample of MC-EKRT events. However, the procedure below can be extended to the computation of all the components of  $T^{\mu\nu}$ . We will leave the studies that take into account the event-by-event fluctuations as well as a complete  $T^{\mu\nu}$  initialization as a future work.

### 1. Free streaming

Each parton  $i$  in an MC-EKRT event has the following information: transverse coordinate  $\mathbf{x}_{\perp,0i}$  of the production point, transverse momentum  $\mathbf{p}_{Ti}$ , and rapidity  $y_i$ . All partons are massless in this work. We assume that each parton is produced at the location  $\mathbf{x}_{\perp,0i}$  and  $z_i = 0$  at time  $t = 0$ . The partons are assumed to travel as free particles along straight line trajectories. In this case, the spacetime rapidity  $\eta_{s,i}$  of the parton  $i$  becomes equivalent to its momentum rapidity  $y_i$ , and longitudinal coordinate of the propagating parton is given by  $z_i(t) = t \tanh \eta_{s,i}$ . The transverse position of the parton at Cartesian coordinate time  $t$  is given by  $\mathbf{x}_{\perp i}(t) = \mathbf{x}_{\perp,0i} + t\mathbf{p}_{Ti}/E_i$ , where  $E_i = p_{Ti} \cosh y_i$ . However, we need to initialize fluid dynamics at a fixed proper time  $\tau_0 = t/\cosh \eta_s$  in the  $\tau$ - $\eta_s$  coordinate system, in which case the parton's coordinates become  $(\tau_0, \mathbf{x}_{\perp i}(\tau_0), \eta_{s,i})$ , where  $\mathbf{x}_{\perp i}(\tau_0) = \mathbf{x}_{\perp,0i} + \tau_0\mathbf{p}_{Ti}/p_{Ti}$ .

### 2. Smearing

In general, the four-momentum  $p^\alpha = (p^\tau, \mathbf{p}_T, p^\eta)$  of a particle at a spacetime location  $x^\alpha = (\tau, \mathbf{x}_\perp, \eta_s)$  in the  $\tau$ - $\eta_s$  coordinates is obtained as

$$p^\alpha = \frac{\partial x^\alpha}{\partial x'^\mu} p'^\mu = \begin{pmatrix} p_T \cosh(y - \eta_s) \\ \mathbf{p}_T \\ \tau^{-1} p_T \sinh(y - \eta_s) \end{pmatrix}, \quad (58)$$

where  $x'^\mu$  and  $p'^\mu$  are the corresponding spacetime point and four-momentum in the Cartesian coordinates.

The total number of partons  $N$  that flow through a surface, whose surface element 4-vector is  $d\Sigma_\mu$ , can be written as

$$N = \int d\Sigma_\alpha N^\alpha(\tau, \mathbf{x}_\perp, \eta_s), \quad (59)$$

where the particle 4-current  $N^\alpha$  in the  $\tau$ - $\eta_s$  coordinates can be written using Eq. (58) as

$$N^\alpha(\tau, \mathbf{x}_\perp, \eta_s) = \int \frac{d^3p}{p^\tau} \tau p^\alpha f(\tau, \mathbf{x}, \mathbf{p}), \quad (60)$$

where we defined  $d^3p = d^2\mathbf{p}_T dp^\eta$ , and  $f$  is a scalar momentum distribution function at a constant  $\tau$ . For a constant- $\tau$  surface, the surface element 4-vector has only the  $\tau$  component,  $d\Sigma_\tau = d^2\mathbf{x}_\perp d\eta_s \tau$ , and the total number of partons can be written as

$$N = \int d^2\mathbf{x}_\perp d\eta_s \tau \int d^2\mathbf{p}_T dp^\eta \tau f(\tau, \mathbf{x}, \mathbf{p}). \quad (61)$$

Now, following Ref. [113], the scalar momentum distribution function for a set of  $N$  partons can be written in terms of delta functions in coordinate and momentum space as

$$f(\tau, \mathbf{x}, \mathbf{p}) = \sum_{i=1}^N \delta^{(3)}(\mathbf{x} - \mathbf{x}_i) \delta^{(3)}(\mathbf{p} - \mathbf{p}_i) / |\det(g)|, \quad (62)$$

where  $\mathbf{x}_i = (\mathbf{x}_{\perp i}, \eta_{s,i})$  is the three-location and  $\mathbf{p}_i = (p_{Ti}, p_i^\eta)$  is the three-momentum of the particle  $i$  at proper time  $\tau$ , and  $\det(g) = -\tau^2$  is the determinant of the metric tensor  $g_{\mu\nu} = \text{diag}(1, -1, -1, -\tau^2)$ . The summation is over all the particles. Substituting Eq. (62) into Eq. (61), it is easy to verify that we consistently arrive at the correct number of particles, i.e. in our case the number of partons from an MC-EKRT event. Similarly, the components of the energy-momentum tensor can be expressed as

$$T^{\alpha\beta}(\tau, \mathbf{x}_\perp, \eta_s) = \int \frac{d^2\mathbf{p}_T dp^\eta}{p^\tau} \tau p^\alpha p^\beta f(\tau, \mathbf{x}, \mathbf{p}). \quad (63)$$

In what follows, we will assume that  $p_i^\eta = 0$ , so that  $y_i = \eta_{s,i}$ . Changing the integration variable from  $p^\eta$  to rapidity  $y$  using Eq. (58), the integral can be then written as

$$T^{\alpha\beta} = \sum_i \int d^2\mathbf{p}_T dy \frac{p^\alpha p^\beta}{p^\tau} \frac{1}{\tau} \cosh(y - \eta_s) \times \delta^{(2)}(\mathbf{x}_\perp - \mathbf{x}_{\perp i}) \delta(\eta_s - \eta_{s,i}) \delta^{(2)}(\mathbf{p}_T - \mathbf{p}_{Ti}) \delta(y - \eta_s). \quad (64)$$

The resulting  $\delta(y - \eta_s)$  ensures that  $y = \eta_s$ , i.e. initial longitudinal scaling flow holds even after we replace the spatial delta functions by Gaussian smearing functions below.

To obtain a smooth density profile for relativistic hydrodynamics from the partons, we replace the spatial delta functions with Gaussian distributions,

$$\delta^{(2)}(\mathbf{x}_\perp - \mathbf{x}_{\perp i}) \delta(\eta_s - \eta_{s,i}) \rightarrow g_\perp(\mathbf{x}_\perp; \mathbf{x}_{\perp i}) g_\parallel(\eta_s; \eta_{s,i}), \quad (65)$$

with

$$g_\perp(\mathbf{x}_\perp; \mathbf{x}_{\perp i}) = \frac{C_\perp}{2\pi\sigma_\perp^2} \exp\left[-\frac{(\mathbf{x}_\perp - \mathbf{x}_{\perp i})^2}{2\sigma_\perp^2}\right], \quad (66)$$

$$g_\parallel(\eta_s; \eta_{s,i}) = \frac{C_\parallel}{\sqrt{2\pi}\sigma_\parallel} \exp\left[-\frac{(\eta_s - \eta_{s,i})^2}{2\sigma_\parallel^2}\right], \quad (67)$$

where  $\sigma_{\perp}$  and  $\sigma_{\parallel}$  are the widths of the distributions in the transverse and longitudinal directions, respectively. Both  $\sigma_{\perp}$  and  $\sigma_{\parallel}$  are considered to be free parameters of our model. Equations (66) and (67) are normalized as

$$\int d^2\mathbf{x}_{\perp} d\eta_s g_{\perp}(\mathbf{x}_{\perp}; \mathbf{x}_{\perp i}) g_{\parallel}(\eta_s; \eta_{s,i}) = 1. \quad (68)$$

To reduce the computational costs, we impose a cut-off on the smearing range to  $\pm 3\sigma$  in each direction from the centre of the Gaussian distribution. However, the cut-off on the integration range and the numerical error originating from the discretization of Gaussian functions violate the normalization condition in Eq. (68). Therefore, the constants  $C_{\perp}$  and  $C_{\parallel}$  in Eqs. (66) and (67) are adjusted in every  $f_i(\tau, \mathbf{x}, \mathbf{p})$  so that the unit normalization is ensured. We checked, however, that  $C_{\perp}$  and  $C_{\parallel}$  are almost unity with the current parameters in the simulations.

With these choices, the initial value of the  $T^{\tau\tau}(\tau_0, \mathbf{x}_{\perp}, \eta_s)$  component of the energy-momentum tensor in hydrodynamics is given as

$$T^{\tau\tau}(\tau_0, \mathbf{x}_{\perp}, \eta_s) = \frac{1}{\tau_0} \sum_i p_{Ti} g_{\perp}(\mathbf{x}_{\perp}; \mathbf{x}_{\perp i}) g_{\parallel}(\eta_s; \eta_{s,i}). \quad (69)$$

In this exploratory study, as we do not yet consider a more detailed spacetime picture of parton production [114], pQCD showering and secondary collisions of partons, and especially as we consider only averaged initial conditions, we follow Ref. [17] and compute only the above initial  $T^{\tau\tau}(\tau_0)$  component, and ignore the initial bulk pressure and shear-stress tensor, as well as set  $T^{\tau i}(\tau_0) = 0$ , or equivalently set the spatial components of the four-velocity  $u^{\mu}(\tau_0) = \gamma(1, \mathbf{v}_T(\tau_0), v^{\eta}(\tau_0))$  initially to zero. Here  $v^{\eta}(\tau_0) = 0$  follows from the condition  $y = \eta_s$  that corresponds to  $v_z = z/t$  in the collision frame. The remaining diagonal components of the energy-momentum tensor are then given by the EoS as  $T^{ij}(\tau_0) = P(e(\tau_0))\delta^{ij}$ , where now in the absence of initial transverse flow,  $e(\tau_0) = T^{\tau\tau}(\tau_0)$ .

We note that this way of initializing does not explicitly conserve energy, but with  $\sigma_{\parallel} = 0.15$  the total energy is increased only by  $\sim 1\%$ , while with e.g.  $\sigma_{\parallel} = 0.5$  already by  $\sim 13\%$ . On the other hand,  $dE/d\eta_s$  with a rapidity independent distribution of particles would be conserved in the smearing. The MC-EKRT distribution is not rapidity independent, but in practice  $dE/d\eta_s$  is almost identical before and after the smearing of parton distribution in the mid-rapidity region. Only at larger rapidities, where experimental data are not available in any case, we start to see the smeared case  $dE/d\eta_s$  deviating from the unsmeared minijet  $dE/d\eta_s$ . This is shown in Fig. 11, where we compare event-averaged  $dE/d\eta_s$  computed from the MC-EKRT partons to those obtained after smearing with different values of  $\sigma_{\parallel}$ .

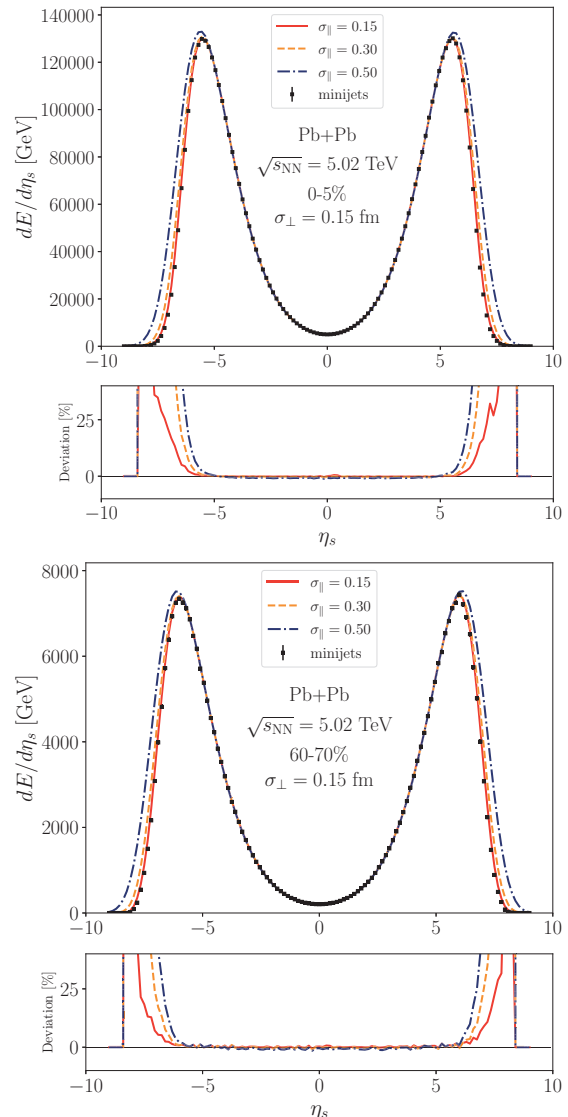


FIG. 11: Spacetime rapidity distribution of the event-averaged initial energy,  $dE/d\eta_s$  as a function of  $\eta_s$ , at  $\tau = \tau_0$  in 0-5% central (a) and 60-70% central (b) 5.02 TeV Pb+Pb collisions, obtained from the minijets before the smearing (markers) and after the smearing with a fixed transverse width  $\sigma_{\perp} = 0.15$  fm and with different longitudinal widths  $\sigma_{\parallel}$  (solid, dashed and dotted-dashed curves). The smaller panels show the relative difference between the smeared and unsmeared cases.

### 3. Averaging initial conditions

The above construction gives us the initial energy density event-by-event. As an example, the energy density distribution at  $\tau = \tau_0$  obtained from a single event is plotted in the  $x$ - $y$  and  $\eta_s$ - $x$  planes in panels (a) and (b)



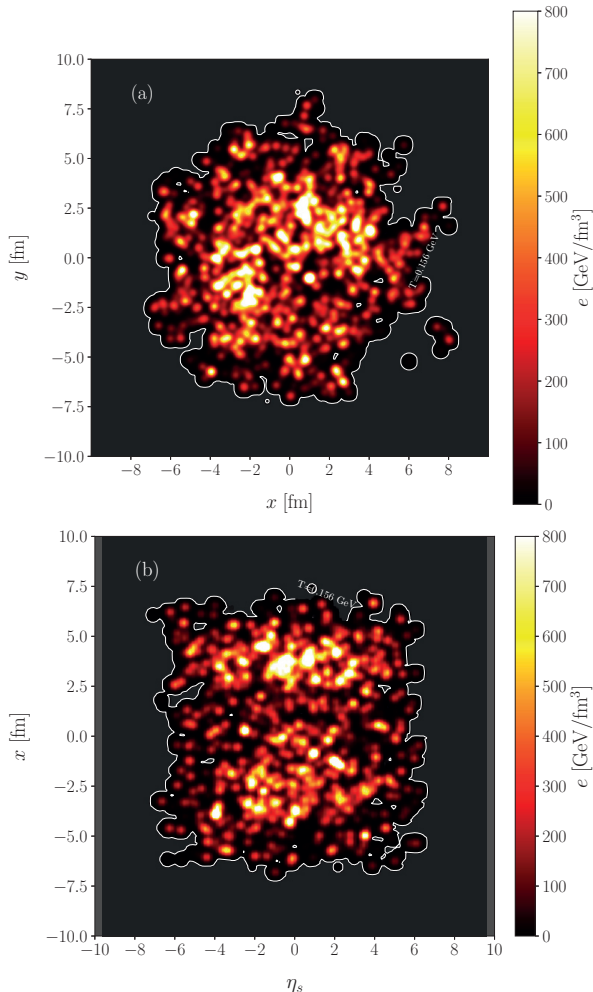


FIG. 12: Initial energy density profile above the QCD transition temperature  $T_c = 0.156$  GeV [115] at  $\tau = \tau_0$  computed from a single MC-EKRT event in the  $x$ - $y$  plane (a), and in the  $\eta_s$ - $x$  plane (b).

of Fig. 12, respectively. Here we, however, want to avoid computationally very intensive 3+1D event-by-event hydrodynamic simulations, and therefore compute event-averaged initial conditions. As explained in Sec. II F, we perform first the centrality selection according to the total initial transverse energy computed from the partons, and average the initial conditions within each centrality class. The hydrodynamic evolution is then computed for each event-averaged initial conditions, i.e. one hydrodynamic simulation per centrality class.

We first convert each event-by-event initial energy-density profile to an entropy-density profile using the EoS, and then average the entropy-density profiles and convert the averaged entropy density back to energy density. The reason for this is that the total initial entropy

and the final hadron multiplicity have nearly a linear relation, and therefore averaging over the entropy-density profiles rather than over the energy-density profiles is a better approximation for obtaining the event-averaged final multiplicities, and their centrality dependence [28]. The difference here comes from the non-linear relation between the energy and entropy densities. The linear relation between the multiplicity and the initial entropy is somewhat broken by event-by-event fluctuations in the entropy production due to dissipation, but those fluctuations relative to total entropy production are typically small in central and semi-central collisions [17].

#### IV. RESULTS

In the following, we have applied MC-EKRT to 5.02 TeV and 2.76 TeV Pb+Pb, and 200 GeV Au+Au collisions. In particular, we explore here how the centrality and pseudorapidity dependence of charged particle multiplicity at different collision energies is affected by different choices of the Gaussian smearing and shear viscosity. We will also discuss the role of the energy conservation at different collision energies.

For each investigated collision system 100 000 minimum bias events were produced and sorted in centrality classes based on their initial transverse energy  $E_T$ . The Gaussian smearing widths were chosen to be  $\sigma_\perp = 0.15$  or 0.4 fm in the transverse plane and the longitudinal smearing width was fixed to  $\sigma_\parallel = 0.15$ . The ratio of shear viscosity to entropy density  $\eta/s$  was taken either as constant, tuned to approximately reproduce the elliptic flow measurements at RHIC and LHC, or to follow the temperature dependent  $\eta/s = param1$  from Ref. [17] (see Fig. 1 there).

The free parameters in the MC-EKRT model, namely  $K$  and  $\kappa_{\text{sat}}$ , were tuned to approximately reproduce the centrality dependence of charged particle multiplicity at midrapidity. The saturation parameter  $\kappa_{\text{sat}}$  was kept the same for all systems, but the pQCD  $K$ -factor was tuned for each collision system separately. We note that the parameter values quoted here are specific to these realizations of MC-EKRT computation, and are different for different choices of e.g. smoothing and viscosity. Also event-by-event fluctuations would likely change these values.

##### A. Data comparison with event-averaged initial state

###### 1. Charged particle pseudorapidity distribution

Figures 13, 14, and 15 show the charged particle pseudorapidity ( $\eta$ ) distributions for  $\sqrt{s_{NN}} = 5.02$  TeV Pb+Pb, 2.76 TeV Pb+Pb, and 200 GeV Au+Au collisions, respectively. The centrality classes are quoted in the figures. We show all the cases tested here, namely

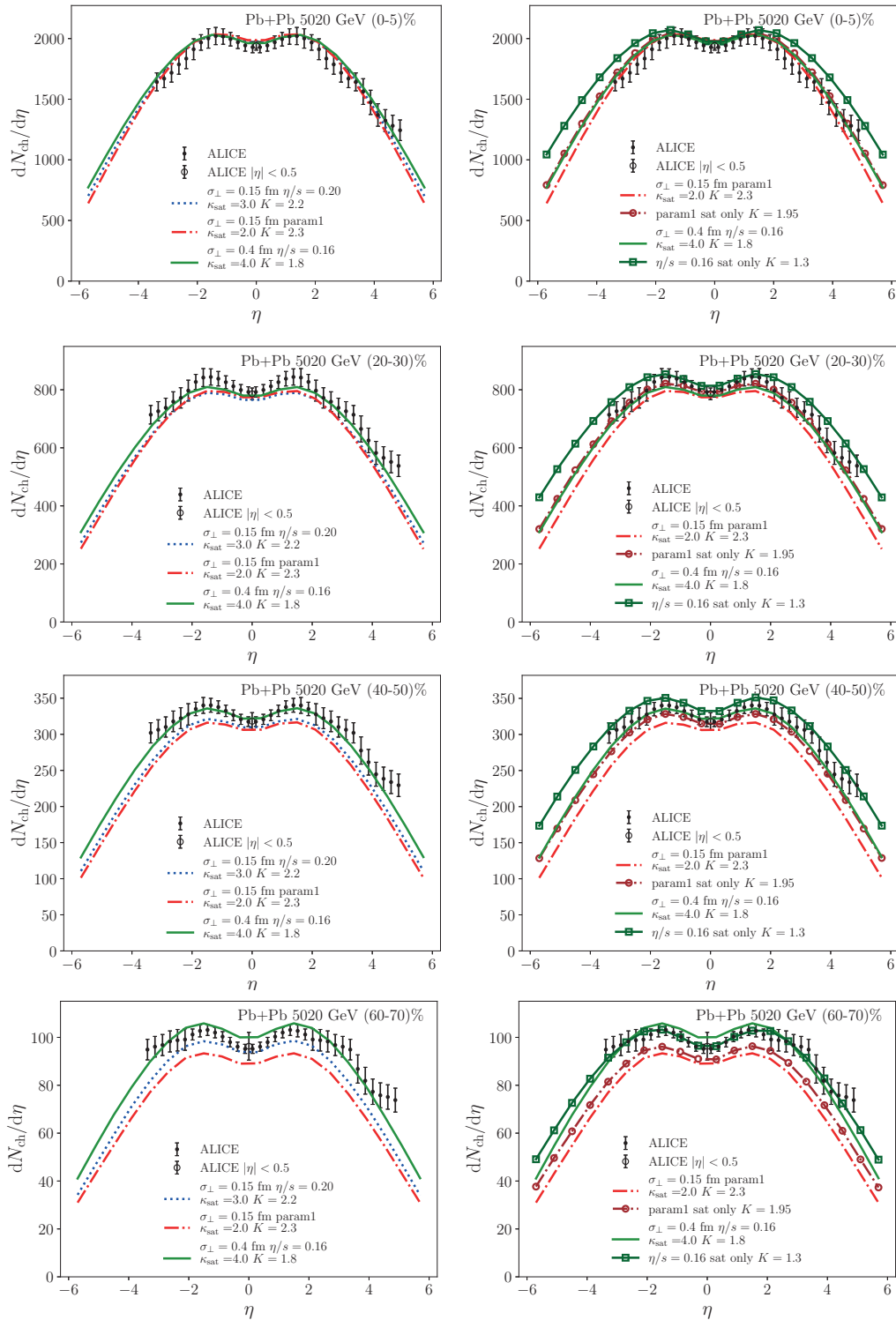


FIG. 13: Charged particle multiplicity  $dN_{ch}/d\eta$  as a function of pseudorapidity in Pb+Pb collisions at  $\sqrt{s_{NN}} = 5.02$  TeV, compared with ALICE data [116] (filled markers) and [117] (open markers). Left panels show the results with all the filters on, and the curves with markers in the right panels show the results with only the saturation filter on. The solid green and dashed-dotted red curves are the same in the left and right panels.

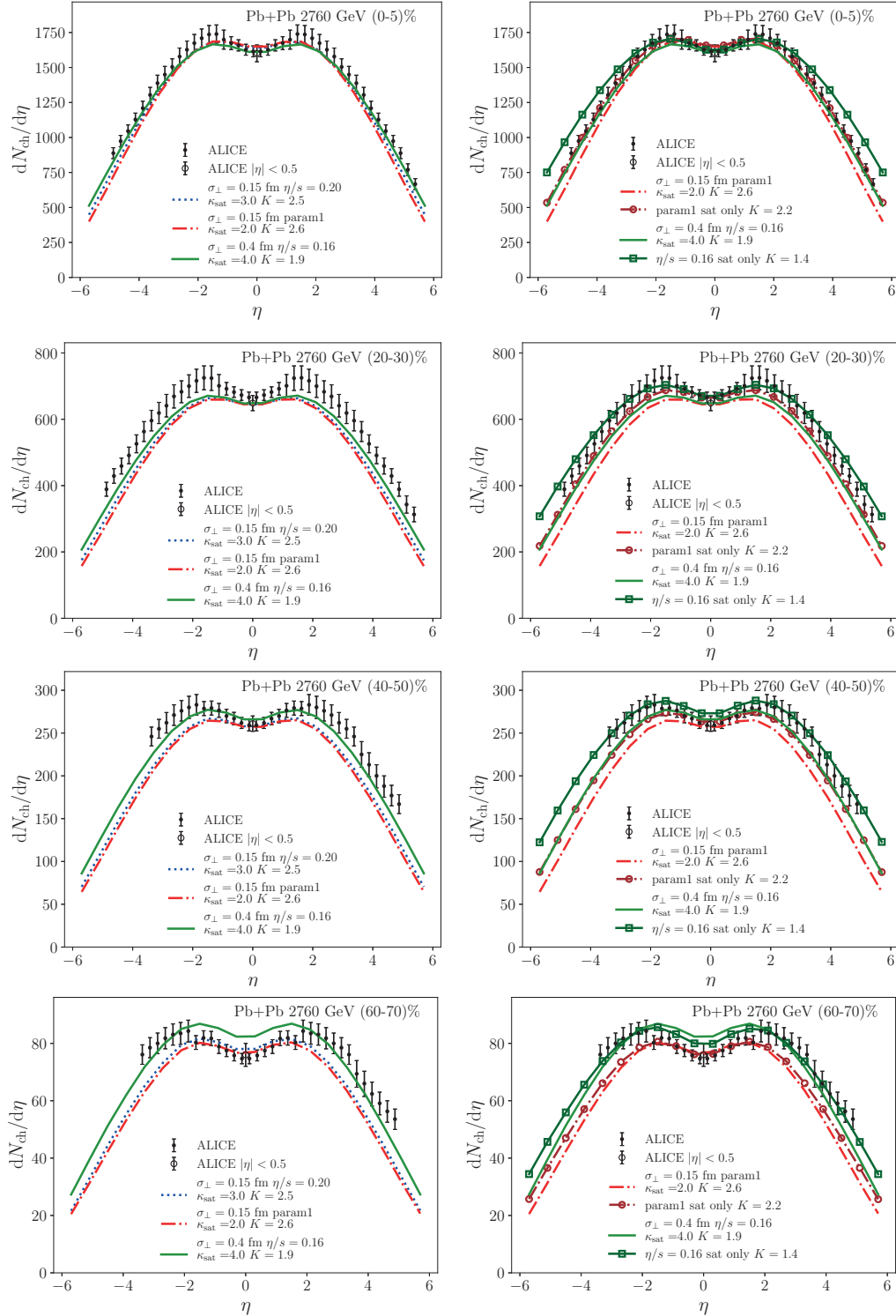


FIG. 14: Charged particle multiplicity  $dN_{\text{ch}}/d\eta$  as a function of pseudorapidity in Pb+Pb collisions at  $\sqrt{s_{NN}} = 2.76$  TeV, compared with ALICE data [118] (filled markers) and [119] (open markers). Left panels show the results with all the filters on, and the curves with markers in the right panels show the results with only the saturation filter on. The solid green and dashed-dotted red curves are the same in the left and right panels.



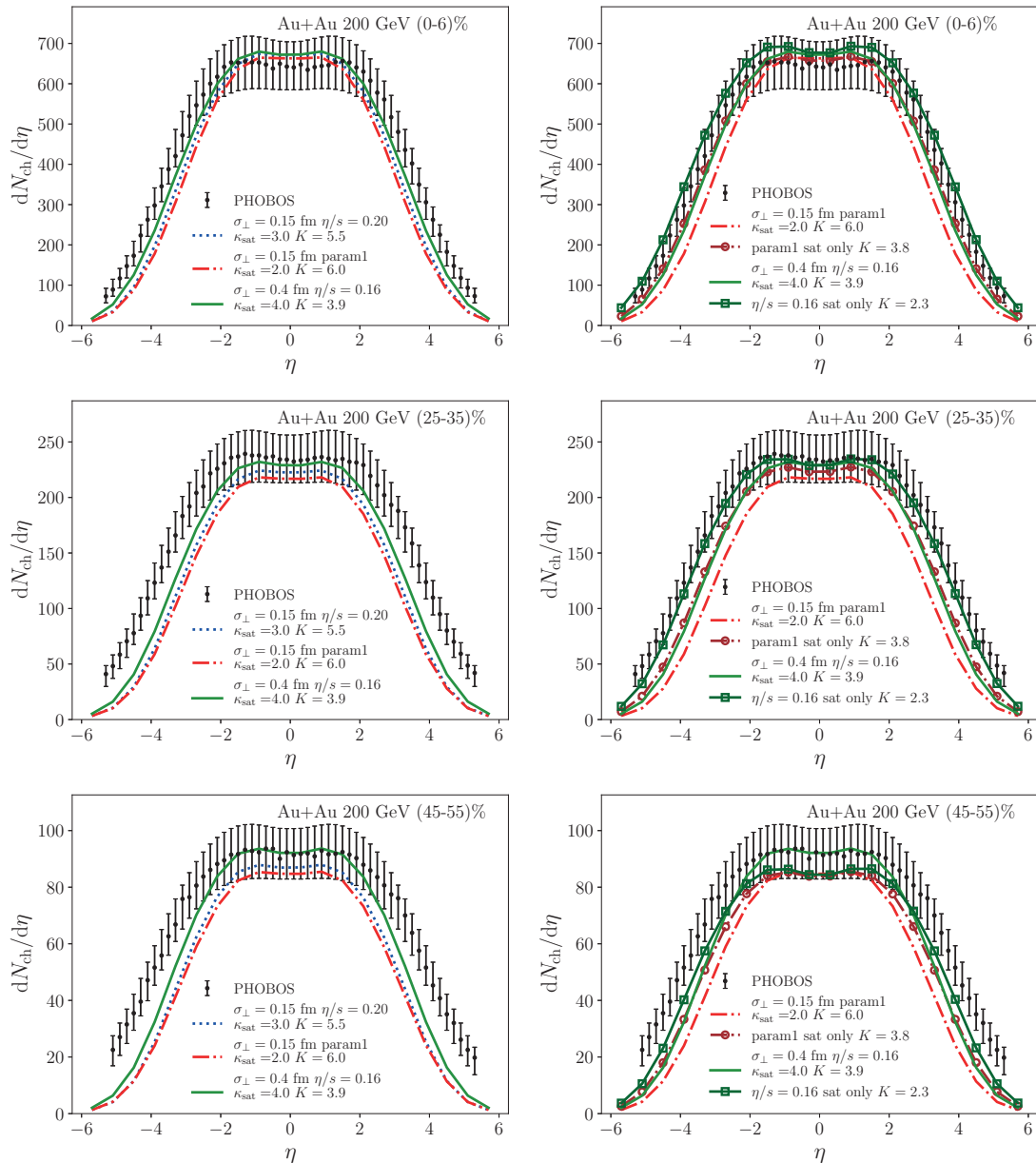


FIG. 15: Charged particle multiplicity  $dN_{\text{ch}}/d\eta$  as a function of pseudorapidity in Au+Au collisions at  $\sqrt{s_{NN}} = 200$  GeV, compared with PHOBOS data [120]. Left panels show the results with all the filters on, and the curves with markers in the right panels show the results with only the saturation filter on. The solid green and dashed-dotted red curves are the same in the left and right panels.

$\sigma_{\perp} = 0.15$  fm with  $\eta/s = 0.20$ ,  $\sigma_{\perp} = 0.15$  fm with  $\eta/s = \text{param1}$ , and  $\sigma_{\perp} = 0.4$  fm with  $\eta/s = 0.16$ . The values of  $\kappa_{\text{sat}}$  and  $K$  for each case are indicated in the figures. The left panels show the full results where saturation, energy conservation, and valence-quark number conservation are taken into account. The curves with

markers in the right panels show the results with saturation only, demonstrating the role of saturation in the energy conservation, as well as the role of the per-nucleon level energy conservation in narrowing the rapidity distributions.

The values for the  $K$  factors that are needed to re-

produce the data are increasing with decreasing collision energy. This is in line with the expectation that NLO corrections become increasingly important towards lower collision energy [66, 67]. We can, however, see that the centrality dependence of the multiplicity is well described by collision energy independent  $\kappa_{\text{sat}}$ . This is already a non-trivial result, even if we have some freedom to tune the centrality dependence by changing  $\kappa_{\text{sat}}$ . The range of the centrality dependence with different values of  $\kappa_{\text{sat}}$  is, as shown in Fig. 9, quite limited. Thus, the centrality dependence of multiplicity is relatively robust prediction of the MC-EKRT model, and the good agreement with the data is similar to the NLO EbyE EKRT model [17], where 2+1 D fluid dynamics was employed.

A significant new feature in the MC-EKRT model is that we can obtain full 3D initial conditions, and subsequently we can compute the pseudorapidity dependence of the charged particle multiplicity. The overall agreement with the rapidity spectra is encouragingly good. At both LHC energies we can essentially reproduce the measurements in all the centrality classes. Only in the most peripheral collisions with  $|\eta| > 2$ , we can start to see some more significant deviations from the shape of the measured rapidity distribution. In the most central collisions at RHIC the agreement is very similar as at the LHC. In peripheral collisions we start to get too narrow spectrum, but even then the agreement remains good up to  $|\eta| \sim 2$ .

The transverse smoothing range  $\sigma_{\perp}$  and the  $\eta/s$  parametrization slightly affect both the centrality dependence and the width of the rapidity spectra. The energy per unit rapidity is independent of  $\sigma_{\perp}$ , but since the conversion from energy density to entropy density is non-linear, the final multiplicity depends on  $\sigma_{\perp}$ . As a result, the rapidity spectra get wider with larger smoothing range. Temperature dependence of  $\eta/s$  also affects the width of the rapidity distribution through the entropy production. If  $\eta/s$  increases with increasing temperature, the relative entropy production becomes larger at higher temperatures or energy densities, and the rapidity distribution becomes narrower than with a constant  $\eta/s$ . Even though the main features of the rapidity spectra are here coming from the MC-EKRT model, the finer details of the obtained spectra depend also on the details of the initialization and on the details of the fluid dynamical evolution.

In the right panels of Figs. 13, 14, and 15 we show the charged particle pseudorapidity distributions with saturation only, i.e. we do not explicitly impose the nucleon-level energy and valence-quark number conservations. As we can see from the figures, comparing the curves with and without the markers, the rapidity distributions become wider without the per-nucleon energy conservation. This is natural, as dijets with large rapidity carry a lot of energy, and are thus more constrained by the energy conservation. It is interesting to note that the saturation-only results can also reproduce the shape of the rapidity distribution in peripheral Au+Au collisions at RHIC.

On the other hand, the saturation-only distributions with  $\kappa_{\text{sat}} = 4$  at the LHC tend to get too wide in the most central collisions.

We have checked that with the saturation-only  $\kappa_{\text{sat}} = 4$  central-collision cases, i.e. with weaker saturation, the energy conservation of the contributing nucleons is violated on the average already by  $\sim 50\%$  at the LHC, and  $\sim 20\%$  at RHIC. Interestingly, however, with the saturation-only  $\kappa_{\text{sat}} = 2$  central-collision cases, i.e. with stronger saturation, the average violation is only  $\sim 5\%$  at the LHC, and energy is practically conserved at RHIC.

These results suggest that, given strong enough saturation, the total energy budget could be conserved even without a requirement of a tight per-nucleon energy conservation, supporting the view that the high-energy nuclear collisions can be described as collisions of two parton clouds rather than as a collection of sub-collisions of individual nucleons.

## 2. Charged particle elliptic flow

Figure 16 shows the pseudorapidity dependence of elliptic flow, the second-order Fourier coefficient  $v_2\{4\}$  of the azimuthal angle distribution of charged hadrons, in semi-central 2.76 TeV Pb+Pb and 200 GeV Au+Au collisions. The model results are calculated using the 4-particle cumulant method [123]. Since our initial energy density profiles are averages over multiple events,  $v_2\{\text{EP}\} \approx v_2\{2\} \approx v_2\{4\}$ <sup>2</sup>.

The  $\eta$ -differential flow is determined with respect to a reference flow vector, which is typically constructed from particles in a separate rapidity bin to avoid autocorrelations. For the comparison with the ALICE data [121], the reference flow vector is calculated using particles in the TPC pseudorapidity acceptance  $|\eta_{\text{ref}}| < 0.8$  and in addition there is also a  $p_T$  cut ( $0.2 < p_T < 5.0$ ) GeV. When calculating  $v_2(\eta)$  in the rapidity bins with  $|\eta| > 2.0$ , the particles in the  $\eta$  bin are correlated with the full reference flow vector. For the rapidity bins with  $|\eta| < 2.0$ , the particles with  $\eta < 0$  are correlated with the positive-rapidity reference particles  $0 < \eta_{\text{ref}} < 0.8$ , while the negative reference  $-0.8 < \eta_{\text{ref}} < 0$  is used for particles with  $\eta > 0$ . In the PHOBOS comparison [122], the reference flow for the  $\eta < 0$  bins is determined from particles in the pseudorapidity range  $0.1 < \eta_{\text{ref}} < 2.0$  and the reference for  $\eta > 0$  is determined from particles in the range  $-2.0 < \eta_{\text{ref}} < -0.1$ .

As our average initial energy density profiles lack event-by-event fluctuations, at present the comparison to  $v_2$  data has to be considered more qualitative than

<sup>2</sup> PHOBOS states in Ref. [122] that their event plane  $v_2\{\text{EP}\}$  results are most consistent with the 4-particle cumulant method, so we consider  $v_2\{\text{EP}\}$  and  $v_2\{4\}$  to be comparable in this particular case.

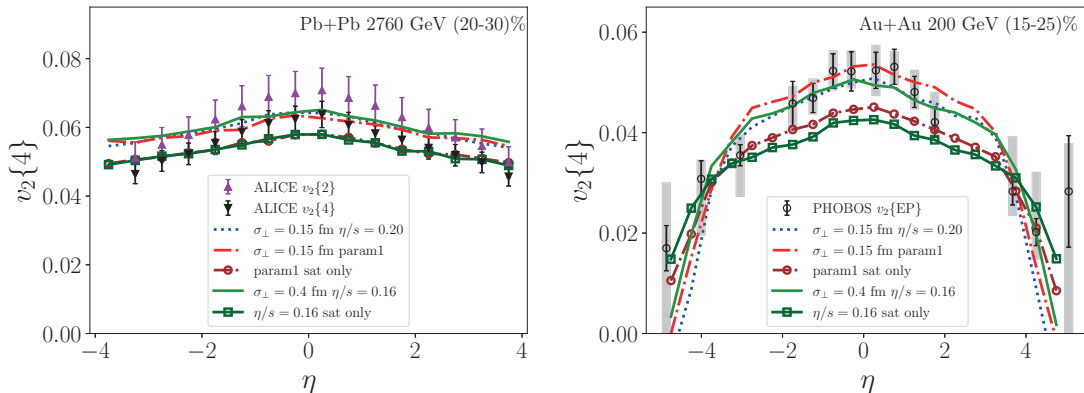


FIG. 16: Charged particle  $v_2\{4\}$  as a function of pseudorapidity in Pb+Pb collisions at  $\sqrt{s_{NN}} = 2.76$  TeV, in the 20-30 % centrality class, compared with ALICE data [121] (left panel), and in Au+Au collisions at  $\sqrt{s_{NN}} = 200$  GeV, in the 15-25 % centrality class, compared with PHOBOS hit-based event plane  $v_2$  data [122] (right panel). The curves without markers show the results with all filters on, and the ones with markers the saturation-only cases. The parameter setups and the curve labelings are the same as in Figs. 13-15.

quantitative in nature. Nevertheless, the currently observed trends look very promising; the magnitude of  $v_2$  is already close to data for both investigated collision systems, and we observe stronger dependence on pseudorapidity at 200 GeV compared to 2.76 TeV, as is also suggested by the data. This steeper fall-off of  $dv_2/d\eta$  at RHIC can be understood as a sign of incomplete conversion of spatial eccentricity into momentum anisotropy due to the shorter lifetime of the hot QCD medium at lower collision energies. This result is rather robust with respect to the implementation details of the MC-EKRT initialization. The largest effect is seen when relaxing the energy conservation requirement, which leads to a visible decrease in  $v_2$ , but in this case we have not tried to adjust  $\eta/s$  to reproduce the data.

### B. Event-by-event fluctuations of the initial state eccentricities

Even though we have not performed here event-by-event fluid dynamical evolution, we can still compute the initial state eccentricities event-by-event, and in particular examine the decorrelation of the eccentricities as a function of spacetime rapidity. The spatial eccentricity vector with the magnitude  $\epsilon_2$  pointing at the angle  $\Psi_2$  can be defined as a complex number constructed from a weighted average,

$$\begin{aligned} \epsilon_2 e^{i2\Psi_2} &= \frac{\sum_k w_k r_k^2 e^{i2\phi_k}}{\sum_k w_k r_k^2} \\ &= \frac{\sum_k w_k r_k^2 (\cos(2\phi_k) + i \sin(2\phi_k))}{\sum_k w_k r_k^2}. \end{aligned}$$

Here  $r$  and  $\phi$  indicate the polar coordinates (radius and angle) in the transverse plane:  $r^2 = \hat{x}^2 + \hat{y}^2$ ,  $\cos(2\phi) =$

$(\hat{x}^2 - \hat{y}^2)/r^2$  and  $\sin(2\phi) = 2\hat{x}\hat{y}/r^2$ , where we have defined  $\hat{x} = x - x_{cm}$  and  $\hat{y} = y - y_{cm}$  with respect to the center-of-mass point  $(x_{cm}, y_{cm}) = \left( \frac{\sum_k w_k x_k}{\sum_k w_k}, \frac{\sum_k w_k y_k}{\sum_k w_k} \right)$ . The weight  $w_k$  is the initial energy density at  $\tau = \tau_0$  in a hydro cell and the sum is over the cells in a transverse slice of the hydro grid which has the width  $\Delta\eta_s$ .

Once we have determined the eccentricities for each event, we can compute the Pearson correlation of the eccentricity magnitudes between different rapidity bins  $\eta_s$  and  $\eta_{s0}$ ,

$$\begin{aligned} c(\epsilon_2(\eta_s), \epsilon_2(\eta_{s0})) &= \frac{\langle (\epsilon_2(\eta_s) - \langle \epsilon_2(\eta_s) \rangle) (\epsilon_2(\eta_{s0}) - \langle \epsilon_2(\eta_{s0}) \rangle) \rangle}{\sigma(\epsilon_2(\eta_s)) \sigma(\epsilon_2(\eta_{s0}))}, \quad (70) \end{aligned}$$

where  $\langle \cdot \rangle$  indicates an average over events and  $\sigma$  is the corresponding standard deviation.

In Fig. 17 we show the event-averaged eccentricities and the Pearson correlations between the eccentricities at finite rapidity  $\epsilon_2(\eta_s)$  and midrapidity  $\epsilon_2(\eta_{s0} = 0)$  in Pb+Pb collisions at  $\sqrt{s_{NN}} = 2.76$  TeV in the LHC and in Au+Au collisions at  $\sqrt{s_{NN}} = 200$  GeV at RHIC. The rapidity bin width was chosen to be  $\Delta\eta_s = 1.0$ . The event-averaged eccentricities remain nearly constant close to midrapidity, but both at RHIC and LHC the eccentricity starts to increase at higher rapidities. We also see that if we relax the energy conservation, the mid-rapidity eccentricities decrease by  $\sim 10\%$  at the LHC, and  $\sim 15\%$  at RHIC, which explains the decrease in  $v_2$  in the saturation-only cases in Fig. 16.

As seen in the right panel of Fig. 17, the Pearson correlation becomes weaker at higher rapidities, and at RHIC the eccentricity beyond  $|\eta_s| \gtrsim 3.5$  is no longer correlated with midrapidity, while at the LHC the correlation spans a considerably larger rapidity range  $|\eta_s| \lesssim 5.0$ . The decreasing number of particles at RHIC compared to the

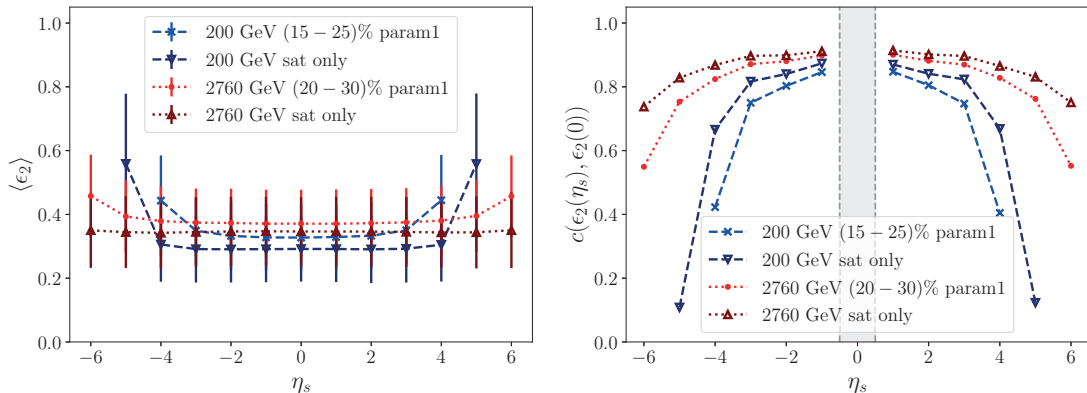


FIG. 17: Spacetime rapidity dependence of the event-averaged eccentricity (left panel) and the Pearson correlation (right panel) between  $\epsilon_2(\eta_s)$  and  $\epsilon_2(\eta_s = 0)$  (midrapidity bin indicated by the gray band) in 20-30 % central Pb+Pb collisions at  $\sqrt{s_{NN}} = 2760$  GeV and in 15-25 % central Au+Au collisions at  $\sqrt{s_{NN}} = 200$  GeV. The dashed blue and dotted red curves show the results with all filters on, and the dashed dark blue and dotted brown curves the saturation-only cases. The errorbars show the standard deviation of the calculation.

LHC, and also towards larger rapidities leads to larger fluctuations of eccentricity, and therefore also to a weaker correlation with midrapidity at RHIC and at large rapidities. In the saturation-only cases the correlation is stronger at large rapidities than in the fully filtered cases. To our understanding, also this is a multiplicity effect, originating from the increased multiplicities at larger rapidities.

We also note that the Pearson correlation from the EbyE initial conditions should not be directly compared to the rapidity dependence of elliptic flow in Fig. 16. The elliptic flow is computed from event-averaged initial conditions, and all the decorrelation effects disappear in the averaging. We rather expect that the decreasing multiplicity at larger rapidity leads to a shorter lifetime in the fluid evolution, and thus the conversion from eccentricity to elliptic flow is not completed at higher rapidities, and we get smaller  $v_2$ . In a full EbyE computation both the lifetime effect and the decorrelation effect would be present.

The CMS collaboration has defined the rapidity dependent correlation ratio [124] as

$$r_2 = \frac{\langle v_2(-\eta)v_2(\eta_{\text{ref}}) \cos 2[\Psi_2(-\eta) - \Psi_2(\eta_{\text{ref}})] \rangle}{\langle v_2(\eta)v_2(\eta_{\text{ref}}) \cos 2[\Psi_2(\eta) - \Psi_2(\eta_{\text{ref}})] \rangle}, \quad (71)$$

where the  $\eta$  bin is somewhere in the central rapidity region  $0 < \eta < 2.5$ , its negative-side counterpart is at  $-\eta$ , and the reference bin will be somewhere further away in forward rapidity  $\eta_{\text{ref}} > 3.0$  to reduce nonflow effects. Since we have performed full MC-EKRT + fluid dynamics simulations only for event-averaged initial profiles, we are not able to study event-by-event fluctuations of  $v_2$ . We can, however, estimate  $r_2$  from the pre-averaging eccentricities, assuming  $v_2(\eta) \approx k\epsilon_2(\eta_s)$  for some proportionality factor  $k$ :

$$r_2 \approx \frac{\langle \epsilon_2(-\eta_s)\epsilon_2(\eta_{s,\text{ref}}) \cos 2[\Psi_2(-\eta_s) - \Psi_2(\eta_{s,\text{ref}})] \rangle}{\langle \epsilon_2(\eta_s)\epsilon_2(\eta_{s,\text{ref}}) \cos 2[\Psi_2(\eta_s) - \Psi_2(\eta_{s,\text{ref}})] \rangle}, \quad (72)$$

where  $\Psi_2$  is obtained from Eq. (70). Using the same replacement  $v_2 \rightarrow \epsilon_2$  we can also investigate the “twist factor”  $R_{n|n;2} \equiv R_2$ , by the ATLAS collaboration [125] where the ratio is controlled by the cosine term:

$$R_2 \approx \frac{\langle \epsilon_2(-\eta_{s,\text{ref}})\epsilon_2(-\eta_s)\epsilon_2(\eta_s)\epsilon_2(\eta_{s,\text{ref}}) \cos 2[\Psi_2(-\eta_{s,\text{ref}}) - \Psi_2(\eta_{s,\text{ref}}) + (\Psi_2(-\eta_s) - \Psi_2(\eta_s))] \rangle}{\langle \epsilon_2(-\eta_{s,\text{ref}})\epsilon_2(-\eta_s)\epsilon_2(\eta_s)\epsilon_2(\eta_{s,\text{ref}}) \cos 2[\Psi_2(-\eta_{s,\text{ref}}) - \Psi_2(\eta_{s,\text{ref}}) - (\Psi_2(-\eta_s) - \Psi_2(\eta_s))] \rangle}. \quad (73)$$

We show the eccentricity correlation ratio  $r_2$  and twist factor  $R_2$  in Fig. 18 in 20-30 % central Pb+Pb collisions at  $\sqrt{s_{NN}} = 2.76$  TeV and in 15-25 % central Au+Au col-

lisions at  $\sqrt{s_{NN}} = 200$  GeV. Both  $r_2$  and  $R_2$  show a similar behavior as the Pearson correlator, i.e. decorrelation at larger rapidities, and the decorrelation is stronger at

RHIC than at the LHC. The decreasing trend of the calculated  $r_2$  and  $R_2$  is similar as seen in the CMS and ATLAS measurements, but the calculated  $r_2$  and  $R_2$  show slightly stronger correlations than the measurements do. However, as we do not perform event-by-event fluid dynamical evolution, a direct comparison is not really feasible here [38], but our results should be rather taken as qualitative.

## V. CONCLUSIONS

We have developed a new MC-EKRT model for computing initial particle production in ultrarelativistic heavy-ion collisions. This is an extension of the EbyE EKRT model [17], which has very successfully predicted the midrapidity low- $p_T$  observables from 200 GeV Au+Au collisions at RHIC to the top energy LHC Pb+Pb collisions. The essential new feature in the new Monte-Carlo framework is the implementation of the dynamical minijet-multiplicity-originating fluctuations in the saturation and particle production. Also energy/momentum conservation and valence-quark number conservation were implemented, together with a new type of spatially dependent nuclear PDFs that cope with the large density fluctuations present in an event-by-event study. As a result, the MC-EKRT model now gives a full 3-dimensional initial state that can be coupled to 3+1 D fluid dynamics.

We have applied the novel MC-EKRT framework to 5.02 TeV Pb+Pb, 2.76 TeV Pb+Pb, and 200 GeV Au+Au collisions. The 3+1 D spacetime evolution is computed with viscous relativistic hydrodynamics [73]. We have studied the uncertainties related to converting the partonic state, given by the MC-EKRT, to an initial state of fluid dynamics, and also discussed the role of energy conservation in rapidity distributions of charged particle multiplicities and elliptic flow coefficients.

Although the MC-EKRT initial state model gives the full 3-dimensional initial state that include all the EbyE fluctuations, we have here made only an exploratory study of the final observables. The main simplification here is that we have first computed the initial conditions by averaging a large number of EbyE MC-EKRT initial states for each centrality class, and then computed the fluid dynamical evolution only for the averaged initial conditions. Obviously, this limits the number of observables that we can study, but it also decreases the computational cost by a huge amount. The averaging of the initial conditions is performed in such a way that the final multiplicities resemble as closely as possible those that would be obtained by a full EbyE computation.

The comparison with the measured charged particle multiplicities at the LHC and RHIC shows that MC-EKRT can describe the centrality dependence of the multiplicity very well, practically at the same level as the earlier EbyE EKRT implementation. Moreover, the new framework describes the rapidity dependence as well.

The overall agreement with the measured shape of the rapidity spectra is very good. This is a non-trivial result, as it is a rather robust outcome from the MC-EKRT model, and essentially dominated by the pQCD minijet production and saturation. Note also that there is no parameter to directly control the rapidity distribution. Only in peripheral collisions at RHIC we start to see larger deviations from the data. Interestingly, we observed that when we give up the detailed nucleon-level energy conservation, the agreement with the data extends all the way to peripheral RHIC collisions. This might indicate that in the view that ultrarelativistic nuclear collision are rather collisions of parton clouds than collisions between individual nucleons, the nucleon-level energy conservation is an unrealistically strict condition.

We have also computed the rapidity dependence of elliptic flow, and the agreement with the LHC and RHIC data is good. The rapidity dependence of the computed  $v_2$  is only slightly weaker than that of the data. Even though the computation of the flow coefficients without EbyE fluctuations should be viewed rather as qualitative than quantitative, the fact that the computed rapidity dependence of the elliptic flow is very similar to what is seen in the data is very promising. Moreover, we see that the EbyE initial state eccentricities at different rapidities are slightly decorrelated. As these decorrelations are not accounted for in the averaged initial state, our result suggests that eventually the computation of the true EbyE flow coefficients that include the decorrelations could show a slightly stronger rapidity dependence than the ones now computed from the averaged initial state.

As an outlook, we can see various exciting avenues along which the current MC-EKRT framework can be developed further. First, similarly to Refs. [66, 67], a well-defined NLO pQCD calculation for the integrated minijet cross section  $\sigma_{jet}^{ab}$ , which determines the multiplicity of the candidate dijets here, can and should be done, and also its snPDF and scale dependencies should be charted. Second, pQCD parton showering should be included as a dynamical way to distribute the initially produced parton's energy and momentum into the phase space. Third, also a more detailed spacetime picture of parton production along the lines of Ref. [114] should be studied, relaxing especially the assumption of all partons being produced at  $z = 0$  and thus making the initial parton production more isotropic. Fourth, pre-thermal evolution, i.e. the effects of the isotropizing and thermalizing secondary collisions of the produced partons [126–137] should be considered. After all these developments, an extraction of the full initial energy-momentum tensor  $T^{\mu\nu}$  for 3+1 D fluid dynamics could be more realistically done, and effects of e.g. initial velocity [36, 138, 139] and shear-stress tensor to observables studied. Finally, we note that the MC-EKRT framework provides a promising platform for jet-quenching studies, where both the QCD-matter initial conditions for fluid dynamics and the high-energy partons that are losing energy are consistently



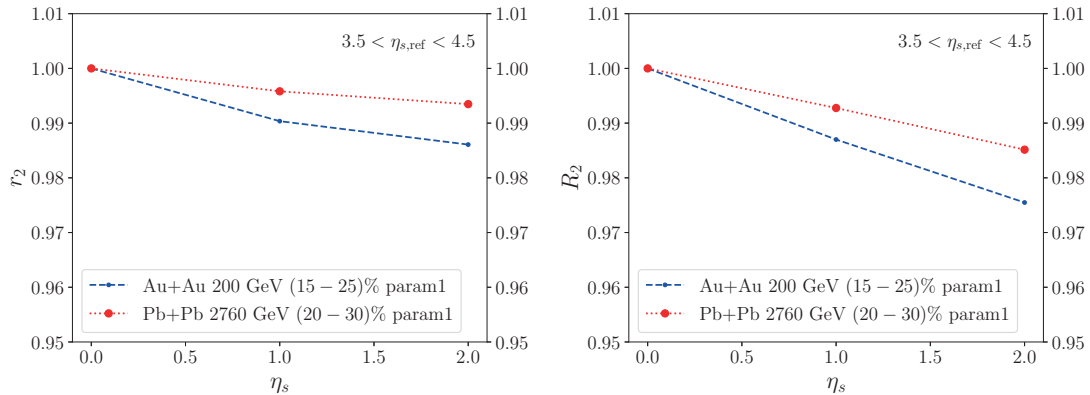


FIG. 18: Spacetime rapidity dependence of the correlation ratio  $r_2$  (left panel) and the twist factor  $R_2$  (right panel) in 20-30 % central Pb+Pb collisions at  $\sqrt{s_{NN}} = 2760$  GeV and in 15-25 % central Au+Au collisions at  $\sqrt{s_{NN}} = 200$  GeV.

obtained from the same computation, event-by-event.

#### Acknowledgments

We thank Vadim Guzey, Ilkka Helenius, Pasi Huovinen, Dong Jo Kim, Tuomas Lappi, Aleksas Mazeliauskas, Etele Molnar, Heikki Mäntysaari, Petja Paakinen, Risto Paatelainen, and Xin-Nian Wang for useful discussions during the preparation of the MC-EKRT framework. In addition, K.J.E. is grateful to Keijo Kajantie and Kimmo Tuominen for discussions at the time of writing Ref. [140] which still influenced our ideas here. We acknowledge the financial support from the Wilho, Yrjö and Kalle Väisälä

Foundation (M.K.) and from the Jenny and Antti Wihuri Foundation (H.H.), and the Academy of Finland Project No. 330448 (K.J.E.). This research was funded as a part of the Center of Excellence in Quark Matter of the Academy of Finland (Projects No. 346325 and 364192). This research is part of the European Research Council Project No. ERC-2018-ADG-835105 YoctoLHC, and the European Union's Horizon 2020 research and innovation program under grant agreement No. 824093 (STRONG-2020). We acknowledge the computation resources from the Finnish IT Center for Science (CSC), project jyy2580, and from the Finnish Computing Competence Infrastructure (FCCI), persistent identifier urn:nbn:fi:research-infras-2016072533.

- 
- [1] A. Bazavov *et al.* [HotQCD], Phys. Rev. D **90**, 094503 (2014) doi:10.1103/PhysRevD.90.094503 [arXiv:1407.6387 [hep-lat]].
- [2] A. Bazavov, P. Petreczky and J. H. Weber, Phys. Rev. D **97**, no.1, 014510 (2018) doi:10.1103/PhysRevD.97.014510 [arXiv:1710.05024 [hep-lat]].
- [3] S. Borsanyi, Z. Fodor, C. Hoelbling, S. D. Katz, S. Krieg and K. K. Szabo, Phys. Lett. B **730**, 99-104 (2014) doi:10.1016/j.physletb.2014.01.007 [arXiv:1309.5258 [hep-lat]].
- [4] S. Borsanyi, G. Endrodi, Z. Fodor, A. Jakovac, S. D. Katz, S. Krieg, C. Ratti and K. K. Szabo, JHEP **11**, 077 (2010) doi:10.1007/JHEP11(2010)077 [arXiv:1007.2580 [hep-lat]].
- [5] [ALICE], “The ALICE experiment – A journey through QCD,” CERN-EP-2022-227, [arXiv:2211.04384 [nucl-ex]].
- [6] P. Romatschke and U. Romatschke, Phys. Rev. Lett. **99**, 172301 (2007) doi:10.1103/PhysRevLett.99.172301 [arXiv:0706.1522 [nucl-th]].
- [7] M. Luzum and P. Romatschke, Phys. Rev. C **78**, 034915 (2008) [erratum: Phys. Rev. C **79**, 039903 (2009)] doi:10.1103/PhysRevC.78.034915 [arXiv:0804.4015 [nucl-th]].
- [8] P. Bozek, Phys. Rev. C **81**, 034909 (2010) doi:10.1103/PhysRevC.81.034909 [arXiv:0911.2397 [nucl-th]].
- [9] B. Schenke, S. Jeon and C. Gale, Phys. Rev. Lett. **106**, 042301 (2011) doi:10.1103/PhysRevLett.106.042301 [arXiv:1009.3244 [hep-ph]].
- [10] B. Schenke, S. Jeon and C. Gale, Phys. Rev. C **82**, 014903 (2010) doi:10.1103/PhysRevC.82.014903 [arXiv:1004.1408 [hep-ph]].
- [11] B. Schenke, S. Jeon and C. Gale, Phys. Rev. C **85**, 024901 (2012) doi:10.1103/PhysRevC.85.024901 [arXiv:1109.6289 [hep-ph]].
- [12] H. Song, S. A. Bass and U. Heinz, Phys. Rev. C **83**, 054912 (2011) [erratum: Phys. Rev. C **87**, no.1, 019902 (2013)] doi:10.1103/PhysRevC.83.054912 [arXiv:1103.2380 [nucl-th]].
- [13] H. Niemi, G. S. Denicol, P. Huovinen, E. Molnar and D. H. Rischke, Phys. Rev. Lett. **106**, 212302 (2011) doi:10.1103/PhysRevLett.106.212302 [arXiv:1101.2442

- [nucl-th].
- [14] C. Gale, S. Jeon, B. Schenke, P. Tribedy and R. Venugopalan, Phys. Rev. Lett. **110**, no.1, 012302 (2013) doi:10.1103/PhysRevLett.110.012302 [arXiv:1209.6330 [nucl-th]].
- [15] H. Niemi, G. S. Denicol, P. Huovinen, E. Molnar and D. H. Rischke, Phys. Rev. C **86**, 014909 (2012) doi:10.1103/PhysRevC.86.014909 [arXiv:1203.2452 [nucl-th]].
- [16] J. Noronha-Hostler, G. S. Denicol, J. Noronha, R. P. G. Andrade and F. Grassi, Phys. Rev. C **88**, no.4, 044916 (2013) doi:10.1103/PhysRevC.88.044916 [arXiv:1305.1981 [nucl-th]].
- [17] H. Niemi, K. J. Eskola and R. Paatelainen, Phys. Rev. C **93**, no.2, 024907 (2015) doi:10.1103/PhysRevC.93.024907 [arXiv:1505.02677 [hep-ph]].
- [18] S. Ryu, J. F. Paquet, C. Shen, G. S. Denicol, B. Schenke, S. Jeon and C. Gale, Phys. Rev. Lett. **115**, no.13, 132301 (2015) doi:10.1103/PhysRevLett.115.132301 [arXiv:1502.01675 [nucl-th]].
- [19] I. A. Karpenko, P. Huovinen, H. Petersen and M. Bleicher, Phys. Rev. C **91**, no.6, 064901 (2015) doi:10.1103/PhysRevC.91.064901 [arXiv:1502.01978 [nucl-th]].
- [20] G. Giacalone, J. Noronha-Hostler, M. Luzum and J. Y. Ollitrault, Phys. Rev. C **97**, no.3, 034904 (2018) doi:10.1103/PhysRevC.97.034904 [arXiv:1711.08499 [nucl-th]].
- [21] G. Nijs, W. van der Schee, U. Gürsoy and R. Snellings, Phys. Rev. C **103**, no.5, 054909 (2021) doi:10.1103/PhysRevC.103.054909 [arXiv:2010.15134 [nucl-th]].
- [22] H. Hirvonen, K. J. Eskola and H. Niemi, Phys. Rev. C **106**, no.4, 044913 (2022) doi:10.1103/PhysRevC.106.044913 [arXiv:2206.15207 [hep-ph]].
- [23] J. Novak, K. Novak, S. Pratt, J. Vredevoogd, C. Coleman-Smith and R. Wolpert, Phys. Rev. C **89**, no.3, 034917 (2014) doi:10.1103/PhysRevC.89.034917 [arXiv:1303.5769 [nucl-th]].
- [24] J. E. Bernhard, J. S. Moreland, S. A. Bass, J. Liu and U. Heinz, Phys. Rev. C **94**, no.2, 024907 (2016) doi:10.1103/PhysRevC.94.024907 [arXiv:1605.03954 [nucl-th]].
- [25] S. A. Bass, J. E. Bernhard and J. S. Moreland, Nucl. Phys. A **967**, 67-73 (2017) doi:10.1016/j.nuclphysa.2017.05.052 [arXiv:1704.07671 [nucl-th]].
- [26] J. E. Bernhard, J. S. Moreland and S. A. Bass, Nature Phys. **15**, no.11, 1113-1117 (2019) doi:10.1038/s41567-019-0611-8
- [27] D. Everett *et al.* [JETSCAPE], Phys. Rev. C **103**, no.5, 054904 (2021) doi:10.1103/PhysRevC.103.054904 [arXiv:2011.01430 [hep-ph]].
- [28] J. Auvinen, K. J. Eskola, P. Huovinen, H. Niemi, R. Paatelainen and P. Petreczky, Phys. Rev. C **102**, no.4, 044911 (2020) doi:10.1103/PhysRevC.102.044911 [arXiv:2006.12499 [nucl-th]].
- [29] J. E. Parkkila, A. Onnerstad and D. J. Kim, Phys. Rev. C **104**, no.5, 054904 (2021) doi:10.1103/PhysRevC.104.054904 [arXiv:2106.05019 [hep-ph]].
- [30] J. E. Parkkila, A. Onnerstad, S. F. Taghavi, C. Mordasini, A. Bilandzic, M. Virta and D. J. Kim, Phys. Lett. B **835**, 137485 (2022) doi:10.1016/j.physletb.2022.137485 [arXiv:2111.08145 [hep-ph]].
- [31] G. Nijs and W. van der Schee, [arXiv:2304.06191 [nucl-th]].
- [32] C. Shen and B. Schenke, Phys. Rev. C **105**, no.6, 064905 (2022) doi:10.1103/PhysRevC.105.064905 [arXiv:2203.04685 [nucl-th]].
- [33] P. Bozek and W. Broniowski, Phys. Rev. C **97**, no.3, 034913 (2018) doi:10.1103/PhysRevC.97.034913 [arXiv:1711.03325 [nucl-th]].
- [34] P. Bozek and I. Wyskiel-Piekarska, Phys. Rev. C **85**, 064915 (2012) doi:10.1103/PhysRevC.85.064915 [arXiv:1203.6513 [nucl-th]].
- [35] L. G. Pang, H. Petersen and X. N. Wang, Phys. Rev. C **97**, no.6, 064918 (2018) doi:10.1103/PhysRevC.97.064918 [arXiv:1802.04449 [nucl-th]].
- [36] L. Pang, Q. Wang and X. N. Wang, Phys. Rev. C **86**, 024911 (2012) doi:10.1103/PhysRevC.86.024911 [arXiv:1205.5019 [nucl-th]].
- [37] G. Denicol, A. Monnai and B. Schenke, Phys. Rev. Lett. **116**, no.21, 212301 (2016) doi:10.1103/PhysRevLett.116.212301 [arXiv:1512.01538 [nucl-th]].
- [38] L. G. Pang, H. Petersen, G. Y. Qin, V. Roy and X. N. Wang, Eur. Phys. J. A **52**, no.4, 97 (2016) doi:10.1140/epja/i2016-16097-x [arXiv:1511.04131 [nucl-th]].
- [39] J. Auvinen, J. E. Bernhard, S. A. Bass and I. Karpenko, Phys. Rev. C **97**, no.4, 044905 (2018) doi:10.1103/PhysRevC.97.044905 [arXiv:1706.03666 [hep-ph]].
- [40] A. Mankolli *et al.* [JETSCAPE], [arXiv:2401.00402 [nucl-th]].
- [41] D. Soeder, W. Ke, J. F. Paquet and S. A. Bass, [arXiv:2306.08665 [nucl-th]].
- [42] H. Hirvonen, K. J. Eskola and H. Niemi, Phys. Rev. C **108**, no.3, 034905 (2023) doi:10.1103/PhysRevC.108.034905 [arXiv:2303.04517 [hep-ph]].
- [43] H. Hirvonen, K. J. Eskola and H. Niemi, [arXiv:2404.02602 [hep-ph]].
- [44] B. Schenke, P. Tribedy and R. Venugopalan, Phys. Rev. Lett. **108**, 252301 (2012) doi:10.1103/PhysRevLett.108.252301 [arXiv:1202.6646 [nucl-th]].
- [45] K. J. Eskola, K. Kajantie, P. V. Ruuskanen and K. Tuominen, Nucl. Phys. B **570**, 379-389 (2000) doi:10.1016/S0550-3213(99)00720-8 [arXiv:hep-ph/9909456 [hep-ph]].
- [46] K. J. Eskola, K. Kajantie and K. Tuominen, Phys. Lett. B **497**, 39-43 (2001) doi:10.1016/S0370-2693(00)01341-1 [arXiv:hep-ph/0009246 [hep-ph]].
- [47] R. Paatelainen, K. J. Eskola, H. Niemi and K. Tuominen, Phys. Lett. B **731**, 126-130 (2014) doi:10.1016/j.physletb.2014.02.018 [arXiv:1310.3105 [hep-ph]].
- [48] T. Pierog and K. Werner, Nucl. Phys. B Proc. Suppl. **196**, 102-105 (2009) doi:10.1016/j.nuclphysbps.2009.09.017 [arXiv:0905.1198 [hep-ph]].
- [49] T. Pierog, I. Karpenko, J. M. Katzy, E. Yatsenko

- and K. Werner, Phys. Rev. C **92**, no.3, 034906 (2015) doi:10.1103/PhysRevC.92.034906 [arXiv:1306.0121 [hep-ph]].
- [50] K. Werner, B. Guiot, I. Karpenko and T. Pierog, Phys. Rev. C **89**, no.6, 064903 (2014) doi:10.1103/PhysRevC.89.064903 [arXiv:1312.1233 [nucl-th]].
- [51] K. Werner, Phys. Rev. C **108**, no.6, 064903 (2023) doi:10.1103/PhysRevC.108.064903 [arXiv:2301.12517 [hep-ph]].
- [52] K. Werner, Phys. Rev. C **109**, no.1, 014910 (2024) doi:10.1103/PhysRevC.109.014910 [arXiv:2306.10277 [hep-ph]].
- [53] K. Werner and B. Guiot, Phys. Rev. C **108**, no.3, 034904 (2023) doi:10.1103/PhysRevC.108.034904 [arXiv:2306.02396 [hep-ph]].
- [54] L. G. Pang, G. Y. Qin, V. Roy, X. N. Wang and G. L. Ma, Phys. Rev. C **91**, no.4, 044904 (2015) doi:10.1103/PhysRevC.91.044904 [arXiv:1410.8690 [nucl-th]].
- [55] Y. Kanakubo, Y. Tachibana and T. Hirano, Phys. Rev. C **101**, no.2, 024912 (2020) doi:10.1103/PhysRevC.101.024912 [arXiv:1910.10556 [nucl-th]].
- [56] Y. Kanakubo, Y. Tachibana and T. Hirano, Phys. Rev. C **105**, no.2, 024905 (2022) doi:10.1103/PhysRevC.105.024905 [arXiv:2108.07943 [nucl-th]].
- [57] C. Bierlich, G. Gustafson, L. Lönnblad and H. Shah, JHEP **10**, 134 (2018) doi:10.1007/JHEP10(2018)134 [arXiv:1806.10820 [hep-ph]].
- [58] P. Carzon, M. Martinez, M. D. Sievert, D. E. Wertepny and J. Noronha-Hostler, Phys. Rev. C **105**, no.3, 034908 (2022) doi:10.1103/PhysRevC.105.034908 [arXiv:1911.12454 [nucl-th]].
- [59] O. Garcia-Montero, H. Elfner and S. Schlichting, Phys. Rev. C **109**, no.4, 044916 (2024) doi:10.1103/PhysRevC.109.044916 [arXiv:2308.11713 [hep-ph]].
- [60] K. Kajantie, P. V. Landshoff and J. Lindfors, Phys. Rev. Lett. **59**, 2527 (1987) doi:10.1103/PhysRevLett.59.2527
- [61] K. J. Eskola, K. Kajantie and J. Lindfors, Nucl. Phys. B **323**, 37-52 (1989) doi:10.1016/0550-3213(89)90586-5
- [62] K. J. Eskola and K. Kajantie, Z. Phys. C **75**, 515-522 (1997) doi:10.1007/s002880050495 [arXiv:nucl-th/9610015 [nucl-th]].
- [63] K. J. Eskola, H. Honkanen, H. Niemi, P. V. Ruuskanen and S. S. Rasanen, Phys. Rev. C **72**, 044904 (2005) doi:10.1103/PhysRevC.72.044904 [arXiv:hep-ph/0506049 [hep-ph]].
- [64] P. F. Kolb, U. W. Heinz, P. Huovinen, K. J. Eskola and K. Tuominen, Nucl. Phys. A **696**, 197-215 (2001) doi:10.1016/S0375-9474(01)01114-9 [arXiv:hep-ph/0103234 [hep-ph]].
- [65] H. Niemi, K. J. Eskola and P. V. Ruuskanen, Phys. Rev. C **79**, 024903 (2009) doi:10.1103/PhysRevC.79.024903 [arXiv:0806.1116 [hep-ph]].
- [66] K. J. Eskola and K. Tuominen, Phys. Rev. D **63**, 114006 (2001) doi:10.1103/PhysRevD.63.114006 [arXiv:hep-ph/0010319 [hep-ph]].
- [67] K. J. Eskola and K. Tuominen, Phys. Lett. B **489**, 329-336 (2000) doi:10.1016/S0370-2693(00)00946-1 [arXiv:hep-ph/0002008 [hep-ph]].
- [68] H. Niemi, K. J. Eskola, R. Paatelainen and K. Tuominen, Phys. Rev. C **93**, no.1, 014912 (2016) doi:10.1103/PhysRevC.93.014912 [arXiv:1511.04296 [hep-ph]].
- [69] K. J. Eskola, H. Niemi, R. Paatelainen and K. Tuominen, Phys. Rev. C **97**, no.3, 034911 (2018) doi:10.1103/PhysRevC.97.034911 [arXiv:1711.09803 [hep-ph]].
- [70] H. Niemi, K. J. Eskola, R. Paatelainen and K. Tuominen, Nucl. Phys. A **982**, 443-446 (2019) doi:10.1016/j.nuclphysa.2018.10.013 [arXiv:1807.02378 [nucl-th]].
- [71] I. Helenius, K. J. Eskola, H. Honkanen and C. A. Salgado, JHEP **07**, 073 (2012) doi:10.1007/JHEP07(2012)073 [arXiv:1205.5359 [hep-ph]].
- [72] The MC-EKRT code will be available at [url:github.com/mialkuha/MC-EKRT](https://github.com/mialkuha/MC-EKRT)
- [73] E. Molnar, H. Holopainen, P. Huovinen and H. Niemi, Phys. Rev. C **90**, no.4, 044904 (2014) doi:10.1103/PhysRevC.90.044904 [arXiv:1407.8152 [nucl-th]].
- [74] R. Paatelainen, K. J. Eskola, H. Holopainen and K. Tuominen, Phys. Rev. C **87**, no.4, 044904 (2013) doi:10.1103/PhysRevC.87.044904 [arXiv:1211.0461 [hep-ph]].
- [75] C. Loizides, J. Kamin and D. d'Enterria, Phys. Rev. C **97**, no.5, 054910 (2018) [erratum: Phys. Rev. C **99**, no.1, 019901 (2019)] doi:10.1103/PhysRevC.97.054910 [arXiv:1710.07098 [nucl-ex]].
- [76] C. W. De Jager, H. De Vries and C. De Vries, Atom. Data Nucl. Data Tabl. **14**, 479-508 (1974) [erratum: Atom. Data Nucl. Data Tabl. **16**, 580-580 (1975)] doi:10.1016/S0092-640X(74)80002-1
- [77] H. De Vries, C. W. De Jager and C. De Vries, Atom. Data Nucl. Data Tabl. **36**, 495-536 (1987) doi:10.1016/0092-640X(87)90013-1
- [78] R. D. Woods and D. S. Saxon, Phys. Rev. **95**, 577-578 (1954) doi:10.1103/PhysRev.95.577
- [79] C. Loizides, J. Nagle and P. Steinberg, SoftwareX **1-2**, 13-18 (2015) doi:10.1016/j.softx.2015.05.001 [arXiv:1408.2549 [nucl-ex]].
- [80] J. R. Cudell *et al.* [COMPETE], Phys. Rev. Lett. **89**, 201801 (2002) doi:10.1103/PhysRevLett.89.201801 [arXiv:hep-ph/0206172 [hep-ph]].
- [81] G. Antchev *et al.* [TOTEM], Eur. Phys. J. C **79**, no.2, 103 (2019) doi:10.1140/epjc/s10052-019-6567-0 [arXiv:1712.06153 [hep-ex]].
- [82] X. N. Wang and M. Gyulassy, Phys. Rev. D **44**, 3501-3516 (1991) doi:10.1103/PhysRevD.44.3501
- [83] S. Chekanov *et al.* [ZEUS], Eur. Phys. J. C **24**, 345-360 (2002) doi:10.1007/s10052-002-0953-7 [arXiv:hep-ex/0201043 [hep-ex]].
- [84] K. J. Eskola, C. A. Flett, V. Guzey, T. Löytäinen and H. Paukkunen, Phys. Rev. C **106**, no.3, 035202 (2022) doi:10.1103/PhysRevC.106.035202 [arXiv:2203.11613 [hep-ph]].
- [85] C. A. Flett, "Exclusive Observables to NLO and Low x PDF Phenomenology at the LHC," Ph.D. thesis, University of Liverpool, 2021
- [86] X. N. Wang, Phys. Rev. D **43**, 104-112 (1991) doi:10.1103/PhysRevD.43.104
- [87] L. Durand and P. Hong, Phys. Rev. Lett. **58**, 303-306 (1987) doi:10.1103/PhysRevLett.58.303
- [88] E. Eichten, I. Hinchliffe, K. D. Lane and



- C. Quigg, *Rev. Mod. Phys.* **56**, 579-707 (1984) doi:10.1103/RevModPhys.56.579
- [89] I. Sarcevic, S. D. Ellis and P. Carruthers, *Phys. Rev. D* **40**, 1446 (1989) doi:10.1103/PhysRevD.40.1446
- [90] K. J. Eskola, H. Paukkunen and C. A. Salgado, *JHEP* **04**, 065 (2009) doi:10.1088/1126-6708/2009/04/065 [arXiv:0902.4154 [hep-ph]].
- [91] K. J. Eskola, P. Paakkinen, H. Paukkunen and C. A. Salgado, *Eur. Phys. J. C* **77**, no.3, 163 (2017) doi:10.1140/epjc/s10052-017-4725-9 [arXiv:1612.05741 [hep-ph]].
- [92] K. J. Eskola, P. Paakkinen, H. Paukkunen and C. A. Salgado, *Eur. Phys. J. C* **82**, no.5, 413 (2022) doi:10.1140/epjc/s10052-022-10359-0 [arXiv:2112.12462 [hep-ph]].
- [93] I. Helenius, M. Walt and W. Vogelsang, *Phys. Rev. D* **105**, no.9, 094031 (2022) doi:10.1103/PhysRevD.105.094031 [arXiv:2112.11904 [hep-ph]].
- [94] R. Abdul Khalek, R. Gauld, T. Giani, E. R. Nocera, T. R. Rabemananjara and J. Rojo, *Eur. Phys. J. C* **82**, no.6, 507 (2022) doi:10.1140/epjc/s10052-022-10417-7 [arXiv:2201.12363 [hep-ph]].
- [95] P. Duwentäster, T. Ježo, M. Klasen, K. Kovařík, A. Kusina, K. F. Muzakka, F. I. Olness, R. Ruijz, I. Schienbein and J. Y. Yu, *Phys. Rev. D* **105**, no.11, 114043 (2022) doi:10.1103/PhysRevD.105.114043 [arXiv:2204.09982 [hep-ph]].
- [96] K. J. Eskola, *Z. Phys. C* **51**, 633-642 (1991) doi:10.1007/BF01565590
- [97] S. R. Klein and R. Vogt, *Phys. Rev. Lett.* **91**, 142301 (2003) doi:10.1103/PhysRevLett.91.142301 [arXiv:nucl-th/0305046 [nucl-th]].
- [98] R. Vogt, *Phys. Rev. C* **70**, 064902 (2004) doi:10.1103/PhysRevC.70.064902
- [99] L. Frankfurt, V. Guzey and M. Strikman, *Phys. Rept.* **512**, 255-393 (2012) doi:10.1016/j.physrep.2011.12.002 [arXiv:1106.2091 [hep-ph]].
- [100] S. Dulat, T. J. Hou, J. Gao, M. Guzzi, J. Huston, P. Nadolsky, J. Pumplin, C. Schmidt, D. Stump and C. P. Yuan, *Phys. Rev. D* **93**, no.3, 033006 (2016) doi:10.1103/PhysRevD.93.033006 [arXiv:1506.07443 [hep-ph]].
- [101] A. Buckley, J. Ferrando, S. Lloyd, K. Nordström, B. Page, M. Rüfenacht, M. Schönherr and G. Watt, *Eur. Phys. J. C* **75**, 132 (2015) doi:10.1140/epjc/s10052-015-3318-8 [arXiv:1412.7420 [hep-ph]].
- [102] H. Hirvonen, M. Kuha, J. Auvinen, K. J. Eskola, Y. Kanakubo, H. Niemi, work in progress
- [103] S. Chatrchyan *et al.* [CMS], *Eur. Phys. J. C* **74**, no.7, 2951 (2014) doi:10.1140/epjc/s10052-014-2951-y [arXiv:1401.4433 [nucl-ex]].
- [104] G. S. Denicol, H. Niemi, E. Molnar and D. H. Rischke, *Phys. Rev. D* **85**, 114047 (2012) [erratum: *Phys. Rev. D* **91**, no.3, 039902 (2015)] doi:10.1103/PhysRevD.85.114047 [arXiv:1202.4551 [nucl-th]].
- [105] W. Israel and J. M. Stewart, *Annals Phys.* **118**, 341-372 (1979) doi:10.1016/0003-4916(79)90130-1
- [106] E. Molnár, H. Niemi, G. S. Denicol and D. H. Rischke, *Phys. Rev. D* **89**, no.7, 074010 (2014) doi:10.1103/PhysRevD.89.074010 [arXiv:1308.0785 [nucl-th]].
- [107] G. S. Denicol, T. Koide and D. H. Rischke, *Phys. Rev. Lett.* **105**, 162501 (2010) doi:10.1103/PhysRevLett.105.162501 [arXiv:1004.5013 [nucl-th]].
- [108] P. Huovinen and P. Petreczky, *Nucl. Phys. A* **837**, 26-53 (2010) doi:10.1016/j.nuclphysa.2010.02.015 [arXiv:0912.2541 [hep-ph]].
- [109] P. Huovinen, *Eur. Phys. J. A* **37**, 121-128 (2008) doi:10.1140/epja/i2007-10611-3 [arXiv:0710.4379 [nucl-th]].
- [110] J. P. Boris and D. L. Book, *J. Comput. Phys.* **11**, 38 (1973).
- [111] E. Molnar, H. Niemi and D. H. Rischke, *Eur. Phys. J. C* **65**, 615-635 (2010) doi:10.1140/epjc/s10052-009-1194-9 [arXiv:0907.2583 [nucl-th]].
- [112] F. Cooper and G. Frye, *Phys. Rev. D* **10**, 186 (1974) doi:10.1103/PhysRevD.10.186
- [113] F. Debbasch, W. A. van Leeuwen, *Physica A* **388**, 1079-1104 (2009).
- [114] K. J. Eskola and X. N. Wang, *Phys. Rev. D* **49**, 1284-1292 (1994) doi:10.1103/PhysRevD.49.1284 [arXiv:nucl-th/9307011 [nucl-th]].
- [115] A. Bazavov *et al.* [HotQCD], *Phys. Lett. B* **795**, 15-21 (2019) doi:10.1016/j.physletb.2019.05.013 [arXiv:1812.08235 [hep-lat]].
- [116] J. Adam *et al.* [ALICE], *Phys. Lett. B* **772**, 567-577 (2017) doi:10.1016/j.physletb.2017.07.017 [arXiv:1612.08966 [nucl-ex]].
- [117] J. Adam *et al.* [ALICE], *Phys. Rev. Lett.* **116**, no.22, 222302 (2016) doi:10.1103/PhysRevLett.116.222302 [arXiv:1512.06104 [nucl-ex]].
- [118] E. Abbas *et al.* [ALICE], *Phys. Lett. B* **726**, 610-622 (2013) doi:10.1016/j.physletb.2013.09.022 [arXiv:1304.0347 [nucl-ex]].
- [119] K. Aamodt *et al.* [ALICE], *Phys. Rev. Lett.* **106**, 032301 (2011) doi:10.1103/PhysRevLett.106.032301 [arXiv:1012.1657 [nucl-ex]].
- [120] B. B. Back, M. D. Baker, D. S. Barton, R. R. Betts, M. Ballintijn, A. A. Bickley, R. Bindel, A. Budzanowski, W. Busza and A. Carroll, *et al.* *Phys. Rev. Lett.* **91**, 052303 (2003) doi:10.1103/PhysRevLett.91.052303 [arXiv:nucl-ex/0210015 [nucl-ex]].
- [121] J. Adam *et al.* [ALICE], *Phys. Lett. B* **762**, 376-388 (2016) doi:10.1016/j.physletb.2016.07.017 [arXiv:1605.02035 [nucl-ex]].
- [122] B. B. Back *et al.* [PHOBOS], *Phys. Rev. C* **72**, 051901 (2005) doi:10.1103/PhysRevC.72.051901 [arXiv:nucl-ex/0407012 [nucl-ex]].
- [123] A. Bilandzic, R. Snellings and S. Voloshin, *Phys. Rev. C* **83**, 044913 (2011) doi:10.1103/PhysRevC.83.044913 [arXiv:1010.0233 [nucl-ex]].
- [124] V. Khachatryan *et al.* [CMS], *Phys. Rev. C* **92**, no.3, 034911 (2015) doi:10.1103/PhysRevC.92.034911 [arXiv:1503.01692 [nucl-ex]].
- [125] M. Aaboud *et al.* [ATLAS], *Eur. Phys. J. C* **78**, no.2, 142 (2018) doi:10.1140/epjc/s10052-018-5605-7 [arXiv:1709.02301 [nucl-ex]].
- [126] K. J. Eskola, K. Kajantie and J. Lindfors, *Phys. Lett. B* **214**, 613-616 (1988) doi:10.1016/0370-2693(88)90130-X
- [127] Z. Xu and C. Greiner, *Phys. Rev. C* **71**, 064901 (2005) doi:10.1103/PhysRevC.71.064901 [arXiv:hep-ph/0406278 [hep-ph]].
- [128] A. Kurkela and E. Lu, *Phys. Rev. Lett.* **113**, no.18, 182301 (2014) doi:10.1103/PhysRevLett.113.182301 [arXiv:1405.6318 [hep-ph]].

- [129] A. Kurkela and Y. Zhu, Phys. Rev. Lett. **115**, no.18, 182301 (2015) doi:10.1103/PhysRevLett.115.182301 [arXiv:1506.06647 [hep-ph]].
- [130] A. Kurkela, A. Mazeliauskas, J. F. Paquet, S. Schlichting and D. Teaney, Phys. Rev. C **99**, no.3, 034910 (2019) doi:10.1103/PhysRevC.99.034910 [arXiv:1805.00961 [hep-ph]].
- [131] A. Kurkela and A. Mazeliauskas, Phys. Rev. D **99**, no.5, 054018 (2019) doi:10.1103/PhysRevD.99.054018 [arXiv:1811.03068 [hep-ph]].
- [132] A. Kurkela, A. Mazeliauskas, J. F. Paquet, S. Schlichting and D. Teaney, Phys. Rev. Lett. **122**, no.12, 122302 (2019) doi:10.1103/PhysRevLett.122.122302 [arXiv:1805.01604 [hep-ph]].
- [133] A. Kurkela and A. Mazeliauskas, Phys. Rev. Lett. **122**, 142301 (2019) doi:10.1103/PhysRevLett.122.142301 [arXiv:1811.03040 [hep-ph]].
- [134] X. Du and S. Schlichting, Phys. Rev. D **104**, no.5, 054011 (2021) doi:10.1103/PhysRevD.104.054011 [arXiv:2012.09079 [hep-ph]].
- [135] X. Du and S. Schlichting, Phys. Rev. Lett. **127**, no.12, 122301 (2021) doi:10.1103/PhysRevLett.127.122301 [arXiv:2012.09068 [hep-ph]].
- [136] P. Carzon, M. Martinez, J. Noronha-Hostler, P. Plaschke, S. Schlichting and M. Sievert, Phys. Rev. C **108**, no.6, 064905 (2023) doi:10.1103/PhysRevC.108.064905 [arXiv:2301.04572 [nucl-th]].
- [137] F. Zhou, J. Brewer and A. Mazeliauskas, [arXiv:2402.09298 [hep-ph]].
- [138] M. Gyulassy, I. Vitev, X. N. Wang and P. Huovinen, Phys. Lett. B **526**, 301-308 (2002) doi:10.1016/S0370-2693(02)01157-7 [arXiv:nucl-th/0109063 [nucl-th]].
- [139] M. Okai, K. Kawaguchi, Y. Tachibana and T. Hirano, Phys. Rev. C **95**, no.5, 054914 (2017) doi:10.1103/PhysRevC.95.054914 [arXiv:1702.07541 [nucl-th]].
- [140] K. J. Eskola, K. Kajantie, P. V. Ruuskanen and K. Tuominen, Phys. Lett. B **543**, 208-216 (2002) doi:10.1016/S0370-2693(02)02457-7 [arXiv:hep-ph/0204034 [hep-ph]].



### III

## EFFECTS OF SATURATION AND FLUCTUATING HOTSPOTS FOR FLOW OBSERVABLES IN ULTRARELATIVISTIC HEAVY-ION COLLISIONS

by






H. Hirvonen, M. Kuha, J. Auvinen, K. J. Eskola, Y. Kanakubo, H. Niemi

Phys. Rev. C 110 3, 034911 (2024).

<https://doi.org/10.1103/physrevc.110.034911>

Reproduced with kind permission of American Physical Society.

## Effects of saturation and fluctuating hotspots for flow observables in ultrarelativistic heavy-ion collisions

Henry Hirvonen, Mikko Kuha , Jussi Auvinen , Kari J. Eskola , Yuuka Kanakubo , and Harri Niemi   
*University of Jyväskylä, Department of Physics, P.O. Box 35, FI-40014 University of Jyväskylä, Finland  
 and Helsinki Institute of Physics, P.O. Box 64, FI-00014 University of Helsinki, Finland*



(Received 3 July 2024; accepted 29 August 2024; published 20 September 2024)

We investigate the effects of saturation dynamics on midrapidity flow observables by adding fluctuating hotspots into the novel Monte Carlo EKRT (MC-EKRT) event generator for high-energy nuclear collisions. We demonstrate that the intensity of the saturation effects significantly affects the ratio between the flow coefficients  $v_3$  and  $v_2$  at the LHC. Adding a hotspot substructure to the nucleons enhances the saturation effects and improves the agreement with the measured data. We show that the collision-energy dependence of the flow coefficients obtained using the MC-EKRT initial states with hotspots is improved in comparison with the earlier event-by-event EKRT model. In addition, we present the results for the charged hadron multiplicity distribution in Pb+Pb collisions at the LHC, and show that the minijet multiplicity originating fluctuations of the saturation scale included in MC-EKRT, as well as the presence of hotspots, are necessary for describing the measured large-multiplicity tail in the distribution.

DOI: [10.1103/PhysRevC.110.034911](https://doi.org/10.1103/PhysRevC.110.034911)

### I. INTRODUCTION

The highest-energy nucleus-nucleus collisions, ultrarelativistic heavy-ion collisions, which are currently performed at the CERN Large Hadron Collider (LHC) and at the Brookhaven National Laboratory (BNL) Relativistic Heavy Ion Collider (RHIC), aim at determining the properties of the nearly net-baryon-free hot quark-gluon plasma (QGP). One also strives for a detailed understanding of the strong-interaction dynamics that is responsible for the creation and further evolution of the QGP in these collisions. See, e.g., Ref. [1] for a review.

According to lattice simulations of quantum chromodynamics (QCD), the theory of the strong interaction, the strongly interacting matter takes the form of the QGP at high temperatures of  $T \gtrsim 150\text{--}160$  MeV [2,3] at a vanishing baryochemical potential. Quarks and gluons can be produced in ultrarelativistic heavy-ion collisions from the kinetic energy of the colliding nuclei so copiously that the effective temperature (energy over particle ratio) of the system clearly exceeds 160 MeV. In these conditions, the normal formation of the color-confined, color-singlet bound states, hadrons, is momentarily inhibited, and a nearly thermalized QGP, where the degrees of freedom are colored gluons, quarks, and anti-quarks, can be formed. The subsequent spacetime evolution stages of such a QCD matter—the expansion and cooling of

the QGP, the crossover transition to a hadron gas, followed by the expansion and cooling of the hadron gas—as well as the simultaneous appearance of the QGP and hadron-gas phases in different density regions of the expanding system, are describable in terms of relativistic dissipative fluid dynamics [4–27]. While QCD is a cornerstone of the standard model of particle physics, relativistic fluid dynamics has become a standard tool in the analysis of heavy-ion observables.

The determination of the QCD matter properties, such as its equation of state and transport properties such as the shear and bulk viscosities, from the measured LHC and RHIC observables is a highly challenging task. Clearly, a precise determination requires a simultaneous analysis of as many heavy-ion observables as possible, from as many collision systems and collision energies as possible—a global analysis of heavy-ion observables [11,14,17,28]. A proper statistical analysis, Bayesian inference [26,29–40] is necessary for setting well-defined uncertainties to the extracted matter properties. Interestingly, neural networks are currently making it possible to include also statistics-expensive observables, such as complicated rare flow correlators, into the global analysis [41,42] (see also Ref. [43]).

The mentioned global analyses of heavy-ion observables are based on a fluid-dynamical description, which takes initial densities and flow velocities of the produced QCD matter as initial conditions. One either parametrizes these initial conditions [26,29–33,35–40,44] or tries to compute them from a QCD dynamical model for the initial production of gluons and quarks [14,17,28,38]. In both cases there is some number of fit parameters that characterize the initial states, and these will obviously be correlated with the actual QCD-matter properties extracted from the data via Bayesian inference. It is therefore important to model the QCD-matter initial states based on

*Published by the American Physical Society under the terms of the Creative Commons Attribution 4.0 International license. Further distribution of this work must maintain attribution to the author(s) and the published article's title, journal citation, and DOI. Funded by SCOAP<sup>3</sup>.*

QCD dynamics as far as is possible, in order to understand the dominant particle production mechanism, to reduce the uncertainties in the extraction of the initial states, and to have predictive power for moving from one system to another.

The EKRT (Eskola-Kajantie-Ruuskanen-Tuominen) model [17,45–47], which treats the nuclear collisions as collisions of parton clouds, and supplements a perturbative QCD (pQCD) calculation for the production of few-GeV partons (minijets) [48,49] with a collinear factorization-inspired QCD saturation mechanism [17,47] for regulating the small- $p_T$  minijet production ( $p_T$  being transverse momentum), is an example of such a QCD-based initial state modeling with predictive power. The event-by-event (EbyE) version of the model, EbyE-EKRT [17], has been quite successful in explaining a large collection of heavy-ion bulk observables at the LHC and RHIC [17,28,34,50–52]. The latest progress here is the novel Monte Carlo (MC)-EKRT event generator, introduced recently in Ref. [53], and employed in the present paper.

The new features in MC-EKRT [53] relative to EbyE-EKRT [17] are that now the produced partonic system contains local fluctuations of the minijet multiplicity, which in turn induce dynamical fluctuations to the saturation controlling the initial parton production. Also per-nucleon conservation of energy and valence-quark numbers are accounted for. MC-EKRT also introduces a new type of spatially dependent nuclear parton distribution functions (snPDFs) that are specific to the nucleon configuration in each event and can cope with the largest density fluctuations of the nucleon densities. Thanks to these new features, MC-EKRT gives initial conditions for full (3+1)-dimensional [(3+1)D] EbyE fluid dynamics, and thus enables the studies of rapidity-dependent observables, such as rapidity distributions of yields and flow coefficients of charged hadrons in Pb+Pb collisions at the LHC and at the highest-energy Au+Au collisions at RHIC, see Ref. [53].

In this paper, we employ the new MC-EKRT framework for computing event-by-event initial conditions for (2+1)D dissipative shear- and bulk-viscous second-order transient fluid dynamics in the midrapidity unit of 5.02 and 2.76 TeV Pb+Pb collisions at the LHC. In particular, we study the sensitivity of the flow coefficients  $v_n$  to the model details, such as the nucleonic width and substructure, the Gaussian smearing in coupling the individual minijets to continuous fluid dynamics, as well as the order in which we do the minijet filtering based on saturation and conservation of energy. In addition, we show how the added minijet multiplicity fluctuations are the piece formerly missing from EbyE-EKRT in explaining the behavior of the charged multiplicity distributions in the most central collisions. The recently developed neural networks for predicting flow observables directly from the initial energy density event by event [41,42], are also utilized. As the main result of this paper, we show that a detailed simultaneous description of the  $v_n$ 's requires saturation to be the driving QCD mechanism for initial parton production. In particular, this result calls for further nucleonic substructure, hotspots, to be introduced in MC-EKRT. We also implement these in MC-EKRT and discuss their interesting interplay with saturation, in describing the  $v_2/v_3$  ratio

as well as in explaining the measured charged multiplicity distributions.

## II. MC-EKRT INITIAL STATE FOR FLUID DYNAMICS

### A. Minijet sampling

The MC-EKRT event generator of Ref. [53] produces partonic initial states, i.e., saturated systems of gluons and quarks with  $p_T \gtrsim p_0 \sim 1$  GeV, that can be fed as initial conditions to (3+1)D event-by-event fluid-dynamical simulations. The generation of such MC-EKRT initial states proceeds via the following steps (for details, see Ref. [53]).

First, the nucleon configurations of the colliding (here spherically symmetric) nuclei  $A$  and  $B$  are generated by sampling the standard two-parameter Woods-Saxon distribution, and by requiring an exclusion radius of 0.4 fm. A squared impact parameter  $b_{AB}^2$  for the  $A + B$  collision, defining the distance between the centers of masses of the colliding nuclei, is sampled from a uniform distribution. In the absence of hotspots (i.e., without subnucleonic density fluctuations), the  $A + B$  collision is triggered using MC Glauberlike black-disc nucleons with a trigger cross section identical to the inelastic nucleon-nucleon cross section  $\sigma_{\text{inel}}^{\text{NN}}$ , which is obtained from the measured total and elastic nucleon-nucleon cross sections as a function of the nucleon-nucleon center-of-momentum system (CMS) energy  $\sqrt{s_{\text{NN}}}$  [54,55].

Once the  $A + B$  collision is triggered, MC-EKRT does not consider nucleonic subcollisions at all but pictures the entire nuclear collision as a collision of two extensive parton clouds. For distributing the parton subclouds spatially around each nucleon, MC-EKRT assumes a Gaussian thickness function,

$$T_N(\bar{s}) = \frac{1}{2\pi\sigma_N^2} \exp\left(-\frac{|\bar{s}|^2}{2\sigma_N^2}\right), \quad (1)$$

with a width parameter  $\sigma_N = \sigma_N(\sqrt{s_{\text{NN}}})$  that is obtained from exclusive photoproduction of  $J/\Psi$  in photon-proton collisions at HERA [56,57]. Then, multiple dijet production, i.e., the number of independent dijets with jet transverse momentum  $p_T \gtrsim p_0 = 1$  GeV, that is assigned to originate from each  $ab$  pair, is sampled from a Poissonian probability distribution with a mean

$$\bar{N}_{\text{jets}}^{ab} = T_{\text{NN}}(\bar{b}_{ab}) \sigma_{\text{jet}}^{ab}(p_0, \sqrt{s_{\text{NN}}}, \{\bar{s}_a\}, \{\bar{s}_b\}), \quad (2)$$

where  $T_{\text{NN}}(\bar{b}_{ab})$  is the nucleonic overlap function and  $\bar{b}_{ab}$  is the impact parameter between the nucleons  $a$  and  $b$ , while  $\sigma_{\text{jet}}^{ab}$  is the integrated pQCD (mini)jet cross section, which MC-EKRT computes using the novel snPDFs for  $a$  and  $b$ , and all possible leading-order (LO) partonic  $2 \rightarrow 2$  subprocesses. A CMS-energy-dependent multiplicative  $K$  factor is introduced to  $\sigma_{\text{jet}}^{ab}$  as a free fit parameter, to account for the missing higher-order contributions. The (mini)jet cross section depends on the transverse momentum cutoff parameter  $p_0$ , on the CMS energy  $\sqrt{s_{\text{NN}}}$ , as well as on the transverse locations  $\bar{s}_a$  and  $\bar{s}_b$  of  $a$  and  $b$  in the nucleon configurations of  $A$  and  $B$ , indicated here with  $\{\bar{s}_a\}$  and  $\{\bar{s}_b\}$ .

As explained in detail Ref. [53], the novel snPDFs are now nucleon-configuration specific and account for the nuclear



modifications of each nucleon's PDFs caused by all other nucleons in the nucleus. In other words, the MC-EKRT snPDFs are nucleon specific and nucleon-configuration specific. Also noteworthy is that these novel snPDFs can fully cope with the event-by-event density fluctuations, which was not the case with the formerly developed spatial nPDFs, such as those in Ref. [58]. The MC-EKRT snPDFs are normalized (averaging over all nucleons in each nucleus and over a large number of nuclei) to the spatially averaged nuclear PDF modifications of the EPS09LO set [59], and CT14LO [60] are employed for the free proton PDFs.

Finally, the transverse location for each produced dijet is sampled from the product of the two overlap functions  $T_N$ , whose transverse integral gives the usual overlap function  $T_{NN}$ . The kinematic variables and the flavor chemistry of the produced partons, along with identifying the valence quark-consuming processes, is sampled from the differential jet sub-cross-sections, as explained in Ref. [53].

### B. Minijet filtering

The next, and decisive, step in MC-EKRT is the filtering of the excessive candidate dijets, based on the EKRT saturation [17,45–47] and conservation of energy and valence quark numbers. As explained in Refs. [17,47,53] saturation here is expected to occur when all the higher-order ( $n > 2$ )  $\rightarrow 2$  parton processes start to dominate over the  $2 \rightarrow 2$  ones. For maintaining collinear factorization at the highest values of jet transverse momenta, the filterings are performed in the order of decreasing factorization scale, which here is the jet  $p_T$ . Then, the highest- $p_T$  partons can remain in the system while the lower- $p_T$  ones may get filtered away.

For the saturation filtering, MC-EKRT assigns a transverse radius  $1/(\kappa_{\text{sat}} p_T)$  for each dijet candidate, where  $\kappa_{\text{sat}}$  is a packing factor, a free parameter to be fitted from the data. The transverse position of each candidate dijet is kept track of, and a candidate dijet gets filtered away if it overlaps with any of the previously accepted dijets. As shown in Ref. [53], after the saturation filtering the  $p_T$  distribution of surviving partons is not anymore sensitive to the original cutoff parameter  $p_0$  but now saturation is the dynamical and local regulation mechanism for these distributions. This is the major difference to the traditional minijet eikonal models (and models alike), which are employed in event generators describing multiparton interactions, such as HIJING [61].

Similarly, MC-EKRT keeps track of all the longitudinal momentum fractions and valence quarks drawn out from their mother nucleons by the candidate dijets. If the candidate dijet would make its mother nucleon exceed its energy or valence-quark budget, again checking the dijet candidates in the order of decreasing  $p_T$ , then that dijet candidate gets filtered away. In the EKRT framework, in the spirit of suggesting saturation as the dominant QCD mechanism that regulates and controls initial parton production in highest-energy nuclear collisions, the default is to do the saturation filtering first, and only then the energy and valence-quark number conservation filterings. There is, however, an option in the code, which we utilize, and consequences we study in this paper, to have all the filterings done simultaneously.

### C. Nucleon substructure and hotspot trigger

The fluctuating substructure to the nucleons of the MC-EKRT framework is implemented as follows. While there is clear evidence that the nucleon substructure is necessary for describing the measured incoherent  $J/\psi$  photoproduction [62], the situation is less clear in heavy-ion collisions. The global analyses performed in Refs. [37,44] provide a slight preference towards the inclusion of the nucleon substructure, but the evidence is not conclusive. However, these analyses use the T<sub>R</sub>ENTo [63] initial-state model, in which the effect of the substructure can partly be compensated with other initial-state parameters.

In the MC-EKRT model, the addition of the nucleon substructure enhances the saturation effects since it confines the minijet production into more localized transverse regions. This leads to a change in the initial geometry, which might have an impact on the flow observables. The nucleon substructure is implemented by introducing Gaussian hotspots to the nucleon thickness function:

$$T_N(\vec{s}) = \frac{1}{N_h} \sum_{i=1}^{N_h} \frac{1}{2\pi\sigma_h^2} \exp\left(-\frac{|\vec{s} - \vec{s}_i^h|^2}{2\sigma_h^2}\right), \quad (3)$$

where  $N_h$  is the number of hotspots, and  $\sigma_h$  is the width of the hotspot. In this paper,  $N_h = 3$  is always used when the nucleon substructure is enabled. The hotspot locations  $\vec{s}_i^h$  are sampled from a two-dimensional Gaussian distribution with a width  $\sigma_s$ . The total nucleon width  $\sigma_N$  is then related to the hotspot widths via  $\sigma_N^2 = \sigma_s^2 + \sigma_h^2$ . Therefore, only two of the three widths are independent. As in Refs. [53,57,64], the energy dependence of the total nucleon width is parametrized as  $\sigma_N = \sqrt{b}$  with

$$b/\text{GeV}^{-2} = b_0 + 4\alpha'_p \ln\left(\frac{W}{W_0}\right), \quad (4)$$

where  $W = \sqrt{s_{NN}}$ , and  $b_0$ ,  $\alpha'_p$ , and  $W_0$  are fit parameters. In the present paper, our default choice of parameters, based on the H1 measurements [64], are  $b_0 = 4.63$ ,  $\alpha'_p = 0.164$ , and  $W_0 = 90$  GeV. This corresponds to  $\sigma_N = 0.517$  fm for 2.76 TeV, and  $\sigma_N = 0.532$  fm for 5.023 TeV collision energies.

In principle, the nucleon substructure needs to be accounted for when performing the triggering of the nuclear collision event [65,66] since otherwise there might be events where the collision is accepted even though there is no hadronic interaction. As mentioned before, without any substructure, the triggering is done by assuming hard-sphere scattering between two nucleons. The event is accepted if the distance  $d_{\text{min}}^{\text{NN}}$  between any nucleons  $a \in A$  and  $b \in B$  satisfy

$$d_{\text{min}}^{\text{NN}} < \sqrt{\frac{\sigma_{\text{inel}}^{\text{NN}}}{\pi}}, \quad (5)$$

where  $\sigma_{\text{inel}}^{\text{NN}}$  is the inelastic nucleon-nucleon cross section. The same kind of geometrical criterion can be extended to account for the locations of the hotspots. That is, the triggering with the nucleon substructure is done based on the minimum

distance between two colliding hotspots  $d_{\min}^{\text{HS}}$ , i.e.,

$$d_{\min}^{\text{HS}} < \sqrt{\frac{\sigma_{\text{HS}}}{\pi}}, \quad (6)$$

where  $\sigma_{\text{HS}}$  is an effective hotspot-hotspot cross section fitted to reproduce the same nucleus-nucleus cross section as obtained with condition (5). Therefore, the value of  $\sigma_{\text{HS}}$  will depend on the hotspot sampling width  $\sigma_s$  and the collision system.

Even though in principle hotspot triggering could have a notable impact, we have noticed that in most cases all the measured observables remain nearly unchanged in the 0–80 % centrality range. The largest effects are most visible in the most peripheral charged particle multiplicity region, where usually no measured data are given. In the 60–80 % centralities, the differences in charged particle multiplicities are only a few percent at most. However, since in MC-EKRT we sample dijets from the same nucleon configuration until at least one is produced in a collision, the addition of hotspot triggering there speeds up the generation of the initial states.

#### D. Initialization of fluid dynamics

The initial condition of fluid dynamics is the energy-momentum tensor  $T^{\mu\nu}$  at some initial proper time  $\tau_0$ . However, MC-EKRT produces a list of massless partons with known momentum rapidities  $y_i$ , transverse momenta  $\mathbf{p}_{Ti}$ , and transverse coordinates  $\mathbf{x}_{\perp,0i}$ . Thus, the partons need to be propagated to the  $\tau_0$  surface and converted to the components of the energy-momentum tensor. Here we assume that all the partons are produced at the longitudinal location  $z_i = 0$  at time  $t = 0$ , and that they propagate as free particles to the proper time  $\tau_0 = 0.2$  fm. Therefore, spacetime and momentum rapidities are equivalent, i.e.,  $\eta_{s,i} = y_i$ . The spacetime coordinates of the parton  $i$  are then  $[\tau_0, \mathbf{x}_{\perp i}(\tau_0), \eta_{s,i}]$  where  $\mathbf{x}_{\perp i}(\tau_0) = \mathbf{x}_{\perp,0i} + \tau_0 \mathbf{p}_{Ti} / p_{Ti}$ .

The components of the energy-momentum tensor in the  $\tau - \eta_s$  coordinates are obtained as in Ref. [53],

$$\begin{aligned} T^{\alpha\beta}(x^\alpha) &= \sum_i \int d^2\mathbf{p}_T dy \frac{p^\alpha p^\beta}{p^\tau} \frac{1}{\tau} \cosh(y - \eta_s) \\ &\times \delta^{(2)}(\mathbf{x}_\perp - \mathbf{x}_{\perp i}) \delta(\eta_s - \eta_{s,i}) \delta^{(2)}(\mathbf{p}_T - \mathbf{p}_{Ti}) \\ &\times \delta(y - \eta_s), \end{aligned} \quad (7)$$

where the four-momentum  $p^\alpha = (p^\tau, \mathbf{p}_T, p^\eta)$  at a spacetime location  $x^\alpha = (\tau, \mathbf{x}_\perp, \eta_s)$  is given by

$$p^\alpha = \begin{pmatrix} p_T \cosh(y - \eta_s) \\ \mathbf{p}_T \\ \tau^{-1} p_T \sinh(y - \eta_s) \end{pmatrix}. \quad (8)$$

Depositing all energy and momentum of a parton into a single cell on a hydro grid as suggested by the delta functions appearing in Eq. (7) would lead to extreme fluctuations in energy and momentum densities. To obtain smooth density distributions, smearing is required. Here we are performing (2+1)D hydrodynamic simulations, where a natural choice is to let all partons that are produced in the midrapidity window  $\Delta y$  contribute to the fluid dynamical initial state. That

is, in Eq. (7) we replace  $\delta(\eta_s - \eta_{s,i}) \rightarrow \theta(\Delta y/2 - |\eta_{s,i}|)/\Delta y$ , where  $\theta$  is the Heaviside theta function. Here we use  $\Delta y = 1.0$ , but we have tested that the final results are practically insensitive to the choice of  $\Delta y$  as long as  $0.5 \leq \Delta y \leq 2.0$ . The smearing in the transverse  $(x, y)$  plane is performed by replacement  $\delta^{(2)}(\mathbf{x}_\perp - \mathbf{x}_{\perp i}) \rightarrow g_\perp(\mathbf{x}_\perp; \mathbf{x}_{\perp i})$ , where

$$g_\perp(\mathbf{x}_\perp; \mathbf{x}_{\perp i}) = \frac{C_\perp}{2\pi\sigma_\perp^2} \exp\left[-\frac{(\mathbf{x}_\perp - \mathbf{x}_{\perp i})^2}{2\sigma_\perp^2}\right] \quad (9)$$

is a Gaussian distribution with transverse smearing width  $\sigma_\perp$ , which is normalized as

$$\int d^2\mathbf{x}_\perp g_\perp(\mathbf{x}_\perp; \mathbf{x}_{\perp i}) = 1. \quad (10)$$

The computation cost is reduced by imposing a  $\pm 3\sigma_\perp$  cutoff on the smearing range, and the coefficient  $C_\perp$  takes care of the unit normalization.

As in Ref. [53], we only consider the local rest frame energy density  $e$  when initializing the fluid dynamical system, i.e., we neglect the initial transverse velocity and the initial components of the shear-stress tensor. Therefore, the initialization is determined by

$$T^{\tau\tau}(\tau_0, \mathbf{x}_\perp, \Delta y) = \frac{1}{\tau_0 \Delta y} \sum_i p_{Ti} g_\perp(\mathbf{x}_\perp; \mathbf{x}_{\perp i}) \theta(\Delta y/2 - |y_i|), \quad (11)$$

which in this case coincides with  $e$ . The remaining components are then obtained, using the equation of state, as  $T^{ij} = P(e)\delta^{ij}$ .

Finally, we emphasize that even if we utilize only the midrapidity minijets in computing the above initial conditions, the underlying MC-EKRT event generation is fully 3D. Thus, the midrapidity initial conditions are influenced also by the finite-rapidity effects in saturation and in energy conservation.

### III. FLUID SIMULATION FRAMEWORK

The simulations performed in this paper focus on midrapidity observables and therefore we assume that the longitudinal expansion of the system is boost invariant. The same framework as in Ref. [28] is used, i.e., we evolve the initially formed strongly interacting matter using dissipative fluid dynamics, and compute the final particle spectra at the dynamical decoupling surface. Additionally, the neural networks trained in Ref. [41] are utilized for significantly decreasing the computation time of the simulations. In this section, we give a brief recapitulation of each aspect of the framework.

#### A. Fluid dynamics

Fluid dynamics is based on the local conservation laws for energy, momentum, and conserved charges. Here we neglect the conserved charges, in which case the conservation law for the energy-momentum tensor,  $\partial_\mu T^{\mu\nu} = 0$ , controls the dynamics. The energy-momentum tensor can be decomposed with respect to four-velocity  $u^\mu$  as

$$T^{\mu\nu} = eu^\mu u^\nu - P\Delta^{\mu\nu} + \pi^{\mu\nu}, \quad (12)$$

where  $\Delta^{\mu\nu} = g^{\mu\nu} - u^\mu u^\nu$  is a projection operator,  $P = -\frac{1}{3}\Delta_{\mu\nu}T^{\mu\nu}$  is the total isotropic pressure,  $e = T^{\mu\nu}u_\mu u_\nu$  is the local rest frame energy density, and  $\pi^{\mu\nu} = T^{(\mu\nu)}$  is the shear-stress tensor. The angular brackets denote the symmetric, traceless part of the tensor that is orthogonal to the fluid four-velocity. Here the fluid velocity is defined in the Landau frame, i.e.,  $T^\mu{}_\nu u^\nu = e u^\mu$ . The bulk viscous pressure is defined as the deviation of the isotropic pressure  $P$  from the equilibrium pressure  $P_0$ , i.e.,  $\Pi = P - P_0$ . The equilibrium pressure is given by the equation of state (EoS) of the QCD matter at zero baryon density,  $P_0 = P_0(e)$ . In this work, we use the *s95p-v1* parametrization [67] for the EoS, which includes the partial chemical decoupling at  $T_{\text{chem}} = 155$  MeV. The partial chemical decoupling is implemented by adding temperature-dependent chemical potentials for each hadron in the hadronic part of the EoS [68–70].

The conservation laws together with the EoS are enough to solve the evolution in equilibrium, but additional constraints are needed when dissipative effects are present. The dissipative parts of the energy-momentum tensor are the shear-stress tensor and the bulk viscous pressure. In the formalism by Israel and Stewart [71], the equations of motion for dissipative parts take a form

$$\tau_\Pi \frac{d}{d\tau} \Pi + \Pi = -\zeta\theta - \delta_{\Pi\Pi}\Pi\theta + \lambda_{\Pi\pi}\pi^{\mu\nu}\sigma_{\mu\nu}, \quad (13)$$

$$\begin{aligned} \tau_\pi \frac{d}{d\tau} \pi^{(\mu\nu)} + \pi^{\mu\nu} &= 2\eta\sigma^{\mu\nu} + 2\tau_\pi \pi_\alpha^{(\mu} \omega^{\nu)\alpha} \\ &\quad - \delta_{\pi\pi}\pi^{\mu\nu}\theta - \tau_{\pi\pi} \pi_\alpha^{(\mu} \sigma^{\nu)\alpha} \\ &\quad + \varphi_7 \pi_\alpha^{(\mu} \pi^{\nu)\alpha} + \lambda_{\pi\Pi}\Pi\sigma^{\mu\nu}, \end{aligned} \quad (14)$$

where  $\theta = \nabla_\mu u^\mu$  is the expansion rate,  $\sigma^{\mu\nu} = \nabla^{(\mu} u^{\nu)}$  is the strain-rate tensor, and  $\omega^{\mu\nu} = \frac{1}{2}(\nabla^\mu u^\nu - \nabla^\nu u^\mu)$  is the vorticity tensor. The first-order transport coefficients  $\eta$  and  $\zeta$  are called shear and bulk viscosity, respectively. In a 14-moment approximation to the massless gas [72–75], the first-order transport coefficients are related to the shear and bulk relaxation times as

$$\tau_\pi = \frac{5\eta}{e + P_0}, \quad \tau_\Pi = \left(15\left(\frac{1}{3} - c_s^2\right)^2 (e + P_0)\right)^{-1} \zeta, \quad (15)$$

and the remaining second-order transport coefficients are

$$\begin{aligned} \delta_{\Pi\Pi} &= \frac{2}{3}\tau_\Pi, & \lambda_{\Pi\pi} &= \frac{8}{5}\left(\frac{1}{3} - c_s^2\right)\tau_\Pi, & \delta_{\pi\pi} &= \frac{4}{3}\tau_\pi, \\ \tau_{\pi\pi} &= \frac{10}{7}\tau_\pi, & \varphi_7 &= \frac{9}{70P_0}, & \lambda_{\pi\Pi} &= \frac{6}{5}\tau_\pi, \end{aligned} \quad (16)$$

where  $c_s$  is the speed of sound. The specific shear viscosity  $\eta/s$  and specific bulk viscosity  $\zeta/s$  are from the  $\eta/s = \text{dyn}$  parametrization introduced in Ref. [28].

### B. Decoupling and particle spectra

The fluid dynamic evolution is continued until reaching the kinetic decoupling surface. Here the decoupling surface

is determined by the dynamical decoupling conditions

$$\text{Kn} = \tau_\pi \theta = C_{\text{Kn}} \quad (17)$$

$$\frac{\gamma \tau_\pi}{R} = C_R, \quad (18)$$

where  $\text{Kn}$  is the Knudsen number,  $\gamma$  is the Lorentz gamma factor, and the coefficients  $C_{\text{Kn}}$  and  $C_R$  are proportionality constants of  $O(1)$ , which are fitted to the measured data. Here, values  $C_{\text{Kn}} = 0.8$  and  $C_R = 0.15$  are used according to Ref. [28]. The size of the system  $R$  is defined as

$$R = \sqrt{\frac{A}{\pi}}, \quad (19)$$

where  $A$  is the area in the transverse  $(x, y)$  plane where  $\text{Kn} < C_{\text{Kn}}$ . Additionally, the decoupling is forced to happen in the hadronic phase of the QCD matter, i.e., when  $T < 150$  MeV. Given these conditions the decoupling surface is determined using the Cornelius algorithm [76].

At the decoupling surface  $\Sigma$  with the directed surface element  $d\Sigma_\mu$ , the Lorentz-invariant particle spectrum for particle type  $i$  is computed according to the Cooper-Frye integral,

$$E \frac{d^3 N_i}{d^3 k} = \int_\Sigma d\Sigma_\mu k^\mu f_i(x, k), \quad (20)$$

where  $E$  and  $k^\mu$  are particles energy and four-momentum, respectively. The distribution function for particle species  $i$  is decomposed into in- and out-of-equilibrium parts as  $f_i = f_{0i} + \delta f_i$ , where the equilibrium part is given by

$$f_{0i}(x, k) = \left[ \exp\left(\frac{k_i^\mu u_\mu - \mu_i}{T}\right) \pm 1 \right]^{-1}, \quad (21)$$

where  $+$  ( $-$ ) sign is for fermions (bosons), and  $\mu_i$  is the chemical potential. Here, the viscous corrections to the equilibrium distribution are of the form [6,77–79]

$$\begin{aligned} \delta f_i &= -f_{0i} \tilde{f}_{0i} \frac{C_{\text{bulk}}}{T} \left[ \frac{m_i^2}{3E_k} - \left(\frac{1}{3} - c_s^2\right) E_k \right] \Pi \\ &\quad + \frac{f_{0i} \tilde{f}_{0i}}{2T^2 (e + P_0)} \pi^{\mu\nu} k_\mu k_\nu, \end{aligned} \quad (22)$$

with  $\tilde{f}_{0i} = 1 \pm f_{0i}$  ( $+$  for bosons and  $-$  for fermions) and the coefficient

$$\frac{1}{C_{\text{bulk}}} = \sum_i \frac{g_i m_i^2}{3T} \int \frac{d^3 \mathbf{k}}{(2\pi)^3 k^0} f_{0i} \tilde{f}_{0i} \left[ \frac{m_i^2}{3E_k} - \left(\frac{1}{3} - c_s^2\right) E_k \right], \quad (23)$$

where  $g_i$  is the degeneracy factor. After computing the spectra from Eq. (20), the two- and three-body decays of unstable particles are computed as in Ref. [80].

### C. Neural networks

To reduce the computational cost of the simulations, deep convolutional neural networks trained in Ref. [41] are utilized here for predicting final-state event-by-event observables at midrapidity. Each neural network takes the discretized initial energy density profile in the transverse-coordinate  $(x, y)$  plane as an input, and outputs one  $p_T$ -integrated observable. Separate neural networks are used to predict flow coefficients  $v_n$ ,



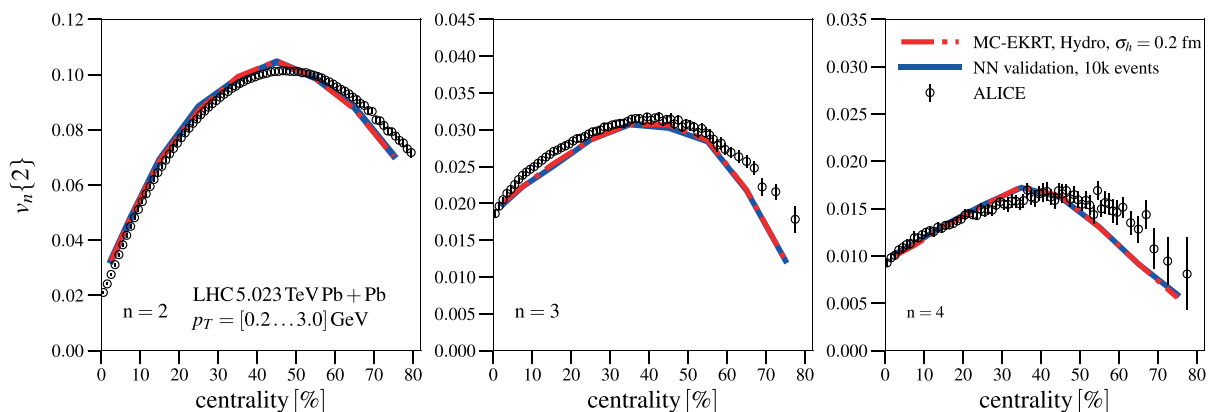


FIG. 1. Neural network validation test for the flow coefficients  $v_2\{2\}$ ,  $v_3\{2\}$ , and  $v_4\{2\}$  in 5.023 TeV Pb+Pb collisions. The networks were trained with the EbyE-EKRT data from Ref. [28] as described in Ref. [41]. The hydro results and the neural network validation results were obtained from 10k MC-EKRT initial states, which included hotspots and multiplicity fluctuations that were not present in the training data. The measured data are from the ALICE Collaboration [81].

charged particle multiplicities  $dN_{\text{ch}}/d\eta$ , and mean transverse momenta  $[p_T]$ . Predicting flow observables with neural networks is many orders of magnitude faster than performing full hydrodynamic simulations. For example, predicting results for  $10^7$  events takes only around 20 h with Nvidia Tesla V100 GPU.

As the training data for the neural networks is from Ref. [28], and the predictions made using these networks emulate the same dynamics as the training data, the viscosities  $\eta/s$ , and  $\zeta/s$ , and other parameters affecting the fluid-dynamical evolution are the same ones as in Ref. [28].

In Ref. [41], it was demonstrated that the neural networks work accurately when using the EbyE version of the EKRT model. However, it is nontrivial that the accuracy of the neural networks, which are trained by the EbyE-EKRT data from Ref. [28], and *not* from MC-EKRT, would extend to the MC-EKRT initial states with hotspots, where the initial geometry can be significantly different. Therefore, the neural networks were validated by generating 10 000 MC-EKRT initial states and comparing the neural network predictions against (2+1)D fluid dynamical simulations for the 5.023 TeV Pb+Pb collision system. The validation tests for the flow coefficients  $v_2$ ,  $v_3$ , and  $v_4$  are shown in Fig. 1. The initial-state parameters used in the validation test were  $\kappa_{\text{sat}} = 2.5$ ,  $K = 2.2$ ,  $\sigma_{\perp} = 0.4$  fm, and  $\sigma_n = 0.2$  fm. The obtained excellent agreement between the fluid dynamical simulations and neural network predictions illustrates the versatility of the neural networks with different initial conditions. Additionally, we have verified that the accuracy of the employed neural networks remains good for other training observables as well.

#### IV. RESULTS

In this section, we present the results of fluid-dynamical simulations with MC-EKRT initial states for midrapidity bulk observables, and compare the results against the earlier EbyE EKRT work [28]. All the fluid dynamical results are generated using our neural networks, and they contain 50 000 collision

events, except the multiplicity distribution results, which are obtained from 150 000 events. As discussed in Sec. III C, the neural network results correspond to the fluid dynamical simulations with the matter properties and decoupling parameters from Ref. [28]. Therefore, any differences between the presented results are due to differences in the initial states.

When examining the effects of the initial-state through final-state observables, it is important to remember that some observables are highly sensitive to the properties of the matter. For instance, the magnitude of flow coefficients is significantly influenced by the shear viscosity to entropy density ratio  $\eta/s$ . In contrast, the ratios of flow coefficients are less sensitive to such details, particularly the ratio between  $v_3$  and  $v_2$ , which can provide valuable insights into the geometry and structure of the initial state [82].

The effect of the Gaussian smearing width  $\sigma_{\perp}$  is demonstrated in Fig. 2, where the ratios of the flow coefficients  $v_2$ ,  $v_3$ , and  $v_4$  in 5.023 TeV Pb+Pb collision system are shown as a function of centrality for different smearing widths. The MC-EKRT initial-state parameters are set to  $\kappa_{\text{sat}} = 1.4$ , and  $K = 2.5$ . Nucleon substructure is not included in these plots. As can be seen in the left panel, the magnitude of flow is sensitive to the Gaussian smearing width  $\sigma_{\perp}$ . However,  $\sigma_{\perp}$  has only little impact on the ratios between the flow coefficients, as shown by the middle and right panels. Therefore, the parameter  $\sigma_{\perp}$  is influencing the flow coefficients in a similar manner as the shear viscosity. Here, and in what follows, we adjust  $\sigma_{\perp}$  to obtain the measured  $v_2$  in midcentral collisions for all different MC-EKRT results. However, we want to emphasize that this is only done to illustrate the capabilities and uncertainties of MC-EKRT. To get the best overall fit to all different observables, a global analysis is needed, but this is beyond the purpose of this study.

An intriguing aspect of the MC-EKRT model is the interplay between the saturation and conservation-law filters. The impact of different filters on the flow coefficients in 5.023 TeV Pb+Pb collisions is illustrated in Fig. 3. In all these scenarios, a value of  $K = 2.5$  is used, while the saturation

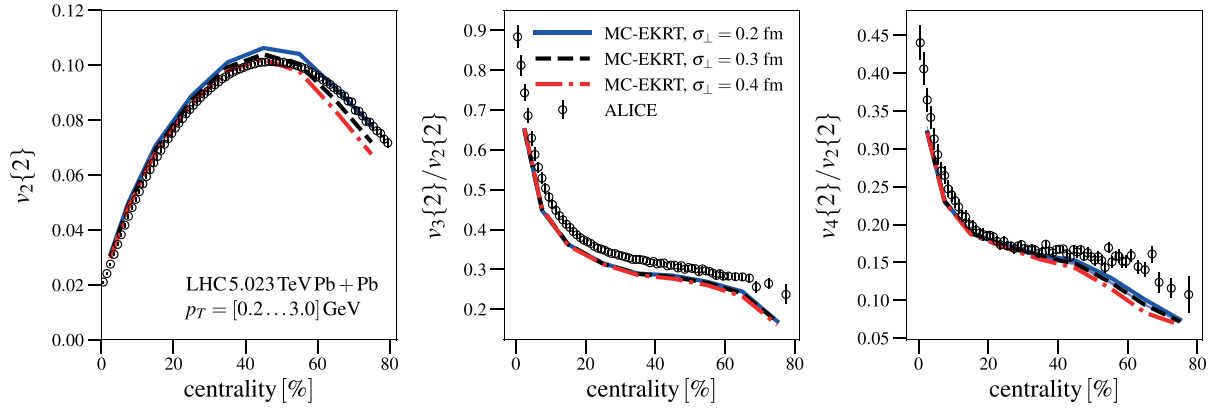


FIG. 2. The effect of the Gaussian smearing width  $\sigma_{\perp}$  on the two-particle flow coefficient  $v_2\{2\}$  (left panel) and the ratios  $v_3\{2\}/v_2\{2\}$  (middle panel), and  $v_4\{2\}/v_2\{2\}$  (right panel) in 5.023 TeV Pb+Pb collisions. No nucleon substructure is included here. The experimental data for the ratios are computed based on the ALICE measurements for the two-particle flow coefficients [81].

parameter  $\kappa_{\text{sat}}$  is adjusted to achieve roughly identical charged particle multiplicities in central collisions. This corresponds to  $\kappa_{\text{sat}} = 1.3$  for the saturation-only case, and  $\kappa_{\text{sat}} = 1.4$  for the other cases. The nucleon width is set according to the default parametrization from Eq. (4), i.e.,  $\sigma_N = 0.53$  fm, and no nucleon substructure is introduced. For the saturation-first case  $\sigma_{\perp} = 0.3$  fm, for the case with all filters at the same time  $\sigma_{\perp} = 0.4$  fm, and for the saturation-only case  $\sigma_{\perp} = 0.3$  fm.

The most notable feature in Fig. 3 is the significant impact of saturation on the ratio between  $v_3$  and  $v_2$ . The case with only saturation reproduces the measured  $v_2$  and  $v_3$  most accurately, while the simultaneous application of all the filters leads to a clear underestimation of  $v_3$ . When saturation is applied before other filters, the results approach those of the saturation-only scenario, as anticipated. The discrepancies in the  $v_3/v_2$  ratio arise from the geometrical differences in saturation and momentum conservation. Saturation does not allow geometrical overlap in the transverse plane. This leads to a more evenly distributed energy density profile. Energy

conservation, on the other hand, gives no direct geometrical constraints. The stronger the saturation the more the eccentricity  $\varepsilon_2$  is suppressed compared to the eccentricity  $\varepsilon_3$ . The reduced eccentricity  $\varepsilon_2$  can be compensated by decreasing the smearing width  $\sigma_{\perp}$  so that the elliptic flow  $v_2$  remains nearly unchanged, while  $\varepsilon_3$  increases. This is reflected in the shown flow coefficients. It is also noteworthy that the  $v_3/v_2$  ratio is very similar between the MC-EKRT model with only saturation and the EbyE-EKRT model, which does not explicitly include momentum conservation. Since strong saturation appears to be necessary for matching the measured  $v_3/v_2$  ratio, we will now focus exclusively on the scenarios where saturation is applied first, followed by the conservation filters. This approach is also theoretically justified because, in principle, saturation should inherently account for conservation laws. However, achieving this would require implementing saturation through momentum-conserving multiparton distributions to all orders, which is not practically feasible.

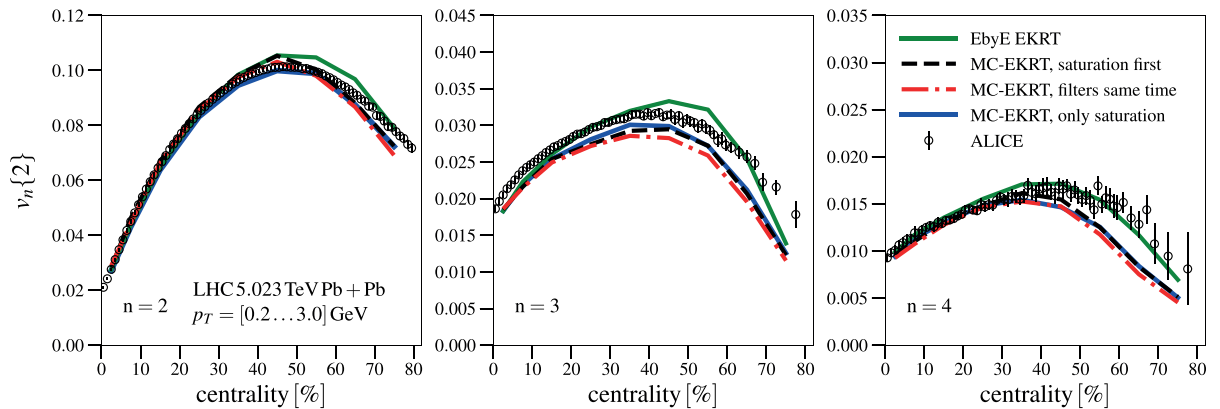


FIG. 3. The flow coefficients  $v_n\{2\}$  as a function of centrality for 5.023 TeV Pb+Pb collisions. The simulation results with different MC-EKRT filter settings are compared against the ALICE measurements [81], and the EbyE-EKRT results from Ref. [28]. No nucleon substructure was included here.

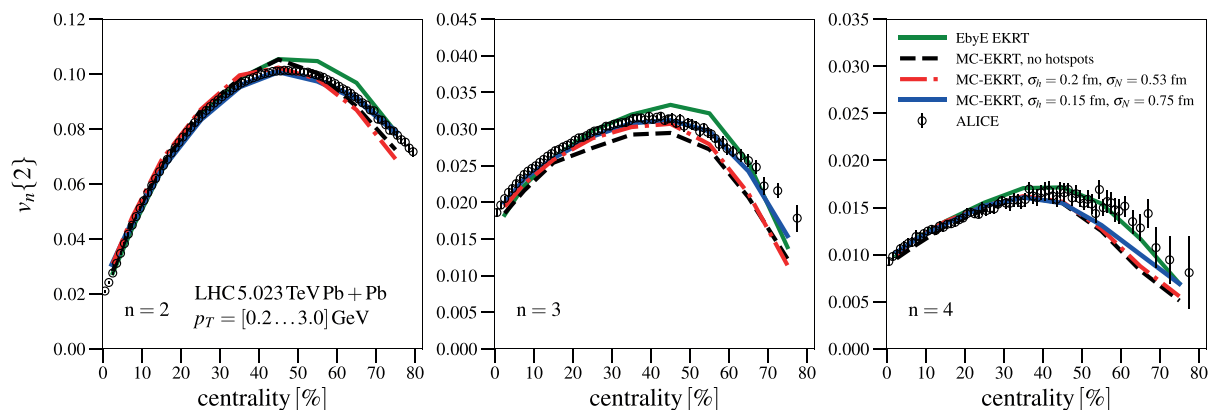


FIG. 4. The flow coefficients  $v_n\{2\}$  as a function of centrality for 5.023 TeV Pb+Pb collisions. The MC-EKRT results with and without nucleon substructure are compared against the ALICE measurements [81], and the EbyE-EKRT results from Ref. [28].

Since saturation is sensitive to the nuclear overlap  $T_A T_B$  (nuclear thickness function  $T_A$  is the sum of  $T_N$ s), the hotspots introduce interesting dynamics. With the hotspots,  $T_A$  can reach  $\approx 10$  times higher values than with the average nucleon geometry. Therefore, one would expect the saturation strength and the  $v_3/v_2$  ratio to increase when hotspots are included.

The effect of hotspots on the flow coefficients is illustrated in Fig. 4, which compares two different hotspot parametrizations. The first parametrization uses the default nucleon width from parametrization Eq. (4), together with hotspots with width  $\sigma_h = 0.2$  fm. In this case, the MC-EKRT parameters are set to  $\kappa_{\text{sat}} = 2.5$ ,  $K = 2.2$ , and  $\sigma_{\perp} = 0.4$  fm. For the second parametrization, the nucleon width is obtained from Eq. (4), but this time a significantly stronger energy dependence with  $\alpha' = 0.6$  is used. This corresponds to a nucleon width  $\sigma_N = 0.75$  fm for 5.023 TeV collision energy. This nucleon width is in line with the many global analyses, where values in the range  $\sim 0.6$ – $1.0$  fm are preferred [33,37,44,83]. With a wider nucleon, a narrower hotspot with  $\sigma_h = 0.15$  fm is used together with parameters  $\kappa_{\text{sat}} = 2.5$ ,  $K = 2.4$ , and  $\sigma_{\perp} = 0.25$  fm. The saturation-first case from Fig. 3 is here left as a reference curve.

As expected, the addition of hotspots appears to increase the  $v_3/v_2$  ratio. The best overall fit to the measurements is obtained with the narrow hotspots, i.e.,  $\sigma_h = 0.15$  fm, corresponding thus to the strongest saturation. In this case, the centrality dependence of  $v_2$ , and  $v_3$  matches nearly perfectly to the ALICE measurements [81], while maintaining a good agreement for  $v_4$ . These findings suggest that the interplay between hotspots and saturation is crucial for the simultaneous description of the flow coefficients and especially of the  $v_3/v_2$  ratio.

In Fig. 5, the flow coefficients are shown for 2.76 TeV Pb+Pb collisions. The different curves correspond to the same cases as in Fig. 4, but the  $K$  factor is adjusted to obtain a reasonable agreement with the measured charged particle multiplicity. The obtained values are  $K = 2.5$  for the  $\sigma_h = 0.2$  fm case, while the  $\sigma_h = 0.15$  fm and the no-hotspots cases both use  $K = 2.7$ . The agreement between the data and the results is quite similar to the 5.023 TeV collision energy results.

At both energies, the narrow-hotspot case with  $\sigma_h = 0.15$  fm can describe the measured flow coefficients well, while the centrality dependence of  $v_2$  is slightly off for the  $\sigma_h = 0.2$  fm case. From Figs. 4 and 5 it can be seen that MC-EKRT with the nucleon substructure captures the energy dependence of the flow coefficients significantly better than the EbyE-EKRT model.

In Fig. 6, the charged particle multiplicity as a function of centrality is shown for the same initial-state parametrizations in 2.76 TeV and 5.023 TeV Pb+Pb collisions. The agreement between the results and the ALICE measurements [84,85] is good in all cases, even though there are some minor discrepancies in the centrality behavior. The initial state without hotspots seems to produce slightly too weak a centrality dependence, while, with the hotspots, the centrality dependence is a bit too steep. However, these are small differences, and further improvements could be obtained by fine tuning the matter properties and initial state parameters.

The MC-EKRT approach adds minijet-multiplicity-originating saturation-scale fluctuations to the EKRT initial state. These fluctuations, together with hotspot fluctuations, should in principle increase the hadron multiplicity fluctuations in the most central collisions. This effect is studied in Fig. 7, where the charged hadron multiplicity distributions from MC-EKRT with and without hotspots are compared against the EbyE-EKRT results, which do not contain multiplicity-originating fluctuations of the saturation scale or hotspots. To make the results comparable with the V0 amplitude measured by ALICE [86], they are normalized to have approximately the same mean as the V0 amplitude. As shown also in Ref. [17], the EbyE-EKRT results almost completely miss the high-multiplicity tail in the distribution. The addition of the further saturation scale fluctuations indeed enhances the high-multiplicity tail in the distribution, and therefore improves the agreement with the measurements as one would expect. The addition of the hotspots is important also for this observable, as it increases the fluctuations and high-multiplicity tail further, leading to a very good agreement with the ALICE data.

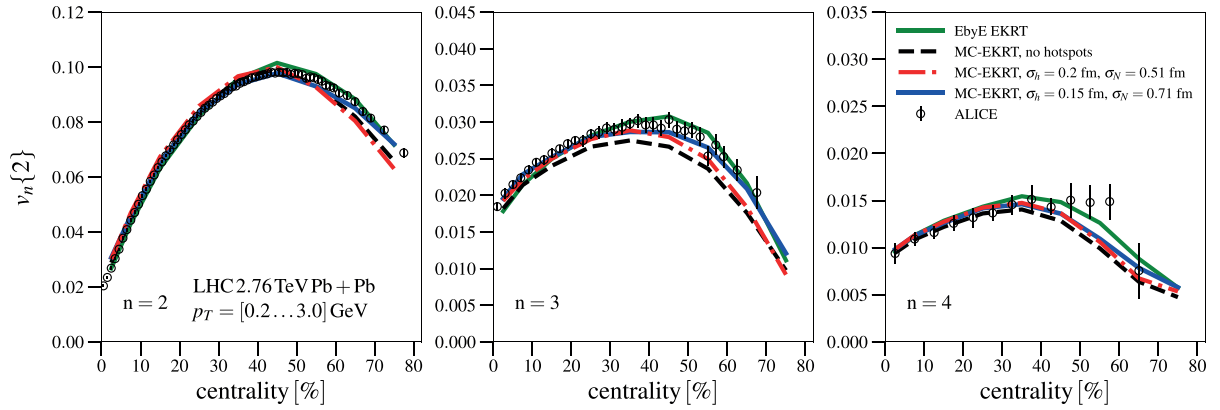


FIG. 5. The flow coefficients  $v_n\{2\}$  as a function of centrality for 2.76 TeV Pb+Pb collisions. The MC-EKRT results with and without nucleon substructure are compared against the ALICE measurements [81], and the EbyE-EKRT results from Ref. [28].

## V. CONCLUSIONS

In this paper, we have studied the effects of the MC-EKRT initial states on midrapidity flow observables. The computationally slow fluid dynamics simulations were replaced with the neural networks, that could predict flow observables directly from the initial state. The networks used here did not contain any information about the MC-EKRT initial states. Even so, the neural networks did accurately describe the flow observables, emphasizing the versatility and usefulness of the neural networks.

We found that essentially the strength of saturation controls the ratio between two-particle flow coefficients  $v_3/v_2$ . Without any nucleon substructure, the measured data preferred that no local momentum conservation was enforced, so that the saturation would be the only effect that regulates the initial low- $p_T$  parton production. The addition of the nucleon substructure enhanced the saturation strength, and led to a good agreement with the measured data, even with the local

momentum conservation imposed. Our flow coefficient results lend support to having relatively narrow hotspots in a relatively wide nucleon, and rather systematic saturation as the decisive QCD mechanism for regulating the initial parton production.

The results from the MC-EKRT initial state with the nucleon substructure managed to improve the agreement with the LHC measurements relative to the previous EbyE-EKRT model. The novel MC-EKRT model now captures the measured energy dependence of the flow coefficients better, while the added saturation scale fluctuations and the inclusion of hotspots systematically improves the agreement with the measured multiplicity distribution in the most central collisions.

Overall, the MC-EKRT results presented here show an excellent agreement with the data for the flow coefficients and the charged particle multiplicity. We want to note that this was achieved even without adjusting the QCD matter properties or the dynamical decoupling conditions from previous works,

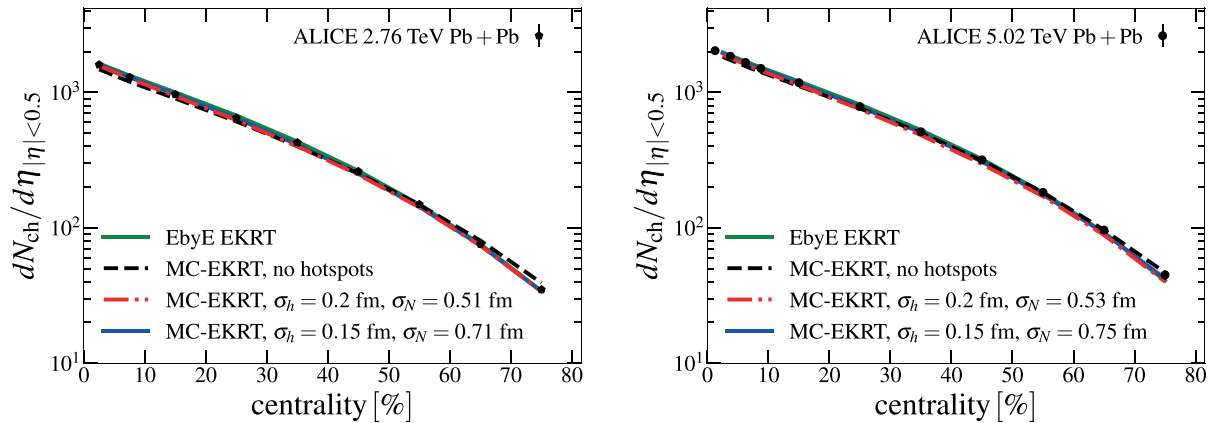


FIG. 6. The charged particle multiplicity as a function of centrality in 2.76 TeV (left panel), and 5.023 TeV (right panel) Pb+Pb collisions. The MC-EKRT results with and without nucleon substructure are compared against the ALICE measurements [84,85], and the EbyE-EKRT results from Ref. [28].

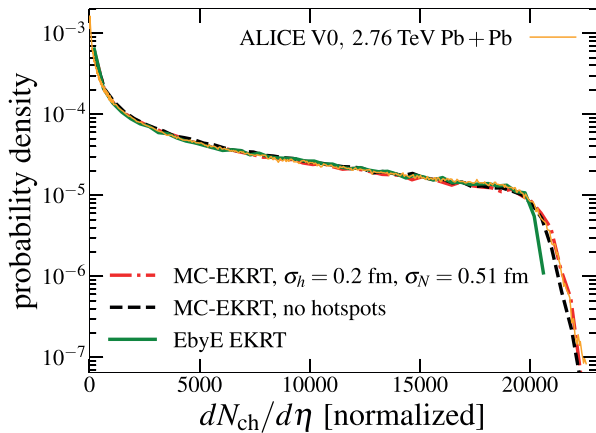


FIG. 7. The probability distribution of charged particle multiplicity for 2.76 TeV Pb+Pb collisions. The MC-EKRT results with and without nucleon substructure are compared against the parametrization of the ALICE V0 amplitude read off from Ref. [86], and the EbyE-EKRT results from Ref. [28].

and therefore this acts as a baseline for what can be achieved. More detailed global analysis with more observables and collision systems should be done to constrain the QCD matter properties. Particularly interesting are the smaller collision

systems, such as proton-nucleus, light-ion, and even proton-proton collisions, which offer also very interesting further tests of the proposed saturation, momentum conservation, and hotspot dynamics, especially because in the smaller systems the effects of fluctuations and longitudinal dynamics become enhanced, see, e.g., Refs. [27,87–93]. Additionally, at the lower collision energies, the finite longitudinal overlap area in the initial collision together with the initial transverse flow can play an important role in the simulations. These aspects were not considered here, but are left as future work.

#### ACKNOWLEDGMENTS

We acknowledge the financial support from the Vilho, Yrjö and Kalle Väisälä Foundation (M.K.) and from the Jenny and Antti Wihuri Foundation (H.H.), and the Academy of Finland Project No. 330448 (K.J.E.). This research was funded as a part of the Center of Excellence in Quark Matter of the Academy of Finland (Projects No. 346325 and No. 364192). This research is part of the European Research Council Project No. ERC-2018-ADG-835105 YoctoLHC, and the European Union’s Horizon 2020 research and innovation program under Grant Agreement No. 824093 (STRONG-2020). We acknowledge the computation resources from the Finnish IT Center for Science (CSC), project jyy2580, and from the Finnish Computing Competence Infrastructure (FCCI), persistent identifier urn:nbn:fi:research-infras-2016072533.

- [1] S. Acharya *et al.* (ALICE Collaboration), *Eur. Phys. J. C* **84**, 813 (2024).
- [2] A. Bazavov, P. Petreczky, and J. H. Weber, *Phys. Rev. D* **97**, 014510 (2018).
- [3] S. Borsanyi, Z. Fodor, C. Hoelbling, S. D. Katz, S. Krieg, and K. K. Szabo, *Phys. Lett. B* **730**, 99 (2014).
- [4] P. Romatschke and U. Romatschke, *Phys. Rev. Lett.* **99**, 172301 (2007).
- [5] M. Luzum and P. Romatschke, *Phys. Rev. C* **78**, 034915 (2008); **79**, 039903(E) (2009).
- [6] P. Božek, *Phys. Rev. C* **81**, 034909 (2010).
- [7] P. Božek and I. Wyskiel-Piekarska, *Phys. Rev. C* **85**, 064915 (2012).
- [8] B. Schenke, S. Jeon, and C. Gale, *Phys. Rev. Lett.* **106**, 042301 (2011).
- [9] B. Schenke, S. Jeon, and C. Gale, *Phys. Rev. C* **82**, 014903 (2010).
- [10] B. Schenke, S. Jeon, and C. Gale, *Phys. Rev. C* **85**, 024901 (2012).
- [11] H. Song, S. A. Bass, and U. Heinz, *Phys. Rev. C* **83**, 054912 (2011); **87**, 019902 (2013).
- [12] H. Niemi, G. S. Denicol, P. Huovinen, E. Molnar, and D. H. Rischke, *Phys. Rev. Lett.* **106**, 212302 (2011).
- [13] L. Pang, Q. Wang, and X. N. Wang, *Phys. Rev. C* **86**, 024911 (2012).
- [14] C. Gale, S. Jeon, B. Schenke, P. Tribedy, and R. Venugopalan, *Phys. Rev. Lett.* **110**, 012302 (2013).
- [15] H. Niemi, G. S. Denicol, P. Huovinen, E. Molnar, and D. H. Rischke, *Phys. Rev. C* **86**, 014909 (2012).
- [16] J. Noronha-Hostler, G. S. Denicol, J. Noronha, R. P. G. Andrade, and F. Grassi, *Phys. Rev. C* **88**, 044916 (2013).
- [17] H. Niemi, K. J. Eskola, and R. Paatelainen, *Phys. Rev. C* **93**, 024907 (2016).
- [18] G. Denicol, A. Monnai, and B. Schenke, *Phys. Rev. Lett.* **116**, 212301 (2016).
- [19] S. Ryu, J. F. Paquet, C. Shen, G. S. Denicol, B. Schenke, S. Jeon, and C. Gale, *Phys. Rev. Lett.* **115**, 132301 (2015).
- [20] L. G. Pang, H. Petersen, G. Y. Qin, V. Roy, and X. N. Wang, *Eur. Phys. J. A* **52**, 97 (2016).
- [21] I. A. Karpenko, P. Huovinen, H. Petersen, and M. Bleicher, *Phys. Rev. C* **91**, 064901 (2015).
- [22] G. Giacalone, J. Noronha-Hostler, M. Luzum, and J. Y. Ollitrault, *Phys. Rev. C* **97**, 034904 (2018).
- [23] P. Božek and W. Broniowski, *Phys. Rev. C* **97**, 034913 (2018).
- [24] L. G. Pang, H. Petersen, and X. N. Wang, *Phys. Rev. C* **97**, 064918 (2018).
- [25] A. Sakai, K. Murase, and T. Hirano, *Phys. Rev. C* **102**, 064903 (2020).
- [26] G. Nijs, W. van der Schee, U. Gürsoy, and R. Snellings, *Phys. Rev. C* **103**, 054909 (2021).
- [27] C. Shen and B. Schenke, *Phys. Rev. C* **105**, 064905 (2022).
- [28] H. Hirvonen, K. J. Eskola, and H. Niemi, *Phys. Rev. C* **106**, 044913 (2022).
- [29] J. Novak, K. Novak, S. Pratt, J. Vredevoogd, C. Coleman-Smith, and R. L. Wolpert, *Phys. Rev. C* **89**, 034917 (2014).
- [30] J. E. Bernhard, J. S. Moreland, S. A. Bass, J. Liu, and U. Heinz, *Phys. Rev. C* **94**, 024907 (2016).



- [31] S. A. Bass, J. E. Bernhard, and J. S. Moreland, *Nucl. Phys. A* **967**, 67 (2017).
- [32] J. E. Bernhard, J. S. Moreland, and S. A. Bass, *Nat. Phys.* **15**, 1113 (2019).
- [33] D. Everett *et al.* (JETSCAPE Collaboration), *Phys. Rev. C* **103**, 054904 (2021).
- [34] J. Auvinen, K. J. Eskola, P. Huovinen, H. Niemi, R. Paatelainen, and P. Petreczky, *Phys. Rev. C* **102**, 044911 (2020).
- [35] J. E. Parkkila, A. Onnerstad, and D. J. Kim, *Phys. Rev. C* **104**, 054904 (2021).
- [36] J. E. Parkkila, A. Onnerstad, S. F. Taghavi, C. Mordasini, A. Bilandzic, M. Virta, and D. J. Kim, *Phys. Lett. B* **835**, 137485 (2022).
- [37] G. Nijs and W. van der Schee, [arXiv:2304.06191](https://arxiv.org/abs/2304.06191).
- [38] J. Auvinen, J. E. Bernhard, S. A. Bass, and I. Karpenko, *Phys. Rev. C* **97**, 044905 (2018).
- [39] A. Mankolli *et al.* (JETSCAPE Collaboration), *EPJ Web Conf.* **296**, 05010 (2024).
- [40] D. Soeder, W. Ke, J. F. Paquet, and S. A. Bass, [arXiv:2306.08665](https://arxiv.org/abs/2306.08665).
- [41] H. Hirvonen, K. J. Eskola, and H. Niemi, *Phys. Rev. C* **108**, 034905 (2023).
- [42] H. Hirvonen, K. J. Eskola, and H. Niemi, *EPJ Web Conf.* **296**, 02002 (2024).
- [43] H. Huang, B. Xiao, Z. Liu, Z. Wu, Y. Mu, and H. Song, *Phys. Rev. Res.* **3**, 023256 (2021).
- [44] J. S. Moreland, J. E. Bernhard, and S. A. Bass, *Phys. Rev. C* **101**, 024911 (2020).
- [45] K. J. Eskola, K. Kajantie, P. V. Ruuskanen, and K. Tuominen, *Nucl. Phys. B* **570**, 379 (2000).
- [46] K. J. Eskola, K. Kajantie, and K. Tuominen, *Phys. Lett. B* **497**, 39 (2001).
- [47] R. Paatelainen, K. J. Eskola, H. Niemi, and K. Tuominen, *Phys. Lett. B* **731**, 126 (2014).
- [48] K. Kajantie, P. V. Landshoff, and J. Lindfors, *Phys. Rev. Lett.* **59**, 2527 (1987).
- [49] K. J. Eskola, K. Kajantie, and J. Lindfors, *Nucl. Phys. B* **323**, 37 (1989).
- [50] H. Niemi, K. J. Eskola, R. Paatelainen, and K. Tuominen, *Phys. Rev. C* **93**, 014912 (2016).
- [51] K. J. Eskola, H. Niemi, R. Paatelainen, and K. Tuominen, *Phys. Rev. C* **97**, 034911 (2018).
- [52] H. Niemi, K. J. Eskola, R. Paatelainen, and K. Tuominen, *Nucl. Phys. A* **982**, 443 (2019).
- [53] M. Kuha, J. Auvinen, K. J. Eskola, H. Hirvonen, Y. Kanakubo, and H. Niemi, [arXiv:2406.17592](https://arxiv.org/abs/2406.17592).
- [54] J. R. Cudell *et al.* (COMPETE Collaboration), *Phys. Rev. Lett.* **89**, 201801 (2002).
- [55] G. Antchev *et al.* (TOTEM Collaboration), *Eur. Phys. J. C* **79**, 103 (2019).
- [56] S. Chekanov *et al.* (ZEUS Collaboration), *Eur. Phys. J. C* **24**, 345 (2002).
- [57] K. J. Eskola, C. A. Flett, V. Guzey, T. Löytäinen, and H. Paukkunen, *Phys. Rev. C* **106**, 035202 (2022).
- [58] I. Helenius, K. J. Eskola, H. Honkanen, and C. A. Salgado, *J. High Energy Phys.* **07** (2012) 073.
- [59] K. J. Eskola, H. Paukkunen, and C. A. Salgado, *J. High Energy Phys.* **04** (2009) 065.
- [60] S. Dulat, T. J. Hou, J. Gao, M. Guzzi, J. Huston, P. Nadolsky, J. Pumplin, C. Schmidt, D. Stump, and C. P. Yuan, *Phys. Rev. D* **93**, 033006 (2016).
- [61] X. N. Wang and M. Gyulassy, *Phys. Rev. D* **44**, 3501 (1991).
- [62] H. Mäntysaari and B. Schenke, *Phys. Rev. Lett.* **117**, 052301 (2016).
- [63] J. S. Moreland, J. E. Bernhard, and S. A. Bass, *Phys. Rev. C* **92**, 011901 (2015).
- [64] A. Aktas *et al.* (The H1 Collaboration), *Eur. Phys. J. C* **46**, 585 (2006).
- [65] C. Loizides, *Phys. Rev. C* **94**, 024914 (2016).
- [66] P. Bożek, W. Broniowski, M. Rybczynski, and G. Stefanek, *Comput. Phys. Commun.* **245**, 106850 (2019).
- [67] P. Huovinen and P. Petreczky, *Nucl. Phys. A* **837**, 26 (2010).
- [68] H. Bebie, P. Gerber, J. L. Goity, and H. Leutwyler, *Nucl. Phys. B* **378**, 95 (1992).
- [69] T. Hirano and K. Tsuda, *Phys. Rev. C* **66**, 054905 (2002).
- [70] P. Huovinen, *Eur. Phys. J. A* **37**, 121 (2008).
- [71] W. Israel and J. M. Stewart, *Ann. Phys. (NY)* **118**, 341 (1979).
- [72] G. S. Denicol, T. Koide, and D. H. Rischke, *Phys. Rev. Lett.* **105**, 162501 (2010).
- [73] G. S. Denicol, H. Niemi, E. Molnar, and D. H. Rischke, *Phys. Rev. D* **85**, 114047 (2012); **91**, 039902(E) (2015).
- [74] E. Molnár, H. Niemi, G. S. Denicol, and D. H. Rischke, *Phys. Rev. D* **89**, 074010 (2014).
- [75] G. S. Denicol, S. Jeon, and C. Gale, *Phys. Rev. C* **90**, 024912 (2014).
- [76] P. Huovinen and H. Petersen, *Eur. Phys. J. A* **48**, 171 (2012).
- [77] A. Hosoya and K. Kajantie, *Nucl. Phys. B* **250**, 666 (1985).
- [78] S. Gavin, *Nucl. Phys. A* **435**, 826 (1985).
- [79] C. Sasaki and K. Redlich, *Phys. Rev. C* **79**, 055207 (2009).
- [80] J. Sollfrank, P. Koch, and U. W. Heinz, *Z. Phys. C* **52**, 593 (1991).
- [81] S. Acharya *et al.* (ALICE Collaboration), *J. High Energy Phys.* **07** (2018) 103.
- [82] E. Retinskaya, M. Luzum, and J. Y. Ollitrault, *Phys. Rev. C* **89**, 014902 (2014).
- [83] G. Nijs, W. van der Schee, U. Gürsoy, and R. Snellings, *Phys. Rev. Lett.* **126**, 202301 (2021).
- [84] K. Aamodt *et al.* (ALICE Collaboration), *Phys. Rev. Lett.* **106**, 032301 (2011).
- [85] J. Adam *et al.* (ALICE Collaboration), *Phys. Rev. Lett.* **116**, 222302 (2016).
- [86] B. Abelev *et al.* (ALICE Collaboration), *Phys. Rev. C* **88**, 044909 (2013).
- [87] P. Bożek and W. Broniowski, *Phys. Rev. C* **88**, 014903 (2013).
- [88] R. D. Weller and P. Romatschke, *Phys. Lett. B* **774**, 351 (2017).
- [89] H. Mäntysaari, B. Schenke, C. Shen, and P. Tribedy, *Phys. Lett. B* **772**, 681 (2017).
- [90] W. Zhao, C. M. Ko, Y. X. Liu, G. Y. Qin, and H. Song, *Phys. Rev. Lett.* **125**, 072301 (2020).
- [91] B. Schenke, C. Shen, and P. Tribedy, *Phys. Rev. C* **102**, 044905 (2020).
- [92] W. Zhao, S. Ryu, C. Shen, and B. Schenke, *Phys. Rev. C* **107**, 014904 (2023).
- [93] Z. Wu, B. Fu, S. Zhao, R. Liu, and H. Song, *Chin. Phys. C* **48**, 104102 (2024).